



HAL
open science

Growth and characterization of lead-free (K, Na)NbO₃-based piezoelectric single crystals

Hairui Liu

► **To cite this version:**

Hairui Liu. Growth and characterization of lead-free (K, Na)NbO₃-based piezoelectric single crystals. Material chemistry. Université de Bordeaux; Technische Universität (Darmstadt, Allemagne), 2016. English. NNT : 2016BORD0197 . tel-01430337

HAL Id: tel-01430337

<https://theses.hal.science/tel-01430337>

Submitted on 9 Jan 2017

HAL is a multi-disciplinary open access archive for the deposit and dissemination of scientific research documents, whether they are published or not. The documents may come from teaching and research institutions in France or abroad, or from public or private research centers.

L'archive ouverte pluridisciplinaire **HAL**, est destinée au dépôt et à la diffusion de documents scientifiques de niveau recherche, publiés ou non, émanant des établissements d'enseignement et de recherche français ou étrangers, des laboratoires publics ou privés.

université
de **BORDEAUX**



TECHNISCHE
UNIVERSITÄT
DARMSTADT

THÈSE EN COTUTELLE PRÉSENTÉE

POUR OBTENIR LE GRADE DE

DOCTEUR DE

L'UNIVERSITÉ DE BORDEAUX

ET DE TECHNISCHE UNIVERSITÄT DARMSTADT

ÉCOLE DOCTORALE UBX

ÉCOLE DOCTORALE DU PARTENAIRE

SPÉCIALITÉ : Physico-Chimie de la Matière Condensée

Par Hairui LIU

**Growth and Characterization of Lead-free
(K,Na)NbO₃-based Piezoelectric Single Crystals**

Sous la direction de M Jürgen Rödel et M Philippe Veber

Soutenue le : 19 Octobre 2016

Membres du jury:

M. Wolfgang Donner	Professeur, TU Darmstadt, Allemagne	Président
M. Philippe Papet	Professeur, CNRS, ICGM, France	Rapporteur
M. Kyle G. Webber	Professeur, FAU Erlangen-Nürnberg, Allemagne	Rapporteur
M. Jürgen Rödel	Professeur, TU Darmstadt, Allemagne	Directeur de thèse
M. Philippe Veber	Ingénieur de Recherche CNRS, ICMCB, France	Directeur de thèse
M. Mario Maglione	Directeur de recherche CNRS, ICMCB, France	Co-directeur de thèse
M. Dragan Damjanovic	Professeur, EPFL, Suisse	Examineur
M. Daniel Rytz	Dr, FEE GmbH, Allemagne	Examineur
M. Hans-Joachim Kleebe	Professeur, TU Darmstadt, Allemagne	Invité



TECHNISCHE
UNIVERSITÄT
DARMSTADT

université
de **BORDEAUX**

Characterization of Lead-free (K,Na)NbO₃-based Piezoelectric Single Crystals

Vom Fachbereich
Material- und Geowissenschaften
der Technischen Universität Darmstadt
und dem
CNRS, ICMCB
L'Université de Bordeaux
zur Erlangung des akademischen Grades eines Doktor-Ingenieurs (Dr.-Ing.)
genehmigte Dissertation

von

Hairui Liu, M.Sc.

geboren am 28. Dezember 1989 in Xuchang, Henan, China

1. Gutachten: Prof. Dr. Jürgen Rödel
2. Gutachten: Research Director Dr. Mario Maglione

D17

Darmstadt 2016

Growth and Characterization of Lead-free (K,Na)NbO₃-based Piezoelectric Single Crystals

Genehmigte Dissertation von Hairui Liu, M.Sc.

1. Gutachten: Prof. Dr. Jürgen Rödel
2. Gutachten: Research Director Dr. Mario Maglione

Tag der Einreichung: 02.09.2016

Tag der Prüfung: 19.10.2016

Darmstadt — D 17

Bitte zitieren Sie dieses Dokument als:

URN: [urn:nbn:de:tuda-tuprints-57693](https://nbn-resolving.org/urn:nbn:de:tuda-tuprints-57693)

URL: <http://tuprints.ulb.tu-darmstadt.de/id/user/7146>

Dieses Dokument wird bereitgestellt von tuprints,

E-Publishing-Service der TU Darmstadt

<http://tuprints.ulb.tu-darmstadt.de>

tuprints@ulb.tu-darmstadt.de



Die Veröffentlichung steht unter folgender Creative Commons Lizenz:

Namensnennung – Keine kommerzielle Nutzung – Keine Bearbeitung 4.0 International

<http://creativecommons.org/licenses/by-nc-nd/4.0/>

Do not, for one repulse, give up the purpose that you resolved to effect.

----William Shakespeare

不要只因为一次失败，就放弃你原来决心想达到的目的。

----莎士比亚

Contents

Acknowledgements	III
List of Figures	VII
List of Tables.....	XIII
List of Symbols	XV
Résumé (French)	XIX
Abstract (English)	XXI
1 Introduction	1
2 Theory and Literature Review	3
2.1 Fundamentals of Ferroelectrics.....	3
2.1.1 Dielectrics.....	3
2.1.2 Piezoelectrics.....	5
2.1.3 Ferroelectrics.....	5
2.1.4 Phase Transitions.....	9
2.1.5 Defects in Perovskite Structure	13
2.2 Fundamentals of Crystal Growth	14
2.2.1 Top-seeded Solution Growth.....	16
2.2.2 Czochralski Method	17
2.2.3 Bridgman-Stockbarger Method.....	18
2.2.4 Conventional Flux Growth Method	19
2.2.5 Submerged-seed Solution Growth.....	21
2.2.6 Solid State Crystal Growth.....	21
2.3 $K_xNa_{1-x}NbO_3$ Polycrystalline Ceramics	22
2.3.1 Li Substitution	24
2.3.2 Sb Substitution	25
2.3.3 Ta Substitution	25
2.3.4 Li, Sb, and /or Ta Substitution	26
2.3.5 Mn Doping	26
2.3.6 The Origin of Enhanced Piezoelectricity in KNN-based Systems	28
2.4 KNN-based Single Crystals	30
2.4.1 Growth of KNN-based Single Crystals	30
2.4.2 Piezoelectric and Ferroelectric Properties	35
2.4.3 Ferroelectric Domains in KNN-based Single Crystals.....	38
3 Experimental Procedure	39
3.1 Crystal Growth.....	39
3.1.1 Submerged-seed Solution Growth.....	39
3.1.2 Top-seeded Solution Growth.....	41
3.2 Chemical Characterization.....	41
3.2.1 Electron Probe Micro Analysis	41
3.2.2 Inductively Coupled Plasma Optical Emission Spectrometry.....	42
3.2.3 The Accuracy of Element Concentrations.....	42
3.3 Structural Characterization	43
3.3.1 X-ray Diffraction.....	43
3.3.2 Laue X-ray Diffraction and Crystal Cutting.....	44
3.3.3 Raman Spectroscopy	45
3.4 Electrical Characterization.....	45
3.4.1 Dielectric Properties	45
3.4.2 Large-signal Electrical Properties	46
3.4.3 Small-signal Electrical Properties	48
3.4.4 Piezoelectric Properties	48

3.5	Transmission Electron Microscopy	49
3.6	Other Techniques	49
3.6.1	Mössbauer Spectroscopy	49
3.6.2	Electron Paramagnetic Resonance	50
4	Crystal Growth, Structural Properties, and Domains	51
4.1	Crystal Growth	51
4.1.1	Initial Compositions and Crystal Growth Results	51
4.1.2	Crystal Compositions	53
4.1.3	Element Segregation	55
4.2	Secondary Phase	61
4.2.1	Phase Structure	61
4.2.2	Influence of Alkali Ion Concentration and K/Li ratio	62
4.3	Temperature Dependence of Structural and Domain Configurations	64
4.3.1	Phase Evolution with Temperature	64
4.3.2	Polarized Light Microscopy	65
4.3.3	Transmission Electron Microscopy	72
4.4	Summary	74
5	Composition Dependence of Phase Transitions and Electrical Properties	77
5.1	Influence of Ta Substitution	77
5.1.1	Crystallographic Structures and Phase Transitions	77
5.1.2	Influence of Ta Content on Room Temperature Electromechanical Properties	80
5.1.3	Temperature-dependent Electromechanical Properties	84
5.1.4	Summary	86
5.2	Influence of Sb Substitution	87
5.2.1	Phase Transition	87
5.2.2	Influence of Annealing on Permittivity	88
5.2.3	Electromechanical Properties	89
5.2.4	¹²¹ Sb Mössbauer Spectra	99
5.2.5	Mechanism of Enhanced Electrical Properties after Annealing in O ₂	101
5.2.6	Summary	103
5.3	Influence of Mn Doping	104
6	Influence of Crystallographic Orientation	109
6.1	Phase and Phase Transitions	110
6.2	Electromechanical Properties	111
6.3	Influence of Electric Field on Electromechanical Properties	114
6.4	Summary	119
7	Remarks and Outlook	121
	Appendix	123
	References	127
	Curriculum Vitae	147

Acknowledgements

The research work presented in this thesis has been carried out under the support of an Erasmus Mundus Joint Doctorate project - the International Doctoral School in Functional Materials (IDS-FunMat), with the collaboration between Nichtmetallisch-Anorganische Werkstoffe (NAW) group at Technische Universität Darmstadt (Darmstadt, Germany), Crystal Growth, High-Pressure, Sintering, Thin Films group at the Institut de la Chimie et de la Matière Condensée de Bordeaux (Bordeaux, France), and the industrial partner, Forschungsinstitut für mineralische und metallische Werkstoffe - Edelsteine/Edelmetalle (FEE) GmbH (Idar-Oberstein, Germany). Since I started my work on 1st, Oct. 2013, I have received many supports and helps from people around me, who I would like to acknowledge here.

First and foremost, I would like to thank my three mentors, Prof. Jürgen Rödel, Dr. Philippe Veber, and Director Dr. Mario Maglione for providing the chance to work in this project and to enjoy the two different kinds of culture in both Germany and France. Moreover, I am very grateful for their selfless academic and scientific support. As the vice president of TU Darmstadt or director of ICMCB, Prof. Rödel and Mario kept scheduling the meeting with me on their full calendars monthly. I, myself, have been upset with the fruitless first year. However, both of them did not show any disappointment with me (at least not obviously), which to some extent encouraged me to move forward.

A special thanks goes to my two supervisors, Dr. Jurij Koruza and Dr. Philippe Veber. As a frequent visitor to their offices, I always received helpful suggestions and information from both wonderful supervisors. They even did not forget to take care of my work when I moved to the other university. I benefitted greatly from their patient scientific share and discussions. More than that, they also helped me a lot to correct and polish my thesis, papers, and posters. I will not forget their encouragement and contributions to my three-year study in Europe. They are more than supervisors or colleagues for me. Thank you so much for this three-year taking-care.

The next acknowledgement goes to Dr. Daniel Rytz, who was my industrial contact. He supplied several crystals for this thesis, which provided me more chance for understanding the perovskite system I focused on. We knew each other when he visited Bordeaux in 2015. As compared to his expertise, my questions on crystal growth and orientations were probably too naive. He, however, always guided me patiently and inspired me to search for the answers. Most importantly, whenever I asked help, he never said no but encouraged me. I am really appreciated all his guidance and suggestions.

I would like to give my thanks to Prof. Philippe Papet from Montpellier (France), Prof. Kyle Webber from Erlangen (Germany), Prof. Rödel, and Mario for reviewing my thesis. I also would like to thank Prof. Wolfgang Donner (Darmstadt), Prof. Hans-Joachim Kleebe (Darmstadt), Prof. Dragan

Damjanovic (Switzerland) for being my committee board members. Thank you again, all my committee members, for the suggested discussion and/or for their long travel to Darmstadt without any hesitation. A special thanks goes to Prof. Dragan Damjanovic, who gave me some suggestions when he visited Bordeaux.

I want to express my gratitude to all colleagues at ICMCB and TU Darmstadt.

As a wonderful engineer at ICMCB, Viraphong Oudomsack built the furnace for us, which promoted our work forwards. I also want to acknowledge supports from Dr. Michel Lahaye, Dr. Nicolas Penin, and Mrs. Laetitia Etienne on chemical analysis, from Mr. Eric Lebraud on XRD measurements, and from Dr. Michaël Josse on dielectric measurements, and from Dr. Mathieu Duttine on EPR measurements. A special thanks goes to all colleagues in the crystal growth group, Dr. Matias Velazquez, Dr. Stanislav Pechev, Engineer Ms. Sonia Buffiere, Dr. Mythili Prakasam, Dr. Gabriel Buşe, and PhD student Xin Cong.

Most of work on electrical measurements in this project was performed at the NAW group of TU Darmstadt. I would like to first thank my two Chinese colleagues, Dr. Jiadong Zang and Jr.-Prof. Haibo Zhang. Although it sounds somehow shameful, I have to admit that my first days in Darmstadt were not so smooth. Both of them helped me to adapt me to the new environment. Jiadong also went to the airport to pick up me. Now, although I have to leave soon, I feel like I am one of the NAW group. This benefits greatly from everyone's help in NAW group, especially after I moved again to Darmstadt from Bordeaux. I am very grateful to Dr. Yoshitaka Ehara, Dr. Deborah Schneider, M.Sc. Virginia Rojas, Dr. Eric Patterson, and also other colleagues for the technique supports. A special thanks goes to Jurij, Eric, M.Sc. Azatuhi Ayrikyan, Dr. Florian Schader, Dr. Deborah Schneider, and M.Sc. Sebastian Steiner, Yoshi, Dr. Martin Blömker, M.Sc. Malte Vögler, and Dipl.-Ing. Daniel Isaia for encouraging me to talk more and more. As my two uncles, Jurij and Eric took care of me a lot and encouraged me to be into this big family. If you asked me my first time to attend a party in Europe, I have to mention Azatuhi. She first showed me Darmstadt and then invited me to join a small party in 2013. I almost knew nothing about what they were talking and honestly did not join the talk, but this motivated me to talk with people around. I will also remember the nice talks and jokes with my officemates, Florian, Debbi, and Sebastian. More than that, they are actually important parts of my nice German translator group. I would like to thank other members in our beer party club or in our Pokemen Go club, including M.Sc. Peter Keil, M.Sc. Florian Weyland, M.Sc. Patrick Breckner, M.Sc. Lukas Porz, Dr. Hongliang Du, Dr. Matias Acosta, Dr. In-Tae Seo, and M.Sc. Jan Schultheiß. I am also grateful to our engineer Michael Heyse for his useful support during sample preparation processing, from cutting to polishing. I also would like to thank all the group leaders and postdocs for their kind help, Dr. Till Frömmling, Dr. Nikola Novak, and Dr. Lalitha Kodumdi venkataraman. My appreciation extends to all former staff of NAW group, Prof.

Wook Jo for giving me the second interview, Gundel Fliß for setting my computer, and Roswita Geier, Dr. Eva Sapper, Dr. Raschid Baraki, and Dipl.-Ing. Philipp Geiger. I had a great time with them.

The supports from other collaborators contributes a lot to my work. Prof. Wolfgang Donner and Florian Pforr showed me how the Laue diffraction setup works. Dr. Leopoldo Molina-Luna and Alexander Zintler discussed with me about TEM measurements and Alex worked a lot for preparation and measurements of TEM samples. The special thanks goes to Prof. Pavel B. Fabritchnyi and Dr. Mikhail I. Afanasov from Moscow State University (Russia) for measuring the Mössbauer spectroscopy, which supports our work greatly. I never imagined that I would manage to visit Spring 8 (Japan) and ESRF (Grenoble) for synchrotron XRD measurements. I enjoyed my visiting to Japan Spring 8 and ESRF, which was due to the help of Prof. Shintaro Yasui (Tokyo Institute of Technology, Japan), my colleague from Darmstadt Yoshi, and Prof. John Daniels (University of New South Wales, Australia). I am also grateful to M.Sc. Xijie Jiang and M.Sc. Na Liu for performing PFM measurements on my samples. It is highly appreciated for me to have the experience of working with them.

Three persons made great contributions to this project: Gila Völzke, Audrey Sidobre, and Christopher Niesen. They explained many stuffs in TU Darmstadt and University Bordeaux when I was new. They helped me to organize my travels, my registration in universities and more. Thank you, all, for making my study and travel easier.

I am very grateful all the friends I met in IDS-FunMat projects: Szu-Hsuan Lee, Sergey A. Basov, Phuong Tuyen, Shun Kashiwaya, Ruihao Qiu, Jiang Xu, and so on. It is really great that I have friends like you. I will remember our discussions, our foods, and our jokes.

One great pity during my three-year study here is I did not learn German or French. My joy of my stay is inseparable from my German/French translators as well as Google Translate. Except all colleagues abovementioned, I would like to give my special thanks to M.Sc. Mengzhe Xiao (Bordeaux), M.Sc. Pan Hu (Darmstadt), and M.Sc. Ying Zhao (Darmstadt). They helped a lot during my stay in France or Germany. They accompanied me to the immigration office, to doctors, and sometimes to shopping, for translating. Thank you, girls, for helping me so much. I therefore would like to acknowledge a special group: my Chinese friends in both cities. I will not forget my first Darmstadt night in Ying's apartment, the Ladies' nights with Na and Pan, the scientific or life-related discussion with Yangbin Ma or Shuai Wang, help without any hesitation from Li Zhao and Hongliang during my defense period. I also would like to thank Ying Liu, Xijie Jiang, Zeying Zhang, Jiquan Liu, Jingnan Shi, Shengyuan Liu, Hongguang Wang, Wenjie Li, Jia Yuan, Qingbo Wen, and so on, for all kind help. Although I have already left Bordeaux one and half years, I still remember the food prepared by Mengzhe, Ruie, Yijun, and Xuesong, and the time we were seated around for eating or playing cards. Thank you, all Chinese friends I met in

Bordeaux, including Xiang Wang, Xuan Wang, Xiaobo Hu and Zhen Zhang. A special thanks goes to my landlady in Darmstadt, Ms. Marianne Mayer, who took care of me like my mother.

I would like to thank my boyfriend Zhanlue Yang for supporting me and for bearing all my abnormal emotion.

My last thanks goes to my family. The supports and encouragements from my parents, my brother Haitao, my uncles, and my aunts motivates me to be optimistic and to be brave throughout my life.

I donot know when it started but I started to be used to German and French accents when I am out of both counties. I feel excited when I heard both languages wherever I was. I am very grateful to all the people I met during my stay. I do not know how many colleagues will read the acknowledgements. I believe in twenty or thirty years later, when I re-read it, it will remind me of my wonderful stay in both cities. Thank you again, everyone, for joining in my life and all my best.

List of Figures

Figure 2.1. Frequency-dependence of the real part of the dielectric permittivity [12].	4
Figure 2.2. (a) Ferroelectric hysteresis and (b) field-induced strain curves of a typical ferroelectric ceramic. The corresponding domain orientations under various fields: (c) $E=0$, (d) $E=E_{\max}$, (e) $E=0$, and (f) $E=-E_C$.	6
Figure 2.3. (a) Neutral, (b) “head-to-head”, and (c) “tail-to-tail” type of 180 ° domain walls, and (d) neutral, (e) “head-to-head” and (f) “tail-to-tail” type of 90 ° domain walls.	8
Figure 2.4. Schematic of the perovskite structure ABO_3 .	9
Figure 2.5. The orientation of P_S for various crystallographic structures: (a) rhombohedral, (b) orthorhombic, and (c) tetragonal phases. Please note that the distortions with respect to the cubic phase are exaggerated in the drawings for better visibility.	10
Figure 2.6. Temperature dependences of (a) dielectric properties and (b) polarization of a $[001]_{PC}$ -oriented single-domain $BaTiO_3$ crystal. Reprinted from Ref. [14], with permission of Springer.	11
Figure 2.7. Domains in tetragonal and rhombohedral PZT crystals with selected orientations. Reprinted from Ref. [14], with permission of Springer.	12
Figure 2.8. (a) Scheme of the TSSG setup. (b)-(g) Photographs of single crystals grown by the TSSG method: (b) PMN-PT [49], (c) PZN-PT [44], (d) $BaTiO_3$ [48], (e) PYN-PMN-PT [52], (f) Mn-doped NBT-BT [56], and (g) $KNbO_3$ [60]. The length of a regular grid in the graph paper in (b)-(e) is 1 mm. Adapted from Ref. [44,48,49,52,56,60], with permission of Elsevier, John Wiley and Sons, Royal Society of Chemistry, American Chemical Society, AIP Publishing LLC, and Elsevier, respectively.	17
Figure 2.9. Typical steps of the Czochralski technique: (a) pulling down the seed, (b) contact with the melt, (c) crystal growth with rotation and slow pulling up, and (d) crystal extraction from the melt after the growth.	18
Figure 2.10. (a) Scheme of the vertical Bridgman method setup and (b) the temperature profile within the crucible [71]. (c) Photograph of a PIN-PMN-PT single crystal [67], and (d) the Ti concentration as a function of the position along the growth direction of the PMN-PT single crystal [72]. Reprinted from Ref. [67,71,72], with permission of AIP Publishing LLC, John Wiley and Sons, and Elsevier, respectively.	19
Figure 2.11. (a) Scheme of the conventional setup for crystal growth by the flux method. Three different ferroelectric crystals grown by the flux method: (b) $(Pb,La)(Zr,Sn,Ti)O_3$ (PLZST) [73], (c) PMN-PT [74], and (d) $[Bi_{0.5}(K_xNa_{1-x})_{0.5}]TiO_3$ [75] single crystals. Note that the length of a regular grid in the graph paper is 1 mm. Reprinted or adapted from Ref. [73,74,75], with permission of Royal Society of Chemistry and Elsevier.	20
Figure 2.12. Schemes of two approaches for the solid-state single crystal growth method. Reprinted from Ref. [37], © 2011 Andreja Benčan.	21
Figure 2.13. Phase diagram of the $K_xNa_{1-x}NbO_3$ solid solution [1,89]. Reprinted from [89], with permission of John Wiley and Sons.	23
Figure 2.14. Influence of chemical modifications on T_{O-T} and T_C of KNN polycrystalline ceramics. Adapted from Ref. [89], with permission of John Wiley and Sons.	23
Figure 2.15. Shift of the T_C and T_{O-T} in Mn-doped KNLTNS ceramics with different MnO contents. Reprinted from Ref. [127], with permission of Elsevier.	27
Figure 2.16: (a) Scanning electron microscopy (SEM) image of a KNN single crystal grown by the SSCG method [161], and (b) photographs of samples grown by the seed-free SSCG method [165]. Reprinted from Ref. [161,165], with permission of Elsevier and John Wiley and Sons.	31

Figure 2.17. Photograph of KNN crystals grown by the flux method. Reprinted from Ref. [169], with permission of Taylor & Francis.	32
Figure 2.18. Photograph of (a) pieces of cut [70] and (b) as-grown KNN crystals obtained by the modified Bridgman method [174], and (c) P - E loop ($f = 20$ Hz) with high leakage current of [001] _{PC} -oriented KNLN single crystals grown by the Bridgman method [70]. Reprinted from Ref. [70], with permission of AIP Publishing LLC and from Ref. [174], © 2014 Dabin Lin.	33
Figure 2.19. (a) Mn-doped KNN crystal grown by the floating zone method. (b) and (c) Cross section SEM images. Reprinted from Ref. [176], with permission of Elsevier.	33
Figure 2.20. Examples of as-grown crystals: (a) colorless cubic KNTN (TSSG) [178], (b) KNLN (SSSG) [46], and (c) KNTN (TSSG) single crystals [179]. Reprinted from Ref. [46,178,179], with permission of Elsevier Masson, Springer, and Royal Society of Chemistry.	34
Figure 2.21. (a) Influence of thermal depoling on room temperature d_{33} in [001] _{PC} -oriented undoped and 0.5 mol% MnO ₂ -doped KNN crystals [186]. (b) Unipolar electric field-induced strain curves ($f = 5$ Hz) for Mn-doped KNLN single crystal, PIN-PMN-PT:Mn single crystal, PZT5 ceramics and KNLN0.19 ceramics [184]. Reprinted from Ref. [184,186], with permission of John Wiley and Sons.	37
Figure 2.22. Leakage current density of the [001] _{PC} -oriented KNN and Mn-doped KNN crystals annealed under various oxidation conditions. Reprinted from Ref. [187], with permission of AIP Publishing LLC. .	37
Figure 2.23. <i>In-situ</i> domain configurations of pure orthorhombic KNN single crystals imaged by PLM at different E fields: (A) 1 kV/mm, (B) 2 kV/mm, (C) -1 kV/mm, and (D) -2 kV/mm. Reprinted from Ref. [192], with permission of Royal Society of Chemistry.	38
Figure 3.1. (a) Photograph of the furnace and (b) schematic diagram of the growth process inside the crucible for the KNN-based crystal growth using the submerged-seed solution growth method.	40
Figure 3.2. Processing route of KNLN solid solutions.	40
Figure 3.3. Illustration of Bragg's law.	44
Figure 3.4. Scheme of the principle of the Laue technique in the back reflection mode.	44
Figure 3.5. Schematic of the Sawyer-Tower circuit.	46
Figure 3.6. Schematics of applied electric field loading signals: (a) bipolar and (b) unipolar.	46
Figure 3.7. Schematic of the virtual ground circuit.	47
Figure 3.8. Excitation signal during small-signal measurements: a large-signal triangular base waveform superposed by a small-signal sinusoidal excitation waveform [199]. Note that the enlarged small-signal sinusoidal waveform is provided.	48
Figure 4.1. Photographs of KNLN boules grown on a platinum spatula: (a) N1, (b) N3, and (c) N5.	52
Figure 4.2. Photographs of Mn-doped KNLN boules grown on a platinum spatula: (a) N2-Mn and (b) N4-Mn.	52
Figure 4.3. Photographs of the as-grown KNLN (N8) crystal by the TSSG method: view from (a) the top, (b) the side, and (c) the bottom.	53
Figure 4.4. k_{eff} of individual element as a function of element concentration in the liquid solution $C_L(\infty)$: (a) all the elements, (b) Li, (c) Na, (d) K, (e) Nb, and (f) Ta.	58
Figure 4.5. Effective segregation coefficients $k_{\text{eff}}(\text{Ta})$ as a function of Ta molar concentration in the initial liquid solutions compared to those deduced from the pseudo-binary KNbO ₃ -KTaO ₃ phase diagram given by Reisman <i>et al.</i> [194].	60
Figure 4.6. Changes of element concentrations along the measurement length in (K _{0.612} Na _{0.359} Li _{0.029})(Ta _{0.024} Nb _{0.976})O ₃ (N1) crystal with the EPMA technique.	60
Figure 4.7. (a) XRD patterns of as-grown N1 and N6 crystals, and (b) photograph of the as-grown N6 crystal. .	62

Figure 4.8. Photographs of remainders solidified in crucibles after the extraction of the perovskite crystal: (a) N1, (b) N5, (c) N6, (d) N2-Mn and (e) N4-Mn attempts.....	62
Figure 4.9. K_2O - Li_2O - Nb_2O_5 phase diagrams from (a) Scott <i>et al.</i> [214] and (b) Ikeda <i>et al.</i> [212]. Note that in (b) L, K, and N represent Li_2O , K_2O and Nb_2O_5 . Red points mark the liquid composition of N1 and N6 attempts. Reprinted from Ref. [212,214], with permission of the Japan Society of Applied Physics and Elsevier.....	63
Figure 4.10. XRD patterns of powders of crushed $(K_{0.612}Na_{0.359}Li_{0.029})(Ta_{0.024}Nb_{0.976})O_3$ (N1) single crystals as a function of temperature: (a) full range, and (b) the enlarged region at around $2\theta = 25.5^\circ$ — 26.5° . Measurements were performed upon heating. The green arrows show the shift directions of the peaks with temperature.....	65
Figure 4.11. Domain configuration of the $(K_{0.612}Na_{0.359}Li_{0.029})(Ta_{0.024}Nb_{0.976})O_3$ (N1) crystal observed by PLM at various temperatures: (a) 25 °C, (b) 125 °C, (c) 300 °C, (d) 450 °C, and (e) 470 °C. The red regions are optically transparent and the green regions are optically cloudy.....	66
Figure 4.12. Domain configurations of (a) transparent regions and (b) cloudy regions; experimental Laue back scattering patterns of (c) transparent regions and (d) cloudy regions for the $(K_{0.612}Na_{0.359}Li_{0.029})(Ta_{0.024}Nb_{0.976})O_3$ (N1) single crystal.....	67
Figure 4.13. XRD patterns of the different regions of the $[001]_{PC}$ -oriented $(K_{0.637}Na_{0.334}Li_{0.029})(Ta_{0.0229}Nb_{0.9768}Mn_{0.0003})O_{2.99955}$ (N2-Mn) single crystal. The small peak appeared in the cloudy region is marked by the blue star.....	68
Figure 4.14. XRD patterns of the $[001]_{PC}$ -oriented $(K_{0.612}Na_{0.359}Li_{0.029})(Ta_{0.024}Nb_{0.976})O_3$ (N1) crystal at various temperatures. The green arrows show the evolution trends of both peaks with temperature.	69
Figure 4.15. Schematic view of the perovskite structure with the cubic (C, black), tetragonal (T, blue) and orthorhombic (O, red) unit cells.	70
Figure 4.16. Representation of domain configurations for the transparent and the cloudy regions observed in the orthorhombic and tetragonal phases of the KNLTN single crystals.....	70
Figure 4.17. Domain configuration of the $[001]_{PC}$ -oriented $(K_{0.612}Na_{0.359}Li_{0.029})(Ta_{0.024}Nb_{0.976})O_3$ (N1) single crystal in the vicinity of 450 °C during cooling process. (a) 450 °C, (b) 449 °C, (c) 448 °C, and (d) 447 °C. The red lines are the moving boundary of the cubic and tetragonal phases, and the green arrows are the directions of the movement.	71
Figure 4.18. <i>In-situ</i> TEM images of ferroelectric domain structure in the $[001]_{PC}$ -oriented $(K_{0.612}Na_{0.359}Li_{0.029})(Ta_{0.024}Nb_{0.976})O_3$ (N1) single crystal. (a) 25 °C, (b) 100 °C, (c) 110 °C, (d) 125 °C, (e) 130 °C, (f) 145 °C, (g) 250 °C, (h) 300 °C, (i) 400 °C, and (j) 450 °C. (k) Enlarged “red-A” zone of (b).	73
Figure 4.19. Temperature-dependent selected area electron diffraction patterns in the $[001]_{PC}$ -oriented $(K_{0.612}Na_{0.359}Li_{0.029})(Ta_{0.024}Nb_{0.976})O_3$ (N1) single crystal: (a) 25 °C, (b) 100 °C, (c) 250 °C, (d) 300 °C, (e) 400 °C, and (f) 450 °C.	74
Figure 5.1. XRD patterns of the crushed KNLTN single crystals with different Ta contents. (a) Full range and (b) enlarged region of $(002)_T/(200)_T$ or $(022)_O/(200)_O$ peaks.....	78
Figure 5.2. Raman spectra of $[001]_{PC}$ -oriented KNLTN single crystals with various Ta contents.	79
Figure 5.3. Temperature-dependent dielectric permittivity and losses of $[001]_{PC}$ -oriented KNLTN single crystals during heating from -100 °C to 450 °C at 10 kHz. The inset displays the change of phase transition temperatures (T_C and T_{O-T}) as a function of the Ta content. The minor discontinuity at 30 °C is related to the use of different measurement setups for the low and high temperature range.....	80
Figure 5.4. Electric field-induced (a) bipolar and (b) unipolar strains of $[001]_{PC}$ -oriented KNLTN single crystals at 2 kV/mm and 10 Hz.....	81

Figure 5.5. (a) E_C , E_i , and (b) piezoelectric constant d_{33}^* at 2 kV/mm of the $[001]_{PC}$ -oriented KNLTN single crystals with different Ta contents.....	82
Figure 5.6. Room temperature ferroelectric hysteresis P - E loops of the $[001]_{PC}$ -oriented (a) N8 single crystal with 13.5 % Ta ($f= 20$ Hz) and (b) N9 single crystal with 18.6 % Ta ($f= 10$ Hz).	83
Figure 5.7. Temperature dependent P - E loops of the $[001]_{PC}$ -oriented N8 single crystal with 13.5 % Ta ($f=20$ Hz).	84
Figure 5.8. Temperature dependent electric field-induced strain curves of the $[001]_{PC}$ -oriented N8 single crystal with 13.5 % Ta. The black curve refers to the S - E curve during the first electric field loading cycle, whereas the red curve corresponds to the second electric field loading cycle.....	85
Figure 5.9. Temperature-dependent (a) maximum positive strain S_{pos} , absolute value of the minimum negative strain $-S_{neg}$ during the first cycle and $-S_{neg}$ during the second cycle, and (b) $-S_{neg,1}/S_{pos,1}$ in the first cycle and negative strain ratios between two cycles $S_{neg,1}/S_{neg,2}$ in the $[001]_{PC}$ -oriented N8 crystal with 13.5 % Ta. Note that 1 represents the first cycle and 2 the second cycle. The orthorhombic-tetragonal phase transition is highlighted by the yellow region.	86
Figure 5.10. Temperature-dependent permittivity of $[001]_{PC}$ -oriented $(K_{0.265}Na_{0.715}Li_{0.020})(Ta_{0.135}Nb_{0.865})O_3$ (KNLTN, N8) and $(K_{0.287}Na_{0.691}Li_{0.022})(Ta_{0.063}Nb_{0.870}Sb_{0.067})O_3$ (KNLTNS, N11-Sb) crystals at 10 kHz.	87
Figure 5.11. Temperature-dependent dielectric permittivity and losses for (a, c) non-annealed, and (b, d) annealed $[001]_{PC}$ -oriented KNLTNS samples. The insets are the enlarged regions from -120 °C to 250 °C.	89
Figure 5.12. P - E loops for the non-annealed $[001]_{PC}$ -oriented KNLTNS single crystal state at various temperatures ($f=1$ Hz).....	90
Figure 5.13. P - E loops for the annealed $[001]_{PC}$ -oriented KNLTNS single crystal state at various temperatures ($f=1$ Hz).....	90
Figure 5.14. Temperature-dependent parameters extracted from P - E loops for the non-annealed and annealed $[001]_{PC}$ -oriented KNLTNS ($f =1$ Hz) and non-annealed $[001]_{PC}$ -oriented KNLTN ($f =20$ Hz) single crystal samples at 3 kV/mm: (a) maximum polarization P_{max} , (b) remanent polarization P_r , and (c) coercive field E_C	92
Figure 5.15. S - E curves for both non-annealed and annealed $[001]_{PC}$ -oriented KNLTNS single crystal state at various temperatures.....	93
Figure 5.16. Temperature dependent S_{pos} (maximum positive strain), $-S_{neg}$ (minimum negative strain) and the ratio between $-S_{neg}/S_{pos}$ for the annealed $[001]_{PC}$ -oriented KNLTNS single crystal sample.....	94
Figure 5.17. Temperature-dependent unipolar strain curves of (a) non-annealed and (b) annealed $[001]_{PC}$ -oriented KNLTNS single crystals. (c) Temperature-dependent maximum unipolar strain and converse piezoelectric coefficient of both $[001]_{PC}$ -oriented samples.	95
Figure 5.18. Small-signal field-dependent permittivity $\epsilon_{33}'/\epsilon_0$ and piezoelectric coefficients d_{33}^* of non-annealed and annealed $[001]_{PC}$ -oriented KNLTNS single crystal states at various temperatures. The arrows in (a) and (c) show the direction of electric field loading processes.	96
Figure 5.19. (a) Bipolar and (b) unipolar P - E , (c) enlarged bipolar P - E , and (d) bipolar and (e) unipolar S - E curves of both $[001]_{PC}$ -oriented KNLTNS single crystal states at room temperature (2^{nd} electric field loading cycles; measured frequencies: 1 Hz for the bipolar and 2 Hz for the unipolar cycles).....	97
Figure 5.20. Temperature-dependent piezoelectric coefficients d_{33} of non-annealed and annealed $[001]_{PC}$ -oriented poled KNLTNS single crystal samples, measured at 8 V/mm and 1 kHz.	99
Figure 5.21. ^{121}Sb Mössbauer spectra of powders of the (a) non-annealed and (b) annealed KNLTNS samples, measured at -173 °C.....	100
Figure 5.22. XRD patterns of powders of crushed crystals without Mn (N1, $(K_{0.612}Na_{0.359}Li_{0.029})(Ta_{0.024}Nb_{0.976})O_3$) and with Mn doping (N2-Mn, $(K_{0.637}Na_{0.334}Li_{0.029})(Ta_{0.0229}Nb_{0.9768}Mn_{0.0003})O_{2.99955}$).	104

Figure 5.23. Temperature-dependent (a) permittivity and (b) dielectric losses of [001] _{PC} -oriented crystals without Mn (N1; (K _{0.612} Na _{0.359} Li _{0.029})(Ta _{0.024} Nb _{0.976})O ₃) and with Mn (N2-Mn; (K _{0.637} Na _{0.334} Li _{0.029})(Ta _{0.0229} Nb _{0.9768} Mn _{0.0003})O _{2.99955} , measured during heating.....	105
Figure 5.24. (a) <i>P-E</i> , (b) bipolar and (c) unipolar <i>S-E</i> curves of [001] _{PC} -oriented non-annealed N1 crystal, and non-annealed and annealed N2-Mn crystals at room temperature and a frequency of 1 Hz (bipolar) or 2 Hz (unipolar).....	105
Figure 5.25. (a) EPR spectra of powders of the crushed non-annealed N2-Mn crystal at various temperatures. Enlarged EPR spectra at (b) RT and (c) -269 °C. The two six-line groups represent the typical hyperfine structure information of Mn ²⁺ and Mn ⁴⁺	107
Figure 6.1. Images of Laue back-scattering for the two orientations: (a) [001] _{PC} and (b) [110] _{PC}	109
Figure 6.2. Temperature-dependent dielectric permittivity and losses of (a,c) the [001] _{PC} -oriented and (b,d) [110] _{PC} -oriented Mn-KNLTN crystals during heating and cooling with the rate of 1 °C/min.	111
Figure 6.3. Temperature-dependent bipolar ferroelectric hysteresis <i>P-E</i> loops (the second electric field loading cycles; 1Hz) of [001] _{PC} and [110] _{PC} -oriented Mn-KNLTN samples.....	112
Figure 6.4. Temperature-dependent bipolar electric field-induced strain curves (the second electric field loading cycles; 1Hz) of [001] _{PC} and [110] _{PC} -oriented Mn-KNLTN samples.....	113
Figure 6.5. Temperature-dependent unipolar electric field-induced strain curves (second electric field loading cycles, 2 Hz) of [001] _{PC} and [110] _{PC} -oriented Mn-KNLTN samples.....	113
Figure 6.6. Temperature-dependent (a) maximum polarization <i>P</i> _{max} , (b) remanent polarization <i>P</i> _r , (c) coercive field <i>E</i> _C , (d) bipolar positive strain <i>S</i> _{pos} and (f) negative strain <i>S</i> _{neg} , and (g) large-signal piezoelectric coefficient <i>d</i> ₃₃ [*] values of [001] _{PC} and [110] _{PC} -oriented Mn-KNLTN samples.....	115
Figure 6.7. Initial polarization distributions for different orientations and polarization distributions at maximum field <i>E</i> _{max} : (a) [110] _{PC} -oriented orthorhombic, (b) [001] _{PC} -oriented tetragonal, (c) [001] _{PC} -oriented orthorhombic, and (d) [110] _{PC} -oriented tetragonal crystals.....	116
Figure 6.8. Change of the domain structure for different orientations when the field increases from 0 to coercive field <i>E</i> _C : (a) [110] _{PC} -oriented orthorhombic, (b) [001] _{PC} -oriented tetragonal, (c) [001] _{PC} -oriented orthorhombic, and (d) [110] _{PC} -oriented tetragonal crystals.....	117
Figure 6.9. Temperature-dependent properties of the [001] _{PC} -oriented Mn-KNLTN sample: (a) large signal <i>S</i> _{pos} and (<i>P</i> _{max} - <i>P</i> _r), and (b) small signal <i>d</i> ₃₃ and permittivity, normalized with respect to room temperature value.	119



List of Tables

Table 2.1. Defect types, which are expected to appear in the investigated materials.	13
Table 2.2. Dimensions and piezoelectric coefficients of selected KNN and KNN-based crystals growth by TSSG.	35
Table 2.3. Comparison of electrical properties of pure KNN single crystals with various K/Na ratios.	35
Table 2.4. Comparison of electrical behavior of Li, Ta, or/and Sb co-modified KNN-based single crystals.....	36
Table 3.1. EPMA reference samples in this work.	42
Table 4.1. Concentrations of starting materials for each growth attempt.	51
Table 4.2. Element concentrations of as-grown crystals grown at ICMCB.....	54
Table 4.3. Element concentrations of as-grown crystals grown at FEE.	55
Table 4.4. Effective segregation coefficients of individual elements for each growth attempt.	56
Table 5.1. Lattice parameters of as-grown KNLTN single crystals with different Ta contents.	78
Table 5.2. Piezoelectric, ferroelectric, and dielectric parameters of [001] _{PC} -oriented KNLTN crystals with various Ta contents.	84
Table 5.3. ¹²¹ Sb Mössbauer parameters for crushed KNLTNS crystals measured at -173 °C.....	100



List of Symbols

Chemical Formula

KNLN	$(\text{K,Na,Li})\text{NbO}_3$
KNLTN	$(\text{K,Na,Li})(\text{Ta,Nb})\text{O}_3$
KNLTNS	$(\text{K,Na,Li})(\text{Ta,Nb,Sb})\text{O}_3$
KNN	$(\text{K,Na})\text{NbO}_3$
KNTN	$(\text{K,Na})(\text{Ta,Nb})\text{O}_3$
KNTNS	$(\text{K,Na})(\text{Ta,Nb,Sb})\text{O}_3$
NBT	$(\text{Na}_{0.5}\text{Bi}_{0.5})\text{TiO}_3$
NBT-BT	$(1-x)(\text{Na}_{0.5}\text{Bi}_{0.5})\text{TiO}_3-x\text{BaTiO}_3$
PIN-PMN-PT	$\text{Pb}(\text{In}_{1/2}\text{Nb}_{1/2})\text{O}_3\text{-Pb}(\text{Mg}_{1/3}\text{Nb}_{2/3})\text{O}_3\text{-PbTiO}_3$
PLN-PMN-PT	$\text{Pb}(\text{Lu}_{1/2}\text{Nb}_{1/2})\text{O}_3\text{-Pb}(\text{Mg}_{1/3}\text{Nb}_{2/3})\text{O}_3\text{-PbTiO}_3$
PLZST	$(\text{Pb,Lu})(\text{Zr,Sn,Ti})\text{O}_3$
PMN-PT	$\text{Pb}(\text{Mg}_{1/3}\text{Nb}_{2/3})\text{O}_3\text{-PbTiO}_3$
PMN-PZ-PT	$\text{Pb}(\text{Mg}_{1/3}\text{Nb}_{2/3})\text{O}_3\text{-PbZrO}_3\text{-PbTiO}_3$
PYN-PMN-PT	$\text{Pb}(\text{Yb}_{1/2}\text{Nb}_{1/2})\text{O}_3\text{-Pb}(\text{Mg}_{1/3}\text{Nb}_{2/3})\text{O}_3\text{-PbTiO}_3$
PZN-PT	$\text{Pb}(\text{Zn}_{1/3}\text{Nb}_{2/3})\text{O}_3\text{-PbTiO}_3$
PZT	$\text{Pb}(\text{Zr,Ti})\text{O}_3$

Techniques

XRD	X-ray diffraction
EPR	Electron paramagnetic resonance
EPMA	Electron probe micro analysis
PLM	Polarized light microscopy
PFM	Piezoresponse force microscopy
ICP-OES	Inductively coupled plasma optical emission spectrometry
SAED	Selected area electron diffraction pattern
SEM	Scanning electron microscopy
SSSG	Submerged-seed solution growth
TSSG	Top-seeded solution growth
TEM	Transmission electron microscopy

Phase Structures

AFE	Antiferroelectric
FE	Ferroelectric
MPB	Morphotropic phase boundary
PPT	Polymorphic phase transition

TTB	Tetragonal tungsten bronze
Transition Temperatures	
T_C	Curie temperature
T_{O-T}	Orthorhombic-tetragonal phase transition temperature
T_{R-O}	Rhombohedral–orthorhombic phase transition temperature
Others	
Q_S	Collected charges of the capacitor
Q_R	Collected charges of the reference capacitor
D	Dielectric displacement
$\tan\delta$	Dielectric loss
χ	Dielectric susceptibility
p	Dipole moment
W_E	Depolarization energy
σ_d	Domain wall density
W_W	Domain wall energy
k_{eff}	Effective segregation coefficient
W_x	Elastic energy
E	Electric field
E_{max}	Applied maximum electric field
E_C	Coercive field
E_i	Internal field
E_C^-	Negative coercive field
E_C^+	Positive coercive field
Q_{33}	Electrostrictive coefficient
Q_{ijkl}	Electrostrictive coefficient tensor
M_{ijkl}	Electrostrictive coefficient tensor
$C_L(\infty)$	Element concentration in the initial liquid solution at the beginning of the growth
C_S	Element concentration in the solid phase, <i>i.e.</i> , in the single crystal
e'	Free electron
h'	Free hole
Γ	Full width half maximum of each individual peak
T	Goldschmidt's tolerance factor
R_O	Ionic radii of oxygen ions
Δ	Isomer shift
V_K', V_{Na}', V_{Li}'	K/Na/Li vacancy
Q_m	Mechanical quality factor

$V_{O^{\cdot\cdot}}$	Oxygen vacancy
$\epsilon_{ij}, \epsilon_{ijk}$	Permittivity tensors
ϵ_0	Permittivity of vacuum
$\epsilon_{33}^T/\epsilon_0$	Measured permittivity
ϵ''	Imaginary permittivity
ϵ'	Real permittivity
ϵ_r	Relative permittivity
d_{33}	Piezoelectric coefficient (Berlincourt method)
d_{33}^*	Piezoelectric coefficient (large-signal)
P	Polarization
$P_{\max}-P_r$	Back switching polarization
α_{el}	Electronic polarizability
P_e	Electronic polarization
α_i	Ionic polarizability
P_i	Ionic polarization
P_{\max}	Maximum polarization
α_o	Orientation polarizability
P_o	Orientation polarization
P_l	Polarization components
P_r	Remanent polarization
$P_{\text{space charge}}$	Space charge polarization
P_s	Spontaneous polarization
$eV_{zz}Q_{5/2}$	Quadrupole coupling constant
C_R	Reference capacitor
A	Relative area
Sb_{Nb}''	Sb^{3+} impurity center
S_{ij}	Strain tensor
S_{pos}	Bipolar positive strain
S_{neg}	Negative strain
S_r	Remanent strain
S_{\max}	Maximum positive strain
k_0	Thermodynamic segregation coefficient
F_1	Total energy
V	Unit volume
$k_{\text{volatilization}}$	Volatilization contribution factor of segregation coefficients
U_S	Voltage drop across the sample
U_R	Voltage drop across the reference capacitor
U_X	Voltage collected in the X channel

U_Y

Voltage collected in the Y channel

Résumé (French)

Les matériaux piézoélectriques sans plomb ont reçu une attention croissante au cours de la dernière décennie en raison des problèmes environnementaux et des problèmes de santé qu'ils peuvent causer. Un intérêt considérable a été porté sur le système à base de $(\text{K,Na})\text{NbO}_3$ (KNN) qui possède une température de Curie relativement élevée et de bonnes propriétés piézoélectriques. De nombreuses publications sur des céramiques polycristallines performantes à base de KNN ont accru l'intérêt pour ce matériau et son étude sous forme monocristalline le rend particulièrement intéressant pour deux raisons principales. La première consiste à s'affranchir du rôle négatif des interactions intergranulaires sur la réponse électromécanique que l'on peut observer dans les céramiques. La deuxième concerne l'ingénierie des domaines. En effet, la relation entre la direction du champ électrique externe, l'orientation cristallographique et les vecteurs de polarisation spontanée pour une structure spécifique peut être établie plus facilement dans des monocristaux. Ceci offre ainsi une voie pour une compréhension approfondie du mécanisme fondamental de la piézoélectricité dans ce type de matériaux et des applications potentielles en découlant. La considérable amélioration des réponses piézoélectriques et ferroélectriques qui a été effectuée dans le passé dans les monocristaux à base de plomb encourage également une exploration plus poussée des cristaux piézoélectriques à base de KNN car ils possèdent la même structure pérovskite.

Le but principal de cette thèse est d'identifier et de mettre en œuvre les approches possibles pour l'amélioration des propriétés électromécaniques de monocristaux piézoélectriques à base de KNN. Après une courte introduction sur les connaissances fondamentales sur les piézoélectriques et les ferroélectriques, une revue bibliographique exhaustive sur le développement actuel de monocristaux à base de KNN en tant que piézoélectriques est présentée dans le chapitre 2. Par la suite dans le chapitre 3, la croissance en solution par deux techniques distinctes est présentée. La TSSG (pour Top-Seeded Solution Growth) et la SSSG (pour Seed-Submerged Solution Growth) sont entreprises afin de faire croître des monocristaux. L'accent est ensuite mis sur les problèmes liés à la croissance cristalline de monocristaux de KNN substitués par Li, Ta et / ou Sb. Les principales conclusions sur les résultats issus de la croissance des cristaux sont ensuite présentées au chapitre 4 et peuvent être résumées comme suit: (i) Pour chaque élément pris individuellement, leurs coefficients de ségrégation reposent fortement sur leurs concentrations initiales dans la solution liquide. La

discussion systématique menée sur le phénomène de ségrégation des éléments a contribué à la formulation adéquate de la composition future des cristaux à base de KNN. (ii) La compétition entre éléments occupant le même site du réseau est démontrée. (iii) Le très faible coefficient de ségrégation de Li dans la matrice KNN est responsable de l'apparition d'une phase secondaire présentant la structure bronze de tungstène quadratique. (iv) Les régions optiquement laiteuses observées dans les monocristaux diminuent la réponse électrique et peuvent être réduites par traitement thermique et refroidissement lent.

Dans la deuxième partie de la thèse, nous avons utilisé trois approches pour améliorer le comportement piézoélectrique et ferroélectrique des monocristaux à base de KNN et elles sont présentées au chapitre 5. La substitution chimique par les ions Ta ou Sb indique qu'une réponse électromécanique améliorée est obtenue lorsque la transition orthorhombique-quadratique est à proximité de la température ambiante, comme cela est observé pour les céramiques polycristallines. Le traitement thermique sous atmosphère d'O₂ pur a conduit au doublement de la valeur du coefficient piézoélectrique et des paramètres ferroélectriques (polarisation maximale et rémanente) d'un monocristal de (K,Na,Li)(Ta,Nb,Sb)O₃. Son coefficient piézoélectrique à la température ambiante, qui constitue un record mondial à l'heure actuelle vis-à-vis de ce qui est reporté dans la littérature internationale, vaut 732 pC.N⁻¹. Ceci est attribué à la plus faible concentration de défauts dans le monocristal après traitement thermique. La troisième approche consiste au dopage des monocristaux de (K,Na,Li)(Ta,Nb)O₃ avec une petite quantité d'ions Mn. Enfin, dans le chapitre 6, la dépendance des propriétés électromécaniques vis-à-vis de l'orientation cristallographique montre que des valeurs élevées de la polarisation maximale, de la polarisation rémanente, du champ coercitif, de la déformation maximale et de la déformation négative sont observées lorsque le champ électrique est orienté le long de la direction de la polarisation spontanée, à la fois dans les phases quadratique et orthorhombique. Ceci est relié à l'effet de la rotation de polarisation sous différentes directions de champ électrique.

Abstract (English)

Lead-free piezoelectric materials have received increasing attention in the last decade, driven by environmental issues and health concerns. Of considerable interest is the (K,Na)NbO₃ (KNN)-based system, which possesses a relatively high Curie temperature and good piezoelectric properties. Abundant publications on KNN-based polycrystalline ceramics increased the interest in studying their single-crystalline form, based on two major concerns. The first concern refers to the negative role of grain interactions on the electromechanical response. The second concern deals with domain engineering. The relationship between external electric field direction, crystallographic orientation, and spontaneous polarization vectors for a specific structure can be more readily established in single crystals and thus offers a pathway for an in-depth understanding of fundamental mechanism and potential applications. The exciting enhancement of both piezoelectric and ferroelectric response in lead-based single crystals also encourages the further exploration of KNN-based piezoelectric crystals, as they possess the same perovskite structure.

The main goal of this thesis is to find possible approaches for improved electromechanical properties in KNN-based piezoelectric single crystals. In Chapter 2, the current development of KNN-based single crystals as piezoelectrics is reviewed, following a short introduction of fundamental knowledge on piezoelectrics and ferroelectrics. Both submerged-seed solution growth and top-seeded solution growth techniques were employed to produce single crystals, as described detailed in Chapter 3. Emphasis is subsequently placed on issues of the crystal growth process, effective methods to enhance electrical properties, and crystallographic orientation-dependent electrical properties in Li-, Ta-, and/or Sb-substituted KNN single crystals. The main conclusions from the crystal growth aspect are presented in Chapter 4 and can be summarized as follows: (i) For individual elements, segregation coefficients highly rely on the initial concentration in the liquid solution. The systematic discussion in this work contributes to future composition design in KNN-based crystals. (ii) A competition between elements occupied on the same lattice site was found. (iii) The very low Li segregation coefficient in the KNN matrix is importantly responsible for the occurrence of a secondary phase with the tetragonal tungsten bronze structure. (iv) The observed optically-cloudy regions in as-grown KNN-based single crystals decrease the electrical response and can be reduced by thermal treatment with slow cooling. In the second part of the thesis we used three approaches to enhance the piezoelectric and ferroelectric behavior of KNN-based single crystals, which is shown in Chapter 5. Chemical substitution with Ta or Sb ions indicates that enhanced electromechanical response is achieved when the orthorhombic-tetragonal phase transition temperature is in the proximity of room temperature, as previously reported for polycrystalline ceramics. Thermal treatment in pure O₂ atmosphere resulted in a twofold increase of the piezoelectric coefficient and ferroelectric parameters (maximum and remanent polarization) of a

(K,Na,Li)(Ta,Nb,Sb)O₃ single crystal. The up-to-date highest room-temperature piezoelectric coefficient in annealed KNN-based single crystals of 732 pC/N was obtained, which is attributed to the lower defect concentration after the thermal treatment. The third approach, doping with a small amount of transition metal Mn ions in (K,Na,Li)(Ta,Nb)O₃ single crystals, is also presented. Orientation dependence of electromechanical properties in Chapter 6 indicates that high maximum polarization, remanent polarization, coercive field, maximum strain, and negative strain were observed when the electric field was applied along one of the spontaneous polarization vectors in both tetragonal and orthorhombic phases. This is related to the effect of polarization rotation under different electric field directions.

1 Introduction

The interconversion between mechanical and electrical energy in ferroelectric materials enables their application in a wide range of devices, such as transducers, actuators, and sensors. Since the 1950s, lead-based piezoelectric materials have been extensively developed due to their excellent piezoelectric coefficients, especially when the compositions are in the vicinity of the morphotropic phase boundary (MPB) [1]. Moreover, the inherent temperature independence of the MPB enables good temperature stability of piezoelectric and ferroelectric performance [1,2]. However, the increasing demand for healthy and sustainable development drives more and more governments to restrict the use of lead-based materials. These efforts resulted in various legislations, such as the “Restriction of the use of certain hazardous substances in electrical and electronic equipment” (RoHS) [3]. Researchers are therefore required to develop lead-free piezoelectric materials to replace the lead-based systems.

In 2004, a high piezoelectric coefficient of 416 pC/N was reported by Saito *et al.* [4] in the textured (K,Na,Li)(Ta,Nb,Sb)O₃ (KNLTNS) polycrystalline ceramics. This report to a great extent stimulated the development of the (K,Na)NbO₃ (KNN)-based systems as promising lead-free candidates for piezoelectric applications. This is evident by their 50 % share in the total number of publications in the lead-free piezoceramic field [5]. The main advantages of the KNN-based systems are high Curie temperature, high mechanical quality factors, fatigue resistance, low density, biocompatibility, and compatibility with base-metal electrodes.

Single crystals enable the study of fundamental mechanisms and the inherent anisotropy of the electromechanical properties of ferroelectrics. This knowledge is of utmost importance for further development of piezoelectric devices. Moreover, the absence of intergranular interactions allows the full exploitation of the induced strain mechanisms. Thus very high piezoelectric and ferroelectric properties have been observed in many lead-based and lead-free perovskite piezoelectric single crystals, such as Pb(Zn_{1/3}Nb_{2/3})O₃-PbTiO₃ (PZN-PT) [6], Pb(Mg_{2/3}Nb_{1/3})O₃-PbTiO₃ (PMN-PT) [7], BaTiO₃ [8], and (Na_{1/2}Bi_{1/2})TiO₃-BaTiO₃ (BNT-BT) [9,10]. However, similar reports about enhanced piezoelectric and ferroelectric properties in KNN-based system are scarce. This is related to several aspects: the appearance of the secondary phase, the low intrinsic response of as-grown crystals which are far from the orthorhombic-tetragonal phase transition, and the high defect concentration resulting from volatilization of A-site alkali ions [11] and the high temperature growth processing.

The main aim of this work is to investigate the factors influencing the electromechanical properties of KNN-based single crystals and to develop approaches of improving their performance. The thesis starts with a short summary of the fundamental knowledge on ferroelectrics, crystal growth methods, and an

up-to-date literature review on KNN-based polycrystalline ceramics and single crystals (Chapter 2). Chapter 3 briefly introduces the utilized experimental procedures.

The crystals presented in this work were obtained by the submerged-seed solution growth and the top-seeded solution growth techniques. Chapter 4 focuses on crystal growth issues for an in-depth understanding of the growth behavior and producing a crystal with the desired composition and high crystalline quality. The influence of element concentrations in the initial liquid on the segregation coefficients is investigated and the reasons for the occurrence of secondary phases during growth of KNN-based crystals are discussed. In addition, temperature dependence of structural parameters and domain configurations is provided.

Chapter 5 describes the relationship between the chemical composition and the dielectric, piezoelectric, and ferroelectric properties of (K,Na,Li)(Ta,Nb)O₃ (KNLTN) and KNLTNS single crystals. The main focus is on Ta and Sb substitutions. The change of the molar ratio between different elements shifts the orthorhombic-tetragonal phase transition (T_{O-T}) and the Curie temperature (T_C), consequently influencing the electrical response. Following the optimization of the chemical composition in KNLTN and KNLTNS single crystals, the chapter describes the comparison of electrical properties before and after thermal annealing in O₂ atmosphere for a KNLTNS single crystal, which offers a promising method to enhance electrical properties. At the same time, the Sb valence states in KNLTNS single crystals are investigated. Subsequently, the influence of doping with transition metal Mn ions on the electrical behavior of KNLTN single crystals is presented.

Chapter 6 highlights the relationship between crystallographic orientations, crystallographic structure, and the electric field-induced polarization and strain curves in a Mn-doped KNLTN single crystal. The cases with electric field parallel and nonparallel to one of the spontaneous polarization vectors are studied and compared.

2 Theory and Literature Review

2.1 Fundamentals of Ferroelectrics

This paragraph gives a brief review of the theoretical background on ferroelectrics, piezoelectrics, and related materials. For a more complete description, the reader is referred to the textbooks of Jaffe *et al.* [1], Waser *et al.* [12], Tagantsev *et al.* [13], and Heywang *et al.* [14], as well as the review papers of Damjanovic [15,16], and Haertling [17].

2.1.1 Dielectrics

If an electric field is applied to an ideal dielectric material, positively and negatively charged centers will be separated. This charge separation is described by the dipole moment \vec{p} , which is defined as the product of charges and the distance between these charges. The sum of all dipole moment vectors in a unit volume V is defined as polarization \vec{P} .

$$\vec{P} = \frac{\sum \vec{p}}{V} \quad (2.1)$$

In a dielectric material, the induced polarization is proportional to the external electric field \vec{E} , and can be expressed as:

$$\vec{P} = \varepsilon_0 \chi \vec{E} \quad (2.2)$$

where χ is the dielectric susceptibility, ε_0 the permittivity of vacuum.

Dielectric displacement in dielectrics can be described by Equation 2.3.

$$\vec{D} = \varepsilon_0 \vec{E} + \vec{P} = \varepsilon_0 (1 + \chi) \vec{E} \quad (2.3)$$

where $1 + \chi$ is the relative permittivity ε_r , describing the degree of polarization in the dielectric materials.

In general, there are four main types of polarization mechanisms: electronic \vec{P}_e , ionic \vec{P}_i , orientation \vec{P}_o , and space charge polarization $\vec{P}_{space\ charge}$. The total polarization \vec{P} in dielectrics is the sum of all cases, written as Equation 2.4.

$$\vec{P} = \vec{P}_e + \vec{P}_i + \vec{P}_o + \vec{P}_{space\ charge} = \alpha_{el} \vec{E} + \alpha_i \vec{E} + \alpha_o \vec{E} + \vec{P}_{space\ charge} \quad (2.4)$$

where α_{el} , α_i , and α_o are the electronic, ionic, and orientation polarizability, respectively.

Electronic polarization \vec{P}_e originates from the separation of the positively charged atomic nuclei and the negatively charged electron cloud after an electric field is applied. Therefore, it is present in all dielectric materials. For an individual atom, the electronic polarizability α_{el} is temperature-independent. Ionic polarization \vec{P}_i , which appears in ionic materials, refers to the distance between positively charged cations and negatively charged anions under an electric field. Orientation polarization \vec{P}_o is related to the rotation of permanent dipole moments after the application of electric field. If no external field is applied, the net polarization is zero due to the random distribution of these permanent dipole moments. The orientation polarizability α_o is dependent on the temperature. Space charge polarization involves the presence and accumulation of mobile charge carriers. In functional dielectric materials, other mechanisms can exist, such as domain wall polarization induced by the movement of domain walls in ferroic materials.

The \vec{P}_e and \vec{P}_i are also referred to as intrinsic contributions to the total polarization due to their lattice dependence, while others are extrinsic contributions. The overall polarization is frequency-dependent due to the different response times of individual species to the electric field, as shown in Figure 2.1 [12]. At a very low frequency, the permittivity has the same response as in the static field. At an increased frequency, the electronic and ionic polarization response are able to follow well the field, whereby the orientation and space charge polarization cannot follow. This time lag is defined as relaxation behavior.

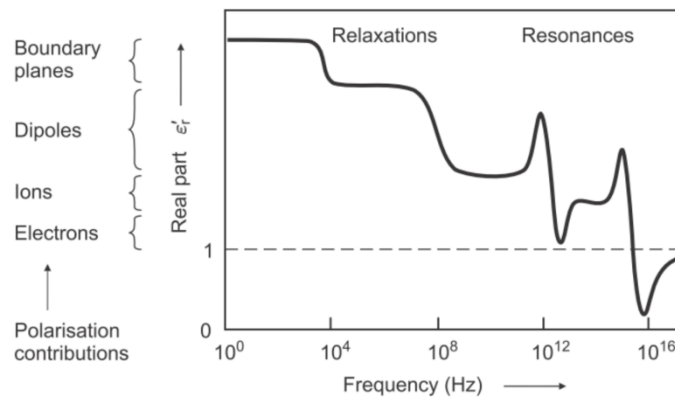


Figure 2.1. Frequency-dependence of the real part of the dielectric permittivity [12].

The relaxation behavior between the applied field and the permittivity response gives rise to the dielectric losses of the system. The permittivity of the system can therefore be described by the complex quantity by Equation 2.5.

$$\varepsilon = \varepsilon' + i\varepsilon'' \quad (2.5)$$

where ε' is the real and ε'' the imaginary part. The imaginary part reflects the contribution of dielectric losses resulting from the conductivity. The dielectric loss $\tan\delta$ can be calculated as the ratio of the imaginary and real parts.

2.1.2 Piezoelectrics

Piezoelectric effects were first discovered in quartz by Pierre and Jacques Curie in 1880. Piezoelectricity is a coupling effect between mechanical and electrical energies in certain materials. It can be expressed by the following two equations:

$$D_i = d_{ijk}\sigma_{jk} \quad (2.6)$$

$$S_{ij} = d_{ijk}E_k \quad (2.7)$$

where D_i is the dielectric displacement vector, σ_{jk} the stress tensor, d_{ijk} the piezoelectric tensor, while i, j , and k represent the three axes. The effect described by Equation 2.6 is the direct piezoelectric effect, whereas Equation 2.7 corresponds to the converse piezoelectric effect.

Piezoelectricity is highly correlated to the symmetry of the crystalline structure of the material and requires a non-centrosymmetric structure, *i.e.*, absence of an inversion center. Out of all 32 point groups, 11 are centrosymmetric. Except the point group 432, all other 20 point groups exhibit piezoelectricity. Among them, 10 point groups display a spontaneous dipole moment and are therefore referred to as polar or pyroelectric. When spontaneous polarization vectors are switchable by an applied electric field, the point group will exhibit ferroelectric properties.

2.1.3 Ferroelectrics

Ferroelectricity is defined as the ability of a material to switch the spontaneous polarization with an external electric field. Dipoles within a region of a ferroelectric material are aligned in the same direction and these regions are referred to as ferroelectric domains (will be shortened to “domains” in the following text). The boundaries separating adjacent domain regions are so-called ferroelectric domain walls (will be shortened to “domain wall”). Multi-domain states typically exist in a ferroelectric material, due to the minimization of the total electrostatic and elastic energies. However, a single-domain state can be achieved in single crystals under specific conditions.

With the application of an electric field, domains can be switched and the polarization aligned with the direction as close as possible to the direction of the electric field. As one of the main features of ferroelectric materials, the electric field-induced domain switching process can be described by the hysteresis loops (P - E loops). The hysteresis is related to the influence of the magnitude and direction of

the external field on the spontaneous polarization, domain switching, and domain wall growth ability. The ferroelectric hysteresis loop is accompanied by a change of the strain.

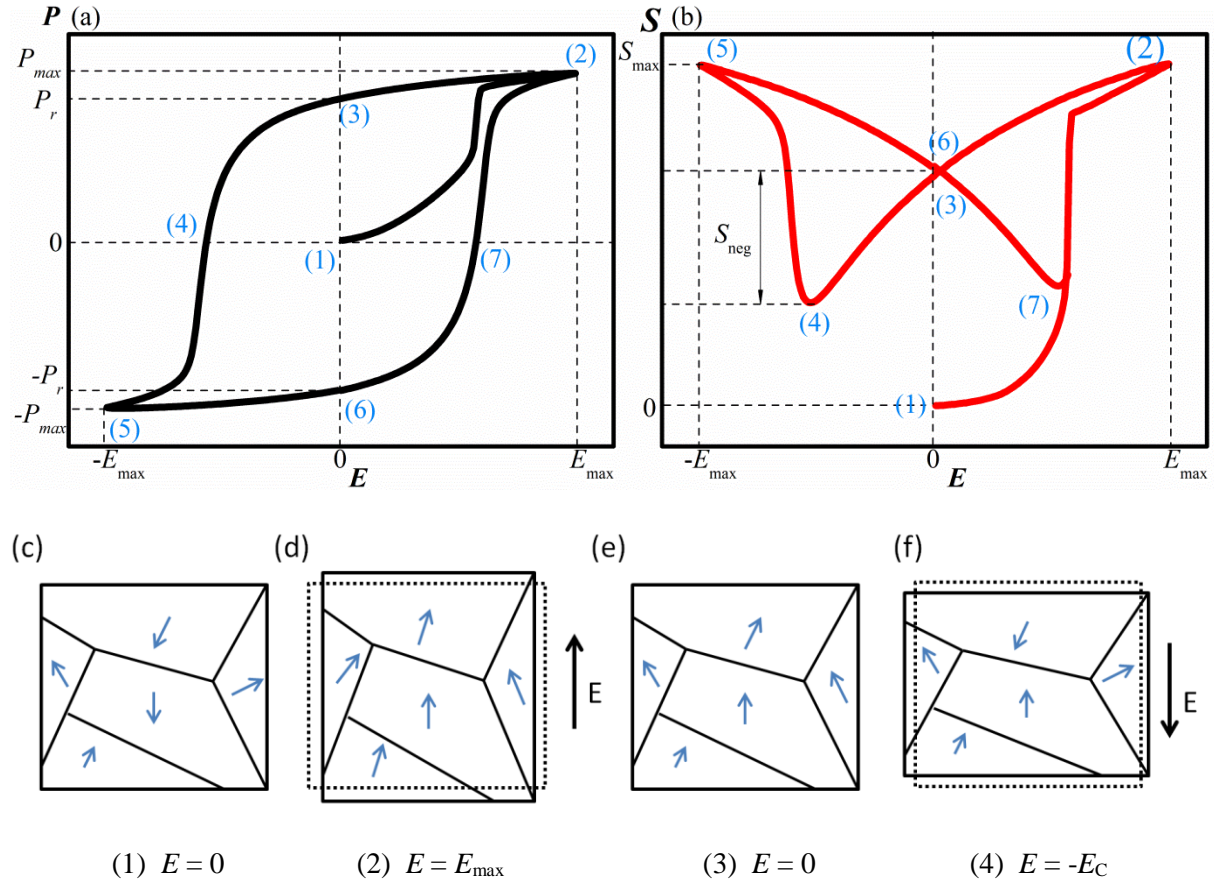


Figure 2.2. (a) Ferroelectric hysteresis and (b) field-induced strain curves of a typical ferroelectric ceramic. The corresponding domain orientations under various fields: (c) $E=0$, (d) $E=E_{max}$, (e) $E=0$, and (f) $E=-E_C$.

Figure 2.2 (a) and (b) show a typical P - E and electric field-induced strain curve (S - E) of a ferroelectric. Zero macroscopic polarization and strain can be observed at the virgin state (1) of Figure 2.2 (a) and (b), resulting from the random distribution of domains, as shown in Figure 2.2 (c). By the application of a low electric field, the polarization and strain increase linearly. If the field is decreased in this region, the polarization and strain can return to the original state because the electric field is not high enough for domain switching to take place. On the contrary, further increasing the field results in irreversible domain switching and both polarization and strain start to increase rapidly and nonlinearly. Higher electric field strength can promote more and more domain switching into the directions close to the

electric field direction. When the field is high enough, the polarization can reach the saturation state P_{\max} with the maximum strain S_{\max} , as observed at state (2) in Figure 2.2 (a), (b), and (d). Continuously decreasing the field, back-switching occurs, and the polarization is reduced. Domain back-switching can induce a decrease in strain because of shrinking of the lattice. Moreover, this back-switching is subjected to hysteresis. After the removal of the electric field, some domains switch back to their initial states, as depicted in Figure 2.2 (e). Therefore, remanent polarization P_r and remanent strain S_r are observed at state (3) in Figure 2.2. In order to change the P_r and S_r , an opposite field has to be applied. When the field reaches $-E_C$, zero polarization can again be observed. Figure 2.2 (f) shows the corresponding domain state, which is similar to the virgin state. Simultaneously, the strain reaches the minimum value. This value may be different with respect to the strain of the virgin state because of possible defects, grain boundaries, irreversible domain switching, and other effects. If the opposite field keeps increasing, dipoles will be aligned along directions as close as possible to the opposite field and the polarization begins to increase in the opposite direction with increasing positive strain. A higher field in the opposite direction also leads to a saturation state (state (5) in Figure 2.2). Decreasing the field in the opposite direction shows similar behavior as when the positive field is applied. The described parameters P_{\max} , P_r , E_C , S_r , and S_{\max} are used to evaluate the ferroelectricity of materials. Note that they can be significantly influenced by the applied frequency.

It should be pointed out that all dielectrics deform under an external field, which corresponds to the so-called electrostriction. In centrosymmetric dielectrics, this deformation is proportional to the square of the magnitude of the field. However, the deformation can be reversed by a small negative signal field due to the domain reorientation in ferroelectrics [18]. In ferroelectrics, the strain can be expressed as:

$$S_{ij} = Q_{ijkl}P_kP_l \quad (2.8)$$

For the longitudinal strain of a poled ferroelectric ceramic,

$$S_3 = Q_{33}(P_r + P_3)^2 = Q_{33}P_r^2 + 2Q_{33}P_rP_3 + Q_{33}P_3^2 \quad (2.9)$$

where Q_{ijkl} and Q_{33} are the electrostrictive coefficients. $Q_{33}P_r^2$ refers to the contribution from the remanent strain, the term $2Q_{33}P_rP_3$ is attributed to the piezoelectric effect as linearized electrostriction. The term $Q_{33}P_3^2$ represents the contribution from the induced polarization to the electrostriction.

According to the angle between the dipoles in the adjacent domain regions, domain walls are in general categorized as non-180 ° and 180 ° types (Figure 2.3). 180 ° domain walls appear in all perovskite ferroelectrics. The non-180 ° domain walls depend on the spontaneous polarization orientations in a

certain crystal structure, which will be discussed in the following paragraph. Note that only non-180° domain walls contribute to the reduction of the ferroelastic energy, while both types reduce the electrostatic energy.

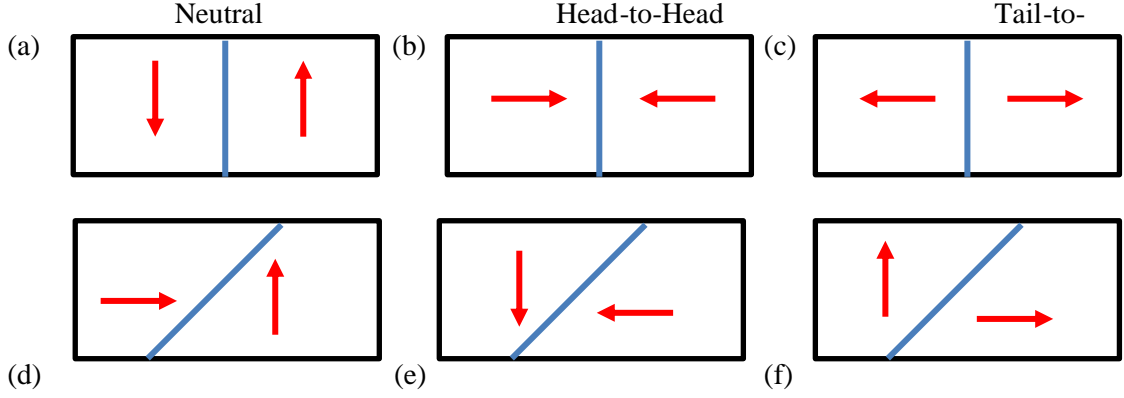


Figure 2.3. (a) Neutral, (b) “head-to-head”, and (c) “tail-to-tail” type of 180° domain walls, and (d) neutral, (e) “head-to-head” and (f) “tail-to-tail” type of 90° domain walls.

When the 180° domain wall is parallel to the spontaneous polarization P_S directions of the domains, it will be electrostatically neutral (Figure 2.3 (a)). However, if the 180° domain wall is not parallel to the P_S , it will be constrained by negative or positive charges, stemming from the “head-to-head” or “tail-to-tail” domain configurations, which can be seen in Figure 2.3 (b) and (c). Similar cases occur for non-180° domain walls, as shown in Figure 2.3 (a)-(d). Charged domain walls are in general energetically less favorable, due to the higher required energy [19]. Higher conductivity can be observed due to the accumulation of electrons or holes at walls [20].

The multi-domain structure in ferroelectric materials is formed according to the requirement of energy minimization. The formation of the domain configuration is driven by the minimization of the total energy F_1 , including elastic W_x , domain wall W_w , and depolarization W_E contributions, as written in Equation 2.10 [21].

$$F_1 = F_1^0 + \int \left(\frac{\alpha}{2} D^2 + \frac{\gamma}{4} D^4 \right) dV + W_w + W_E \quad (2.10)$$

The magnitude of the depolarization energy W_E is related to the geometry of the crystal and the domain configuration at the surfaces. The depolarization field is usually proportional to the polarization, so that W_E can be described as,

$$W_E = \frac{1}{2} \int_V \vec{D} \vec{E} dV = \frac{1}{2} \int \frac{\epsilon}{\epsilon_0} L^2 P^2 dV \quad (2.11)$$

where L is the depolarization factor. The domain wall energy W_w depends on the domain wall density σ_d for a given domain geometry. In the volume V , W_w depends on the domain width d :

$$W_w = \left(\frac{\sigma_d}{d} \right) V \quad (2.12)$$

It should be noted that the formation of the domains is the most common mechanism for the reduction of the depolarizing fields, but it is not the only one. Other mechanisms include electrode screening, charge flow due to the electrical conduction, compensation by the surrounding medium, and others.

2.1.4 Phase Transitions

Among the most common structures of ferroelectric materials is the perovskite structure, described by the chemical formula ABO_3 , where the valence of the A site can be +1, +2, or +3 and the valence of the B site can be +3, +4, +5, or +6. The corners and body-centered positions of the unit cell are occupied by A-site and B-site cations, respectively, while the O^{2-} ions are located on the face-centered positions (Figure 2.4).

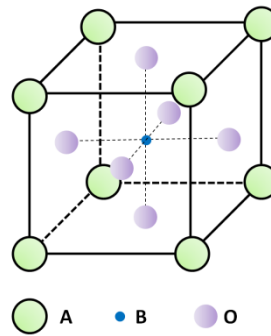


Figure 2.4. Schematic of the perovskite structure ABO_3 .

An ideal perovskite material has a cubic structure. It can also be described as consisting of BO_6 octahedra sharing corners with intermediate A-site cations in 12-fold coordination sites. A cubic perovskite shows neither ferroelectric nor piezoelectric properties because of the coincidence of positively and negatively charged centers. The paraelectric cubic structure can evolve into tetragonal, orthorhombic or rhombohedral with lower symmetry, originating from thermal- or stress-induced lattice distortions. Figure 2.5 displays the possible spontaneous polarization P_S orientations for various crystallographic structures. Common materials with perovskite structure include BaTiO_3 , PbTiO_3 , KNbO_3 , etc.

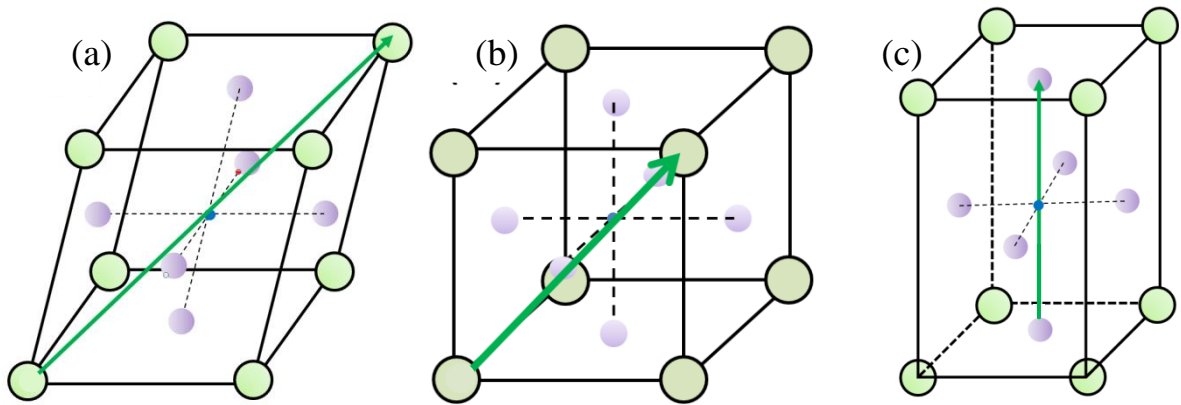


Figure 2.5. The orientation of P_S for various crystallographic structures: (a) rhombohedral, (b) orthorhombic, and (c) tetragonal phases. Please note that the distortions with respect to the cubic phase are exaggerated in the drawings for better visibility.

In the following section, BaTiO_3 will be taken as an example to describe ferroelectric phase transitions. Figure 2.6 shows temperature-dependent dielectric properties and polarization of single domain BaTiO_3 crystals. BaTiO_3 has a cubic structure without any macroscopic polarization above 120°C . Note that BaTiO_3 goes into the hexagonal phase above 1539°C [22]. As this phase is too far from the ferroelectric phase, it is not discussed for ferroelectric properties generally. A phase transition between paraelectric and ferroelectric phase occurs when BaTiO_3 is cooled below the so-called Curie temperature T_C . The structure changes to tetragonal and correspondingly exhibits a lattice distortion. The spontaneous polarization vector P_S is oriented along the axes of $\langle 001 \rangle_{\text{PC}}$ family. Note that “PC” stands for “pseudo-cubic” and the corresponding directions or planes mentioned in this thesis represent those of a cubic structure. Upon further cooling, the orientations of P_S switch to $\langle 110 \rangle_{\text{PC}}$ and the structure becomes orthorhombic. Eventually, P_S changes to $\langle 111 \rangle_{\text{PC}}$ when the rhombohedral symmetry appears. As shown

in Figure 2.6 (b), a relationship between the magnitudes of P_s for various phases exists in a BaTiO_3 single domain [14]:

$$P_s(\text{Tetra.}) = \sqrt{2} * P_s(\text{Ortho.}) = \sqrt{3} * P_s(\text{Rhomb.}) \quad (2.13)$$

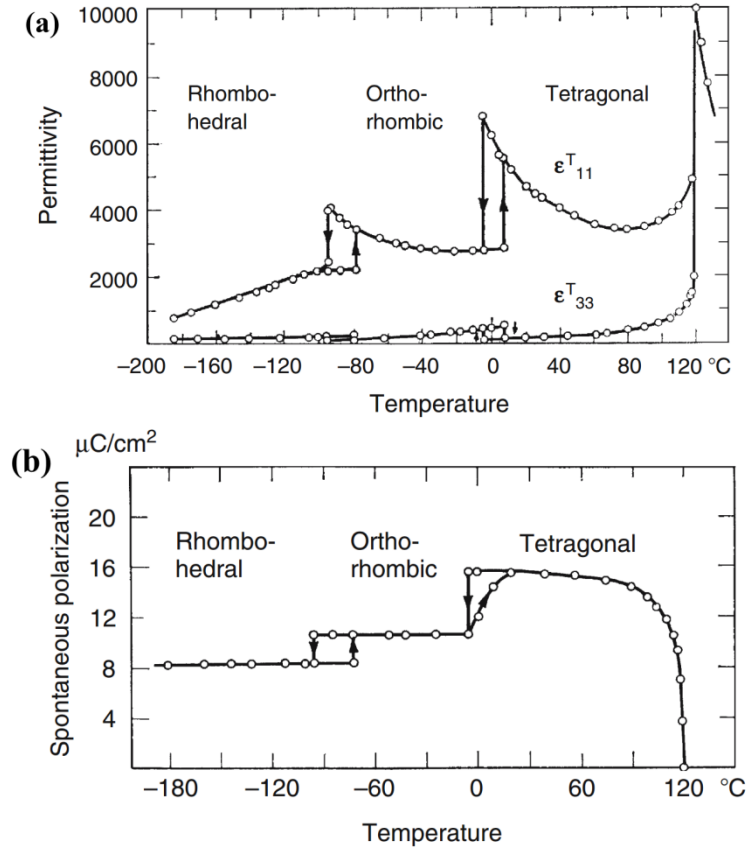


Figure 2.6. Temperature dependences of (a) dielectric properties and (b) polarization of a $[001]_{\text{PC}}$ -oriented single-domain BaTiO_3 crystal. Reprinted from Ref. [14], with permission of Springer.

The domain configuration is therefore strongly dependent on crystallographic structures, especially for the non-180 ° domains. In the tetragonal ferroelectric, non-180 ° domain walls are of 90 ° type. In the orthorhombic phase, one refers to 60 °, 90 ° and 120 ° domain walls [23]. In the rhombohedral phase, the types are of 71 ° and 109 °. These non-180 ° domain walls make important contributions to the ferroelastic properties. Figure 2.7 schematically shows the domains in tetragonal and rhombohedral $\text{Pb}(\text{Zr},\text{Ti})\text{O}_3$ (PZT) crystals with selected orientations [14].

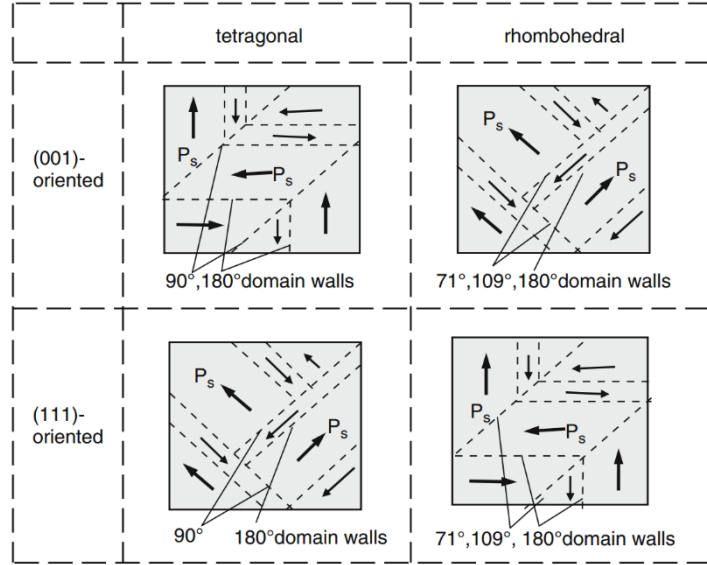


Figure 2.7. Domains in tetragonal and rhombohedral PZT crystals with selected orientations. Reprinted from Ref. [14], with permission of Springer.

Due to the versatility, the perovskite structure can be modified by the addition of various cations. This is an important routine to obtain a desired functional material due to the different atomic size and polarizability, *i.e.* with high ferroelectric or piezoelectric constant at room temperature, or good temperature stability of electrical properties.

In order to roughly classify the perovskite structures and the degree of distortion, Goldschmidt's tolerance factor t was defined based on the ionic radii [24],

$$t = \frac{R_A + R_O}{\sqrt{2}(R_B + R_O)} \quad (2.14)$$

where R_A , R_B , and R_O represent average ionic radii of A-site, B-site cations, and oxygen ions, respectively. The tolerance factor t of an ideal cubic structure, such as SrTiO_3 , equals to 1. The ions in the structure do not have the ability to move freely. When a smaller A ion or a larger B ion is doped into a perovskite structure, the t value will be smaller than 1. In this case, B-site ions can easily move to off-center positions, which often results in rhombohedral or orthorhombic lattice distortion. If t becomes larger than 1, the A ion can increase or the B ion decrease, which typically results in tetragonal symmetry. The prerequisite of a stable perovskite structure is $0.9 < t < 1.1$ [25]. The t values outside this range will lead to an unstable perovskite structure.

2.1.5 Defects in Perovskite Structure

The electrical properties of ferroelectrics are influenced not only by the lattice and domains, but also by structural defects. Therefore, the understanding of the defect chemistry of perovskite-type ferroelectric materials is very important for altering their electrical performance. The Kröger-Vink notation is typically used to classify the defects, using a main symbol, a subscript, and a superscript [26,27]. The main symbol refers to the defect species, denoted by the atomic symbol or V if it is a vacant lattice site. The subscript represents the lattice site the defect occupies, which may be a lattice or interstitial site. The superscript represents the charge at the defect site. A dot “·” denotes a positive charge, while a comma “’” stands for a negative charge. The zero net charge is indicated as “x”. Moreover, several conservation rules need to be considered: the conservation of mass, charge, structure, and electronic states. Table 2.1 lists some defects, which are expected to appear in the investigated materials in this work.

Table 2.1. Defect types, which are expected to appear in the investigated materials.

Defect type	Kröger-Vink notation
Oxygen vacancy	$V_{O^{\bullet\bullet}}$
K/Na/Li vacancy	$V_{K'}', V_{Na'}', V_{Li'}'$
Sb^{3+} impurity center	Sb_{Nb}''
Free electron	e'
Free hole	h^{\bullet}

Defects can be created unintentionally during the processing of ferroelectrics. In addition, they can also be created intentionally with small amounts of isovalent or aliovalent doping, in order to obtain the desired functional properties. Defects can be located in the bulk, near the grain boundaries, or at domain walls. When a material is chemically substituted with lower valence ions, referred to as acceptor doping. Typical examples are Fe^{3+} doped $Pb(Zr,Ti)O_3$, Cu^{2+} doped $PbTiO_3$, or Mn^{2+} doped $BaTiO_3$. In order to compensate charges, oxygen vacancies will be created simultaneously. It was demonstrated that these defects, such as, Cu_{Ti}'' , Fe_{Ti}' , Mn_{Ti}'' centers, are driven by a strong chemical force to form defect associations with oxygen vacancies, also denoted as defect dipoles [28]. With the application of electric or thermal fields, defect dipoles can align along the orientation parallel to spontaneous polarization vectors [29,30] and stabilize the domain structure [31]. Acceptor doping therefore typically hardens the ferroelectricity, accompanied by a larger coercive field, smaller polarization, and appearance of an

internal bias field. On the other hand, when high valence ions are introduced into a material (donor doping), such as Nb⁵⁺-doped PZT [32], the ferroelectricity can soften. This leads to a lower coercive field, lower oxygen vacancy concentration, large electromechanical coefficients, and large nonlinearity.

In addition, the charged defects also influence the electrical conductivity. For example, if the activation energy of conductivity is low, high mobility of oxygen vacancies will induce a high leakage current.

2.2 Fundamentals of Crystal Growth

Crystal growth refers to the separation of a solid-state phase from a solid, a liquid, or a gas state [33]. Oxide compounds with a high crystallization temperature, such as KTaO₃- or BaTiO₃-type materials, are usually grown from a high temperature liquid phase. There are two kinds of crystal growth methods: growth from the melt for congruently-melting compounds and growth from the solution for the others. Besides, single crystal growth from solid state is also reported. In this part, several crystal growth techniques are introduced briefly, including: Czochralski, Bridgman-Stockbarger, the conventional flux growth, top-seeded solution growth, and solid-state crystal growth methods. Most information is taken from the textbooks of Elwell and Scheel [34], Dhanaraj *et al.* [35], Jackson *et al.* [36], and Benčan *et al.* [37], and the review papers of Sun *et al.* [38], and Kang *et al.* [39].

Growth from Melts

For a crystallization process from the melt, the crystal is separated from the melt by directional solidification without any solvent. The composition of the as-grown crystal is the same as that of the melt. Crystals, which can be grown from the melt, must satisfy the following conditions:

1. The compound melts congruently, meaning that the liquidus and solidus curves coincide at the crystallization temperature. The crystallization temperature occurs at the melting temperature of the compound.
2. The compound does not decompose below the melting point.
3. No destructive solid–solid phase transition, particularly the first-order phase transition, occurs between the melting and room temperature.

Growth methods from the melt include the Czochralski growth method, Bridgman-Stockbarger method, and floating zone method among others. Note that the latter can also be used for non-congruent melting compounds. The growth rate of crystals from a melt is usually much higher than that of crystals grown from a solution due to the same chemical nature of both liquid phase and the crystals.

However, a large variety of crystals do not satisfy the above mentioned conditions due to the incongruent melting points, volatile components, or phase transitions. Moreover, high viscosity melts may lead to

the formation of glasses. A very high melting point ($T_M > 2000$ °C) also limits the use of the growth techniques from the melt because of the introduction of defects into the as-grown crystals, such as oxygen vacancies, thermal stresses, dislocations, and fractures, and because of the requirements of the setup.

Growth from High Temperature Solutions

Crystals, which cannot be obtained from their melts, are grown from a solution, such as an aqueous solution for hydrothermal growth or from a high temperature inorganic solution for the flux growth. For the solution crystallization process, the crystal is solidified from a solution with the addition of a solvent, which is called the flux. The crystallization process thus occurs at the saturation temperature of the solution, analogous to the melting temperature for congruently-melting materials.

The flux growth method is often applied to obtain ferroelectric single crystals. Simple inorganic compounds are selected as fluxes due to the low melting temperatures, such as B_2O_3 , Bi_2O_3 , $BaCl_2$, PbO , Na_2CO_3 , KOH , PbF_2 , and others. The selected compound should not incorporate into the as-grown crystal. One of the disadvantages of the flux method is the appearance of flux inclusions inside the as-grown crystals. It is a great challenge to produce large-scale crystals with high crystallographic quality by the conventional flux method. Other techniques have been developed by combining with the flux method, for instance, the solution Bridgman-Stockbarger growth [40,41,42] and the top-seeded solution growth method [43,44,45], which is widespread for $(K,Na)NbO_3$ (KNN)-based crystal growth. The self-flux method has been employed to produce single crystals when element species of the flux are contained in the desired crystal [46], and therefore avoids the foreign element contamination.

Crystal growth has three sub-processes: nucleation, growth, and the termination of the growth process. Homogeneous nucleation occurs when the nuclei start to appear anywhere in the liquid. However, heterogeneous nucleation generally occurs due to the lower free enthalpy of the formation of stable nuclei. It is therefore much easier for the nuclei to crystallize at the preferential locations, such as the crucible wall or the impurities. However, the heterogeneous nucleation process is quite uncontrollable. Generally, seeds (oriented single crystalline form or random polycrystalline form) are used during crystal growth process to provide a heterogeneous nucleation.

In the following section, the details of the Czochralski growth, Bridgman-Stockbarger, the conventional flux, top-seeded solution growth, and submerged-seed solution growth techniques are described. Moreover, a description of the solid-state crystal growth method, which is well-known in ferroelectric crystal growth, is also provided.

2.2.1 Top-seeded Solution Growth

In order to obtain large size crystals by the flux method, the top-seeded solution growth (TSSG) technique is undertaken with oriented single crystalline seeds. As compared to the Czochralski method, the TSSG setup has a similar geometrical and thermal configuration. However, a lower thermal gradient as well as the high temperature solution instead of a melt are employed in the flux growth method. Figure 2.8 (a) shows a scheme of the TSSG setup. The mixture of starting materials for the desired composition is loaded into a crucible and placed into a furnace. After being molten, the batch is soaked for 10–24 h in order to homogenize the solution. A seed crystal with an adequate orientation is then dipped into the solution at about the saturation temperature in order to reach the solubility equilibrium. Then, the crystal starts to grow by cooling the system at a small rate, for example 1 °C/day, and with slow pulling out of the crystal. At the end of the growth, the as-grown crystal is pulled out of the liquid solution and then cooled down to room temperature at a relatively higher cooling rate in the range of 5–30 °C/h. The TSSG method was successfully used to grow many perovskite crystals such as BaTiO₃ [6,47,48], PMN-PT [49,50], PIN-PMN-PT [51], Pb(Yb_{1/2}Nb_{1/2})O₃-Pb(Mg_{1/3}Nb_{2/3})O₃-PbTiO₃ (PYN-PMN-PT) [52], PZN-PT [44], NBT-BT [53,54,55], Mn-doped NBT-BT [56], Na_{1/2}Bi_{1/2}TiO₃-K_{1/2}Bi_{1/2}TiO₃ (NBT-KBT) [57], Na_{1/2}Bi_{1/2}TiO₃-Bi(Zn_{1/2}Ti_{1/2})O₃ (NBT-BZT) [58], KNbO₃ [59,60,61], and (K,Na)NbO₃ [62]. Figure 2.8 (b)-(g) shows various perovskite crystals grown by the TSSG technique. It should be pointed out that the crystal shapes are correlated to the seed orientations during the growth of KNbO₃ single crystals [59]. In fact, the growth time, growth parameters, and crystal habits also affect the shape of the crystals. Generally, single crystals with good quality can be grown by the TSSG method due to the small temperature gradient and slow growth process [50]. However, the growth rate by the TSSG method is lower compared with the Czochralski method, which makes the growth lasting several weeks for centimeter-sized single crystals. For example, a crystal with a few cm length was produced in 2 weeks in the present work.

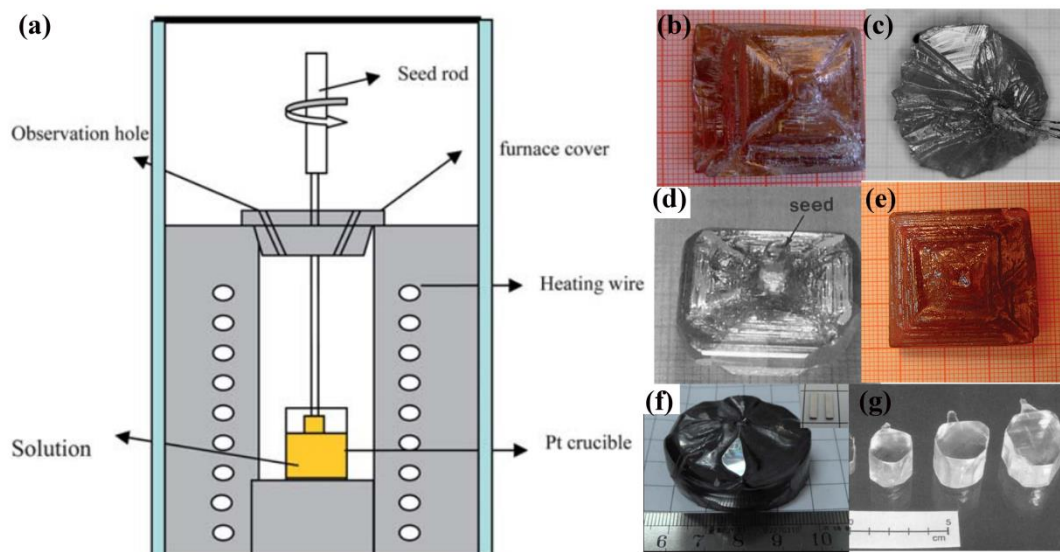


Figure 2.8. (a) Scheme of the TSSG setup. (b)-(g) Photographs of single crystals grown by the TSSG method: (b) PMN-PT [49], (c) PZN-PT [44], (d) BaTiO₃ [48], (e) PYN-PMN-PT [52], (f) Mn-doped NBT-BT [56], and (g) KNbO₃ [60]. The length of a regular grid in the graph paper in (b)-(e) is 1 mm. Adapted from Ref. [44,48,49,52,56,60], with permission of Elsevier, John Wiley and Sons, Royal Society of Chemistry, American Chemical Society, AIP Publishing LLC, and Elsevier, respectively.

2.2.2 Czochralski Method

The Czochralski technique is used to grow large-scale single crystals in a relatively short time. The process is determined by the temperature distribution in the melt and the heat convection between the melt, the crystal, and air, which are related to the thermal conductivity and heat capacity of the melt and the crystal. The growth technique is widely used to produce crystals that melt congruently, without any phase transition during growth process, such as Si or Ge single crystals.

Figure 2.9 describes the typical steps of the Czochralski technique. Powder mixture is loaded into a crucible made of an inert material. The selection rule of the crucible depends on the chemical bond in the compounds of the solution. For example, oxide compounds, of which chemical bonds are generally ionic covalent, are usually grown in a metallic crucible such as gold, platinum, or iridium in order to minimize chemical interactions. The load is molten in the suitable crucible at high temperature, and then the seed is inserted into the melt from the top and slowly pulled out from the melt with the rotation of the seed holder. The temperature gradient, pulling rate, and rotation speed need to be controlled accurately. The real-time observation of the temperature, image, and mass during the whole process can be recorded by thermocouples, cameras, and an electronic balance, respectively. Note that the rotation speed has a significant influence on the thermal distribution and mass transfer. A suitable rotation speed

can provide a symmetric thermal field and a homogeneous composition, as well as a suitable solid—liquid growth interface geometry, and this provides an environment for a steady growth. The Czochralski technique can supply high quality, centimeter-sized single crystals quickly in a few days. For example, Si single crystals with the length of 1 m and the diameter of 40 cm can be obtained within 3 days.

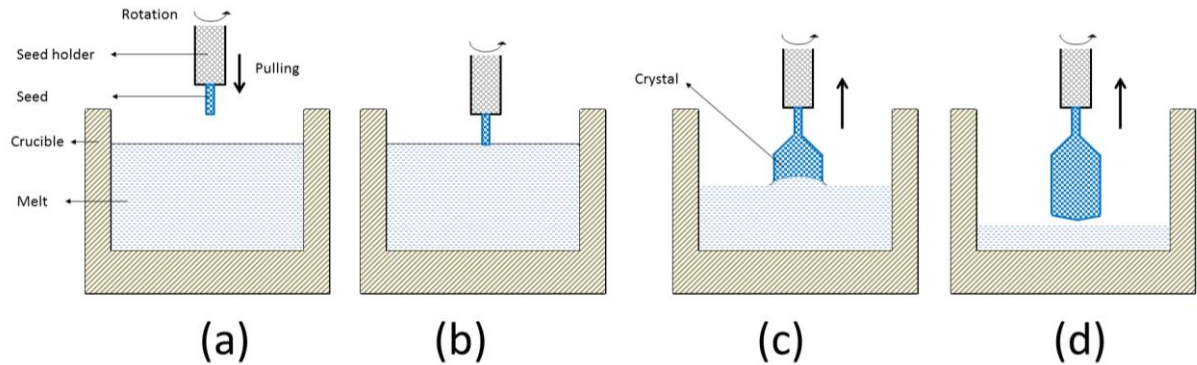


Figure 2.9. Typical steps of the Czochralski technique: (a) pulling down the seed, (b) contact with the melt, (c) crystal growth with rotation and slow pulling up, and (d) crystal extraction from the melt after the growth.

Some simple perovskite single crystals have been grown by the Czochralski method [63,64]. However, complex compositions of most ferroelectric solid solutions do not allow the use of this technique, due to incongruent melting (*i.e.*, $(\text{K,Na})\text{NbO}_3$ (KNN), $(\text{Na}_{0.5}\text{Bi}_{0.5})\text{TiO}_3$ (NBT)), preferential volatilization of some components (TiO_2 during BaTiO_3 growth), and solid—solid phase transitions (BaTiO_3 phase transition from hexagonal to cubic structure around 1539°C [22]).

2.2.3 Bridgman-Stockbarger Method

The Bridgman-Stockbarger furnace generally has three zones: an upper zone where the temperature is higher than the melting point of the material to be grown, a lower zone where the temperature is lower than the melting point, and an adiabatic zone in between. There are two configurations: vertical and horizontal furnaces. Figure 2.10 (a) shows a scheme of the vertical Bridgman-Stockbarger method with the corresponding thermal profile (b). The seed is located at the bottom of the growth ampoule and is molten on its half-length in order to obtain a monocrystal—liquid interface. The crucible is then pulled down at a slow rate of about 0.2–1.0 mm/h. Driven by supercooling, the epitaxy and growth of the crystal proceed from the molten solution above the interface when the crucible passes through the temperature gradient zone. The bottom of the crucible can be designed as a tip in order to reduce the number of nuclei. The vertical Bridgman-Stockbarger method is used extensively for growing perovskite ferroelectric single crystals [38], such as PMN-PT [65,66], $\text{Pb}(\text{Zn}_{1/3}\text{Nb}_{2/3})\text{O}_3\text{-PbTiO}_3$ (PZN-

PT) [40], $\text{Pb}(\text{In}_{1/2}\text{Nb}_{1/2})\text{O}_3\text{-Pb}(\text{Mg}_{1/3}\text{Nb}_{2/3})\text{O}_3\text{-PbTiO}_3$ (PIN-PMN-PT) [67], $\text{Pb}(\text{Lu}_{1/2}\text{Nb}_{1/2})\text{O}_3\text{-Pb}(\text{Mg}_{1/3}\text{Nb}_{2/3})\text{O}_3\text{-PbTiO}_3$ (PLN-PMN-PT) [68], $(\text{Na}_{0.5}\text{Bi}_{0.5})\text{TiO}_3\text{-BaTiO}_3$ (NBT-BT) [69], and KNN-based [70] crystals. Figure 2.10 (c) illustrates a PIN-PMN-PT single crystal grown by the Bridgman-Stockbarger method. Although large-size crystals can be obtained using this method, segregation phenomena will induce compositional inhomogeneities, as plotted in Figure 2.10 (d).

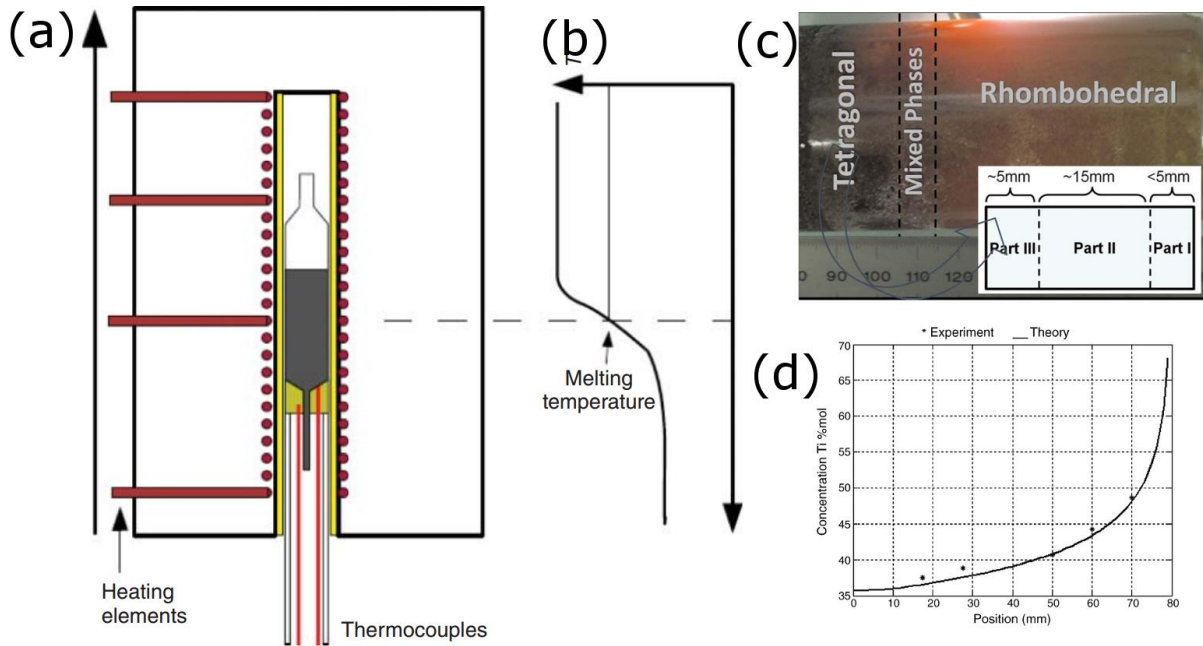


Figure 2.10. (a) Scheme of the vertical Bridgman method setup and (b) the temperature profile within the crucible [71]. (c) Photograph of a PIN-PMN-PT single crystal [67], and (d) the Ti concentration as a function of the position along the growth direction of the PMN-PT single crystal [72]. Reprinted from Ref. [67,71,72], with permission of AIP Publishing LLC, John Wiley and Sons, and Elsevier, respectively.

2.2.4 Conventional Flux Growth Method

The principle of the flux method is based on the chemical concept of solutions and solubility of a solute in a solvent. This method is dedicated to produce a single crystal at a lower temperature than its melting or its decomposition point, such as a peritectic transition, by mixing another compound (solute) to the raw material. Generally, high temperature growth process creates defects. The addition of the flux decreases the crystallization temperature, and therefore reduces the defect density. In order to obtain the desired composition, extensive experimental work is necessary to find the flux with the suitable chemical compounds and concentration, as well as the saturation temperature of the mixture. The crystal growth process with a flux is driven by the supersaturation of the liquid solution provided by the cooling

process below the saturation temperature. Hence, the crystallization occurs steadily by following the liquidus curve of the solute–solvent phase diagram at thermodynamically stable state.

The mixture, containing the starting materials and the flux, is first loaded into an inert crucible, covered by a lid and placed into a sealed alumina crucible. The whole system is heated to a temperature higher than the liquidus of the solution. In order to make the liquid solution stable and homogenous, it is soaked at a high temperature for several hours and then cooled with a slow rate, typically less than 1 °C/h. When the growth ends, higher cooling rates can be applied. The main drawback of this method is the formation of flux inclusions and the incorporation of impurities, resulting from the flux, into the as-grown crystals. In addition, it is difficult to obtain large-size crystals due to the absence of a seed and random spontaneous nucleation at the crucible wall. Figure 2.11 (a) displays the scheme of the conventional setup for crystal growth by the flux method. Three different perovskite single crystals grown by this technique are shown in Figure 2.11 (b)-(d).

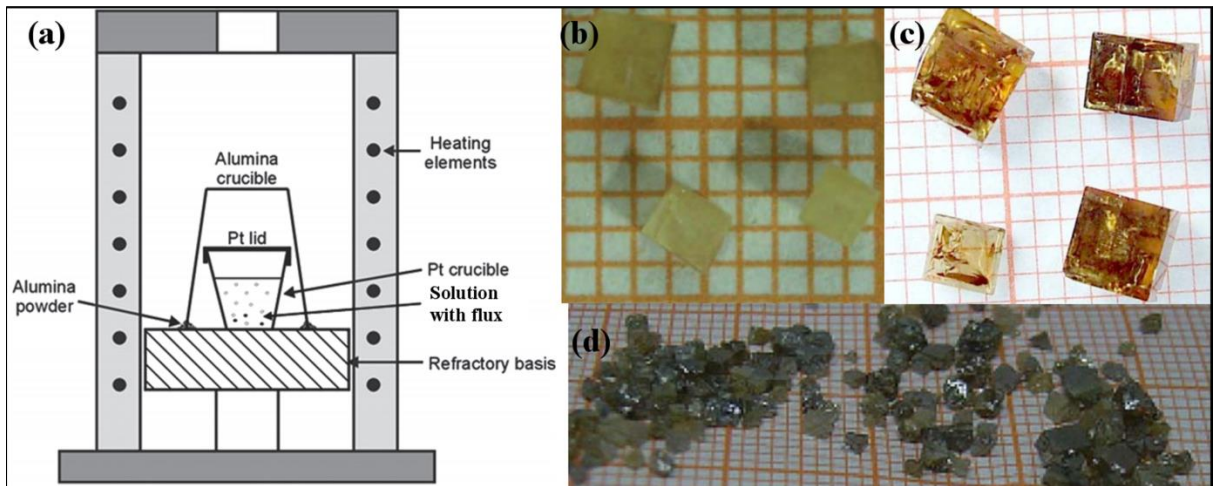


Figure 2.11. (a) Scheme of the conventional setup for crystal growth by the flux method. Three different ferroelectric crystals grown by the flux method: (b) $(\text{Pb},\text{La})(\text{Zr},\text{Sn},\text{Ti})\text{O}_3$ (PLZST) [73], (c) PMN-PT [74], and (d) $[\text{Bi}_{0.5}(\text{K}_x\text{Na}_{1-x})_{0.5}]\text{TiO}_3$ [75] single crystals. Note that the length of a regular grid in the graph paper is 1 mm. Reprinted or adapted from Ref. [73,74,75], with permission of Royal Society of Chemistry and Elsevier.

2.2.5 Submerged-seed Solution Growth

An alternative to the TSSG technique is the submerged-seed solution growth (SSSG) method. The geometrical and thermal configuration of the system is similar to the TSSG technique. Unlike the TSSG method, a polycrystalline seed is employed and is submerged in the core of the liquid solution during growth process. Natural growth crystallographic planes are always displayed in the as-grown single crystals. In our case, a platinum spatula was used as an active nucleation site for the crystal growth. This technique presents the advantage to perform a steady growth by avoiding the influence of thermal fluctuations, occurring at the solid-liquid interface on the top of the solution and induced by the compound volatilization, as compared to the TSSG method. These thermal fluctuations are more likely to induce flux inclusions in as-grown crystals. Note that in addition the heterogeneous nucleation process will occur at the crucible wall and impurities during the crystal growth process with the SSSG method, which is difficult to control.

2.2.6 Solid State Crystal Growth

The solid state crystal growth (SSCG) method is classified into two types. As described in Figure 2.12 (a), a seed crystal is embedded into a pressed matrix with polycrystalline powders of the targeted composition. The whole system is then heated at a high temperature below the melting point and the single crystal will grow from the seed into the polycrystalline part. Figure 2.12 (b) shows another method, whereby the seed crystal is placed on the top of a pre-sintered ceramic followed by the heating of the system. The single crystal starts to grow downwards from the seed into the polycrystalline ceramic [37].

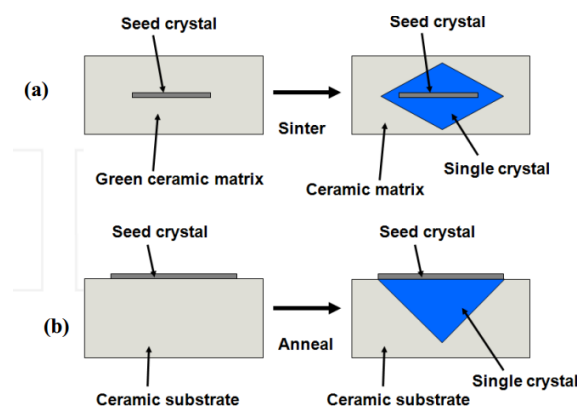


Figure 2.12. Schemes of two approaches for the solid-state single crystal growth method. Reprinted from Ref. [37], © 2011 Andreja Benčan.

In 1964, DeVries [76] first used the SSCG method for growing BaTiO₃ single crystals. Later, the SSCG method has been used for many perovskite ferroelectric single crystals, for instance BaTiO₃ [77], Ba(Zr,Ti)O₃ [78], PMN-PT [79,80,81], Pb(Mg_{1/3}Nb_{2/3})O₃-PbZrO₃-PbTiO₃ (PMN-PZ-PT) [82], BiScO₃-Pb(Mg_{1/3}Nb_{2/3})O₃-PbTiO₃ [83], and (K,Na)NbO₃ [37]. The as-grown crystals obtained with this method are often porous and thus of limited use for the ferroelectric and piezoelectric applications. On the other hand, the processing temperature is lower than the melting point, which enables good chemical homogeneity and lower costs.

2.3 K_xNa_{1-x}NbO₃ Polycrystalline Ceramics

K_xNa_{1-x}NbO₃ (KNN)-based materials are considered as one of the important alternatives to lead-based piezoelectric materials, due to their good piezoelectric performance and their relatively high Curie temperatures T_C . Saito *et al.* [4] reported an excellent textured (K,Na,Li)(Ta,Nb,Sb)O₃ (KNLTNS) ceramic with a high d_{33} of 416 pC/N and a high planar mode coupling coefficient k_p of 0.61, which could compete with those of Pb(Zr,Ti)O₃ (PZT) polycrystalline ceramics.

Pure KNN is a solid solution of ferroelectric (FE) KNbO₃ and antiferroelectric (AFE) NaNbO₃. Upon heating, the KNbO₃ undergoes the following sequence of phase transitions: rhombohedral–orthorhombic at -50 °C, orthorhombic–tetragonal at 220 °C, and tetragonal–paraelectric cubic at 434 °C [84,85]. The phase transition sequence of the NaNbO₃ upon heating is: ferroelectric monoclinic (F_{MON}) – antiferroelectric orthorhombic (A_o) at -55 °C, antiferroelectric orthorhombic (A_o) – paraelectric orthorhombic (P_{OM}) at 355 °C, paraelectric orthorhombic (P_{OM}) – paraelectric pseudotetragonal (P_{TM3}) at 430 °C, paraelectric pseudotetragonal (P_{TM3}) – paraelectric pseudotetragonal (P_{TM2}) at 470 °C, paraelectric pseudotetragonal (P_{TM2}) – paraelectric tetragonal (P_{TM}) at 530 °C, and paraelectric tetragonal (P_{TM1}) – paraelectric cubic (P_C) at 640 °C [1,21,86,87]. Shirane *et al.* [88] obtained enhanced ferroelectric properties when Na was substituted by 50 mol% K, leading to the well-known composition K_{0.5}Na_{0.5}NbO₃. Figure 2.13 shows the phase diagram of KNN, published by Li *et al.* [89] based on the work of Jaffe *et al.* [1] and Ahtee *et al.* [1,90,91].

Extensive work on perovskite ferroelectrics highlights that the electric performance can be enhanced by shifting the orthorhombic–tetragonal polymorphic phase transition (PPT) to room temperature, as shown in Figure 2.14 [89,92]. One of the effective methods to achieve this goal is chemical modification on the perovskite A or/and B sites. Saito *et al.* [4,93] successfully shifted the T_{O-T} of KNN to room temperature by the addition of Li, Ta, and Sb. These chemical modifications will be described in detail in the following.

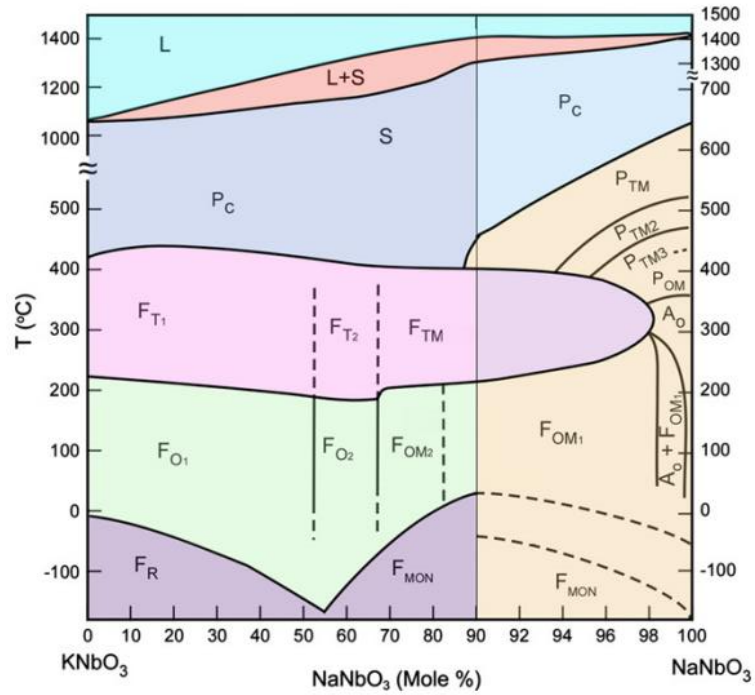


Figure 2.13. Phase diagram of the $K_xNa_{1-x}NbO_3$ solid solution [1,89]. Reprinted from [89], with permission of John Wiley and Sons.

Symbols here represent phase regions. *L*: liquid, *S*: solid, *P_C*: paraelectric cubic, *P_{TM}*, *P_{TM2}*, and *P_{TM1}*: paraelectric tetragonal, *P_{OM}*: paraelectric orthorhombic, *F_{T1}*, *F_{T2}*, and *F_{TM}*: ferroelectric tetragonal, *A_o*: antiferroelectric orthorhombic, *F_{O1}*, *F_{O2}*, *F_{OM1}*, and *F_{OM2}*: ferroelectric orthorhombic, *F_R*: ferroelectric rhombohedral, and *F_{MON}*: ferroelectric monoclinic.

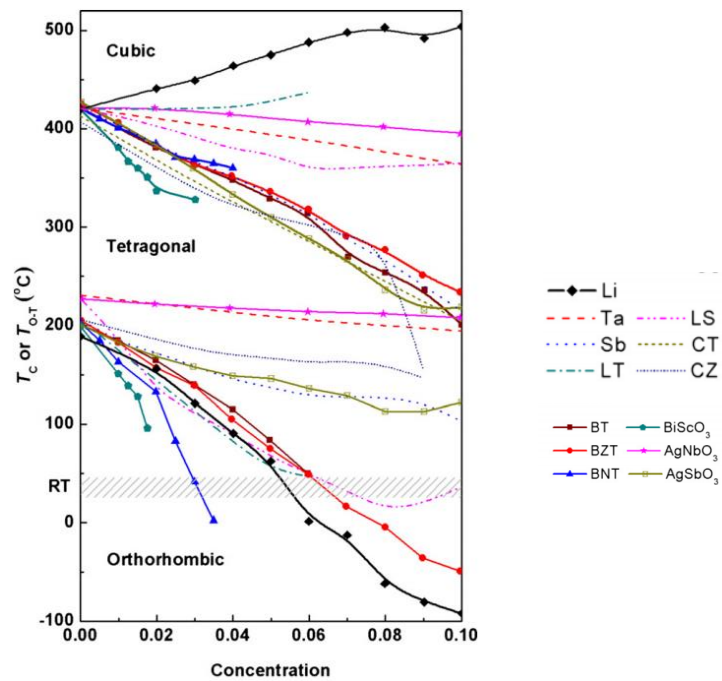


Figure 2.14. Influence of chemical modifications on T_{O-T} and T_C of KNN polycrystalline ceramics. Adapted from Ref. [89], with permission of John Wiley and Sons.

2.3.1 Li Substitution

As an alkali metal, Li is one of the leading modifiers in the KNN system. Although Li-, Ta-, and Sb-co-modified KNN ceramics show excellent piezoelectric properties, Li-modified KNN (KNLN) itself still attracts much interest due to the high cost of Ta and the toxicity of Sb. Guo *et al.* [94] studied the orthorhombic–tetragonal phase boundary in $[(K_{0.5}Na_{0.5})_{1-x}Li_x]NbO_3$ ceramics in the range of $0.05 < x < 0.07$. It was found that A-site Li substitution can shift the T_C to a higher temperature, while the T_{O-T} is shifted to a lower temperature due to the large lattice distortion. However, the $K_3Li_2Nb_5O_{15}$ secondary phase with a tetragonal tungsten bronze structure starts to appear if x is higher than 0.08.

A slight shift of the phase transition temperature and a lower sintering temperature of KNLN ceramics (1080 °C), as compared to pure KNN (1120 °C), was found by Du *et al.* [95]. The lower sintering temperature is expected to enhance the electrical properties by improving the density and stoichiometry, which results from the lower volatilization of K and Na elements [11].

One open question for KNLN system is the existence of a monoclinic phase. Klein *et al.* [96] reported that KNLN ceramics show a phase transition sequence similar to the one of pure KNN when x is below 0.05. However, a new phase was found between the orthorhombic phase and the tetragonal phase for higher Li concentrations based on Raman spectra. This new phase was believed to be monoclinic by Ge *et al.* [97] according to refinement results of X-ray diffraction. However, the existence of the monoclinic phase is still under discussion.

Li displays a similar influence also in $(K,Na,Li)(Ta,Nb)O_3$ (KNLTN) and $(K,Na,Li)(Ta,Nb,Sb)O_3$ (KNLTNS) systems. Lin *et al.* [98] reported increased T_C and decreased T_{O-T} with increasing the Li content in $((K_{0.5}Na_{0.5})_{1-x}Li_x)(Nb_{0.8}Ta_{0.2})O_3$ ceramics. An impurity phase started to form when x reached 0.06. Sintering temperatures were also reported to decrease with increasing x . Optimized room temperature coercive field E_C and P_r can be achieved at $x = 0.04$, in the vicinity of the orthorhombic–tetragonal phase boundary.

Based on the investigation on KNLN [94], $(K,Na)(Ta,Nb)O_3$ (KNTN), [98,99] and $(K,Na)(Ta,Nb,Sb)O_3$ (KNTNS) [100] ceramics, the increase rate of T_C is about 8–12 °C/mol% Li, while the decrease rate for T_{O-T} is about 22–35 °C/mol% Li. However, due to the much smaller ionic radius of Li^+ ($R(Li^+)=0.092$ nm, $R(Na^+)=0.118$ nm, and $R(K^+)=0.152$ nm [101]), a secondary phase will appear if the Li concentration is too high. The increasing E_C might be due to the shift of T_{O-T} to lower temperature and the increased unit-cell volume of the tetragonal phase with higher Li concentration.

2.3.2 Sb Substitution

B-site substitution is another effective approach for enhancing the piezoelectricity of KNN, which can be achieved with Sb or Ta. Higher electronegativity of Sb than Nb induces a higher degree of covalency, enhancing the off-centering movement of the B-site ions [4].

Recently, Wu *et al.* [102] investigated the role of Sb in $(\text{K}_{0.48}\text{Na}_{0.52})(\text{Nb}_{1-x}\text{Sb}_x)\text{O}_3$ ceramics. Increasing x shifted both T_C and T_{O-T} to lower values, but increased the rhombohedral–orthorhombic phase transition temperature (T_{R-O}). The decrease rates for T_C and T_{O-T} were 22 °C/mol% and 12 °C/mol%, respectively, while the T_{R-O} was increased by 10.5 °C/mol%. A mixed phase of rhombohedral and orthorhombic structures at room temperature was found when x was 0.08. However, a secondary phase and inhomogeneous distribution of Sb were detected for higher x values. On the other hand, the addition of Sb also increased the sintering temperature, which shows an opposite trend with Li substitution. Interestingly, an enhanced room temperature piezoelectric response did not appear at the rhombohedral–orthorhombic phase boundary ($x = 0.08$) but in the rhombohedral phase. Decrease rates of T_C and T_{O-T} in $(\text{K}_{0.4425}\text{Na}_{0.52}\text{Li}_{0.0375})(\text{Ta}_{0.0375}\text{Nb}_{0.9625-x}\text{Sb}_x)\text{O}_3$ ceramics were 14.9 °C/mol% and 17.5 °C/mol%, respectively [103]. E_C was also reported to decrease with increasing Sb content. Chang *et al.* [104] found that the tetragonality of the $(\text{K}_{0.44}\text{Na}_{0.52}\text{Li}_{0.04})(\text{Ta}_{0.2}\text{Nb}_{0.8-x}\text{Sb}_x)\text{O}_3$ ceramics decreased with increasing the Sb content.

Although the addition of Sb can improve piezoelectricity of KNN-based materials, its toxicity [105] to some extent limits its further usage.

2.3.3 Ta Substitution

Since the ionic radii of Nb and Ta are similar, B-site Ta substitution has also attracted a lot of attention for higher electrical performance. Moreover, unlike Li and Sb substitutions, larger amounts of Ta ions can diffuse into KNN materials.

With increasing Ta concentration, both T_C and T_{O-T} were shifted to lower temperatures in KNTN [106,107,108], $(\text{K,Na,Li})(\text{Ta,Nb})\text{O}_3$ (KNLTN) [98,109], and KNLTN [3,110]. In KNTN ceramics, the decrease rates of T_C and T_{O-T} were calculated to be 5–7 °C/mol% and 3–5 °C/mol [106,107,108]. Similar rates can be calculated in KNLTN ceramics [98,109]. The role of Ta ions in the appearance of polarization in KNLTN ceramics was studied using extended X-ray absorption fine structure by Huan *et al.* [111]. Three distinct peaks corresponding to the nearest neighbor Ta–O bond were observed at the orthorhombic–tetragonal phase transition, indicating the contribution of Ta displacements along different crystallographic orientations ($[001]_{\text{PC}}$ and $[110]_{\text{PC}}$) to the enhanced ferroelectric properties at T_{O-T} .

Note that Ta substitution also increases the melting temperature and sintering temperature of KNTN [106,112] and KNLTN [98] ceramics. One main disadvantage of Ta substitution is its high price.

2.3.4 Li, Sb, and /or Ta Substitution

It is a great challenge to shift the T_{O-T} to room temperature with only one of the above mentioned elements. Li substitution fails due to the possible appearance of the secondary phase, while Sb substitution increases the T_{R-O} , which cannot provide enhanced electrical properties. Only Ta addition enables to obtain the orthorhombic–tetragonal phase boundary at room temperature. However, the small decrease rate requires a large amount of Ta ions. Moreover, the T_C of KNTN compositions with room temperature T_{O-T} will be strongly decreased, thus limiting the usage of these materials. Therefore, simultaneous substitution of two or three of the mentioned ions is typically adopted to form a solid solution, for example, the addition of LiTaO_3 [113,114,115], and LiSbO_3 [116,117,118].

Although T_{O-T} in Li-, Ta-, and/or Sb-modified KNN systems can reach room temperature, the low temperature stability of piezoelectric and ferroelectric properties often prevents its application. Some other perovskite systems, such as CaTiO_3 [119,120,121], BaTiO_3 [122,123], SrTiO_3 [124], and CaZrO_3 [125,126] were proposed to modify the KNN systems instead, by which the deviations between tetragonal and orthorhombic lattice distortion are smoothed.

2.3.5 Mn Doping

Mn has three possible oxidation states, namely Mn^{2+} , Mn^{3+} , and Mn^{4+} . Oxides of all these states have been introduced into KNN-based ceramics: MnO [127,128,129], Mn_2O_3 [130], and MnO_2 [131,132,133,134,135,136,137,138,139]. MnO_2 is the most frequently used one.

Mn doping can effectively improve the density of KNN-based ceramics as a sintering aid [130,131,133,136]. Moreover, the grain size becomes larger with increasing the Mn concentration [131,132,136,137]. Zuo *et al.* [132] found that the grain size of KNLN ceramics increased from 2.7 μm to 7.1 μm when the MnO_2 content increased from 0 mol% to 1.5 mol%. The phase structure at room temperature also changed with Mn concentration. The tetragonality c/a decreased with increasing Mn contents [129,135]. Note that impurity phases will appear when the amount of Mn is higher than 1% [124,127,128].

Both T_C and T_{O-T} phase transition temperatures are dependent on the added amount of Mn. Rubio-Marcos *et al.* [127] reported that T_C decreased monotonously with MnO content in KNLTNs ceramics. However, T_{O-T} showed a decrease with a small amount of MnO, followed by an increase with higher MnO contents, as shown in Figure 2.15. Lin *et al.* [139] found that the addition of MnO_2 in KNN ceramics did not shift the T_C , but the T_{O-T} to lower temperature markedly, when its content changed from

0.25 mol% to 1.5 mol%. No apparent change of T_C with the addition of MnO_2 in KNLN ceramics was detected in other works [132]. Park *et al.* [136] even found increased T_C and decreased T_{O-T} with increasing MnO_2 from 0 mol% to 0.8 mol%. Mgbemere *et al.* [133] reported that upon increasing MnO_2 from 0 mol% to 10 mol %, T_C increased, but T_{O-T} decreased initially and then increased with a higher content.

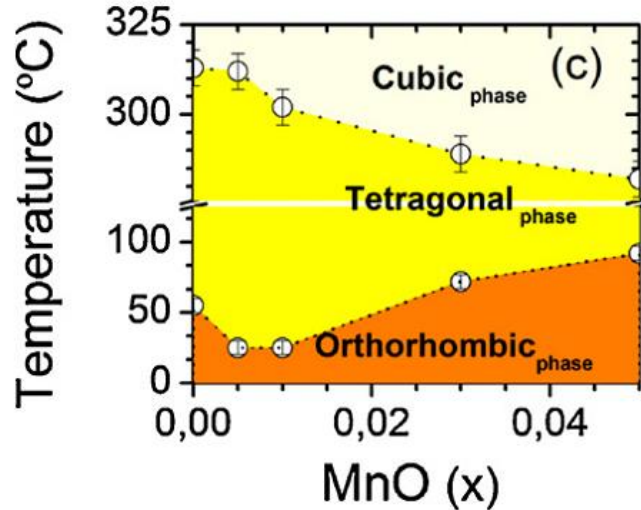


Figure 2.15. Shift of the T_C and T_{O-T} in Mn-doped KNLN ceramics with different MnO contents. Reprinted from Ref. [127], with permission of Elsevier.

The influence of Mn doping on dielectric properties was also investigated. Both dielectric permittivity and loss values at room temperature decreased with Mn content [127,131,133,139]. Zuo *et al.* [132] reported that Mn doping in KNLN ceramics decreased the dielectric loss in the lower temperature region but increased the loss in the higher temperature region, especially when the temperature was higher than T_C . Larger dielectric loss resulting from Mn doping at high temperature was also reported by Tian *et al.* [137] and Rubio-Marcos *et al.* [127]. With the Mn doping, the dielectric loss is decreased below T_C and increased above T_C [140]. The increased loss above T_C results from the increased concentration of oxygen vacancies. The decreased loss below T_C indicates the possible enhancement of electromechanical properties with Mn doping.

Zuo *et al.* [132] found that a small amount of Mn doping (0.3 and 0.6 mol%) pinched the ferroelectric hysteresis loops and decreased the E_C . On further increasing the Mn content, both E_C and P_r increased. However, Ogawa *et al.* [130] found the opposite trend: P_r and E_C increased with a small amount of Mn

doping but decreased with a large amount. Lin *et al.* [139] showed that P_r increased initially, but decreased with more Mn doping, while E_C decreased. Wongsanmal *et al.* [135] reported increasing E_C and decreasing P_r , while Rubio-Marcos *et al.* [127] found that E_C increased initially and then decreased, whereas P_r decreased monotonously. Therefore, the influence of Mn doping on P_r and E_C might be related to the composition of KNN-based ceramics and the Mn contents. It might be also related to the sintering conditions, such as the sintering temperature and sintering time, due to the volatilization of the alkali elements.

Furthermore, Mn doping can affect the electric field-induced strain curves. Decreased negative strains and positive strain with increasing Mn content were observed [132,133]. However, more experimental work about the influence of Mn content on electric field-induced strain curve is necessary for discussions. One suggestion is that Mn doping influences domain switching and domain wall movements in KNN-based materials. Zuo *et al.* [132] held the opinion that the substitution of Mn for Nb ions created oxygen vacancies that formed defect dipoles, which could provide an internal bias field and inhibit the domain switching by pinning effects.

Another feature is that the mechanical quality factor Q_m of KNN-based ceramics can be improved with increasing Mn content [124,127,132,136,139], which is helpful to limit the heat generation.

The ionic radii for individual elements in Mn-doped KNN-based ceramics are 0.067 nm for Mn^{2+} , 0.064 nm for Mn^{3+} , 0.053 nm for Mn^{4+} , 0.064 nm for Nb^{5+} , 0.064 nm for Ta^{5+} , 0.06 nm for Sb^{5+} , 0.152 nm for K^+ , 0.118 nm for Na^+ and 0.092 nm for Li^+ , based on the database of Ionic radii [101]. Mn ions may change their valence states with heating or cooling and may therefore enter into A or B sites of the perovskite structure. For example Rubio-Marcos *et al.* [127] reported that Mn enters the A site for small amounts, but enters both A and B sites for high Mn amounts. At present, the location and valence of Mn in KNN-based materials are still unclear.

2.3.6 The Origin of Enhanced Piezoelectricity in KNN-based Systems

The flattened free energy surface at structural phase boundaries gives rise to enhanced piezoelectric and ferroelectric response in most perovskite ferroelectric systems [141]. Several mechanisms have been proposed to clarify the enhanced electrical response. Nevertheless, this topic is still under intense discussion.

The most wide-spread opinion is the coexistence of mixed phases at the morphotropic (MPB) [1] or polymorphic (PPT) [142] phase boundaries. More energetically equivalent spontaneous polarization directions facilitate the polarization to switch from one state to another. Akdogan *et al.* [142] reported the coexistence of orthorhombic and tetragonal phases at the phase boundary, where the maximum

polarization was observed in KNLTNS polycrystalline ceramics due to a lowered energy barrier. This is similar to the KNbO_3 system, considering that Li-, Ta-, and/or Sb- modified KNN ceramics show the same sequence of polymorphic transitions.

Enhanced piezoelectric and ferroelectric properties with excellent temperature stability have been presented in lead-based MPB compositions. Therefore, some researchers investigated the possible formation of MPB in KNN-based compositions. Wang *et al.* [143] reported the appearance of the MPB with coexistence of rhombohedral and tetragonal phases in the $(\text{K,Na})(\text{Nb,Sb})\text{O}_3\text{-xBi}_{0.5}(\text{K,Na})_{0.5}\text{ZrO}_3$. Piezoelectric coefficient as high as 490 pC/N was observed at $x=0.04$. Cheng *et al.* [144] developed the $(\text{K,Na})(\text{Nb,Sb})\text{O}_3\text{-xBi}_{0.5}(\text{K,Na,Li})_{0.5}\text{ZrO}_3$ system and obtained a composition with high piezoelectric coefficient (380 pC/N) and improved temperature stability of piezoelectric coefficient. Recently, Wang *et al.* [145] investigated the temperature stability of several key piezoelectric parameters in $0.92(\text{K}_{0.5}\text{Na}_{0.5})\text{NbO}_3\text{-0.02}(\text{Bi}_{1/2}\text{Li}_{1/2})\text{TiO}_3\text{-0.06BaZrO}_3$ polycrystalline ceramics with the MPB structure. The piezoelectric coefficient decreased from ~ 350 pC/N to ~ 200 pC/N from room temperature to ~ 230 °C, while the planar electromechanical coupling coefficient decreased from $\sim 50\%$ to $\sim 35\%$. Despite the indication of improved piezoelectric properties and temperature stability, the exact nature of the rhombohedral phase and the appearance of a MPB remain controversial and further structural investigations are needed.

In addition, the appearance of an intermediate monoclinic phase would contribute to the improved piezoelectric properties with 24 available polarization vectors [146]. The intermediate monoclinic phase is also considered as a bridge between different spontaneous polarization vector families under the application of an electric field and enables easier polarization rotation [147,148,149,150]. In KNN-based system, a new phase according to the Raman spectra was assigned as the monoclinic structure [96].

It is believed that enhanced piezoelectric activity at the phase transition originates from enhancing intrinsic or extrinsic contributions [16,151]. The intrinsic contributions refer to phenomena originating from the local atomic displacements with the lattice distortion, whereas the extrinsic contributions are related to domain wall movements and interphase boundaries. Peng *et al.* [152] found that both intrinsic and extrinsic contributions increased to maximum below $T_{\text{O-T}}$ and decreased remarkably above $T_{\text{O-T}}$ in KNLTN ceramics. Note that the extrinsic contributions decrease faster than the intrinsic ones in tetragonal phase, while the opposite trend was observed in the orthorhombic phase.

The presence of nanodomains in ferroelectric materials is another explanation for the high piezoelectric and ferroelectric response. Using transmission electron microscopy (TEM), Fu *et al.* [153] observed nanodomain arrangements within microdomains for the composition of KNLTNS ceramics with enhanced piezoelectric coefficients. Only domains with irregularly shaped boundaries were observed in

the orthorhombic phase, whereas the tetragonal phase showed clear parallel stripes without nanodomains. The lower domain wall energy of the nanodomains allows them to reorient readily, therefore enhancing piezoelectricity. Nanodomains with 20–50 nm width were also observed by Huan *et al.* [154] and were believed to be the origin of high electric field-induced strain. Note that the extrinsic contribution from the nanodomains decreases after poling process due to the rearrangement of dipoles under an external field.

Polarization extension following the E field-induced phase transition was proposed to explain the high electrical properties of lead-based systems near the MPB [145,148,155]. Recently, Ge *et al.* [156] reported an analogous phenomenon for $[001]_{PC}$ -oriented NBT-BT crystals near the depolarization temperature. A similar field-induced phase transition was also observed near the T_{O-T} in $[001]_{PC}$ -textured KNLN ceramics [157]. Feng *et al.* [158] observed an E field-induced phase transition in KNLN polycrystalline ceramics with orthorhombic and tetragonal mixed structure and a higher piezoelectric coefficient. Iamsasri *et al.* [159] also proposed an E field-induced phase transition in KNLN polycrystalline ceramics according to the changed volume of the monoclinic and tetragonal phases near T_{O-T} detected by *in-situ* high energy X-ray diffraction, which was used to observe the structural evolution of KNN-based ceramics under the applied electric field.

2.4 KNN-based Single Crystals

2.4.1 Growth of KNN-based Single Crystals

Pure KNN single crystals for piezoelectric applications were grown with a self-flux method by Kizaki *et al.* [160] in 2006, following the breakthrough report by Saito *et al.* [4] on excellent properties of KNN-based textured ceramics. The high leakage currents were decreased by B-site Mn-doping. A remanent polarization P_r of 40 $\mu\text{C}/\text{cm}^2$ and a coercive field E_c of 1.2 kV/mm were reported in a Mn-doped KNN single crystal [160].

In 2007, $\text{K}_{0.5}\text{Na}_{0.5}\text{NbO}_3$ single crystals were first grown by the SSCG method [161]. A $[001]_C$ -oriented KTaO_3 seed with the size $2 \times 2 \times 0.5 \text{ mm}^3$ was embedded in KNN powders (1.2 g). $\text{K}_4\text{CuNb}_8\text{O}_{23}$ was selected as a sintering aid. After being pressed, the whole assembly was placed on a Pt foil in a sealed alumina crucible and sintered at 1100 °C for 10 h. Although the crystal grew along the length, its thickness was only about 160 μm due to the low growth rate and many pores were distributed in the volume, as presented in Figure 2.16. Hot pressing was used to reduce the porosity, but the crystal became much thinner. It was reported that the dimension and crystalline quality are dependent on the sintering aid content [162]. Note that the investigated single crystals were chemically homogenous. By optimizing

the density of the matrix before the growth process, the thickness of the single crystal regions increased but it was still difficult to remove the pores [163]. Moreover, the pore size increased with increasing growth time. This SSCG method was also used to grow $(\text{K,Na,Li})(\text{Ta,Nb})\text{O}_3$ single crystals [164].

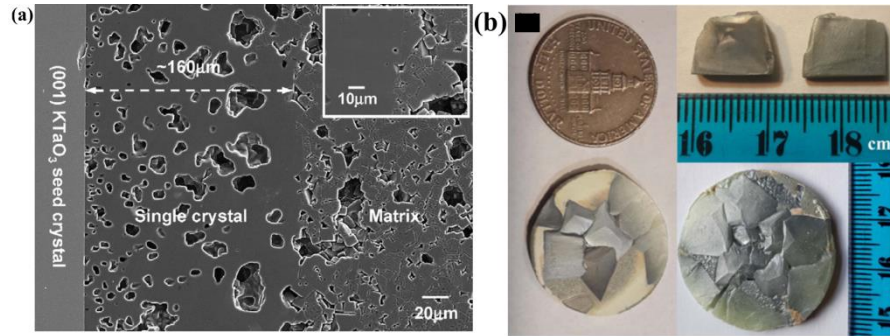


Figure 2.16: (a) Scanning electron microscopy (SEM) image of a KNN single crystal grown by the SSCG method [161], and (b) photographs of samples grown by the seed-free SSCG method [165]. Reprinted from Ref. [161,165], with permission of Elsevier and John Wiley and Sons.

Uršič *et al.* [166] reported the electromechanical properties of a $[131]_O$ -oriented $\text{K}_{0.5}\text{Na}_{0.5}\text{NbO}_3$ single crystal grown by the SSCG method: $P_r = 17 \mu\text{C}/\text{cm}^2$; $E_C = 2.4 \text{ kV}/\text{mm}$; $d_{33}^* = 67 \text{ pm}/\text{V}$ and $\epsilon_r = 1015$. Recently, Jiang *et al.* [165] obtained KNN-based single crystals by the seed-free SSCG. As shown in Figure 2.16 (b), the average area for a single crystalline piece was about $10 \times 7 \text{ mm}^2$ and the thickness about several micrometers. Due to the influence of multiple grains on the disk shaped sample, it was difficult to obtain large-size single crystals. The crystal dimensions and quality can be improved by the cold isostatic pressing. Recently, Yang *et al.* [167] obtained a crystal with dimensions of $6 \times 5 \times 2 \text{ mm}^3$ by the same growth method. This crystal showed a high piezoelectric coefficient d_{33} of $689 \text{ pC}/\text{N}$ and a high T_C of $432 \text{ }^\circ\text{C}$.

Many efforts have been made to grow KNN-based crystals with the flux method. Inagaki *et al.* [168] studied the influence of growth conditions of Mn-doped KNN crystals with a KF-NaF eutectic flux. It was found that a suitable cooling rate was important for dimensions and electrical properties of the single crystals. When a cooling rate of $0.5 \text{ }^\circ\text{C}/\text{min}$ was selected, excellent ferroelectric properties with $P_r = 45 \mu\text{C}/\text{cm}^2$ and $E_C = 0.72 \text{ kV}/\text{mm}$ were obtained. Figure 2.17 provides a photograph of $\text{K}_{0.56}\text{Na}_{0.44}\text{NbO}_3$ single crystals grown by the slow-cooling technique in 2009 [169]. The largest crystal among was about $4 \times 4 \times 8 \text{ mm}^3$. However, the authors found that crystallographic phases of crystals grown at different positions were very different, indicating chemical inhomogeneity. The room temperature d_{33} and the maximum d_{33} at T_{O-T} along the $[001]_{PC}$ orientation were $132 \text{ pC}/\text{N}$ and $220 \text{ pC}/\text{N}$, respectively.

KNN single crystals with sizes $2 \times 2 \times 0.5 \text{ mm}^3$ and $8 \times 3 \times 3 \text{ mm}^3$ were grown using K_2CO_3 and B_2O_3 as the flux by Rafiq *et al.* [170]. High maximum permittivity, P_r ($19 \mu\text{C}/\text{cm}^2$) and d_{33} (160 pC/N) were observed. Saravanan *et al.* [171] investigated the influence of the addition of B_2O_3 in the flux during KNN crystal growth. The selected flux was a mixture of KF, NaF, and B_2O_3 . They found that larger-size crystals can be grown by optimizing the amount of B_2O_3 in the flux. The crystal with 1.5 wt% B_2O_3 in the flux showed the highest d_{33} of about 106 pC/N and a wider ferroelectric domain. A (K,Na,Li) NbO_3 single crystal [172] with $10 \times 11 \times 6 \text{ mm}^3$ and a (K,Na,Li)(Nb,Sb) O_3 single crystal [173] with $9 \times 8 \times 4 \text{ mm}^3$ were also grown with a mixture of Na_2CO_3 , K_2CO_3 , and Li_2CO_3 as the flux. Although the sizes were larger than other crystals grown by the flux method, the P_r of both crystals were less than $8 \mu\text{C}/\text{cm}^2$.

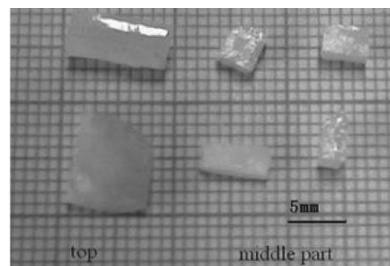


Figure 2.17. Photograph of KNN crystals grown by the flux method. Reprinted from Ref. [169], with permission of Taylor & Francis.

In 2007, Chen *et al.* [70] obtained a KNLN single crystal with an excellent d_{33} of 405 pC/N by the Bridgman method. The pre-densified polycrystalline sample was sealed into a Pt crucible and heated to $1300 \text{ }^\circ\text{C}$. After being soaked for 10 h, the crucible was pulled down at the rate of 0.4–0.6 mm/h, whereas the temperature gradient near the solid–liquid interface was maintained between 30 and $50 \text{ }^\circ\text{C}/\text{cm}$. Several pieces with $4 \times 6 \times 0.5 \text{ mm}^3$ were cut from the boule, as shown in the Figure 2.18 (a). Unfortunately, the P - E loop exhibited very high leakage currents (see Figure 2.18 (c)). A Na-rich KNN single crystal with high dielectric losses was grown by the same method, as shown in Figure 2.18 (b) [174].

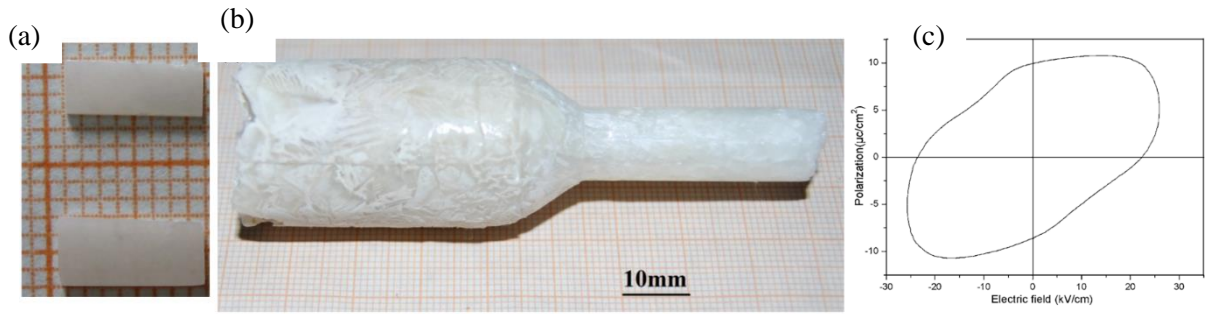


Figure 2.18. Photograph of (a) pieces of cut [70] and (b) as-grown KNN crystals obtained by the modified Bridgman method [174], and (c) P - E loop ($f = 20$ Hz) with high leakage current of $[001]_{PC}$ -oriented KNLN single crystals grown by the Bridgman method [70]. Reprinted from Ref. [70], with permission of AIP Publishing LLC and from Ref. [174], © 2014 Dabin Lin.

Liu *et al.* [175] studied the effects of MnO_2 on the properties of MnO_2 -doped KNLN single crystals, which were grown by the Bridgman method using $KCl-K_2CO_3$ as the flux. Although the highest d_{33} (226 pC/N) is lower than the one report by Chen *et al.* [70], the crystals with Mn showed improved ferroelectric properties. Inagaki *et al.* [176] reported KNN and Mn-doped KNN single crystals grown by the floating zone method in air. The long green body of 6 mm in diameter was pre-pressed and then put into an infrared convergence-type floating furnace with two ellipsoidal mirrors. Set at the focal points of the ellipsoid, two halogen lamps were used as infrared sources. The growth rate and the rotation speed of the upper and lower shafts were fixed as 3 mm/h and 25 rpm, respectively. Finally, a Mn-doped KNN crystal of approximate 4–5 mm in diameter and 12.5 mm in length was obtained, which is shown in Figure 2.19 (a). In Figure 2.19 (b) and (c), Scanning electron microscopy (SEM) images showed the crystal was in fact a polycrystalline stack of tabular layers of 50–200 μm width and of 2 μm thickness along directions parallel and perpendicular to the growth direction.

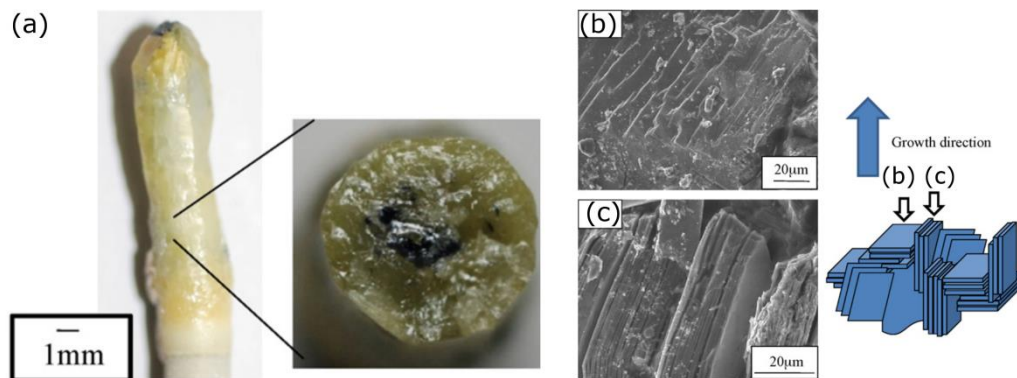


Figure 2.19. (a) Mn-doped KNN crystal grown by the floating zone method. (b) and (c) Cross section SEM images. Reprinted from Ref. [176], with permission of Elsevier.

However, KNN crystals grown by the floating method were short along the growth direction due to the difficulty in maintaining a stable molten zone. In order to improve the stability, KNN crystals were grown in nitrogen or oxygen atmospheres [177]. These crystals were about 30 mm longer than the ones grown in air.

The TSSG technique is one of the most popular methods for the growth of KNN-based single crystals, due to the possibility to obtain large-size crystals. Figure 2.20 (a) presents a $(\text{K}_{0.95}\text{Na}_{0.05})(\text{Ta}_{0.61}\text{Nb}_{0.39})\text{O}_3$ single crystal with high crystal quality grown by the TSSG method [178]. Unfortunately, its T_C was lower than room temperature, which is not practical for applications. In 2013, Prakasam *et al.* [46] grew centimeter-sized $(\text{K,Na,Li})(\text{Ta,Nb,Sb})\text{O}_3$ (KNLTNS) single crystals by a similar method, where a platinum spatula was used instead of a seed. This was one of the early reports on KNLTNS single crystals with high T_C (370 °C). Compared with the TSSG method, the crystals did not show well-arranged shapes due to random nucleation at the beginning of the growth, as shown in Figure 2.20 (b). The small crystals were absorbed by large crystals step by step and several crystals with similar composition for every attempt were obtained. For a better understanding of the growth of KNN-based single crystals, the segregation phenomena of individual elements were investigated for the first time.



Figure 2.20. Examples of as-grown crystals: (a) colorless cubic KNTN (TSSG) [178], (b) KNLTNS (SSSG) [46], and (c) KNTN (TSSG) single crystals [179]. Reprinted from Ref. [46,178,179], with permission of Elsevier Masson, Springer, and Royal Society of Chemistry.

An orthorhombic KNTN piezoelectric single crystal with the size of $12 \times 11 \times 11 \text{ mm}^3$ was grown by Zheng *et al.* [179]. The synthesized KNTN powders were loaded into a Pt crucible and heated at 1140 °C. Then the seed was dipped into the liquid solution and pulled out at a rate of 0.2–0.5 mm/h with slow rotation. Although the crystal was not as clear and transparent as the cubic KNN-based single crystals, it was uniform, as shown in Figure 2.20 (c). Table 2.2 summarizes dimensions and piezoelectric coefficients of selected KNN and KNN-based single crystals grown by TSSG.

Table 2.2. Dimensions and piezoelectric coefficients of selected KNN and KNN-based crystals growth by TSSG.

Crystal	Structure at RT	Dimension	d_{33} at RT (pC/N)	Ref.
KNN	Orthorhombic	Φ 30 mm x 10 mm	145	[180]
KNN	Orthorhombic	16 x 16 x 20 mm ³	161	[62]
KNT	Tetragonal	/	142	[181]
KNTN	Orthorhombic	12 x 11 x 11 mm ³	200	[179]
KNLTN	Orthorhombic	18 x 18 x 10 mm ³	255	[182]
KNLTNS	Tetragonal	8.5 x 8.5 x 13.5 mm ³	173	[183]
Mn: KNLTN	Ortho.-Tetra. Mixed	5 x 5 x 9 mm ³	630	[184]

2.4.2 Piezoelectric and Ferroelectric Properties

Pure KNN Single Crystals

Several researchers focused on the growth of pure KNN single crystals due to the simpler composition [62,180], as compared to modified KNN systems. It was expected that pure KNN single crystals should show much better properties than the corresponding polycrystalline ceramics. Pure KNN single crystals with different K/Na molar ratios were successfully grown using the TSSG method by Tian *et al.* [62]. The authors made a comparison between electrical properties with various K/Na molar ratios, as shown in Table 2.3. The highest d_{33} of 161 pC/N was achieved for a K/Na molar ratio of 62.2/37.8. Although this value is comparable to most KNN polycrystalline ceramics, it was still much lower than for PZT polycrystalline ceramics. This was related to the weaker intrinsic ferroelectricity of pure KNN system.

Table 2.3. Comparison of electrical properties of pure KNN single crystals with various K/Na ratios.

K/Na molar ratio	Growth Method	T_{O-T} (°C)	T_C (°C)	$\epsilon_{33,r}/\epsilon_0$	$\tan\delta$ at RT (%)	E_C (kV/cm)	P_r ($\mu\text{C}/\text{cm}^2$)	d_{33} (pC/N)	Ref.
33.4/66.6	TSSG	174	395	68	0.4	11.59	11.2	105	[62]
45.5/54.5	TSSG	181	397	73	0.5	11.10	8.3	142	[62]
53.8/46.2	TSSG	195	418	339	0.3	12.93	11.8	145	[62]
62.2/37.8	TSSG	199	424	70	0.3	14.24	10.8	161	[62]
88.2/11.8	TSSG	220	436	69	0.2	18.78	9.2	110	[62]
25/75	TSSG	187	396	375	/	8.4	7.2	145	[180]
56/44	Cooling	214	433	/	/	/	/	130	[169]
51/49	Flux	215	429	300	/	10.6	19.4	160	[170]
50/50	SSCG	192	410	1015	0.01	24.0	17.0	/	[166]

Li, Ta or/and Sb Co-Modified KNN Single Crystals

In order to shift the T_{O-T} to room temperature, KNLN, KNTN, (K,Li)(Ta,Nb)O₃ (KLTN), KNLTN, KNLNS, and KNLTNS single crystals were investigated, as summarized in Table 2.4. Compositions with T_{O-T} near room temperature in Li, Ta, or/and Sb co-modified KNN single crystals, however, have been rarely reported. The possible reason is the different segregation coefficients for individual elements and for different growth conditions. As a consequence, the initial composition of the starting materials is typically very different from the one of the as-grown single crystal. In addition, no exceptionally high electrical properties were reported for these KNN-based single crystals, which might be due to high leakage currents.

Table 2.4. Comparison of electrical behavior of Li, Ta, or/and Sb co-modified KNN-based single crystals.

Crystal	Growth Method	T_{O-T} (°C)	T_C (°C)	$\epsilon_{33,r}/\epsilon_0$	$\tan\delta$ at RT (%)	E_c (kV/cm)	P_r ($\mu\text{C}/\text{cm}^2$)	d_{33} (pC/N)	Ref.
KNT	TSSG	8	92	3900	/	/	/	142	[181]
KNLN	Flux	220	420	/	/	8.02	4.01	115	[172]
KNLN	Bridgman	192	426	/	0.011	/	/	405	[70]
KNLN	SFSSCG	75	432	500	<0.1	13.9	24.1	689	[167]
KNTN	TSSG	121	291	267	0.004	/	/	200	[179]
KNTN	TSSG	85	253	255	/	/	/	150	[185]
KNLTN	TSSG	79	276	/	0.01	/	/	255	[142]
KNLNS	Flux	205	355	833	/	15.45	3.66	125	[173]
KNLTNS	TSSG	-10	210	912	/	8.165	9.045	173	[183]
KNLTNS	SSSG	160	370	/	/	/	/	/	[46]

Mn-Doped KNN-Based Single Crystals

Mn doping was used to decrease the leakage current [62,70,177,183] and dielectric losses [166,175,182] of KNN-based single crystals [160]. Lin *et al.* [186] found that addition of 0.5 mol% Mn increased the permittivity of KNN crystals at room temperature from 240 to 730. Moreover, the piezoelectric coefficients d_{33} (Figure 2.21 (a)) were also improved due to the lower leakage current density and smaller domain size. Recently, a high d_{33} of 630 pC/N in a Mn-doped KNLTN single crystal has been reported by Huo *et al.* [184]. The large-signal piezoelectric coefficient d_{33}^* , calculated from unipolar strain curves, reached 870 pm/V, which is comparable to the values of PZT ceramics and PIN-PMN-PT single crystals,

as shown in Figure 2.21 (b). The origin of the excellent piezoelectricity may be due to the proximity of T_{O-T} (30 °C) to room temperature.

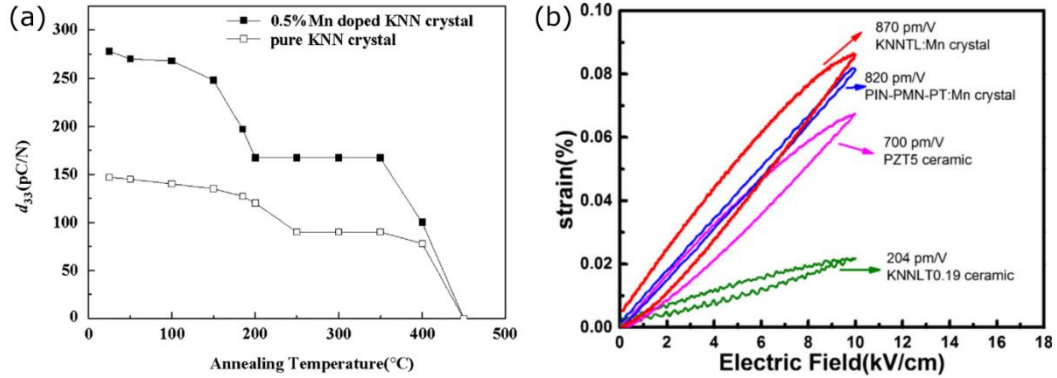


Figure 2.21. (a) Influence of thermal depoling on room temperature d_{33} in $[001]_{PC}$ -oriented undoped and 0.5 mol% MnO_2 -doped KNN crystals [186]. (b) Unipolar electric field-induced strain curves ($f = 5$ Hz) for Mn-doped KNLTN single crystal, PIN-PMN-PT:Mn single crystal, PZT5 ceramics and KNLTN0.19 ceramics [184]. Reprinted from Ref. [184,186], with permission of John Wiley and Sons.

Influence of Annealing Process

As mentioned in the last paragraph, KNN-based single crystals often suffer from high leakage currents [62,70,177,183] and high dielectric losses [166,175,182]. They are believed to originate from the volatilization of alkali elements [11], the possible existence of Nb^{4+} ions and oxygen vacancies [160]. This limits their further applications in the piezoelectric field. Kizaki *et al.* [187] and Noguchi *et al.* [188] found that the leakage current densities of pure KNN crystals have been reduced after annealing in air or O_2 , as shown in Figure 2.22. However, the underlying conductivity mechanisms of $(K,Na,Li)(Ta,Nb,Sb)O_3$ single crystals are currently still unclear and need further investigations.

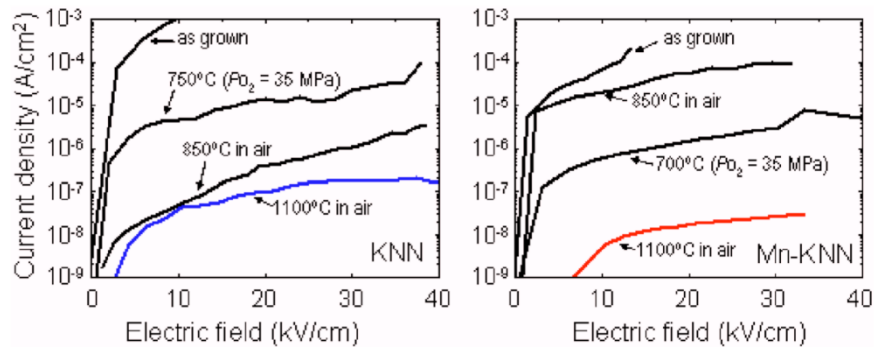


Figure 2.22. Leakage current density of the $[001]_{PC}$ -oriented KNN and Mn-doped KNN crystals annealed under various oxidation conditions. Reprinted from Ref. [187], with permission of AIP Publishing LLC.

2.4.3 Ferroelectric Domains in KNN-based Single Crystals

The static and dynamic domain configurations in KNN-based single crystals were investigated using different techniques, such as polarized light microscopy (PLM) [189], transmission electron microscopy (TEM), piezoresponse force microscopy (PFM) [170], and confocal Raman microscopy [190].

Inagaki *et al.* [191] investigated the influence of cooling rates during crystal growth on the domain configuration and ferroelectric properties. They found that small-scale domains are formed with slower cooling rates due to the releasing of internal stress. In addition, 60° domains were formed easier with slower cooling rates, thus improving the ferroelectricity. Zheng *et al.* [189] observed the domain evolution of $[001]_{\text{PC}}$ -oriented KNTN crystals at various temperatures. The orientations of domain walls changed from $\{110\}_{\text{PC}}$ to $\{010\}_{\text{PC}}$. They found that the domain structure is temperature stable in the orthorhombic phase region. Deng *et al.* [192] reported lamellar domains with reduced domain width under 2 kV/mm in pure orthorhombic KNN single crystals, as shown in Figure 2.23.

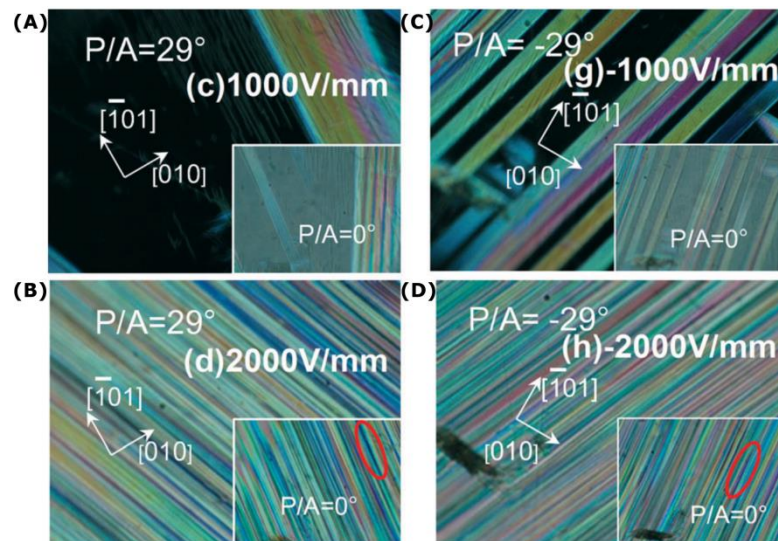


Figure 2.23. *In-situ* domain configurations of pure orthorhombic KNN single crystals imaged by PLM at different E fields: (A) 1 kV/mm, (B) 2 kV/mm, (C) -1 kV/mm, and (D) -2 kV/mm. Reprinted from Ref. [192], with permission of Royal Society of Chemistry.

3 Experimental Procedure

3.1 Crystal Growth

Since (K,Na)NbO₃ (KNN)-based materials are solid solutions, the liquidus and solidus curves in the corresponding phase diagrams are separated [193]. All the crystals presented in this work were therefore grown from high temperature solutions by the flux method [34]. The use of a solvent (flux) allows the crystallization of a compound (solute) under a thermodynamically stable condition. Among the wide choice of possible fluxes, a great advantage of the self-flux method is that the solvent and desired solute have the same element species, avoiding the contamination of the crystals by foreign elements. In this work, a self-flux consisting mostly of excess Li₂O and K₂O was employed.

Two slightly different flux growth techniques were employed using resistive heating furnaces and platinum crucibles in air atmosphere. The longitudinal thermal gradient in the furnace was less than 1°C/cm.

3.1.1 Submerged-seed Solution Growth

Crystal Growth Set-up

Crystal growth attempts performed at ICMCB were implemented using a platinum spatula mounted on an alumina rod. As shown in Figure 3.1 (a), the furnace for the KNN-based single crystal growth was equipped with an electronic balance with an accuracy of 10⁻² g. The electronic balance was connected with a home-made Lab-View program in order to accurately monitor the mass change and the different sub-processes during the growth. The furnace assembly with translation, rotation devices and Lab-View program was set up by the ICMCB engineer assistant, Mr. Oudomsack Viraphong.

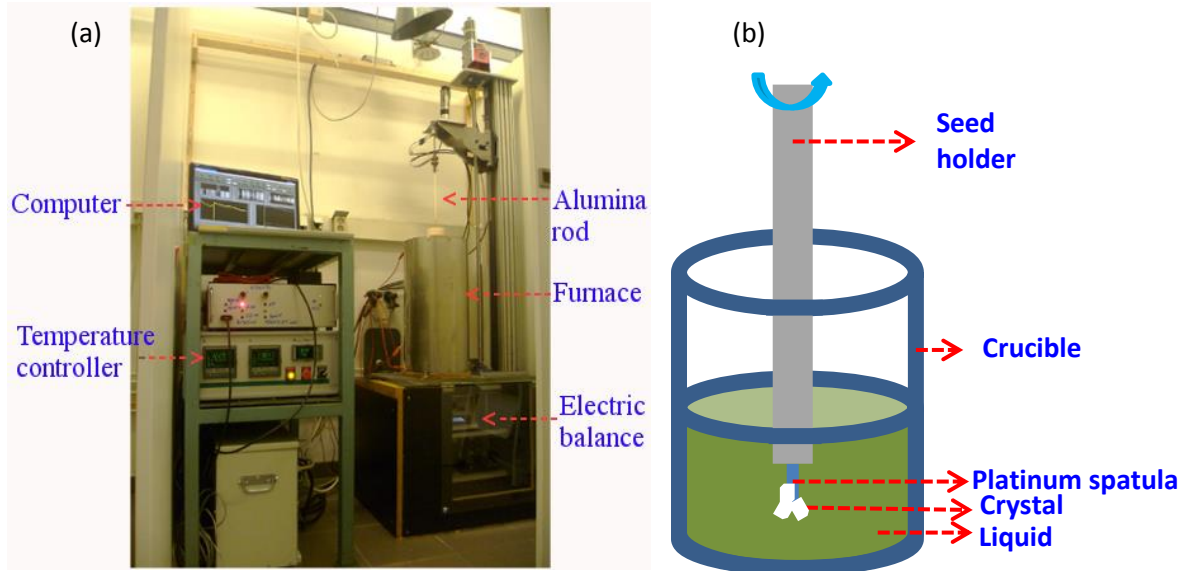


Figure 3.1. (a) Photograph of the furnace and (b) schematic diagram of the growth process inside the crucible for the KNN-based crystal growth using the submerged-seed solution growth method.

Experimental Process

The starting materials were high-purity (99.99 %) MnO_2 , K_2CO_3 , Na_2CO_3 , Li_2CO_3 , Nb_2O_5 , and Ta_2O_5 (Furukawa Chemicals Co. Ltd). The powders were first weighed according to desired compositions and the influence of segregation phenomenon, followed by the 24 h dry mixing process. The mixture was put into a platinum crucible and calcined for 12 h at 450 °C and then for 12 h at 850 °C. The processing route to obtain $(\text{K,Na,Li})(\text{Ta,Nb})\text{O}_3$ (KNLTN) solid solutions is illustrated in Figure 3.2.

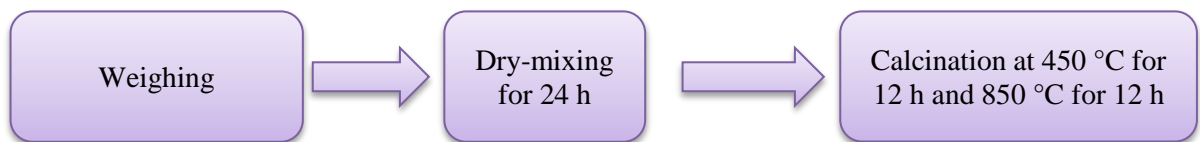
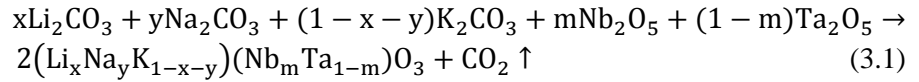


Figure 3.2. Processing route of KNLTN solid solutions.

The following solid state reaction occurs during the calcination process:



The calcined powder was heated and melted above 1200 °C. The platinum spatula was subsequently immersed into the liquid solution, followed by a 24 h-continuous stirring at a rate of 40 rpm at a soaking temperature about 20 °C above the saturation temperature. Then the rotation speed was set to 10–35 rpm and the solution was slowly cooled at a rate of 0.1–0.5 °C/h, in order to grow crystals within the liquid solution. Longitudinal pulling was not performed during the growth. When the crystal growth was stopped, the as-grown crystals hung on the platinum spatula were pulled out from the solution and kept 5 mm above the liquid surface. The whole system was then cooled down to room temperature at the speed of 0.3–0.5 °C/min.

3.1.2 Top-seeded Solution Growth

Crystals grown by the top-seeded solution growth method were supplied by our industrial partner, Forschungsinstitut für mineralische und metallische Werkstoffe -Edelsteine/ Edelmetalle (FEE) GmbH, Germany. Similar furnace and geometrical configurations were used as described in Section 3.1.1. [001]_C-oriented KTaO₃ seed crystals were used as the preferential nucleation sites instead of the platinum spatula. The KTaO₃ shows similar perovskite structure and chemical composition to the KNLTN(S) composition, but has no phase transition in the temperature range of the KNN-based single crystal growth. In addition, the melting point of KTaO₃ ($T_M = 1352$ °C) [194] is higher than the saturation temperatures of KNLTN(S) single crystals, making it a suitable seed. High purity (99.99 %) starting materials were supplied by Aran Isles Chemical Inc. For certain attempts, Sb₂O₃ with high purity (99.99 %) is also contained in the starting materials. Unlike the SSSG method with which crystal growth occurs beneath the surface of the liquid solution, the TSSG technique provides a method to grow crystals at the top of the liquid solution at a pulling rate of 0.1-0.6 mm/h.

3.2 Chemical Characterization

3.2.1 Electron Probe Micro Analysis

The amounts of all elements (except Li) were detected on a carbon coated polished sample using a CAMECA SX-100 electron probe micro analysis (EPMA) instrument (Gennevilliers, France) with a wavelength-dispersive x-ray spectrometry system. The operating conditions were 20 keV and 20 nA.

The measurements were performed by Dr. Michel Lahaye from ICMCB. EPMA reference samples [195] used to determine element concentrations are described in Table 3.1.

Table 3.1. EPMA reference samples in this work.

Elements to be detected	EPMA references
Li	Undetected
Na	NaCl
K	KNbO ₃ single crystal
Nb	KNbO ₃ single crystal
Ta	Ta ₂ O ₅ ceramics (99.99 %)
Sb	Sb or Sb ₂ O ₃ polycrystalline ceramic (99.99 %)

3.2.2 Inductively Coupled Plasma Optical Emission Spectrometry

The microwave digestion method was used in order to dissolve KNN-based single crystals into acid solution. This technique provides a shorter time and sufficient accuracy due to the high operating temperature and pressure during the dissolution process. Approximately 50 mg of powders of the crushed single crystals were dispersed into 20 ml of 40 vol% HF acid solution. The mixed system was transferred into a closed Teflon reactor. This reactor was then placed into a microwave oven (CEX MarsExpress) and heated to 180 °C in 15 min with a gradually increasing autogenous pressure. After being kept at 180 °C and 5 bars for 30 min, the mixture was cooled down to room temperature. Subsequently, the solution was moved into a 100 ml flask and diluted up to 100 ml with distilled water. This procedure was performed by Dr. Nicolas Penin at ICMCB. In order to measure the content of Li, inductively coupled plasma optical emission spectrometry (ICP-OES) measurements were carried out with a VARIAN 720-ES spectrometer by Mrs. Laetitia Etienne at ICMCB.

3.2.3 The Accuracy of Element Concentrations

The experimental errors of element concentrations in EPMA measurements are determined by the concentration and the atomic number of the investigated element. The larger the concentration and the atomic number, the lower the error. The measurement error of element concentrations with the ICP-OES technique depends on element concentrations and the difference of concentrations between the investigated sample and the standard solution. If the element concentration is out of the concentration range of standard solutions, the error will increase. In this work, element concentrations were calculated by averaging EPMA and ICP-OES results. Thus, absolute accuracies for each elements are ± 0.24 mol% for Li, ± 2.5 mol % for Na and K, and ± 0.5 mol % for Nb, Ta, and Sb.

For certain as-grown crystals, the concentrations of Na and K ions show significant difference between the EPMA and ICP-OES results, as compared to the concentration of Nb, Ta and Sb. This reconfirms the low relative concentration accuracy of Na and K. One of the possible origins is the different measurement scopes: EPMA provides local element concentrations of the surface layers (up to a few microns), whereas ICP-OES investigates the whole volume. Indeed, the element concentrations at the sample surface may be slightly different from the bulk after the machining step (cutting, polishing), due to possible preferential removal of light elements such as alkali ions.

3.3 Structural Characterization

3.3.1 X-ray Diffraction

X-rays will be scattered by atoms in arbitrary directions when the incident X-ray beam hits a substance's atoms at an angle θ . As presented in Figure 3.3, when the path difference between the scattered waves is an integral multiple of the wavelength λ of the incident wave, the coherent reflected waves will produce a wave with a maximum intensity [196]. This phenomenon results from the phase matching between incident and diffracted X-ray beams, and reciprocal space vectors of (hkl) crystallographic planes, as described by Bragg's law in the following equation,

$$2d_{hkl}\sin\theta_{hkl} = n\lambda \quad (3.2)$$

where n is an integer and d_{hkl} represents the interplanar distance.

Powder XRD data of crushed single crystals were recorded in order to determine the crystallographic structure and phase purity. The powders were first placed into a holder made of an aluminium alloy. XRD measurements at room temperature were carried out using a PANalytical X'pert Pro MPD diffractometer with Cu K_{α} radiations ($\lambda_{K_{\alpha 1}} = 1.5406 \text{ \AA}$ and $\lambda_{K_{\alpha 2}} = 1.5444 \text{ \AA}$), and Bragg-Brentano geometry. 2θ was in the range between 8° and 80° with a step size of 0.02° .

In-situ XRD measurements in air at high temperature were performed with a PANalytical X'pert Pro diffractometer with Co K_{α} radiation ($\lambda_{K_{\alpha}} = 1.7902 \text{ \AA}$).

All XRD measurements were carried out by Mr. Eric Lebraud at ICMCB.

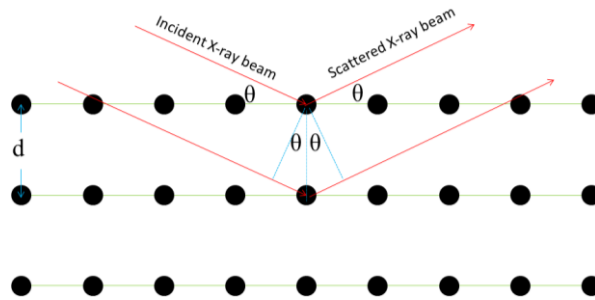


Figure 3.3. Illustration of Bragg's law.

3.3.2 Laue X-ray Diffraction and Crystal Cutting

The orientations of single crystals were determined by the back-scattering Laue method. A CCD-camera, through which a white incident X-ray beam passes, was used to collect the reflected X-ray patterns (see Figure 3.4).

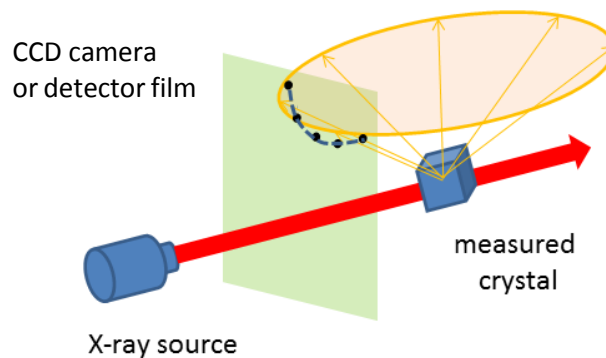


Figure 3.4. Scheme of the principle of the Laue technique in the back reflection mode.

The crystal was mounted on a goniometer and illuminated with the incident white X-ray beam, composed of the Bremsstrahlung and the characteristic X-ray waves of a Mo anticathode. A spherical wave of scattered radiations was formed for each crystal plane, building a series of cone surfaces. When cone surfaces are intersected with the detector (CCD camera or film), hyperbolas with several diffraction spots appear. These hyperbolas are correlated to the symmetry, as well as the orientation of the crystal. The spots on the detector represent the nodes (hkl) of the reciprocal space.

To obtain a sample with the desired plane, the relative position of the crystal was changed by adjusting the goniometer, followed by cutting with a diamond wire saw. The mismatch of the obtained plane with respect to the desired crystallographic orientation is less than 1 °. Most work on the orientation was performed at ICMCB with a Laue setup (Dual lens coupled X-ray Laue system, Photonic Science Ltd., Robertsbridge, UK) and OrientExpress program [197] (Institut Laue-Langevin, Grenoble, France). Part of the work was carried out at TU Darmstadt with a Huber Laue diffraction setup (1001 Model, Huber, Rimsting, Germany) and the Cologne Laue indexation program (Version 4.0 beta2) in Prof. Wolfgang Donner's group.

3.3.3 Raman Spectroscopy

Micro-Raman spectra of investigated single crystals were recorded using a LabRAM HR800 Raman spectrometer at room temperature. The 633 nm radiation from a He-Ne laser with the spot size of 514 nm was selected.

3.4 Electrical Characterization

3.4.1 Dielectric Properties

Temperature-dependent dielectric properties in the temperature range from room temperature to 500 °C were measured at selected frequencies using a HP 4284A LCR meter (Hewlett Packard Corporation, Palo Alto, USA), equipped with a Nabertherm furnace (LE4/11/R6, Nabertherm GmbH, Lilienthal, Germany). A Novocontrol Alpha-A high performance frequency analyzer (Novocontrol technologies, Hundsangen, Germany) equipped with a cryostat was used from -100 °C to 30 °C. The heating or cooling rate was selected to either 2 or 1 °C/min.

The capacitance (C) and dielectric loss of samples were obtained during the measurements. As a sample can be considered as a parallel plate capacitor, its permittivity value can be calculated using the following equation:

$$\varepsilon_{33}^T/\varepsilon_0 = \frac{C \cdot d}{\varepsilon_0 \cdot A} \quad (3.3)$$

where C is the capacitance, d is the thickness of the measured sample, A is its effective surface area and ε_0 is the vacuum permittivity. $\varepsilon_0 = 8.854 \cdot 10^{-12}$ F/m. The error of the permittivity was primarily determined by the error of the thickness and the surface area. Assuming that errors for the thickness and area are 0.01 mm and 0.1 mm², respectively, the error of permittivity is estimated to be about 1 %.

3.4.2 Large-signal Electrical Properties

The large-signal ferroelectric hysteresis loops at room temperature were measured with a Sawyer-Tower setup. In the Sawyer-Tower circuit, the sample capacitor and the reference capacitor are in series, as presented in Figure 3.5. The applied voltage and the voltage drop across the reference capacitor were recorded by the oscilloscope (DS06014A, Agilent Technologies, Deutschland GmbH, Böblingen, Germany). The voltage was supplied by a function generator (Agilent 33220A, Agilent technologies Deutschland GmbH, Böblingen, Germany) and amplified by a high voltage amplifier (20/20C, TREK Inc., Medina, NY, USA).

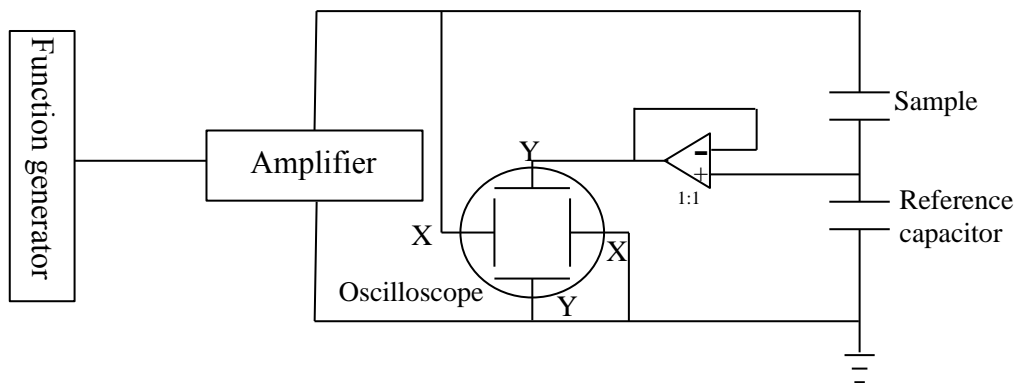


Figure 3.5. Schematic of the Sawyer-Tower circuit.

The typical triangular waveform with a certain frequency and amplitude was selected, as shown in Figure 3.6: (a) bipolar and (b) unipolar electric field loading signals.

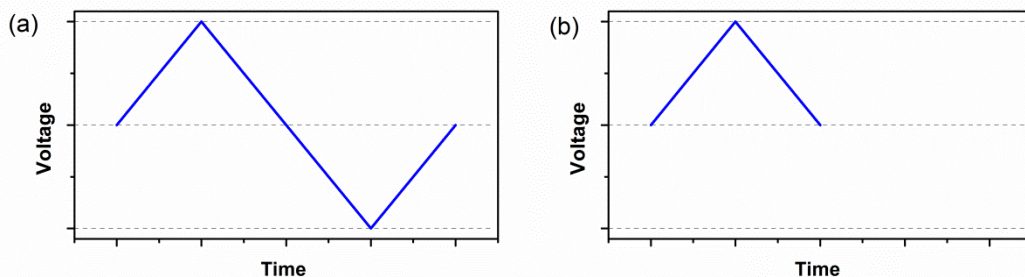


Figure 3.6. Schematics of applied electric field loading signals: (a) bipolar and (b) unipolar.

In the Sawyer-Tower circuit, the capacitance of the reference capacitor (C_R) is set to be much higher than that of the sample (C_S). The voltage drop across the sample is therefore approximated to be the applied voltage. The polarization (P) of the measured sample and the applied electric field (E) can be calculated by the following equations,

$$P = \frac{Q_S}{A} = \frac{Q_R}{A} = \frac{C_R \cdot U_R}{A} = \frac{C_R}{A} \cdot U_Y \quad (3.4)$$

$$E = \frac{U_S}{d} = \frac{1}{d} \cdot U_X \quad (3.5)$$

where Q_S and Q_R represent the collected charges of the sample and the reference capacitor (C_R), U_S and U_R represent the voltage drops across the sample and the reference capacitor, respectively. The U_X and U_Y are the voltages recorded by the oscilloscope in the X and Y channels. The experimental error of polarization results from the errors of the measured voltage and the sample area, which is estimated to be 2 %.

Simultaneously, an optical displacement sensor (Philtex, Inc., Annapolis, MD, USA) was equipped to measure the strain along the axial direction in the setup. The error of strain is relative to the errors of sample thickness and the resolution of the sensor. It is estimated as 3%.

Large-signal ferroelectric hysteresis and electric field-induced strain curves at high temperatures were measured with an AixACCT ferroelectric testing system. The polarization was calculated based on the recorded current using the virtual ground method, as provided by Figure 3.7 [198]. The strain was recorded by the built-in laser interferometer.

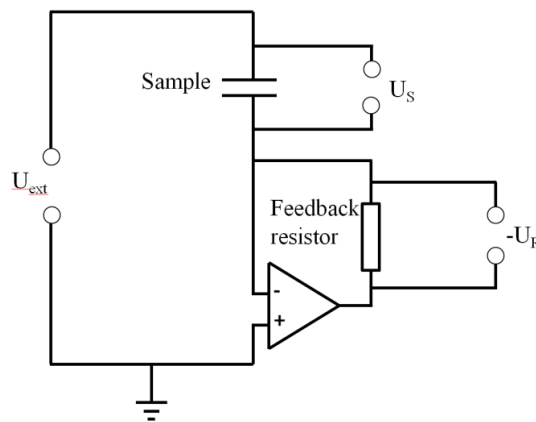


Figure 3.7. Schematic of the virtual ground circuit.

3.4.3 Small-signal Electrical Properties

Small-signal permittivity $\varepsilon_{33}'/\varepsilon_0$, dielectric losses $\tan\delta$ and piezoelectric coefficient d_{33} as a function of electric field were measured. The excitation signal was a large-signal triangular base waveform superposed by a small-signal sinusoidal excitation waveform, as presented in Figure 3.8 [199]. Normally, selected frequencies of the base and small signal waveforms were 0.05 Hz and 1 kHz, respectively. The small-signal waveform had an amplitude of 10 V.

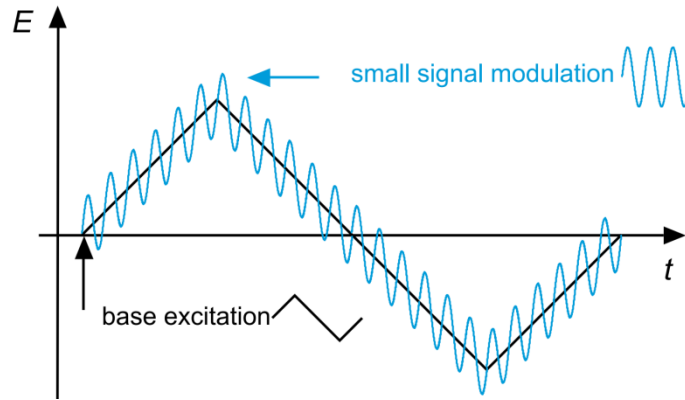


Figure 3.8. Excitation signal during small-signal measurements: a large-signal triangular base waveform superposed by a small-signal sinusoidal excitation waveform [199]. Note that the enlarged small-signal sinusoidal waveform is provided.

3.4.4 Piezoelectric Properties

The large-signal converse piezoelectric coefficients d_{33}^* were calculated from the unipolar maximum strain S_{\max} and the applied maximum electric field E_{\max} , as described by,

$$d_{33}^* = \frac{S_{\max}}{E_{\max}} \quad (3.6)$$

Prior to the measurements of the small-signal direct piezoelectric coefficient d_{33} , the samples were poled in a silicone oil bath. Unless mentioned, the poling electric field was 3 kV/mm. The poling temperature was selected between 50–100 °C. The room temperature d_{33} was measured by a Berlincourt piezoelectric meter after 24 h aging (PM 300, Piezotest Pte. Ltd., Singapore; 110 Hz, 2 N).

Temperature-dependent converse small-signal d_{33} measurements were performed with a Doppler laser vibrometer (Polytec sensor head OFV-505 and front-end VDD-E-600). The measured sample was placed in a furnace with a point contact on the top and a metal base contact on the bottom. An alumina

cap and a steel cover were subsequently placed over both the sample and the upper contact in order to provide a thermally stable environment and a sealed atmosphere. The sample was connected to a Keithley electrometer (6517B), which provided an AC sinusoidal voltage with the amplitude of 10 V and the frequency of 1000 Hz. The displacement of the sample along the electric field direction was measured by the laser vibrometer and recorded by the Polytec vibrometer software 4.5.

3.5 Transmission Electron Microscopy

Transmission electron microscopy (TEM) requires the specimen to be transparent for electrons. The selected single crystals with 1 mm thickness were ground and polished to a thickness of about 20 μm with the diamond pastes of 30 μm , 15 μm , 6 μm , 3 μm , 1 μm , and 0.25 μm . The polishing steps were performed on a precision MultiprepTM polishing system (Allied High Tech Products Inc., United States). The specimen with the thickness of 20 μm was then mounted on a copper ring by Epoxy Bond 110 (Allied High Tech Products Inc., United States). This step was followed by an Ar⁺ ion beam milling step (Model 600, Gatan GmbH, München, Germany) with 4 kV and then 2.5 kV, in order to obtain a specimen with a thickness of about 80 nm. The *in-situ* TEM measurements were performed on a 2100F TEM setup (JEOL Ltd., Japan) with a double-tilt heating holder (model 652, Gatan Inc., United States). The heating stage was equipped with a SmartSet Hot-Stage Controller (Model 901, Gatan Inc., United States), which can be operated between 25 °C and 500 °C. TEM measurements were performed by Alexander Zintler in the group of Prof. Hans-Joachim Kleebe at TU Darmstadt.

3.6 Other Techniques

3.6.1 Mössbauer Spectroscopy

A conventional MS-1104 spectrometer, with a Ca^{121m}SnO₃ source and a constant acceleration mode was used to record ¹²¹Sb Mössbauer spectra. The resonant absorption measurements were carried out by a 8.5 keV escape peak, created by the Mössbauer gamma ray ($E_\gamma = 37.15$ keV) in a thin NaI(Tl) scintillator. The absorbers were powders from the crushed single crystals. A copper bar with the Ca^{121m}SnO₃ source and the investigated powder sample was dipped into liquid nitrogen, in order to perform the measurements at a low temperature. The approximated amounts of chemically-different antimony species can be calculated according to the relative area between corresponding spectral peaks at -173 °C [200]. The number, position, shape, and relative intensity of absorption lines of Mössbauer spectra are features of hyperfine interactions. These features can be described by the isomer shift (δ), the quadrupole coupling constant ($eV_{zz}Q_{5/2}$), the full width at half maximum of each individual peak (Γ), and the relative

area (A). All these parameters are strongly dependent on the local electronic environment of the investigated atom, such as coordination number and oxidation state. The reported isomer shift values are referred to the Ca^{121m}SnO₃ source.

All Mössbauer spectra were fitted by a superposition of Lorentzian lines. The hyperfine interaction parameters were calculated from the Hamiltonian by characterizing ¹²¹Sb M1 transition from the ground state with spin $I_g = 5/2$ to the excited state $I_e = 7/2$. All measurements and simulations of Mössbauer spectra were performed by Pavel B. Fabritchnyi and Mikhail I. Afanasov (Department of Chemistry, M.V. Lomonosov Moscow State University, Russian Federation).

3.6.2 Electron Paramagnetic Resonance

Electron paramagnetic resonance (EPR) spectra were measured to investigate the possible valence states of Mn in Mn-doped (K,Na,Li)(Ta,Nb)O₃ single crystals. EPR spectra were recorded with a Bruker EMX spectrometer at an X-band frequency of 9.45 GHz and an Oxford Instruments ESR 900 liquid helium cryostat in the temperature range from -269 °C to room temperature. During the recording, the magnetic field modulation frequency was set to be 100 kHz and the amplitude was in the range between 0.2 mT to 0.8 mT. The microwave power was 20 mW and the resolution of the spectra was 0.1-0.7 mT/pt. The calibration standard of the spectrometer was 2,2-diphenyl-1-picrylhydrazyl (DPPH). All EPR spectra were simulated with the WINEPR and SIMFONIA software for the estimation of g values and hyperfine interaction parameters. The EPR measurements and simulations were performed by Dr. Matthieu Duttine at ICMCB.

4 Crystal Growth, Structural Properties, and Domains

4.1 Crystal Growth

Eleven growth attempts of KNN-based crystals with different compositions, numbered from N1 to N11, have been carried out, in order to obtain desired compositions with high quality and high piezoelectric and ferroelectric properties. As solid solutions, $(\text{K,Na,Li})(\text{Ta,Nb})\text{O}_3$ (KNLTN) and $(\text{K,Na,Li})(\text{Ta,Nb,Sb})\text{O}_3$ (KNLTNS) crystals were grown by the self-flux method [34] using either a seed or, in most cases because no seed was available, a platinum spatula acting as a preferential nucleation site. Suitable growth conditions and concentrations of starting materials in the solution have been set in order to reduce the influence of the segregation phenomena occurring during the growth process.

4.1.1 Initial Compositions and Crystal Growth Results

Concentrations of starting materials for each growth attempt are listed in Table 4.1. Note that N1, N2-Mn, N3, N4-Mn, N5, and N6 attempts were carried out by the submerged-seed solution growth (SSSG) method at ICMCB, as described in Section 3.1.1, whereas N7, N8, N9, N10 and N11-Sb attempts were performed using the top-seeded solution growth (TSSG) method at FEE. Among them, crystals of the N2-Mn and N4-Mn attempts were doped with a small amount of Mn and crystal of the N11-Sb attempt was substituted with a few molar percent of Sb.

Table 4.1. Concentrations of starting materials for each growth attempt.

Attempt Number	Amount on A site (mol %)			Amount on B site (mol %)				Method, Growth Place
	Li	Na	K	Nb	Ta	Sb	Mn	
N1	15.00	10.74	74.26	99.21	0.79	/	/	SSSG; ICMCB, France
N2-Mn	15.00	10.74	74.26	99.21	0.79	/	1.00	
N3	11.38	21.54	67.08	97.10	2.90	/	/	
N4-Mn	11.38	21.54	67.08	97.10	2.90	/	1.00	
N5	15.39	12.37	72.24	94.75	5.25	/	/	
N6	15.39	10.11	74.50	95.12	5.88	/	/	
N7	/	5.00	95.00	100.00	/	/	/	TSSG; FEE, Germany
N8	11.38	21.54	67.08	97.10	2.90	/	/	
N9	15.30	16.05	68.65	95.00	5.00	/	/	
N10	15.30	16.05	68.65	80.00	20.00	/	/	
N11-Sb	11.30	21.40	67.30	91.90	1.50	6.60	/	

As shown in Figure 4.1 and Figure 4.2, polycrystalline boules composed of several centimeter-sized single crystals are produced by the SSSG technique, when the polycrystalline Pt spatula is used as the nucleation site. If a single crystalline seed is used, a single crystalline boule is grown using the TSSG method (Figure 4.3).

As-grown KNLTN polycrystalline boules with large-scale single crystals for (a) N1, (b) N3, and (c) N5 attempts are shown in Figure 4.1. Figure 4.2 provides photographs of as-grown Mn-doped KNLTN boules for (a) N2-Mn and (b) N4-Mn attempts. Crystals without Mn doping are white milky, whereas those with Mn doping are yellow. Black regions were observed in Mn-doped KNLTN boules at boundaries between crystals or at their peripheries, which is attributed to the segregation of Mn in the flux. The low segregation coefficient of Mn makes this element difficult to enter in the perovskite matrix.

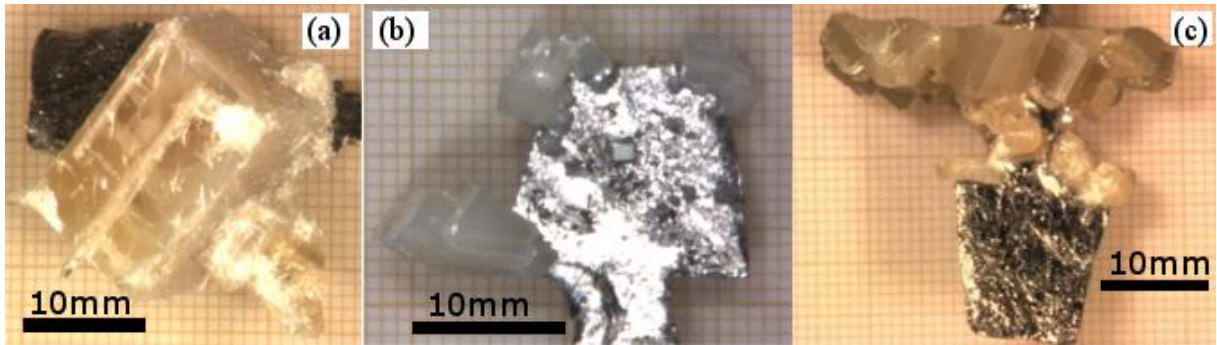


Figure 4.1. Photographs of KNLTN boules grown on a platinum spatula: (a) N1, (b) N3, and (c) N5.

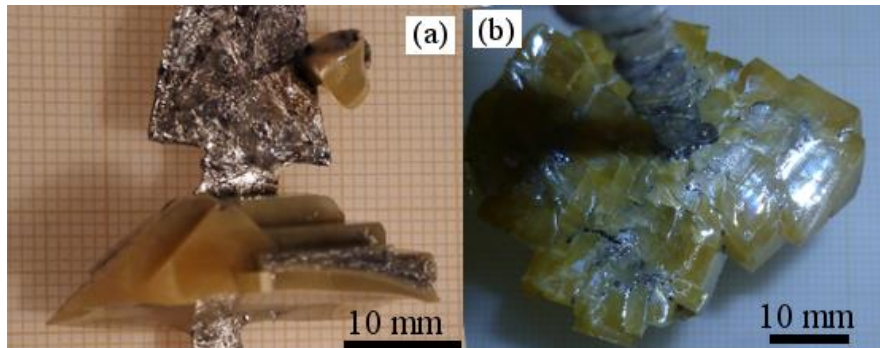


Figure 4.2. Photographs of Mn-doped KNLTN boules grown on a platinum spatula: (a) N2-Mn and (b) N4-Mn.

Based on Figure 4.1 and Figure 4.2, shape prediction of crystals grown by the SSSG method on a platinum spatula is a great challenge if active nucleation sites are located at a polycrystalline Pt spatula [201]. Due to the random spontaneous nucleation, randomly-oriented small-sized crystals are observed on the surface of the platinum spatula. The further a crystal is from the Pt spatula during the growth, the larger its size (Figure 4.2 (b)). This phenomenon results from the growth of small nuclei occurring on the spatula surfaces in the early stage of the growth. It has been determined that the biggest observed crystallographic planes of as-grown crystals are the $\{001\}_{PC}$ faces, indicating their slowest growth rate and crystal habits of KNN-based perovskite crystals [34,36].

The N8 crystal (KNLTN) grown by the TSSG method at FEE is shown in Figure 4.3. The shape is very different from crystals grown by the SSSG technique due to the oriented single crystalline seed. The N8 crystal looks milky, which is similar to the color of crystals in Figure 4.1. The milky color is related to crystal defects and inclusions created during crystal growth, as well as phase transitions during cooling.

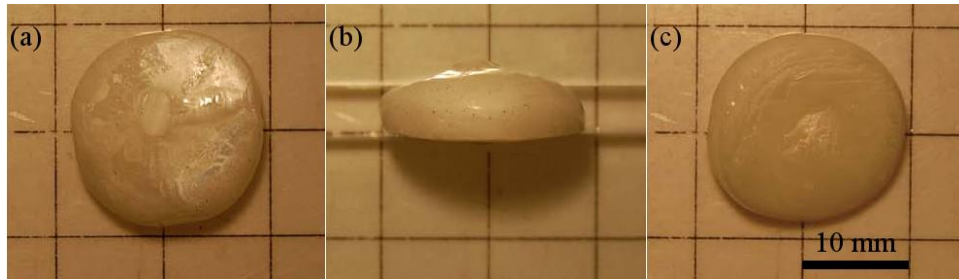


Figure 4.3. Photographs of the as-grown KNLTN (N8) crystal by the TSSG method: view from (a) the top, (b) the side, and (c) the bottom.

4.1.2 Crystal Compositions

EMPA and ICP-OES techniques were combined in order to determine average compositions of as-grown crystals, as described in Section 3.2. Table 4.2 and Table 4.3 summarize crystal compositions of all attempts, except the N6 attempt during which only the tetragonal tungsten bronze (TTB) structure was observed in the as-grown single crystal.

Table 4.2. Element concentrations of as-grown crystals grown at ICMCB.

The molar amount ratio between A-site ions and B-site ions is 1, except for N6.

Attempt Number	Chemical analysis	Amount on A site (mol %)			Amount on B site (mol %)		
		Li	Na ^a	K ^b	Nb	Ta	Mn
N1	EPMA	/	39.46	60.54	97.32	2.68	/
	ICP-OES	2.89	33.43	63.69	97.84	2.16	/
	Composition	2.89	35.87	61.24	97.58	2.42	/
N2-Mn	EPMA	/	39.31	60.69	97.67	2.33	0.03
	ICP-OES	2.90	28.54	68.56	97.75	2.25	/
	Composition	2.90	33.35	63.75	97.68	2.29	0.03
N3	EPMA	/	61.38	38.62	92.32	7.68	/
	ICP-OES	2.84	59.47	37.69	92.05	7.95	/
	Composition	2.84	59.55	37.61	92.18	7.82	/
N4-Mn	EPMA	/	68.53	31.47	89.86	10.14	0.14
	ICP-OES	2.56	62.18	35.26	89.91	10.09	/
	Composition	2.56	64.48	32.96	89.75	10.11	0.14
N5	EPMA	/	55.77	44.23	81.86	18.14	/
	ICP-OES	3.83	41.76	54.41	83.67	16.33	/
	Composition	3.83	47.70	48.47	82.77	17.23	/
N6	EPMA	Li _x (K _{72.32} Na _{27.68}) ₃ (Nb _{82.91} Ta _{17.09}) ₅ O ₁₅					
	Composition	Li₂(K_{72.32}Na_{27.68})₃(Nb_{82.91}Ta_{17.09})₅O₁₅^c					

Note: ^{a, b} Na and K concentrations measured by the EPMA and ICP-OES technique have a high error. Their relatively high concentrations in the crystals increase the error induced by the reference solution in the ICP-OES measurements. The segregation phenomena, which will be discussed later, result in the chemical inhomogeneous distribution in as-grown crystal boules.

^c Subscript of Li in the chemical formula of the N6 crystal is assumed to be 2, based on the stoichiometry of the TTB structure [202].

Table 4.3. Element concentrations of as-grown crystals grown at FEE.

The molar amount ratio between A-site ions and B-site ions is 1.

Attempt Number	Chemical analysis	Amount on A site (mol %)			Amount on B site (mol %)			
		Li	Na	K	Nb	Ta	Sb	Mn
N7	EPMA	/	11.00	89.00	100.00	/	/	/
	ICP-OES	/	12.80	87.20	100.00	/	/	/
	Composition	/	11.90	88.10	100.00	/	/	/
N8	EPMA	/	73.79	26.21	85.65	14.35	/	/
	ICP-OES	2.01	70.67	27.33	87.31	12.69	/	/
	Composition	2.01	71.49	26.51	86.48	13.52		/
N9	EPMA	/	63.87	36.13	80.82	19.18	/	/
	ICP-OES	2.02	55.91	42.07	82.06	17.94	/	/
	Composition	2.02	59.24	38.74	81.44	18.56		/
N10	EPMA	/	64.90	35.10	65.56	34.44	/	/
	ICP-OES	1.65	58.62	39.73	66.89	33.11	/	/
	Composition	1.65	61.22	37.13	66.23	33.77		/
N11-Sb	EPMA	/	72.79	27.21	87.82	6.14	6.03	/
	ICP-OES	2.18	67.05	30.77	86.28	6.38	7.34	/
	Composition	2.18	69.13	28.70	87.05	6.26	6.68	/

4.1.3 Element Segregation

It should be noted that chemical compositions of as-grown crystals (Table 4.2 and Table 4.3) were very different from their corresponding initial liquid compositions (Table 4.1). This is explained by the different solubility of each individual element in the liquid phase and the solid phase under thermodynamic equilibrium state. This phenomenon is defined as effective segregation [203,204] and depends on initial solution concentrations, as well as thermokinetic parameters, such as the solute diffusion and the crystallization velocity in the solid-liquid front (*i.e.*, growth rate).

The difference of investigated element concentrations in the crystal and in the initial liquid solution can be described by the classical effective segregation coefficient k_{eff} [36]:

$$k_{\text{eff}} = \frac{1}{1 + \left(\frac{1}{k_0} - 1\right) \exp\left(\frac{-v\delta}{D}\right)} \times \frac{1}{k_{\text{volatilization}}} \quad (4.1)$$

where k_0 is the thermodynamic segregation coefficient, $k_{\text{volatilization}} \geq 1$ is defined as the volatilization contribution factor to the effective segregation coefficient, v is the growth rate, δ is the thickness of the solid-liquid boundary layer, and D is the diffusion coefficient of the element in the liquid solution.

As described in Section 2.2.4, the growth rate for the flux growth method is very slow and can therefore be assumed to be zero. Element volatilization during the high temperature growth process has a large influence on the effective segregation phenomenon with respect to the growth time. Therefore, effective segregation coefficient is defined as:

$$k_{\text{eff}} \approx \frac{k_0}{k_{\text{volatilization}}} \quad (4.2)$$

There is no composition gradient in each phase at the equilibrium state. Considering the slow growth rate in this work, it can be assumed that the equilibrium was reached during the growth process and therefore both solid and liquid phases can be assumed to be uniform at a given time. Hence, the effective segregation coefficient k_{eff} can be expressed as Scheil's equation [205]:

$$k_{\text{eff}} = \frac{C_S}{C_{L(\infty)}} \quad (4.3)$$

where C_S is the element concentration in the solid phase, *i.e.*, in the single crystal, and $C_{L(\infty)}$ element concentration in the initial liquid solution at the beginning of the growth.

All effective segregation coefficients of individual elements for each attempt are listed in Table 4.4. It is obvious that the effective segregation coefficient of each element relies on the relative content of the element on the site it occupies.

Table 4.4. Effective segregation coefficients of individual elements for each growth attempt.

	A site			B site		
	Li	Na	K	Nb	Ta	Sb
N1	0.19	3.34	0.82	0.98	3.07	/
N2-Mn	0.19	3.11	0.86	0.98	2.90	/
N3	0.25	2.76	0.56	0.95	2.69	/
N4-Mn	0.22	2.99	0.49	0.93	3.49	/
N5	0.25	3.86	0.67	0.87	3.28	/
N7	/	2.38	0.93	1.00	/	/
N8	0.18	3.32	0.40	0.89	4.66	/
N9	0.13	3.69	0.56	0.86	3.71	/
N10	0.11	3.81	0.54	0.83	1.69	/
N11	0.19	3.23	0.43	0.95	4.18	1.01

Segregation coefficients k_{eff} as a function of the concentration in the initial liquid solutions $C_{L(\infty)}$ are plotted in Figure 4.4 (a). Three regions can be identified: the yellow and the light blue regions with k_{eff} values smaller than 1, and the grey region with k_{eff} values larger than 1. Both K and Nb ions are located in the yellow region (k_{eff} is lower than 1) when the concentration in the initial liquid is high enough. In the light blue region, where lower k_{eff} are obtained at a relatively lower concentration in the initial liquid, only Li ions are observed. Both Na and Ta ions appear in the grey region due to their high segregation coefficient k_{eff} with a low concentration in the initial liquid.

In the cases of binary solutions with unlimited solubility, such as $\text{KNbO}_3\text{-NNbO}_3$ or $\text{KTaO}_3\text{-KNbO}_3$ pseudo-binary systems, the magnitude of k_{eff} depends on the molar fraction ratio of elements between the solid and liquid phases, as well as the sign of the slopes of the liquidus and solidus curves. The influence can be described as follows: if k_{eff} of an element is higher than 1, it is preferentially absorbed by the crystal due to the higher melting point (T_M) of the corresponding component compared to the similar component but without the element. For example, T_M of KTaO_3 (1352 °C) [194] is higher than that of KNbO_3 (1050 °C) [194], which leads to $k_{\text{eff}}(\text{Ta}) > 1$. Same phenomena with other Ta- and Nb-based components are observed, such as $T_M(\text{NaTaO}_3, 1810 \text{ °C}) [206] > T_M(\text{NaNbO}_3, 1420 \text{ °C}) [193]$ and $T_M(\text{LiTaO}_3, 1650 \text{ °C}) > T_M(\text{LiNbO}_3, 1257 \text{ °C}) [207]$. Moreover, we found the same tendency for Na with a $k_{\text{eff}}(\text{Na}) > 1$, since $T_M(\text{NaNbO}_3) > T_M(\text{KNbO}_3)$ and $T_M(\text{NaTaO}_3) > T_M(\text{KTaO}_3)$. This comparison confirms that segregation coefficients of Na and Ta are higher than 1. On the other hand, the elements with k_{eff} lower than 1 are rejected by the crystals (K and Nb), as evident by the lower melting points in their corresponding compounds. For example, for the K element, $T_M(\text{KNbO}_3, 1050 \text{ °C}) < T_M(\text{NaNbO}_3, 1420 \text{ °C})$; and for the Nb element, $T_M(\text{NaNbO}_3, 1420 \text{ °C}) < T_M(\text{NaTaO}_3, 1810 \text{ °C})$.

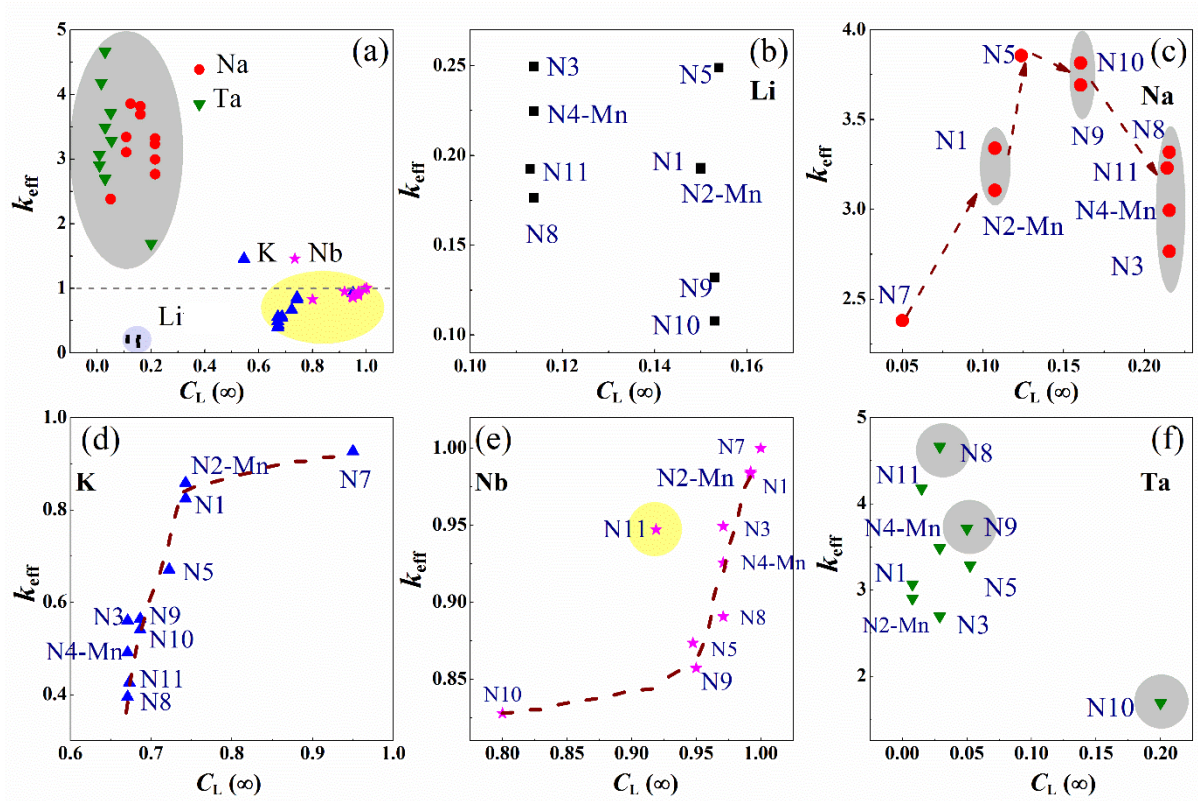


Figure 4.4. k_{eff} of individual element as a function of element concentration in the liquid solution $C_L(\infty)$: (a) all the elements, (b) Li, (c) Na, (d) K, (e) Nb, and (f) Ta.

The segregation coefficients of Li, $k_{\text{eff}}(\text{Li})$, for each attempt are plotted in Figure 4.4 (b). Average $k_{\text{eff}}(\text{Li})$ of all KNN-based crystals is found to be approximately 0.19 and is very low compared to other elements. The $k_{\text{eff}}(\text{Li})$ calculated from Hofmeister *et al.* [208] in $(\text{K}_{1-y}\text{Li}_y)(\text{Ta}_{0.35}\text{Nb}_{0.65})\text{O}_3:\text{Cu}$ crystals is about 0.125, which is consistent with this work. Sadel *et al.* [209] grew a $(\text{Na}_{0.98}\text{Li}_{0.02})\text{NbO}_3$ crystal with the NaBO_2 flux at 1147 °C, and a comparatively high $k_{\text{eff}}(\text{Li})$ of 0.25 was calculated. To some extent, this implies that the volatilization of Li-containing components plays an important role in its effective segregation coefficient during the growth of perovskite crystals. From the experience of this work, the saturation temperature for KNN-based crystal growth process is in the range from 1100 °C to 1200 °C, and $k_{\text{eff}}(\text{Li})$ is influenced by its volatilization from the liquid solution at high temperature. Indeed, the contribution of volatilization of Li-based components in Sadel's *et al.* [209] work can be ignored due to the relatively low growth temperature. The $k_{\text{eff}}(\text{Li})$ is thus considered as the pure thermodynamic segregation coefficient k_0 of Li during the growth of the $(\text{Na}_{0.98}\text{Li}_{0.02})\text{NbO}_3$ crystal. The same pure thermodynamic segregation coefficient value is assumed in the present work. According to the similar Li concentrations in initial solutions in Sadel's and present work, $k_{\text{volatilization}}$ factor has been estimated to

be in the range from 1.39 to 2.27. This reflects the fact that the volatilization phenomenon decreases the Li segregation in the crystal by a factor between 1.39 and 2.27, in addition to the thermodynamic segregation. Note that it is difficult to understand the trend of $k_{\text{eff}}(\text{Li})$, due to the limited sample quantity and the measurement error.

Segregation coefficients of Na, $k_{\text{eff}}(\text{Na})$, for all investigated attempts are enlarged in Figure 4.4 (c). According to the evolution trends of liquidus and solidus curves in $\text{NaNbO}_3\text{-KNbO}_3$ pseudo-binary system [193], the segregation coefficient of Na should increase monotonically with increasing Na content in the initial liquid solution. As presented by arrows in Figure 4.4 (c), $k_{\text{eff}}(\text{Na})$ increases first and then decreases with the Na content in the initial liquid. This seems to disagree with the expected trend observed in the previously reported binary system where only two ions were introduced into A site [193,194]. It suggests a stronger competition between the three alkali elements in the present work, regarding their incorporation into the A sites. Moreover, it appears that the presence of Li increases $k_{\text{eff}}(\text{Na})$ in KNLTN crystals compared to systems without Li.

Figure 4.4 (d) and (e) provide segregation coefficients of K and Nb, respectively, for all investigated attempts. Increasing the K and Nb contents in the initial liquid solutions result in the increase of their k_{eff} , although the trends are not exactly the same. This is directly related to the sign of the slope of liquidus and solidus curves, as described by analogy in $\text{NaNbO}_3\text{-KNbO}_3$ and $\text{KNbO}_3\text{-KTaO}_3$ phase diagrams where two ions on A or B site were considered [193,194]. Note that the point in the yellow region of Figure 4.4 (e) does not follow the trend due to the Sb substitution in the crystal.

The segregation coefficient trend of Ta, $k_{\text{eff}}(\text{Ta})$, is plotted in Figure 4.4 (f). According to the binary $\text{KNbO}_3\text{-KTaO}_3$ phase diagram [194], $k_{\text{eff}}(\text{Ta})$ decreases with increasing the Ta content in the liquid solution, as plotted in Figure 4.5. The $k_{\text{eff}}(\text{Ta})$ of the N8, N9, and N10 attempts, which show similar A-site ion ratio, are plotted in Figure 4.5. The $k_{\text{eff}}(\text{Ta})$ trend as a function of its concentration in the liquid solution follows the expectation: increasing Ta content in liquid solution induces a decrease of $k_{\text{eff}}(\text{Ta})$. In addition, it can be inferred that a $k_{\text{eff}}(\text{Ta})$ larger than 1 leads to a strong depletion of Ta in the liquid solution and subsequently to a step by step decrease of its incorporation into the crystal as the growth proceeds. The $k_{\text{eff}}(\text{Ta})$ might be influenced by the species on A sites, as evident by its deviation from the calculated curves for samples with different A-site ion contents. However, further investigations are required to better understand this phenomena.

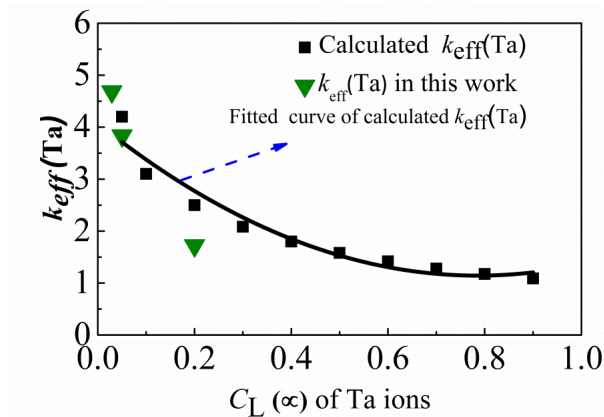


Figure 4.5. Effective segregation coefficients $k_{\text{eff}}(\text{Ta})$ as a function of Ta molar concentration in the initial liquid solutions compared to those deduced from the pseudo-binary $\text{KNbO}_3\text{-KTaO}_3$ phase diagram given by Reisman *et al.* [194].

As described above, changes in element concentrations are detected along the growth directions of all crystals, as shown in Figure 4.6. The compositional inhomogeneity might affect electrical properties. However, due to the small sample sizes (typically 5-8 mm), the concentration of elements has been considered as chemically homogeneous for further electrical characterization. The deviation of the chemical composition for an 8 mm sample is expected to be maximum ± 0.1 mol % for B site ions and ± 0.2 mol % for A site ions.

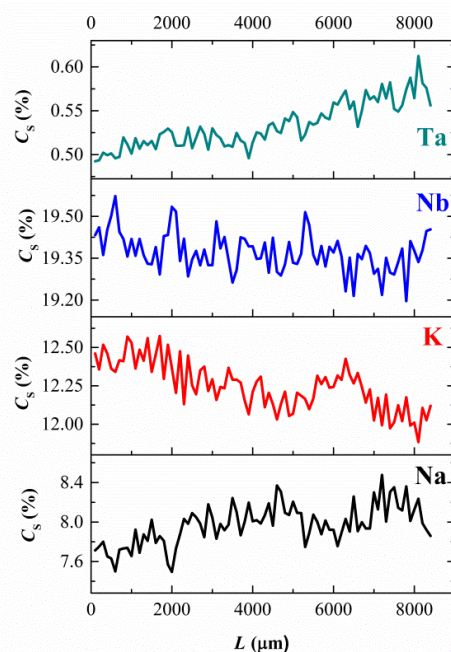


Figure 4.6. Changes of element concentrations along the measurement length in $(\text{K}_{0.612}\text{Na}_{0.359}\text{Li}_{0.029})(\text{Ta}_{0.024}\text{Nb}_{0.976})\text{O}_3$ (N1) crystal with the EPMA technique.

4.2 Secondary Phase

As described in Section 2.3.1, the addition of Li to KNN-based systems can increase the T_C and decrease the T_{O-T} , giving rise to improved electrical response. However, from previous reports on KNN-based polycrystalline ceramics [94,96], a high Li content can lead to the formation of a secondary tetragonal tungsten bronze phase (TTB). The secondary TTB phase is ascribed to the limited solubility of Li in the KNN lattice, which is described in the following section.

4.2.1 Phase Structure

XRD patterns of as-grown N1 and N6 crystals are shown in Figure 4.7. In the case of the N1 growth attempt, the secondary phase were found at the periphery of the perovskite crystal boules (see Figure 4.1 (a), Page 52). This is an indication that the growth of the secondary crystal follows the growth of the perovskite crystals. There is a risk of obtaining non-perovskite phase crystals, as evident by the N6 XRD pattern in Figure 4.7 (a). These undesired crystals obtained in the N6 attempt (Figure 4.7 (b)) can be assigned to two different TTB structures: $\text{Li}_2\text{K}_3\text{Ta}_5\text{O}_{15}$ (ICDD No. 00-040-0349) and $\text{Li}_2\text{K}_3\text{Nb}_5\text{O}_{15}$ (ICDD No. 00-034-0122). Due to the complex chemical compositions of the A (Li, Na, and K) and B (Nb and Ta) sites, it is assumed that the undesired phase is the $\text{Li}_2(\text{K,Na})_3(\text{Ta,Nb})_5\text{O}_{15}$ solid solution [210,211]. It is worth mentioning that undesired crystals with the TTB structure were also observed during the growth process of the N2-Mn and N5 attempts. Figure 4.8 provides photographs of the remainders in the crucible, which is solidified during after the pulling out of the as-grown perovskite crystals. The long and slender bars in the crucibles of N1, N5, N6, and N2-Mn attempts exhibit the TTB structure. The TTB crystals are dark if Mn is added in the attempts (Figure 4.8 (d)), but are transparent and/or white for the attempts without Mn (Figure 4.8 (a), (b), and (c)). Note that the TTB phase was not found in the N4-Mn attempt, as shown in Figure 4.8 (e).

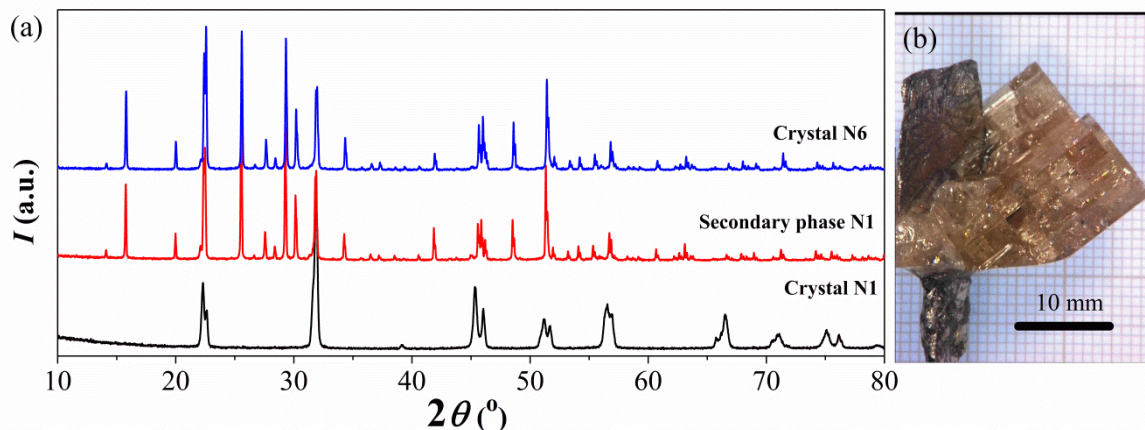


Figure 4.7. (a) XRD patterns of as-grown N1 and N6 crystals, and (b) photograph of the as-grown N6 crystal.

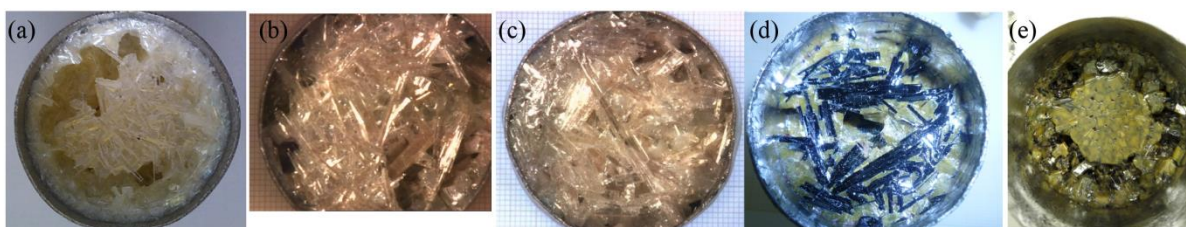


Figure 4.8. Photographs of remainders solidified in crucibles after the extraction of the perovskite crystal: (a) N1, (b) N5, (c) N6, (d) N2-Mn and (e) N4-Mn attempts.

4.2.2 Influence of Alkali Ion Concentration and K/Li ratio

The Appearance of the TTB Structure

According to $\text{Li}_2\text{O}-\text{K}_2\text{O}-\text{Nb}_2\text{O}_5$ phase diagrams shown in Figure 4.9 [212,213,214], the appearance of either the perovskite or the TTB structure depends on the molar ratio of each alkali cation in the initial liquid solution. Considering the general formula of the TTB structure $\text{A}_2\text{BC}_2\text{M}_5\text{O}_{15}$, it is assumed that Na and K ions are located at the A and B sites, Li ions at the C site, and Nb and Ta ions at the M site [202]. It is found that increasing Li content in liquid solution induces the appearance of the TTB phase, as shown by the monovariant line and sub-solidus regions of ternary phase diagrams of Scott *et al.* [214] and Ikeda *et al.* [212] (Figure 4.9). The initial liquid compositions of N1 and N2-Mn attempts are located in the regions with two mixed phases, as provided by the red points in Figure 4.9 (a) and (b). Compared to the N1 attempt, the N6 attempt has 0.39 mol % more Li and 0.24 mol % more K in the initial liquid solution (Table 4.1, Page 51). However, as-grown crystals for the two attempts have different structure. For the N1 attempt, a perovskite crystal and a TTB secondary phase are observed, while for the N6

attempt, only the TTB crystals were obtained. In contrast, in the attempt N5, which has only 2.02 mol % less K in the initial liquid solution compared to the N6 attempt, a perovskite crystal was obtained.

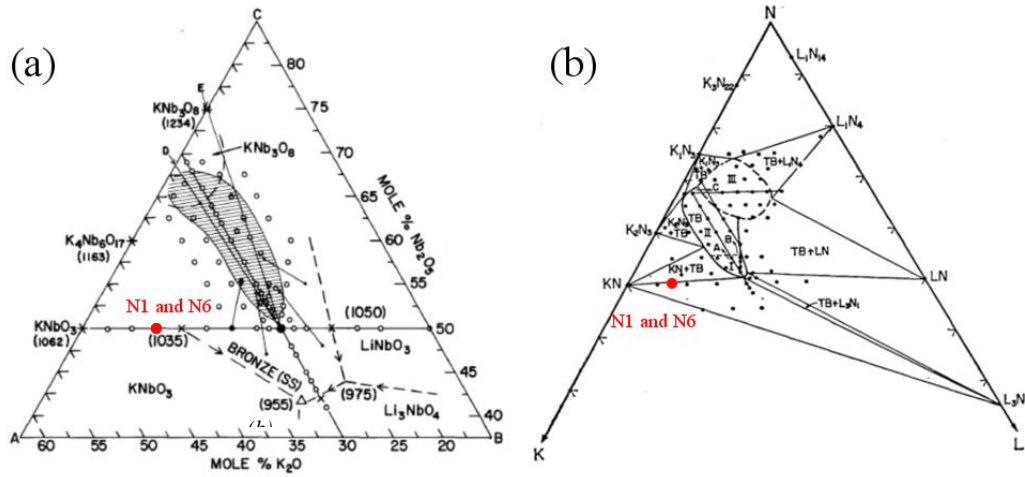


Figure 4.9. K_2O - Li_2O - Nb_2O_5 phase diagrams from (a) Scott *et al.* [214] and (b) Ikeda *et al.* [212]. Note that in (b) L, K, and N represent Li_2O , K_2O and Nb_2O_5 . Red points mark the liquid composition of N1 and N6 attempts. Reprinted from Ref. [212,214], with permission of the Japan Society of Applied Physics and Elsevier.

In order to enhance the room temperature electrical response of the KNN-based system, the Li content should be about 0.03-0.06 % on A sites [4,215]. However, as described in Figure 4.4 (b) (Page 58), the very low segregation coefficient of Li in KNN-based perovskite matrix [208] requires a relatively high concentration in the liquid solution. Therefore, during the growth of Li-modified KNN-based crystals, there is a high risk to produce a TTB secondary phase after the Li concentration reaches a critical value.

Besides, the K/Li ratio in the initial liquid composition has also an influence on the appearance of the TTB phase. It was found that the TTB phase appeared when the K/Li ratio in the initial liquid solution was lower than 5, as observed in N1, N2-Mn, N5, and N6 attempts. In contrast, when the K/Li ratio was about 5.9 (N3 and N4-Mn attempts), the TTB phase did not appear during the growth process.

Note that it is difficult to explain the influence of Mn doping on the TTB structure and segregation coefficients due to the small amount of samples and the higher inaccuracy in chemical analysis of the low Mn content. For example, in N2-Mn and N4-Mn attempts, a reverse tendency of segregation coefficients of Na ions is observed compared to Mn-free N1 and N3 attempts, even though the initial liquid contents for other elements are exactly the same in each group (see Table 4.1, Page 51).

Limitations of the Growth Method

One of the aims of the present work was to obtain a crystal with the LF4 composition $(\text{K}_{0.44}\text{Na}_{0.52}\text{Li}_{0.04})(\text{Ta}_{0.10}\text{Nb}_{0.86}\text{Sb}_{0.04})\text{O}_3$ reported by Saito *et al.* [4], which exhibits excellent piezoelectric behaviour. In addition, the LF3 composition $(\text{K}_{0.485}\text{Na}_{0.485}\text{Li}_{0.03})(\text{Ta}_{0.20}\text{Nb}_{0.80})\text{O}_3$ was also targeted because of the similar alkali ion concentrations on A-site and the absence of the hazardous Sb. Based on the relationship between the compositions of the as-grown crystals and their structures with respect to the initial liquid solution composition, we argue that it may be impossible to grow a perovskite single crystal with LF3 or LF4 compositions [4,215] by using the self-flux method due to the competition among A-site ions and the appearance of the TTB structure.

A possible approach to achieve single crystals with LF3 or LF4 compositions by the self-flux method would be to control and suppress the volatilization of Li and thus enhance its segregation coefficient $k_{\text{eff}}(\text{Li})$. This would require a controlled atmosphere in order to saturate the vapour pressure of lithium-based components during the growth. If one wants to obtain the LF3 or LF4 crystal without producing a TTB structure, it is suggested to decrease the initial K content in a small proportion, as compared to the N5 or N6 attempts. Another method is to decrease the saturation temperature by adding a suitable flux, which requires further experimental work.

4.3 Temperature Dependence of Structural and Domain Configurations

4.3.1 Phase Evolution with Temperature

Full range XRD patterns of powders of crushed $(\text{K}_{0.612}\text{Na}_{0.359}\text{Li}_{0.029})(\text{Ta}_{0.024}\text{Nb}_{0.976})\text{O}_3$ (N1) single crystals as a function of temperature are presented in Figure 4.10 (a). All peaks correspond to the perovskite phase and no secondary structure is detected for all patterns. Two phase transitions are detected at 105 °C and 420 °C. According to the relative intensities and the positions of the peaks at around $2\theta = 25.5^\circ - 26.5^\circ$ in Figure 4.10 (b), the $(\text{K}_{0.612}\text{Na}_{0.359}\text{Li}_{0.029})(\text{Ta}_{0.024}\text{Nb}_{0.976})\text{O}_3$ single crystal is indexed with an orthorhombic cell at room temperature. It evolves into the tetragonal phase above 105 °C. Further increasing up to 450 °C, a pure paraelectric cubic phase is observed. Note that the peak indexed as $(001)_\text{O}$ (Figure 4.10 (b)) keeps shifting to a lower angle by increasing the temperature. This $(001)_\text{O}$ peak evolves into $(001)_\text{T}$ above 105 °C and then to $(001)_\text{C}$ at $T=450^\circ\text{C}$. A different behaviour has been found for the peak indexed as $(110)_\text{O}$ at room temperature. Its position does not change below 105 °C and it disappears at higher temperature. On the other hand, a new peak referring to $(100)_\text{T}$ appears and shifts to higher angles with increasing temperature. Upon heating to 450 °C, this peak is merged into $(001)_\text{C}$.

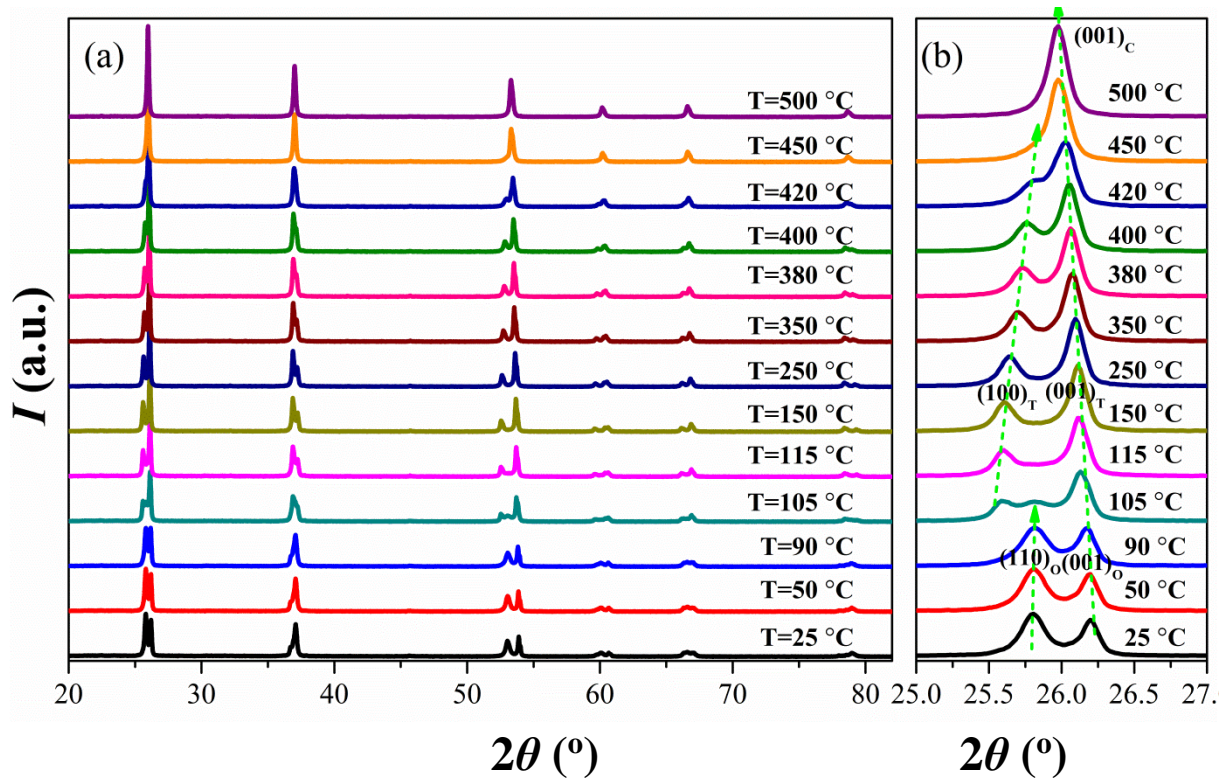


Figure 4.10. XRD patterns of powders of crushed $(\text{K}_{0.612}\text{Na}_{0.359}\text{Li}_{0.029})(\text{Ta}_{0.024}\text{Nb}_{0.976})\text{O}_3$ (N1) single crystals as a function of temperature: (a) full range, and (b) the enlarged region at around $2\theta = 25.5^\circ$ — 26.5° . Measurements were performed upon heating. The green arrows show the shift directions of the peaks with temperature.

4.3.2 Polarized Light Microscopy

The as-grown KNN-based piezoelectric single crystals in the present work were milky, as also previously reported by others [70,182,185]. Two different optical regions exist in these crystals and were observed by polarized light microscopy (PLM). By considering the $(\text{K}_{0.612}\text{Na}_{0.359}\text{Li}_{0.029})(\text{Ta}_{0.024}\text{Nb}_{0.976})\text{O}_3$ (N1) crystal as an example (Figure 4.11 (a)), optically transparent (marked red) and cloudy regions (marked green) coexist.

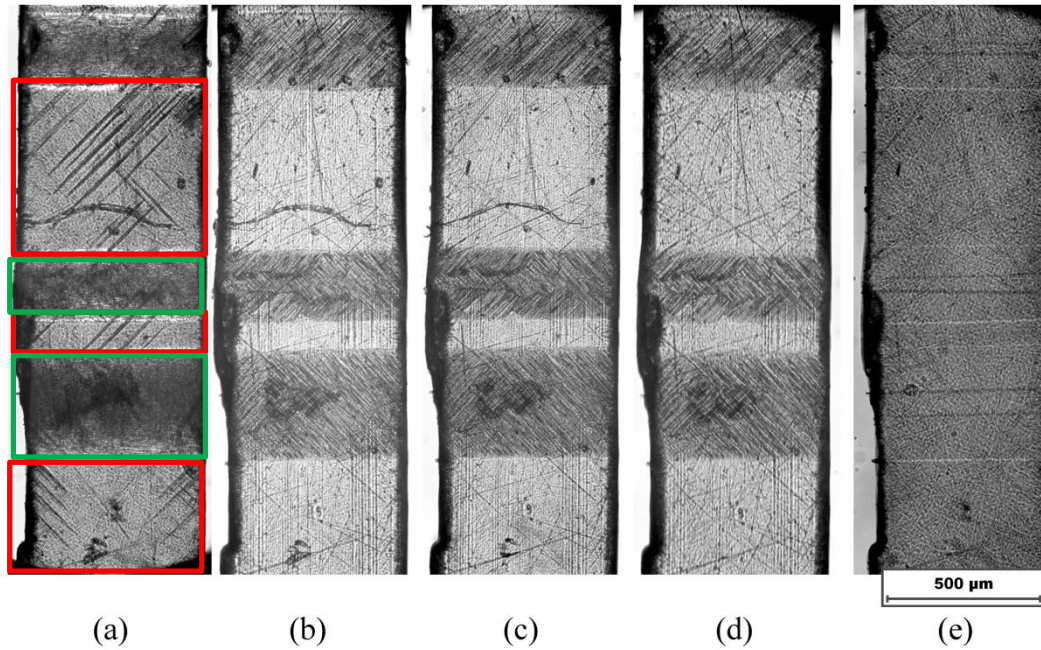


Figure 4.11. Domain configuration of the $(\text{K}_{0.612}\text{Na}_{0.359}\text{Li}_{0.029})(\text{Ta}_{0.024}\text{Nb}_{0.976})\text{O}_3$ (N1) crystal observed by PLM at various temperatures: (a) 25 °C, (b) 125 °C, (c) 300 °C, (d) 450 °C, and (e) 470 °C. The red regions are optically transparent and the green regions are optically cloudy.

Figure 4.11 displays domain evolution of the $[001]_{\text{PC}}$ -oriented N1 single crystal at various temperatures using the PLM technique. As shown in Figure 4.11 (a), domain walls of transparent regions are along $\{110\}_{\text{PC}}$ planes, whereas those of cloudy regions are along $\{001\}_{\text{PC}}$ planes at room temperature. Domain structures of both regions change when the crystal is heated to 125 °C, as displayed in Figure 4.11 (b). The $\{110\}_{\text{PC}}$ family walls disappear and $\{010\}_{\text{PC}}$ walls appear in transparent regions. On the other hand, $\{110\}_{\text{PC}}$ family walls appear in cloudy regions. These domain structures remain stable throughout the tetragonal temperature regions from 125 °C to 450 °C, as shown in Figure 4.11 (b), (c), and (d). When the crystal is in the cubic phase (Figure 4.11 (e)), all domain walls disappear and the whole crystal becomes transparent. However, some lines along $\{100\}_{\text{C}}$ can be observed, which results from the nucleation process of tetragonal domains when the crystal starts evolving to the tetragonal phase [191]. Note that due to the operating temperature of the utilized heating stage, the crystal could not be heated to a higher temperature for the observation of the possible disappearance of these lines.

Figure 4.12 (a) and (b) show enlarged images of domains in both regions. The domain size in the transparent regions is about 10 times larger than that in the cloudy regions. The back-scattering Laue pattern of the transparent region (Figure 4.12 (c) and (d)) displays clear and well-defined diffraction spots whereas that of the cloudy region displays splitting and not well-shaped diffraction spots. The latter spot morphology could be induced by crystal defects such as dislocations, twins, planar faults, or

internal strains due to chemical disorder [13]. Furthermore, in ferroelectric crystals, multi-domain structure is also one of the origin of this phenomenon [216], which is the more likely case in this work.

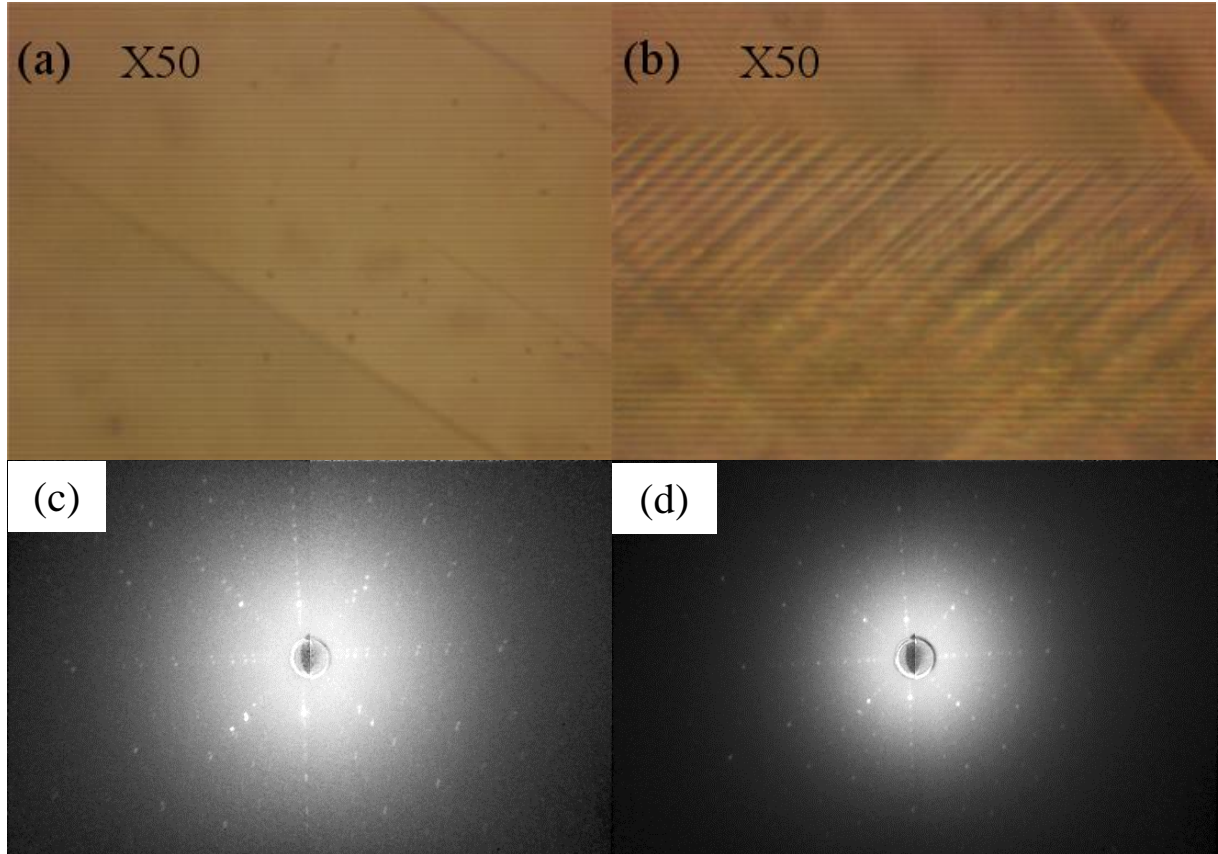


Figure 4.12. Domain configurations of (a) transparent regions and (b) cloudy regions; experimental Laue back scattering patterns of (c) transparent regions and (d) cloudy regions for the $(\text{K}_{0.612}\text{Na}_{0.359}\text{Li}_{0.029})(\text{Ta}_{0.024}\text{Nb}_{0.976})\text{O}_3$ (N1) single crystal.

For a better understanding of the appearance of the cloudy regions, XRD measurements were performed on the $[001]_{\text{PC}}$ -oriented $(\text{K}_{0.637}\text{Na}_{0.334}\text{Li}_{0.029})(\text{Ta}_{0.0229}\text{Nb}_{0.9768}\text{Mn}_{0.0003})\text{O}_{2.99955}$ (N2-Mn) crystal in which relatively large transparent regions were observed. Figure 4.13 compares XRD patterns of the transparent region and the cloudy region. It was found that the small peak at $2\theta = 22.5^\circ$ (marked as the blue star), present in the cloudy region, and disappears in the transparent regions. The appearance of the small peak is not clear. It can be induced by impurity phase, multi-domain structure, or dislocations.

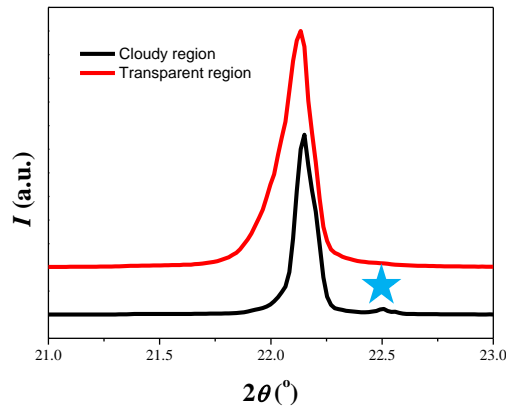


Figure 4.13. XRD patterns of the different regions of the $[001]_{PC}$ -oriented $(K_{0.637}Na_{0.334}Li_{0.029})(Ta_{0.0229}Nb_{0.9768}Mn_{0.0003})O_{2.99955}$ (N2-Mn) single crystal. The small peak appeared in the cloudy region is marked by the blue star.

Figure 4.14 displays XRD patterns of the $[001]_{PC}$ -oriented $(K_{0.612}Na_{0.359}Li_{0.029})(Ta_{0.024}Nb_{0.976})O_3$ (N1) crystal at various temperatures. Two peaks were observed for this crystal at room temperature, similar to the black pattern in Figure 4.13 for the cloudy regions. The small peak keeps shifting towards lower angles during heating, while the large peak shifts first to a lower angle and then to a higher angle when the temperature is higher than $105\text{ }^{\circ}\text{C}$. Note that this temperature corresponds to the T_{O-T} phase transition temperature. When the temperature approaches $500\text{ }^{\circ}\text{C}$, these two peaks merge into $(001)_C$. Compared to XRD patterns of the powder of crushed N1 single crystals (Figure 4.10 (b), Page 65), the small and large peaks in Figure 4.14 reveal similar behaviour as $(001)_O$ and $(110)_O$ peaks in Figure 4.10 (b) (Page 65), indicating that the transparent regions should have a $[110]_O$ orientation, while the cloudy regions should be $[001]_O$ orientation.

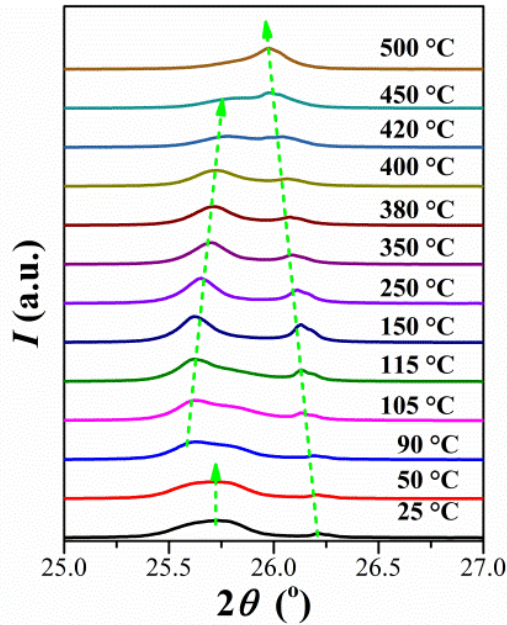


Figure 4.14. XRD patterns of the [001]_{PC}-oriented $(\text{K}_{0.612}\text{Na}_{0.359}\text{Li}_{0.029})(\text{Ta}_{0.024}\text{Nb}_{0.976})\text{O}_3$ (N1) crystal at various temperatures. The green arrows show the evolution trends of both peaks with temperature.

Figure 4.15 provides a schematic view of the cubic, tetragonal, and orthorhombic unit cells of the KNLTN perovskite structure. Upon cooling, KNLTN single crystals undergo two phase transitions: from cubic to tetragonal phase and from tetragonal to orthorhombic phase. The tetragonal unit cell can be considered as the consequence of oxygen octahedron distortions along the edges of the original cubic unit cell, creating 90° domain walls in order to release stresses during cooling. The orthorhombic unit cell is formed by the elongation along face diagonals of the original cubic unit cell, leading to 60° and 90° domain walls. On the other hand, Figure 4.15 confirms that the peaks corresponding to $(110)_O$ and $(001)_O$ crystallographic planes are originated from the $(001)_C$ peak splitting during the cooling process.

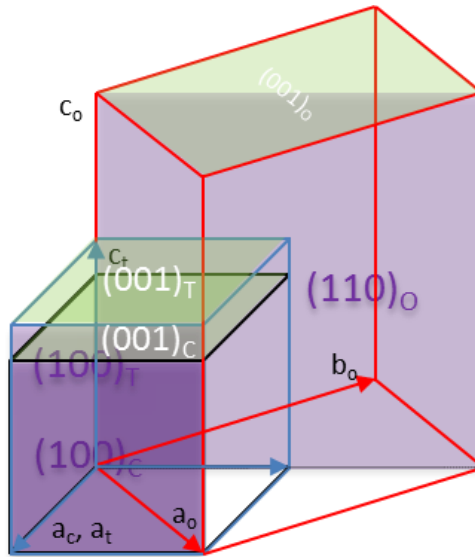


Figure 4.15. Schematic view of the perovskite structure with the cubic (C, black), tetragonal (T, blue) and orthorhombic (O, red) unit cells.

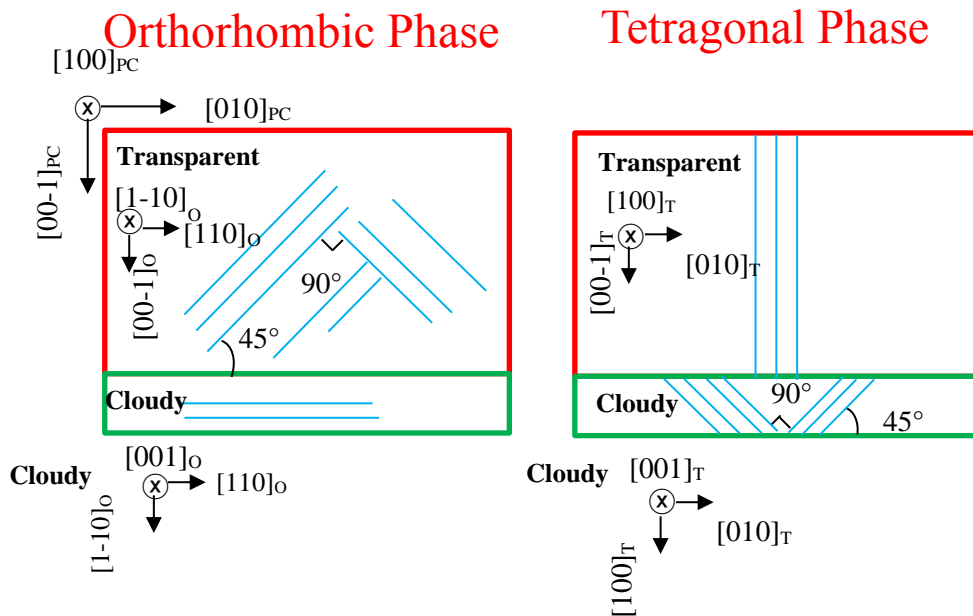


Figure 4.16. Representation of domain configurations for the transparent and the cloudy regions observed in the orthorhombic and tetragonal phases of the KNLTN single crystals.

Domain configurations of both regions in the orthorhombic and the tetragonal phase are illustrated in Figure 4.16. The transparent and cloudy regions coexist by sharing the $[110]_O$ and $[010]_T$ edge in the orthorhombic and tetragonal phase, respectively.

Figure 4.17 shows the domain configuration of the same crystal piece in Figure 4.11 (Page 66) in the proximity of the cubic-tetragonal phase transition during cooling with a rate of $0.5\text{ }^\circ\text{C}/\text{min}$. When the temperature is close to $450\text{ }^\circ\text{C}$, the cubic-tetragonal phase transition is observed with instantaneous formation of domain walls, as shown in Figure 4.17 (a). With further cooling, all parts evolve into the tetragonal phase according to the movement of cubic-tetragonal phase transition planes (see the red lines in Figure 4.17). Note that the distribution of the cloudy regions in Figure 4.17 is not the same with that of Figure 4.11 (Page 66). This is an indication of the movement of the cloudy regions with thermal treatment. The different shape and size of the cloudy region are due to relatively high cooling rate and a slight thermal gradient induced by the heating stage. However, this experiment confirms that the appearance of the cloudy regions is related to the domain nucleation process when the crystal is cooled down from the cubic phase to the tetragonal phase. If the crystal is cooled too fast below T_C , some of the tetragonal nuclei with two directions will be generated from the cubic phase, leading to the appearance of twinning. Cooling down of the as-grown crystals at a lower speed should therefore increase the chance to obtain high quality homogeneous crystals.

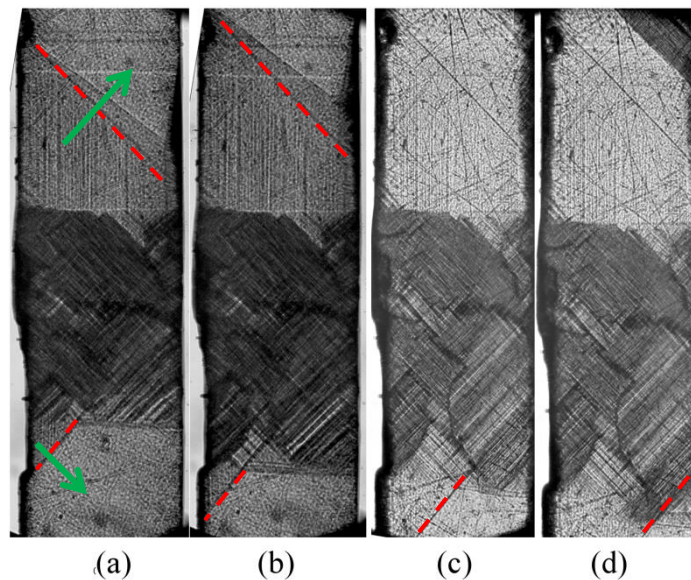


Figure 4.17. Domain configuration of the $[001]_{PC}$ -oriented $(K_{0.612}Na_{0.359}Li_{0.029})(Ta_{0.024}Nb_{0.976})O_3$ (N1) single crystal in the vicinity of $450\text{ }^\circ\text{C}$ during cooling process. (a) $450\text{ }^\circ\text{C}$, (b) $449\text{ }^\circ\text{C}$, (c) $448\text{ }^\circ\text{C}$, and (d) $447\text{ }^\circ\text{C}$. The red lines are the moving boundary of the cubic and tetragonal phases, and the green arrows are the directions of the movement.

4.3.3 Transmission Electron Microscopy

Figure 4.18 shows the domain evolution of the $[001]_{PC}$ -oriented $(K_{0.612}Na_{0.359}Li_{0.029})(Ta_{0.024}Nb_{0.976})O_3$ (N1) single crystal as a function of temperature using the *in-situ* hot stage TEM with a double tilt heating holder. At room temperature (Figure 4.18 (a)), lamellar-type domain structure is observed. The corresponding selected area electron diffraction pattern (SAED) in Figure 4.19 (a) confirms the orientation of domain walls along $\langle 110 \rangle_{PC}$ family in the orthorhombic phase. With temperature increasing from room temperature to 145 °C, the lamellar domains gradually disappear. Note that at 145 °C, orthorhombic domain walls are still dimly visible (marked with C) in Figure 4.18 (f). From Figure 4.18 (c) to (f), bend contours start to appear when the sample is heated from 110 °C to 145 °C. This is explained by the decrease of the elastic compliance at the orthorhombic-tetragonal phase transition [118].

When the temperature approaches 145 °C, a new type of domain wall with a long-bar structure begins to grow (marked with B) in Figure 4.18 (f). Due to the limited number of domain structures in this region, a new region was selected for imaging from 150 °C to 450 °C, as seen in Figure 4.18 (g)-(k). The long-bar domain walls form a T-shape-like domain structure. Based on their SAED patterns in Figure 4.19 (c)-(e), domain walls in tetragonal phase are along the $\langle 001 \rangle_{PC}$ direction. We note that the appearance of tetragonal domains was instantaneous, confirming that the orthorhombic-tetragonal phase transition in KNN-based single crystals is of the first order. Similar domain structure in a Sb-doped KNLTN polycrystalline ceramic has been observed using the TEM technique by Lu *et al.* [217]. When the crystal is in the tetragonal region, the T-type domain structure also disappeared gradually with increasing temperature. Even if the temperature is increased to 450 °C, at which the crystal evolves into the cubic phase, tetragonal domain structures are still weakly visible.

The TEM images and the SAED patterns at various temperatures provide information about domain evolution at phase transition and the relationship between the orientations of domain walls and crystallographic structure. Hierarchical nanodomain structures [153,154] are expected to be observed in the vicinity of the T_{O-T} . However, the unstable domain structure near the T_{O-T} and the high temperature stage make it difficult to focus on details. Therefore, no nanodomain was detected during the measurements. Figure 4.18 (k) provides the enlarged view of “red-A” zone in Figure 4.18 (b) and a fingerprint-type domain structure is presented.

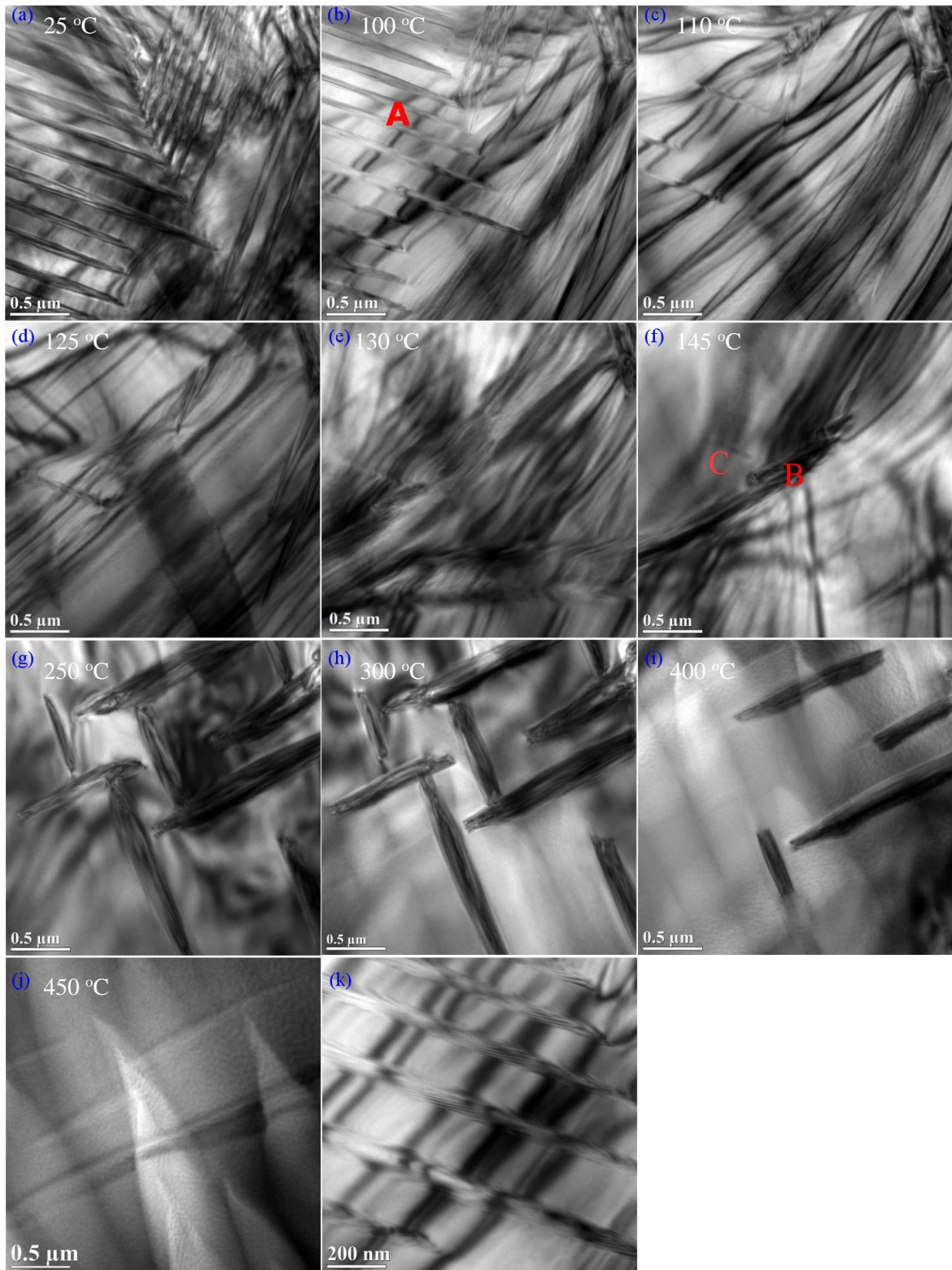


Figure 4.18. *In-situ* TEM images of ferroelectric domain structure in the $[001]_{PC}$ -oriented $(K_{0.612}Na_{0.359}Li_{0.029})(Ta_{0.024}Nb_{0.976})O_3$ (N1) single crystal. (a) 25 °C, (b) 100 °C, (c) 110 °C, (d) 125 °C, (e) 130 °C, (f) 145 °C, (g) 250 °C, (h) 300 °C, (i) 400 °C, and (j) 450 °C. (k) Enlarged “red-A” zone of (b).

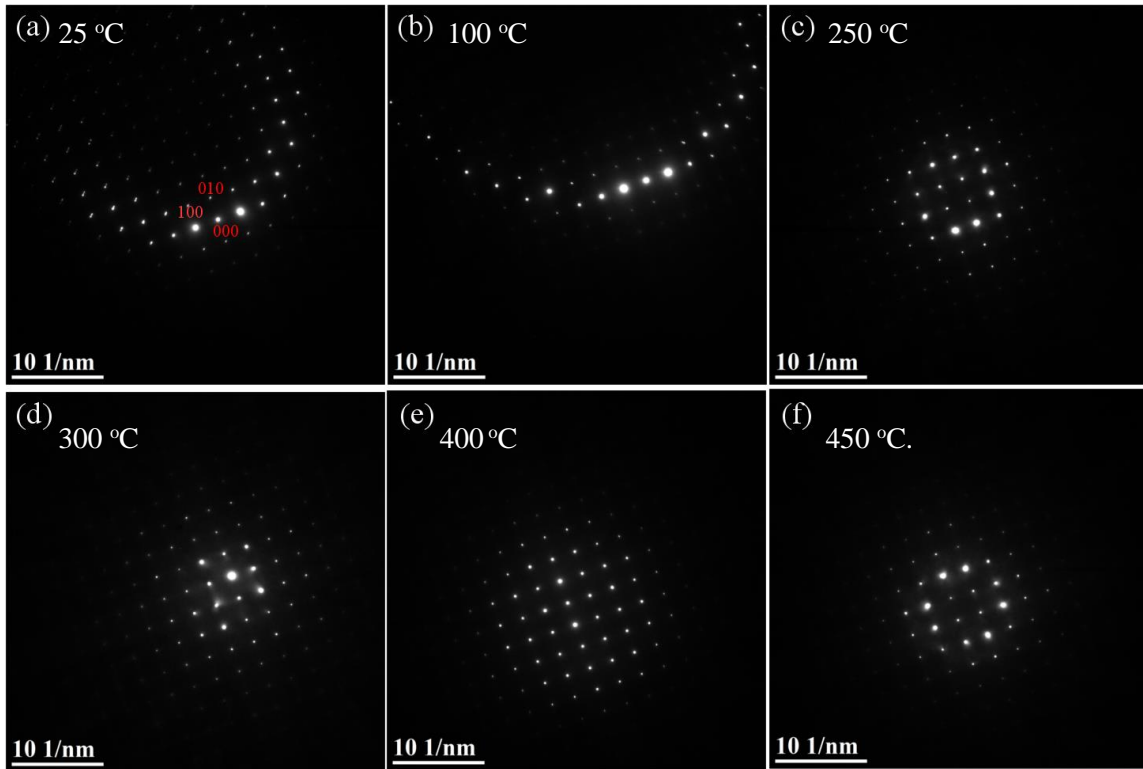


Figure 4.19. Temperature-dependent selected area electron diffraction patterns in the $[001]_{PC}$ -oriented $(K_{0.612}Na_{0.359}Li_{0.029})(Ta_{0.024}Nb_{0.976})O_3$ (N1) single crystal: (a) 25 °C, (b) 100 °C, (c) 250 °C, (d) 300 °C, (e) 400 °C, and (f) 450 °C.

4.4 Summary

Eleven KNN-based piezoelectric single crystals were grown by the submerged-seed solution growth or the top-seeded solution growth method. The relationship between the effective segregation coefficients and the initial liquid concentrations for individual elements were discussed. It was found that Na and Ta ions are preferentially absorbed by the crystal during the growth process because their effective segregation coefficients are larger than 1, while K and Nb ions show the opposite behavior with the effective segregation coefficients less than 1. For the B-site ions, the segregation coefficient of Nb increases with its concentration in the initial liquid solution, whereas that of Ta shows a decreasing trend. For the A-site ions, K ions display a similar trend, as compared to Nb ions. The behavior of Na is complex and non-monotonic, due to the competition between Li, Na, and K ions.

The segregation coefficient of Li was found to be very low, approximately 0.19. In order to produce the $(\text{K},\text{Na},\text{Li})(\text{Ta},\text{Nb})\text{O}_3$ (KNLTN) and $(\text{K},\text{Na},\text{Li})(\text{Ta},\text{Nb},\text{Sb})\text{O}_3$ (KNLTNS) crystal with a $T_{\text{O-T}}$ in the vicinity of room temperature, 17 — 25 mol % Li in the initial liquid solution is required, which greatly increases the risk of the appearance of the tetragonal tungsten bronze phase. We therefore argue that it is difficult to obtain a KNLTN(S) crystal with a room temperature $T_{\text{O-T}}$.

Temperature-dependent structure evolutions of the $(\text{K}_{0.612}\text{Na}_{0.359}\text{Li}_{0.029})(\text{Ta}_{0.024}\text{Nb}_{0.976})\text{O}_3$ (N1) crystal were studied using polarized light microscopy and X-ray diffraction techniques. Optically transparent regions with wider domains and opaque regions with narrow domains were observed in the crystal. Different domain walls for the two regions were observed. Based on the comparison of the temperature-dependent XRD measurements between the powders and the $[001]_{\text{PC}}$ orientation, the cloudy regions were assigned to the $(001)_{\text{O}}$ plane. Temperature-dependent TEM images of the $[001]_{\text{PC}}$ -oriented $(\text{K}_{0.612}\text{Na}_{0.359}\text{Li}_{0.029})(\text{Ta}_{0.024}\text{Nb}_{0.976})\text{O}_3$ (N1) single crystal showed the domain walls shift from $[110]_{\text{PC}}$ to $[001]_{\text{PC}}$ direction when the phase changed from orthorhombic to tetragonal.



5 Composition Dependence of Phase Transitions and Electrical Properties

5.1 Influence of Ta Substitution

The four crystals, N7, N8, N9, and N10, are selected to investigate the influence of Ta content on the structure and electromechanical properties of (K,Na,Li)(Ta,Nb)O₃ (KNLTN) single crystals. As stated in Table 4.3 (Page 55), their compositions are N7: (K_{0.881}Na_{0.119})NbO₃, N8: (K_{0.265}Na_{0.715}Li_{0.020})(Ta_{0.135}Nb_{0.865})O₃, N9: (K_{0.387}Na_{0.593}Li_{0.020})(Ta_{0.186}Nb_{0.814})O₃, and N10: (K_{0.371}Na_{0.612}Li_{0.017})(Ta_{0.338}Nb_{0.662})O₃. The slight differences in A-site cation ratios between N8, N9, and N10 crystals result from the different initial compositions of the liquid, as well as the difficulty in keeping crystal growth conditions the same for each attempt. Note that the N7 crystal is selected as a reference for pure (K,Na)NbO₃.

5.1.1 Crystallographic Structures and Phase Transitions

Figure 5.1 (a) shows XRD patterns measured on crushed single crystals. It is observed that all four crystals exhibit single perovskite phase without any secondary phases. Moreover, enlarged 2θ regions at about 45 ° are highlighted in Figure 5.1 (b), revealing that the crystallographic structure of KNLTN crystals evolves from orthorhombic to tetragonal with increasing Ta content. For the N7 and N8 samples, the intensity ratio $I_{(022)O}/I_{(200)O}$ is close to 2, while the $I_{(002)T}/I_{(200)T}$ changes to about 0.5 for the N9 and N10 samples. The origin of this evolution is the substitution of Nb ions ($R=0.069$ nm; CN6) by the slightly smaller Ta ions ($R=0.068$ nm; CN6) [218], which was also reported for Ta-modified KNN-based polycrystalline ceramics [109,110]. Lattice distortions (η) of orthorhombic (Ortho.) and tetragonal (Tetra.) phases are calculated by the following equations,

$$\eta(\text{Ortho.}) = \left(\frac{c_o}{\sqrt{2}a_o} - 1 \right) * 100 \quad (5.1)$$

$$\eta(\text{Tetra.}) = \left(\frac{c_T}{a_T} - 1 \right) * 100 \quad (5.2)$$

The calculated lattice parameters, lattice distortions, and crystallographic structures are summarized in Table 5.1. The lattice distortion in the tetragonal phase is slightly higher than that in the orthorhombic phase in the vicinity of the T_{O-T} , which is consistent with the previous work on KNN-based polycrystalline ceramics [219].

Table 5.1. Lattice parameters of as-grown KNLTN single crystals with different Ta contents.

Sample	Ta content (%)	Lattice parameters			Lattice distortion (%)	Phase
		a (Å)	b (Å)	c (Å)		
N7	0	3.963	5.681	5.707	1.84	Ortho.
N8	13.5	3.970	5.587	5.704	1.61	Ortho.
N9	18.6	/ ^a	/ ^a	/ ^a	/ ^a	Tetra.
N10	33.8	3.997	3.997	4.073	1.90	Tetra.

^a The lattice parameters and the distortion of this composition could not be determined due to the presence of a minor amount of orthorhombic phase in the predominantly tetragonal sample. This is a consequence of the vicinity of the phase transition.

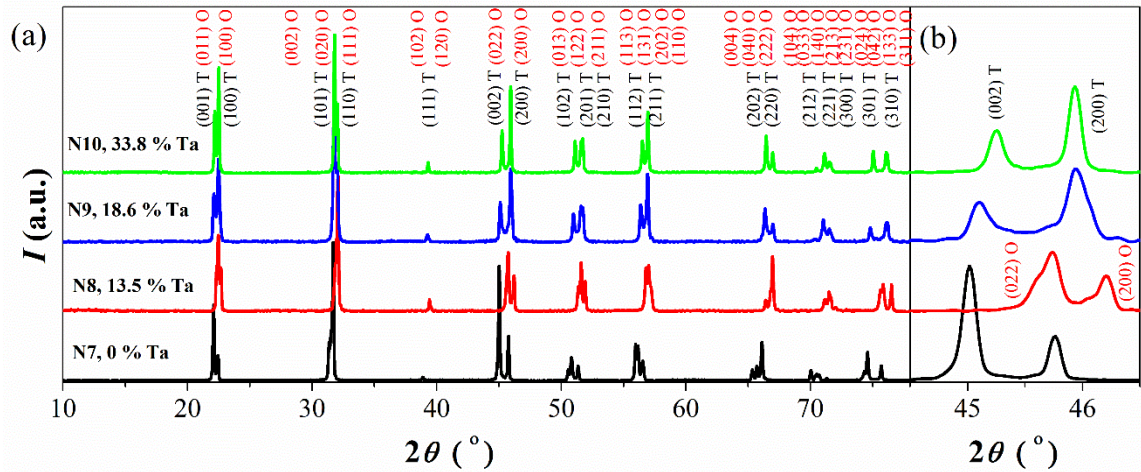


Figure 5.1. XRD patterns of the crushed KNLTN single crystals with different Ta contents. (a) Full range and (b) enlarged region of (002)_T/(200)_T or (022)_O/(200)_O peaks.

Raman spectra of [001]_{PC}-oriented KNLTN single crystals at room temperature in the range from 100 cm⁻¹ to 1000 cm⁻¹ are shown in Figure 5.2. Theoretically, six soft modes exist in KNLTN systems, related to the vibrational movement of BO₆ octahedra: 1A_{1g}(ν₁)+1E_g(ν₂)+2F_{1u}(ν₃,ν₄)+F_{2g}(ν₅)+F_{2u}(ν₆), among which 1A_{1g}(ν₁)+1E_g(ν₂)+1F_{1u}(ν₃) are stretching modes and others are bending modes [220]. Raman peaks between 100 cm⁻¹ and 200 cm⁻¹ are ascribed to the translational modes of A-site cations and the rotations of the BO₆ octahedra, while the ones between 200 cm⁻¹ and 1000 cm⁻¹ to the stretching and bending vibrations of the BO₆ octahedra [220,221]. As shown in Figure 5.2, the ν₂ mode at about 550 cm⁻¹ and the shoulder of ν₅ at about 200–300 cm⁻¹ become weaker with increasing Ta content, as a consequence of the phase evolution from the orthorhombic to the tetragonal phase. When compared to the pure KNN single crystal (N7), KNLTN single crystals exhibit stronger ν₁ and ν₅ modes, but a weaker

$\nu_5+\nu_1$ coupling mode and ν_4 mode. The decoupling effect of ν_1 and ν_5 modes results from the weaker interactions among the BO_6 octahedron after Li and Ta substitutions.

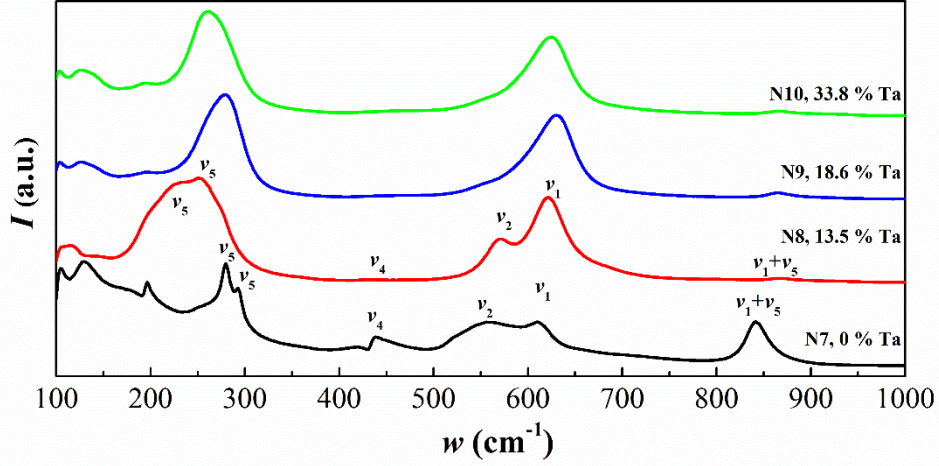


Figure 5.2. Raman spectra of $[001]_{\text{PC}}$ -oriented KNLTN single crystals with various Ta contents.

The temperature-dependent permittivity and dielectric losses of $[001]_{\text{PC}}$ -oriented KNLTN single crystals measured at 10 kHz are provided in Figure 5.3. The inset in Figure 5.3 displays the relationship between phase transition temperatures, extracted from the permittivity measurements, and the Ta contents. This relationship can be linearly fitted by following equations:

$$T_C(^{\circ}\text{C}) = -(4.6 \pm 0.23) \cdot x (\text{mol}\%) + (436 \pm 4.7) \quad (5.3)$$

$$T_{O-T}(^{\circ}\text{C}) = -(8.6 \pm 1.25) \cdot x (\text{mol}\%) + (204 \pm 26.19) \quad (5.4)$$

where x is the Ta content in mol %. The decrease rates of T_C and T_{O-T} are $4.6^{\circ}\text{C}/\text{mol}\%\text{Ta}$ and $8.6^{\circ}\text{C}/\text{mol}\%\text{Ta}$, respectively. This shift of both phase transition temperatures is attributed to the different electronegativity between Ta and Nb [4], as well as the change of the Goldschmidt tolerance factor t [24]. Lower electronegativity of Ta weakens the B-O bond and therefore reduces the ability for off-center movements of B-site ions during the tetragonal–cubic phase transition.

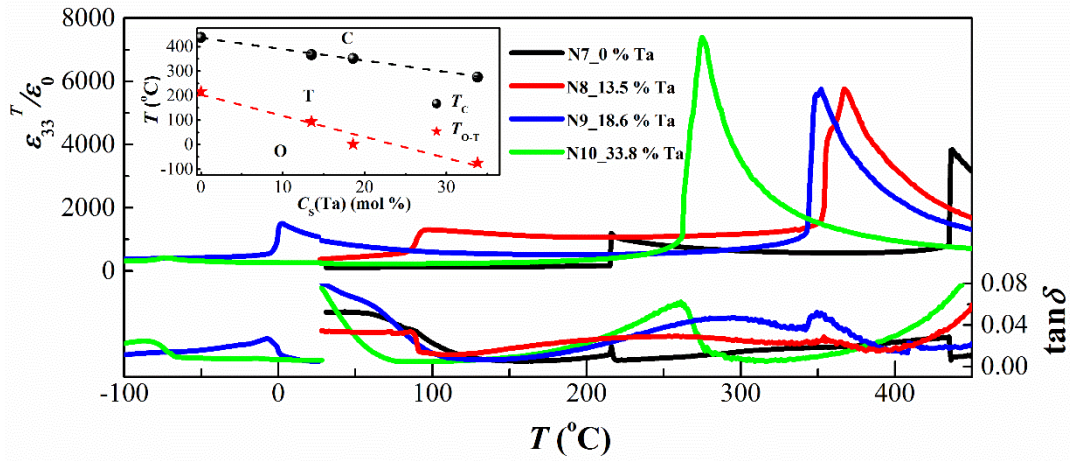


Figure 5.3. Temperature-dependent dielectric permittivity and losses of [001]_{PC}-oriented KNLTN single crystals during heating from -100 °C to 450 °C at 10 kHz. The inset displays the change of phase transition temperatures (T_C and T_{O-T}) as a function of the Ta content. The minor discontinuity at 30 °C is related to the use of different measurement setups for the low and high temperature range.

The influence of the K/Na ratio on transition temperatures was previously studied by Zhang *et al.* in polycrystalline (K,Na)NbO₃ ceramics [222]. When the K/Na ratio was changed from 70/30 to 30/70, both phase transition temperatures T_C and T_{O-T} decreased by less than 10 °C. Similar results were also obtained by others [223,224]. Therefore, the shift of both T_C and T_{O-T} observed in this work can be ascribed primarily to the changing Ta content, and the influence of the K/Na ratio can be neglected.

Relative dielectric permittivity values $\epsilon_{33}^T/\epsilon_0$ of N7, N8, N9, and N10 crystals at 30 °C are 107, 371, 964, and 231, respectively. The N9 crystal with 18.6 % Ta exhibits the highest dielectric permittivity at room temperature, which is higher than the values from most other literature reports, as listed in Table 2.3 (Page 35) and Table 2.4 (Page 36). This is related to the vicinity of the T_{O-T} to room temperature, which will be described in more detail in the following sub-chapter and in Chapter 6.

5.1.2 Influence of Ta Content on Room Temperature Electromechanical Properties

Figure 5.4 (a) depicts bipolar electric field-induced strain curves ($S-E$) of [001]_{PC}-oriented KNLTN single crystals. Butterfly-shaped $S-E$ loops with evident negative strain (S_{neg}) are observed for all crystals. Figure 5.4 (b) plots the corresponding unipolar strain curves. Highest bipolar and unipolar strains at 2 kV/mm are observed in the N9 crystal with 18.6 % Ta content. The enhanced strain in the N9 crystal results from the proximity of its T_{O-T} to room temperature (Figure 5.3) and the resulting lower energy barrier for polarization rotation [1,142].

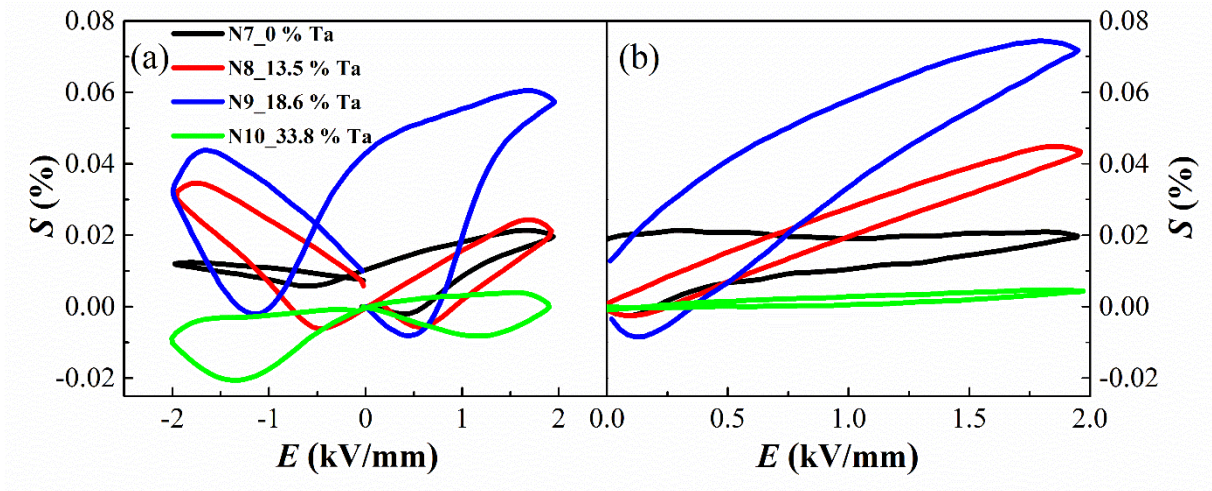


Figure 5.4. Electric field-induced (a) bipolar and (b) unipolar strains of [001]_{PC}-oriented KNLTN single crystals at 2 kV/mm and 10 Hz.

Bipolar strain curves also exhibit an asymmetric shape, which indicates the existence of an internal bias field E_i . Coercive field E_C and internal field E_i are calculated by Equations (5.5) and (5.6) and are plotted in Figure 5.5 (a).

$$E_C = \frac{|E_C^+|}{2} + \frac{|E_C^-|}{2} \quad (5.5)$$

$$E_i = \left| \frac{|E_C^+|}{2} - \frac{|E_C^-|}{2} \right| \quad (5.6)$$

where E_C^+ and E_C^- represent the positive and negative coercive fields, respectively. Note that the coercive field E_C was taken as the electric field where the minimum strain is obtained in bipolar strain curves [225,226].

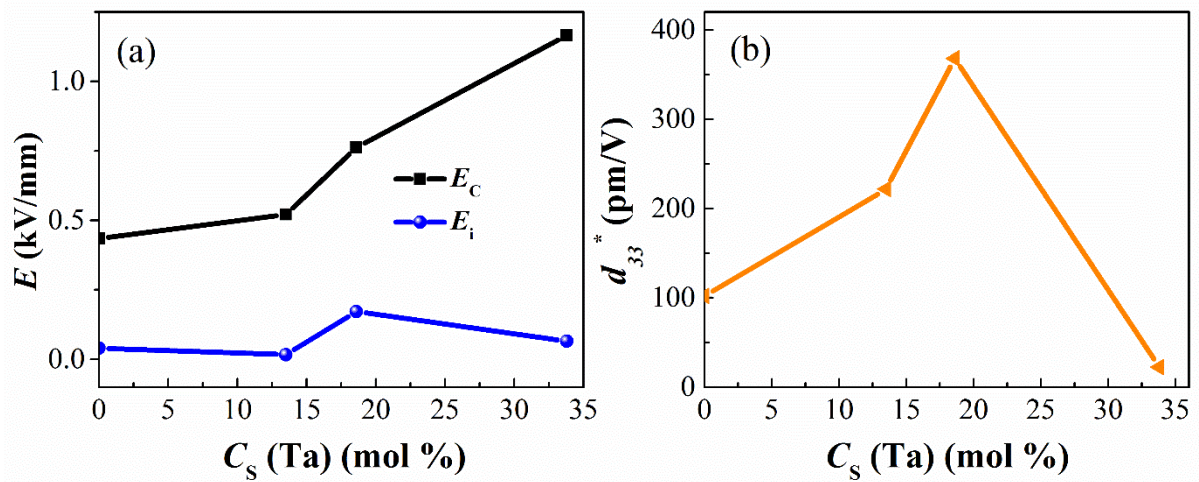


Figure 5.5. (a) E_C , E_i , and (b) piezoelectric constant d_{33}^* at 2 kV/mm of the [001]_{PC}-oriented KNLTN single crystals with different Ta contents.

It can be observed in Figure 5.5 (a) that internal bias fields are up to 20 % of the corresponding coercive field values. The reason for the appearance of internal bias fields in KNLTN crystals is still unclear, but may be related to defects created during crystal growth. The evaporation of A-site alkali ions [11] during the high-temperature growth process results in the formation of V_A' vacancies and the charge-compensating V_O'' vacancies.

As shown in Figure 5.4 (a), the maximum positive strain S_{pos} (0.06 %) of [001]_{PC}-oriented KNLTN crystals was obtained with 18.6 % Ta. A remarkable decrease of S_{pos} is observed when Ta content increases to 33.8 %. Interestingly, for the N10 crystal with 33.8 % Ta, the absolute S_{neg} value is much higher than its S_{pos} . This phenomenon was previously observed in $0.62\text{Pb}(\text{Mg}_{1/3}\text{Nb}_{2/3})\text{O}_3\text{-}0.38\text{PbTiO}_3$ (PMN-PT) single crystals [225]. It was proposed that the depolarization field and internal stresses are too small to produce significant back-switching of the polarization in the absence of grain boundaries. However, studies of lead-based single crystals revealed that the shape of the bipolar strain curve depends on the crystallographic orientation and phase structure [155]. A detailed discussion of the influence of the orientation on the properties of KNN-based single crystals is given in Chapter 6.

It is observed that the coercive field E_C of N10 sample with 33.8 % Ta is more than 2 times higher as compared to other crystals with lower Ta content (Figure 5.5 (a)), which can be related to the formation of the tetragonal phase with fewer spontaneous polarization vectors and increased lattice distortion. Figure 5.5 (b) shows the large-signal converse piezoelectric coefficients d_{33}^* of [001]_{PC}-oriented KNLTN single crystals, which are calculated from the maximum unipolar strain measurements. The values for N7, N8, N9, and N10 are 102, 221, 368, and 22 pm/V, respectively. The highest d_{33}^* is obtained when Ta content is 18.6 % (N9 crystal), due to the proximity of the T_{O-T} to room temperature.

The ferroelectric hysteresis loop of the $[001]_{\text{PC}}$ -oriented N8 with 13.5 % Ta and N9 single crystal with 18.6 % Ta are presented in Figure 5.6. The high leakage currents of the N7 crystal with 0 % Ta and the N10 crystal with 33.8 % Ta made it impossible to study their ferroelectric properties. For the N9 single crystal with 18.6 % Ta (Figure 5.6 (b)), the remanent polarization is approximately $5 \mu\text{C}/\text{cm}^2$ and the coercive field is 0.80 kV/mm, which is in agreement with the value 0.76 kV/mm obtained from the bipolar strain loop. Note that the P - E loop of this crystal at 3 kV/mm field amplitude could not be obtained due to the lower breakdown field. As compared to the N9 single crystal with 18.6 % Ta, the P_r of $3 \mu\text{C}/\text{cm}^2$ at 3 kV/mm in the N8 single crystal (13.5 % Ta) is lower, which is also ascribed to the proximity of $T_{\text{O-T}}$ to room temperature in the N9 crystal.

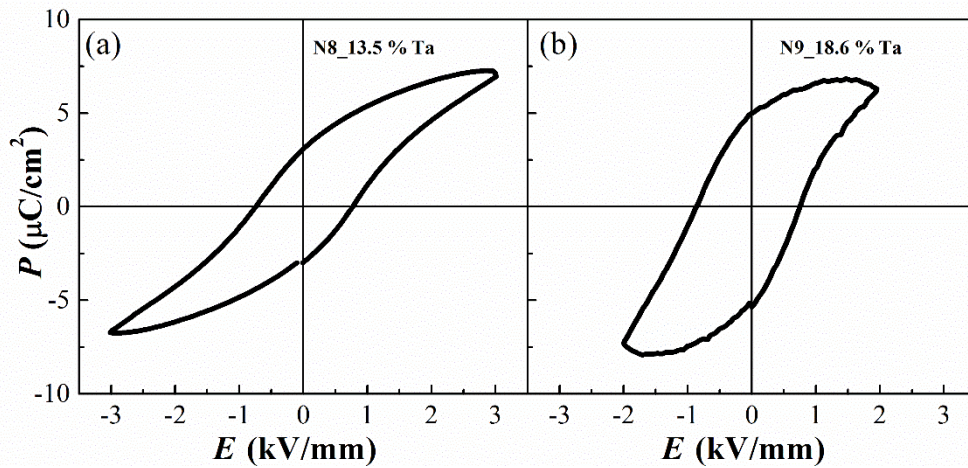


Figure 5.6. Room temperature ferroelectric hysteresis P - E loops of the $[001]_{\text{PC}}$ -oriented (a) N8 single crystal with 13.5 % Ta ($f=20$ Hz) and (b) N9 single crystal with 18.6 % Ta ($f=10$ Hz).

Piezoelectric, ferroelectric, and dielectric parameters of all $[001]_{\text{PC}}$ -oriented KNLTN single crystals with different Ta contents are summarized in Table 5.2.

Table 5.2. Piezoelectric, ferroelectric, and dielectric parameters of [001]_{PC}-oriented KNLTN crystals with various Ta contents.

Sample (Ta mol%)	d_{33}^* (pm/V)	S_{pos} (%) ^a	$-S_{\text{neg}}$ (%) ^a	S_{max} (%) ^b	E_C (kV/mm)	E_i (kV/mm)	$\epsilon_{33}^T/\epsilon_0$ (RT)	$\epsilon_{33}^{\text{max}}/\epsilon_0$ (T_C)	T_{O-T} (°C)	T_C (°C)
N7 (0)	102	0.020	0.002	0.020	0.44	0.040	107	3814	216	437
N8 (13.5)	221	0.024	0.005	0.044	0.52	0.017	371	5765	94	367
N9 (18.6)	368	0.060	0.008	0.074	0.76	0.172	964	5743	1	352
N10 (33.8)	22	0.004	0.008	0.004	1.17	0.065	231	7394	-75	275

^a Obtained from bipolar strain curves.

^b Obtained from unipolar strain curves.

5.1.3 Temperature-dependent Electromechanical Properties

Temperature-dependent ferroelectric hysteresis loops (2nd electric field loading cycle) for the [001]_{PC}-oriented N8 single crystal with 13.5 % Ta ($T_{O-T} = 94$ °C) are presented in Figure 5.7. The P - E loop at 20 °C exhibits the maximum remanent polarization P_r (3 $\mu\text{C}/\text{cm}^2$) and maximum polarization P_{max} (6.9 $\mu\text{C}/\text{cm}^2$). The local maximum P_r of 2.8 $\mu\text{C}/\text{cm}^2$ is achieved at 90 °C, originating from the orthorhombic-tetragonal phase transition.

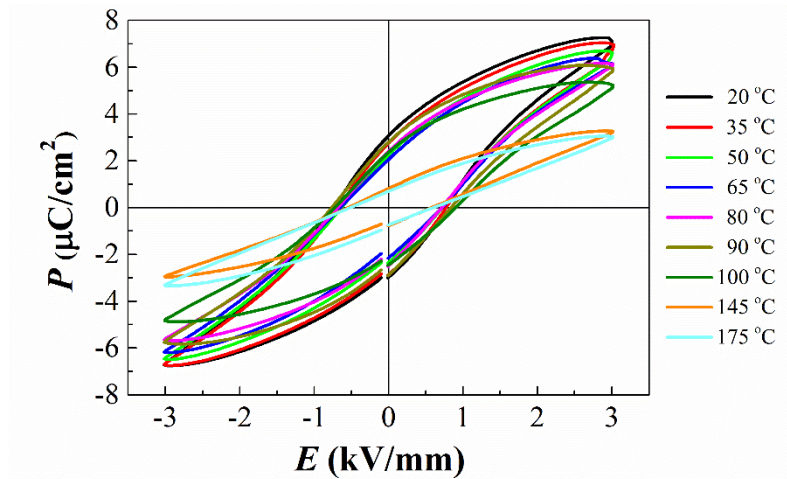


Figure 5.7. Temperature dependent P - E loops of the [001]_{PC}-oriented N8 single crystal with 13.5 % Ta ($f=20$ Hz).

Temperature-dependent electric field-induced strain curves of the $[001]_{\text{PC}}$ -oriented N8 single crystal with 13.5 % Ta are plotted in Figure 5.8. For all measured temperatures, the main difference of S - E curves between the first and the second electric field loading cycle is the initial process when the field increases from 0 to the positive maximum E_{max} (3 kV/mm in this work). This is due to the irreversible domain switching and domain wall movement processes.

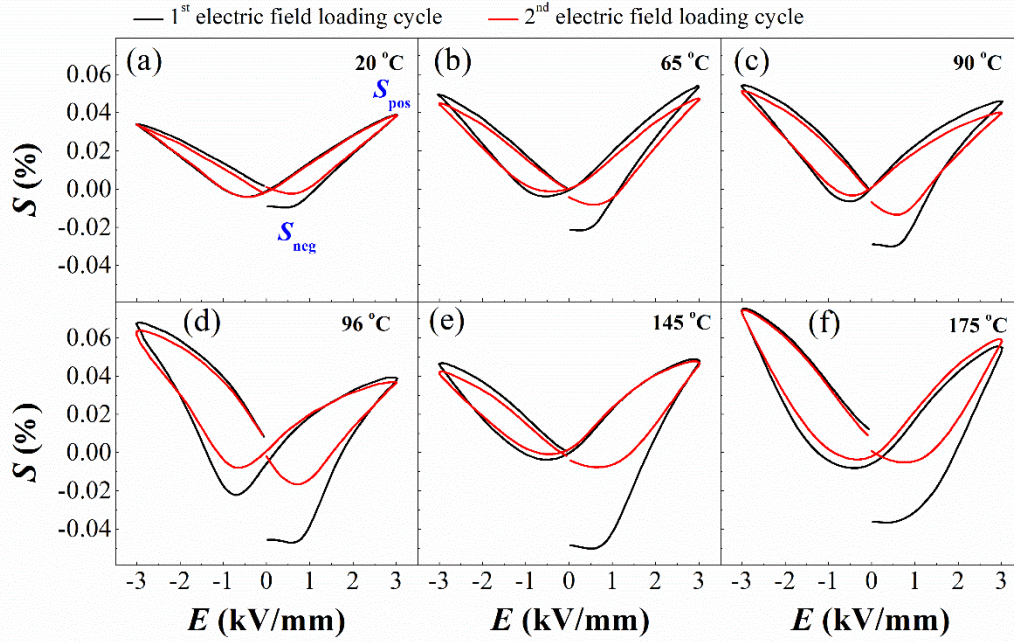


Figure 5.8. Temperature dependent electric field-induced strain curves of the $[001]_{\text{PC}}$ -oriented N8 single crystal with 13.5 % Ta. The black curve refers to the S - E curve during the first electric field loading cycle, whereas the red curve corresponds to the second electric field loading cycle.

The maximum positive strain S_{pos} for the first cycle and the absolute values of minimum negative strain $-S_{\text{neg}}$ for both cycles in the $[001]_{\text{PC}}$ -oriented N8 crystal (13.5 % Ta) are shown in Figure 5.9 (a). The ratio $-S_{\text{neg},1}/S_{\text{pos},1}$ in the first cycle and $S_{\text{neg},2}/S_{\text{neg},1}$ for both cycles are plotted in Figure 5.9 (b). Note that ‘ $-S_{\text{neg}}$ ’ is the absolute value of S_{neg} . The maximum values of S_{pos} are achieved at the orthorhombic side, in the vicinity of the $T_{\text{O-T}}$: $S_{\text{pos}}(65\text{ °C}) = 0.054\%$; and $S_{\text{pos}}(80\text{ °C}) = (0.053\%)$. The maximum $-S_{\text{neg}}$ are obtained at the tetragonal side in the vicinity of the $T_{\text{O-T}}$: $-S_{\text{neg}}$ (first cycle, $100\text{ °C}) = 0.061\%$ and $-S_{\text{neg}}$ (second cycle, $100\text{ °C}) = 0.017\%$. The blue curve in Figure 5.9 (b) indicates that $-S_{\text{neg},1}/S_{\text{pos},1}$ (for the first cycle) is smaller than 0.5 in the orthorhombic phase from 20 °C to 80 °C , whereas it is higher than 1 in the tetragonal phase from 100 °C to 140 °C . The maximum ratio of 2 is observed at 100 °C . The $S_{\text{neg},2}/S_{\text{neg},1}$ ratio in Figure 5.9 (b) increases linearly from 25 % to 45 % during heating from 20 °C to 90 °C . When the temperature approaches $T_{\text{O-T}}$, it decreases from 45 % to 35 %, followed by a decrease in the tetragonal phase. Since the main difference between the two electric field loading cycles is the

contribution of the irreversible domain switching and domain wall movement processes, the relatively larger $S_{\text{neg},2}/S_{\text{neg},1}$ in the orthorhombic phase indicates the lower contribution of irreversible processes during the initial field loading, as compared to the tetragonal phase.

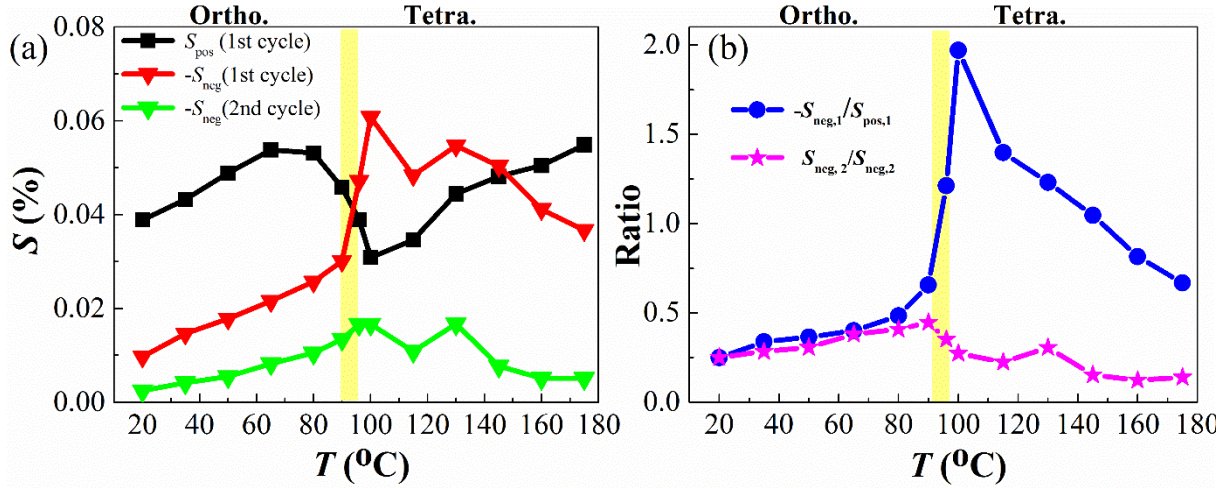


Figure 5.9. Temperature-dependent (a) maximum positive strain S_{pos} , absolute value of the minimum negative strain $-S_{\text{neg}}$ during the first cycle and $-S_{\text{neg}}$ during the second cycle, and (b) $-S_{\text{neg},1}/S_{\text{pos},1}$ in the first cycle and negative strain ratios between two cycles $S_{\text{neg},1}/S_{\text{neg},2}$ in the $[001]_{\text{PC}}$ -oriented N8 crystal with 13.5 % Ta. Note that 1 represents the first cycle and 2 the second cycle. The orthorhombic-tetragonal phase transition is highlighted by the yellow region.

5.1.4 Summary

The influence of the Ta content on the structure and electrical properties was investigated in Li, Ta-modified KNN single crystals. The evolution from the orthorhombic to the tetragonal phase with increasing Ta content was detected by XRD and Raman techniques. The T_{C} and $T_{\text{O-T}}$ were found to linearly shift to lower temperatures with increasing Ta content. Highest room temperature electrical properties ($d_{33}^* = 368$ pm/V, $\epsilon_{33,r}/\epsilon_0 = 964$) were found for the $[001]_{\text{PC}}$ -oriented N9 single crystal with 18.6 % Ta. This is attributed to the proximity of the $T_{\text{O-T}}$ of the N9 single crystal to room temperature. The observed asymmetric strain may be correlated to the presence of defects, created during the high-temperature crystal growth. Temperature-dependent polarization P - E and strain S - E curves were studied in the $[001]_{\text{PC}}$ -oriented N8 single crystal with 13.5 % Ta. The remanent polarization P_{r} reached the local maximum at 90 $^{\circ}\text{C}$, which is in the vicinity of $T_{\text{O-T}}$ (94 $^{\circ}\text{C}$). The influence of temperature on the maximum positive strain S_{pos} during the first electrical poling cycle and minimum negative strain S_{neg} during both the first and the second electric field loading cycles have been studied. The maximum of S_{pos} of 0.053 % was obtained at 80 $^{\circ}\text{C}$ at the orthorhombic side in the vicinity of $T_{\text{O-T}}$. The maxima of $-S_{\text{neg}}$ of 0.061 % in the first cycle and 0.017 % in the second cycle were obtained at 100 $^{\circ}\text{C}$ at the

tetragonal side in the vicinity of T_{O-T} . The higher $S_{\text{neg},2}/S_{\text{neg},1}$ in the orthorhombic phase indicates the lower irreversible contribution of domain switching and domain wall movement processes.

5.2 Influence of Sb Substitution

5.2.1 Phase Transition

The influence of Sb on the ferroelectric and piezoelectric response was studied using two crystals: $(\text{K}_{0.287}\text{Na}_{0.691}\text{Li}_{0.022})(\text{Ta}_{0.063}\text{Nb}_{0.870}\text{Sb}_{0.067})\text{O}_3$ (KNLTNS; growth attempt N11-Sb) and the $(\text{K}_{0.265}\text{Na}_{0.715}\text{Li}_{0.020})(\text{Ta}_{0.135}\text{Nb}_{0.865})\text{O}_3$ (KNLTN; growth attempt N8, presented in the previous section).

As shown in Figure 5.10 (a), the substitution of 6.7 % Sb on the B-site shifts the T_{O-T} from 94 °C to 50 °C and the T_C from 367 °C to 285 °C. The decrease rate of T_{O-T} (6.6 °C/mol%) is half of that of T_C (12.2 °C/mol%) and indicates narrowing of the tetragonal temperature range. This trend is opposite as in the case of Ta substitution, where a broadening of the tetragonal temperature range was observed (see Section 5.1.2). Note that the decrease rates are only half of the values reported for the Sb-substituted KNN-based polycrystalline ceramics [102,103]. This difference may be related to intergranular interactions; however, further experimental work is needed to understand this phenomenon. The T_{O-T} of the N11-Sb crystal was shifted to 50 °C, which is in the vicinity of room temperature. Moreover, decreased dielectric losses below T_C are observed for the N11-Sb crystal (Figure 5.10 (b)).

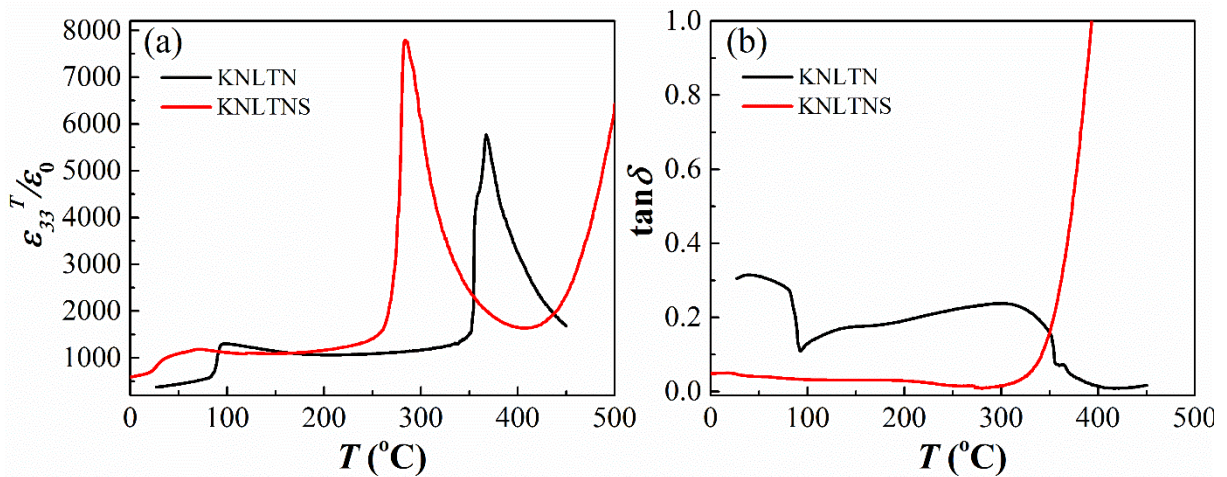


Figure 5.10. Temperature-dependent permittivity of $[001]_{\text{PC}}$ -oriented $(\text{K}_{0.265}\text{Na}_{0.715}\text{Li}_{0.020})(\text{Ta}_{0.135}\text{Nb}_{0.865})\text{O}_3$ (KNLTN, N8) and $(\text{K}_{0.287}\text{Na}_{0.691}\text{Li}_{0.022})(\text{Ta}_{0.063}\text{Nb}_{0.870}\text{Sb}_{0.067})\text{O}_3$ (KNLTNS, N11-Sb) crystals at 10 kHz.

5.2.2 Influence of Annealing on Permittivity

The abnormal increase of the dielectric permittivity and dielectric losses above T_C in the as-prepared $[001]_{PC}$ -oriented KNLTNS single crystal (Figure 5.10; N11-Sb) could indicate the presence of defects. Kizaki *et al.* [187] and Noguchi *et al.* [188] reported that leakage current density of pure KNN crystals decreased after annealing in air or O_2 . However, the underlying conductivity mechanisms and the method to improve the weak piezoelectric and ferroelectric response ($d_{33} = 173$ pC/N, and $P_r = 9$ $\mu\text{C}/\text{cm}^2$ along the $[001]_{PC}$ orientation [183]) of KNLTNS single crystals are currently still under discussions. In the present section, an annealing process is employed in order to investigate the improvement of the electrical performance. Annealing was performed at 900 °C in pure O_2 atmosphere for one week.

Figure 5.11 presents the temperature-dependent dielectric permittivity and dielectric losses of two $[001]_{PC}$ -oriented single crystals with Sb: (a, c) non-annealed, and (b, d) annealed in O_2 . Phase transition temperatures T_{O-T} and T_C remained almost the same, whereas an increase of the permittivity was observed for the annealed sample. The noticeable decrease of the high-temperature dielectric losses after annealing indicates the changed defect state of the sample. The anomaly in the dielectric losses of the non-annealed sample at approximately 450 °C shows a strong frequency dependence and increases at lower frequencies, indicating that the conductivity behaviour of the KNLTNS single crystal is related to low-frequency relaxation processes [227]. This relaxation behaviour becomes weaker after annealing.

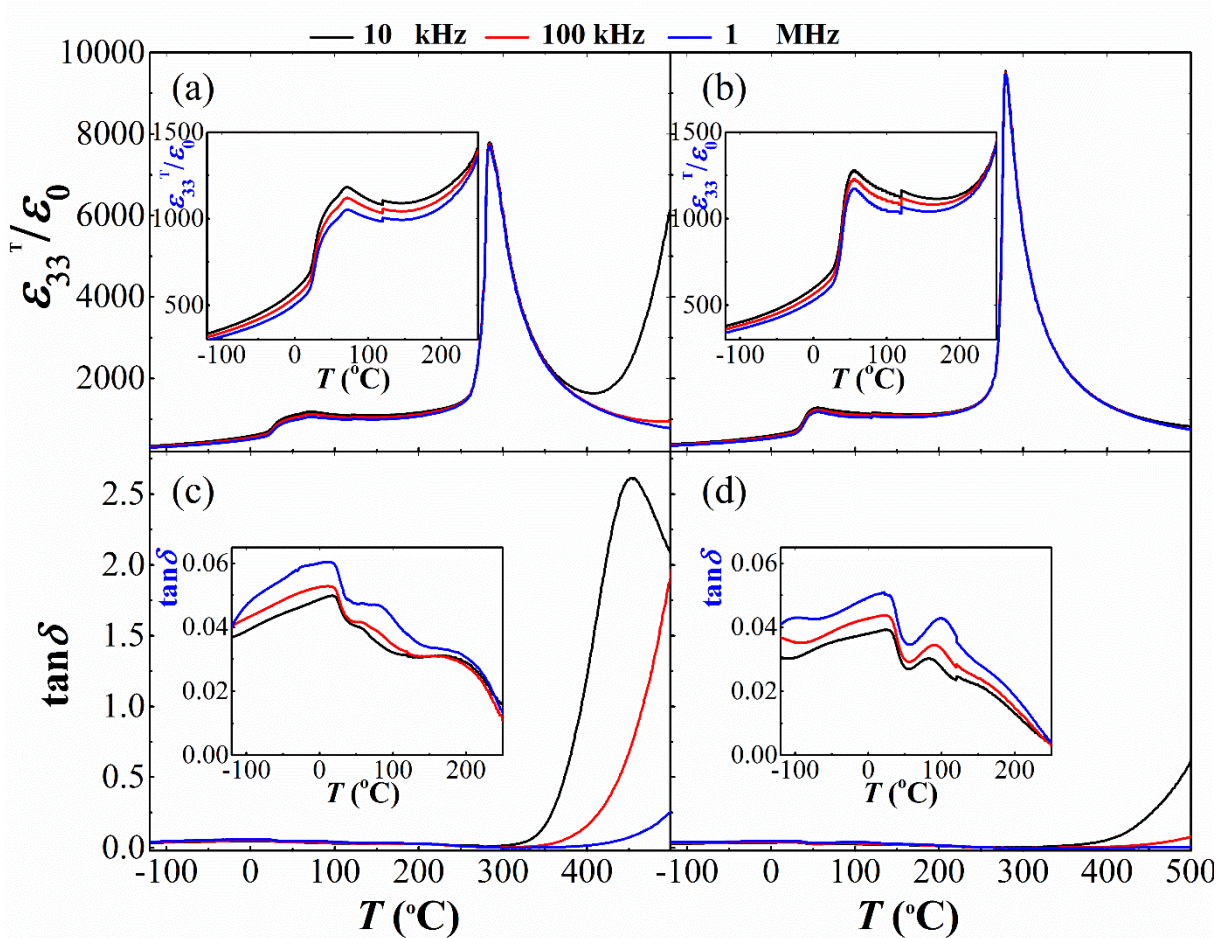


Figure 5.11. Temperature-dependent dielectric permittivity and losses for (a, c) non-annealed, and (b, d) annealed $[001]_{PC}$ -oriented KNLTNS samples. The insets are the enlarged regions from $-120\text{ }^{\circ}\text{C}$ to $250\text{ }^{\circ}\text{C}$.

5.2.3 Electromechanical Properties

Temperature-dependent Large-signal Polarization Hysteresis

P - E loops at various temperatures for the non-annealed $[001]_{PC}$ -oriented KNLTNS single crystal are presented in Figure 5.12. Field amplitudes were selected to be 0.5, 1, 1.5, 2, and 3 kV/mm, at a frequency of 1 Hz. The investigated temperature range is from room temperature to $170\text{ }^{\circ}\text{C}$, during which the crystallographic phase of the KNLTNS crystal changes from orthorhombic to tetragonal. At $20\text{ }^{\circ}\text{C}$, a contribution from high leakage current is observed in the P - E loop and prevents the evaluation of the remanent polarization P_r and coercive field E_c . When the temperature approaches $30\text{ }^{\circ}\text{C}$, the P - E loop becomes narrower and the leakage current contribution decreases to a negligible level. This is in agreement with the relatively high dielectric losses in the orthorhombic phase for the non-annealed

sample in the inset of Figure 5.11 (c). The phenomenon has been also observed in several polycrystalline ceramics [118,228]; however, the origin of this behaviour is still not understood and requires further studies.

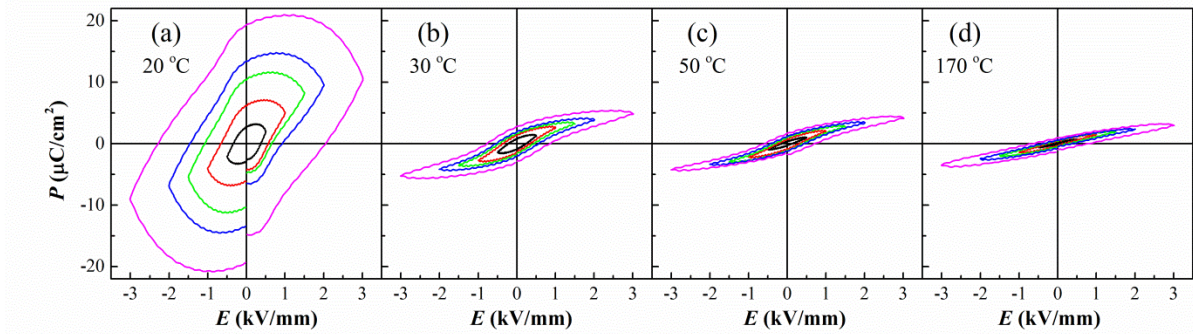


Figure 5.12. P - E loops for the non-annealed $[001]_{PC}$ -oriented KNLTNS single crystal state at various temperatures ($f=1$ Hz).

Figure 5.13 provides the temperature-dependent large-signal P - E loops for the annealed $[001]_{PC}$ -oriented KNLTNS single crystal. Enhanced ferroelectric properties with rectangular shaped loops and better temperature stability are obtained in the annealed samples.

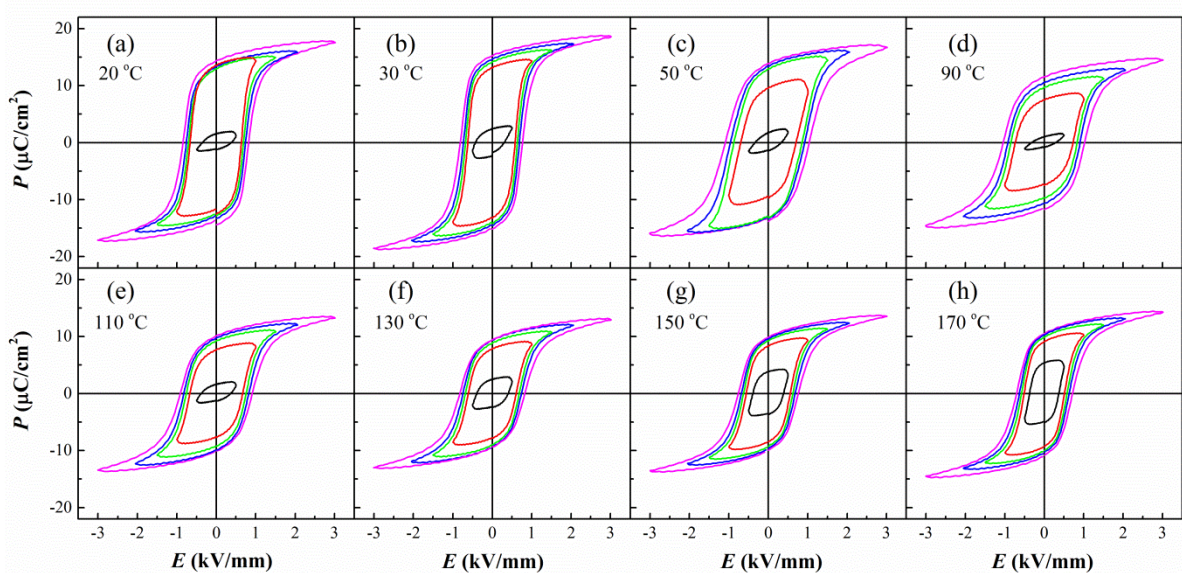


Figure 5.13. P - E loops for the annealed $[001]_{PC}$ -oriented KNLTNS single crystal state at various temperatures ($f=1$ Hz).

Figure 5.14 summarizes the temperature-dependent maximum polarization P_{\max} , remanent polarization P_r , and coercive field E_C of non-annealed and annealed KNLTNS single crystals, and of the KNLTN (non-annealed, N8) crystal along the $[001]_{\text{PC}}$ orientation at 3 kV/mm. Note that the latter was measured at a higher frequency (20 Hz) due to a higher leakage current contribution.

The non-annealed KNLTNS sample reveals slightly lower P_{\max} and P_r , as shown in Figure 5.14 (a) and (b). For the KNLTN sample, maximum P_{\max} and P_r values are achieved at 90 °C, which is in the vicinity of its $T_{\text{O-T}}$ (94 °C in Figure 5.10 (a)). However, no enhancement of P_{\max} and P_r is observed at $T_{\text{O-T}}$ (50 °C) in the non-annealed KNLTNS sample. Overall, no obvious changes in P_{\max} and P_r are obtained after the substitution of 6.7 % Sb on the B site before annealing, although trends for both KNLTN and KNLTNS single crystals are not the same. On the other hand, the temperature stability of polarization was improved with the substitution of Sb. The coercive field E_C (see Figure 5.14 (c)) of the KNLTN sample (non-annealed) is higher than that of the non-annealed KNLTNS sample from 50 °C to 100 °C.

The P_{\max} and P_r of the annealed KNLTNS sample are about 3–5 times higher compared to the non-annealed sample, which can be seen in Figure 5.14 (a) and (b). In fact, the P_{\max} and P_r of the annealed KNLTNS single crystal at 0.5 kV/mm are comparable to the non-annealed sample at 3 kV/mm (Figure 5.12 (Page 90) and Figure 5.13 (Page 90)). With increasing temperature, the P_{\max} and P_r first increase and then decrease above 50 °C. From 130 °C to 170 °C, both P_{\max} and P_r increase again slightly. The maximum of P_{\max} and P_r at 50 °C is ascribed to the orthorhombic-tetragonal phase transition, resulting from the larger number of spontaneous polarization directions in the orthorhombic phase. The increase of both P_{\max} and P_r above 130 °C originates from the reduced E_C and the non-saturated state at 3kV/mm, which enables more domain switching events.

At 30 °C, coercive fields of both non-annealed and annealed KNLTNS samples are close to each other. The coercive field for the non-annealed sample decreases above 30 °C, while the values of the annealed crystal are 1.3–1.4 times higher. However, the coercive field of the annealed sample decreases from 20 °C to 30 °C, increases from 30 °C to 70 °C, and then decreases again. The local minimum at 30 °C is ascribed to the orthorhombic-tetragonal phase transition. In the proximity of $T_{\text{O-T}}$, coercive field decreases with temperature in the orthorhombic phase side but increases with temperature in the tetragonal phase side. This is explained by the relatively lower lattice distortion of the orthorhombic phase, as compared to the tetragonal phase [219].

The comparison of ferroelectric properties between the non-annealed and annealed KNLTNS single crystals indicates that the annealing process in O_2 is effective to enhance the ferroelectric properties of this system, as compared to the chemical substitution. Several KNN-based single crystals reported in the literature show a high piezoelectric coefficient but low P_{\max} and P_r [70,184]. For example, Chen *et*

al. [70] reported a KNN single crystal with a piezoelectric coefficient of 405 pC/N but a P - E loop with high leakage current (Figure 2.18, Page 33). Huo *et al.* [184] reported a Mn-doped KNLTN single crystal with a piezoelectric coefficient of 630 pC/N but a P_r of 3.45 $\mu\text{C}/\text{cm}^2$.

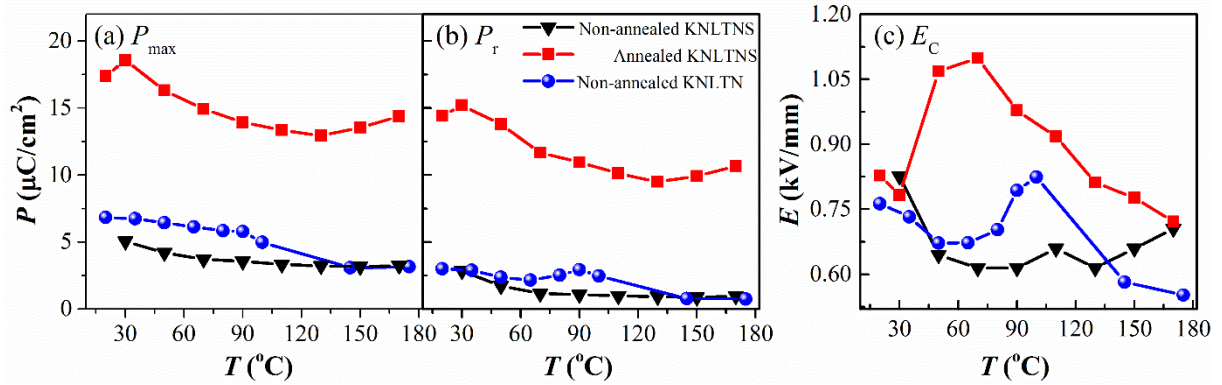


Figure 5.14. Temperature-dependent parameters extracted from P - E loops for the non-annealed and annealed $[001]_{\text{PC}}$ -oriented KNLTNS ($f=1$ Hz) and non-annealed $[001]_{\text{PC}}$ -oriented KNLTN ($f=20$ Hz) single crystal samples at 3 kV/mm: (a) maximum polarization P_{\max} , (b) remanent polarization P_r , and (c) coercive field E_c .

Temperature-dependent Large-signal Strain Curves

The large-signal electric field-induced strain curves for both the non-annealed and annealed $[001]_{\text{PC}}$ -oriented KNLTNS single crystal samples were measured at various temperatures and are presented in Figure 5.15. The electric field-induced strain increases almost 3 times after the annealing process, especially above 30 $^{\circ}\text{C}$. For the non-annealed sample, the maximum positive strain (S_{pos}) at the maximum field (E_{max}) decreases with temperature and the absolute minimum negative strain ($-S_{\text{neg}}$) is much lower than S_{pos} . Note that a strong asymmetry of the curves is observed in the orthorhombic phase, which is strongly reduced in the tetragonal phase above 50 $^{\circ}\text{C}$.

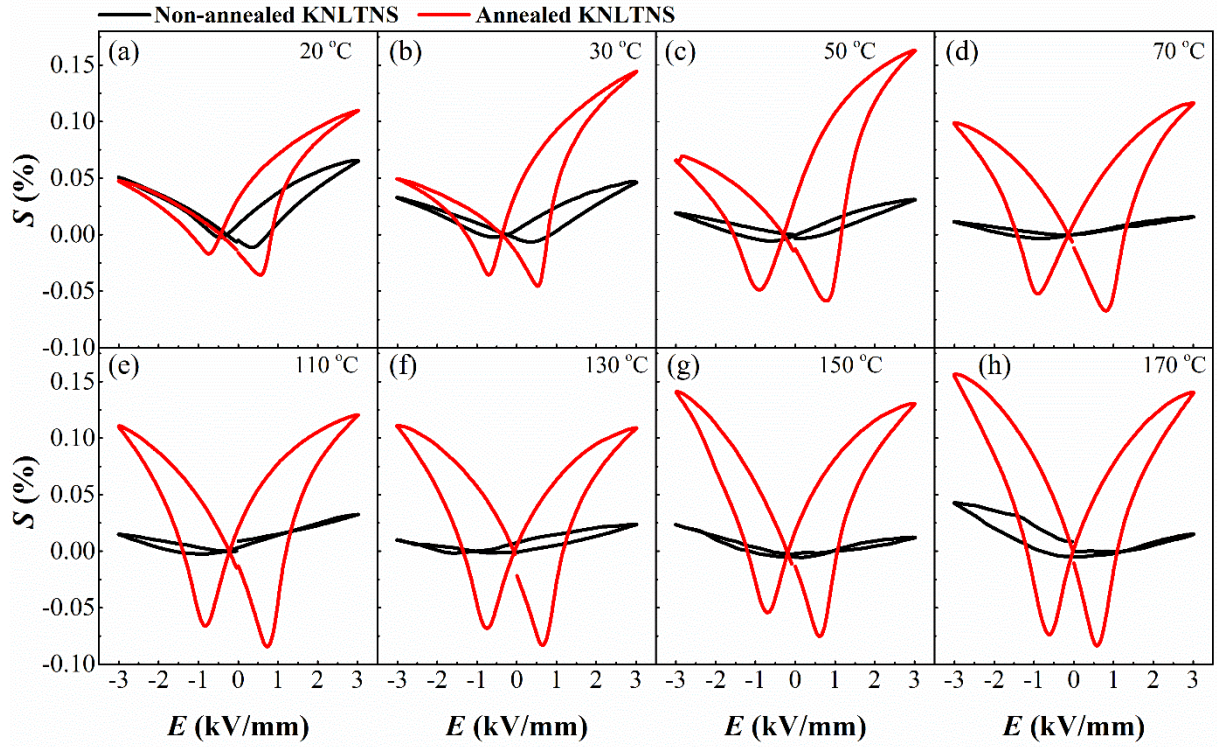


Figure 5.15. S - E curves for both non-annealed and annealed $[001]_{PC}$ -oriented KNLTNS single crystal state at various temperatures.

Figure 5.16 presents the changes of the maximum positive strain (S_{pos}), absolute negative strain ($-S_{neg}$) and the ratio between $-S_{neg}/S_{pos}$ of the annealed KNLTNS single crystal sample at different temperatures. Note that only the values at positive fields are used for this discussion because of the asymmetric curves. The S_{pos} reaches a maximum (0.16 %) at 50 °C at the tetragonal side of the T_{O-T} . However, a remarkable change in the increase rate below and above T_{O-T} is observed. The $-S_{neg}$ keeps increasing from room temperature to 110 °C, followed by a slight decrease above 110 °C. The S_{pos} and S_{neg} of the annealed $[001]_{PC}$ -oriented KNLTNS single crystal are in the range of 0.11–0.16 % and 0.01–0.08 %, which are suitable for piezoelectric applications. It is a great challenge to explain the trend of $-S_{neg}/S_{pos}$ ratio in the whole temperature range, which depends on the composition, defects, crystalline quality, and other factors. Based on the strain results of the annealed KNLTNS single crystal (Figure 5.16) and the non-annealed KNLTN single crystal (Figure 5.9, Page 86), it is concluded that $-S_{neg}/S_{pos}$ ratio keeps increasing with temperature in the orthorhombic phase and $-S_{neg}/S_{pos}$ is higher in the tetragonal phase than in the orthorhombic phase in the vicinity of T_{O-T} for the samples with the $[001]_{PC}$ orientation. This is believed to originate from the different contributions from 180 ° and non-180 ° domain switching when the angle between the electric field and spontaneous polarization changes, which will be discussed in detail in Chapter 6.

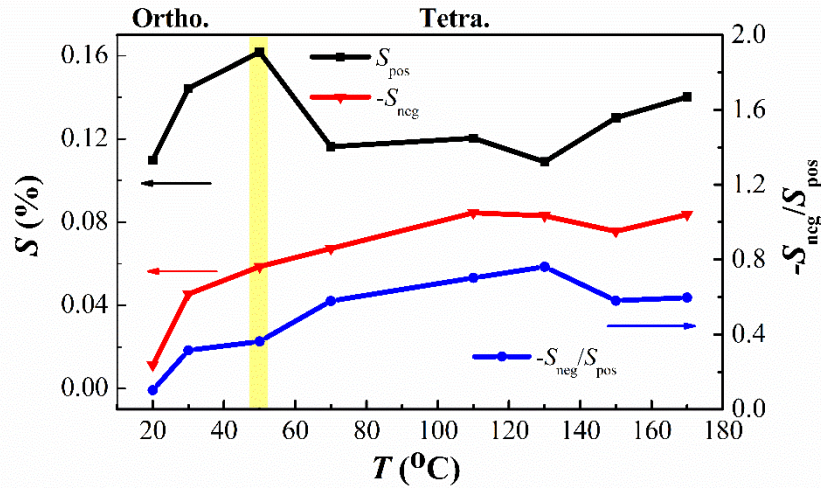


Figure 5.16. Temperature dependent S_{pos} (maximum positive strain), $-S_{neg}$ (minimum negative strain) and the ratio between $-S_{neg}/S_{pos}$ for the annealed $[001]_{PC}$ -oriented KNLTNS single crystal sample.

The unipolar strain curves of both non-annealed and annealed KNLTNS single crystals are shown in Figure 5.17 (a) and (b), which were measured at 3 kV/mm and 2 Hz. The maximum unipolar strain S_{max} and the calculated large-signal converse piezoelectric constants d_{33}^* are summarized in Figure 5.17 (c), respectively. Both S_{max} and d_{33}^* of the non-annealed sample initially decrease with temperature and then slightly increase above 70 °C. The low S_{max} and d_{33}^* values of the non-annealed sample may result from the difficulty in poling under AC fields. On the other hand, the annealed crystal exhibits larger S_{max} and d_{33}^* . The largest S_{max} and d_{33}^* values for the annealed sample are achieved at 170 °C, which are 0.16 % and 530 pm/V, respectively. The local maximum S_{max} and d_{33}^* at 50 °C for the annealed sample are 0.12 % and 390 pm/V, respectively. Note that the annealed sample shows good temperature stability of unipolar S_{max} and d_{33}^* from 20 °C to 150 °C, which is important for many piezoelectric applications.

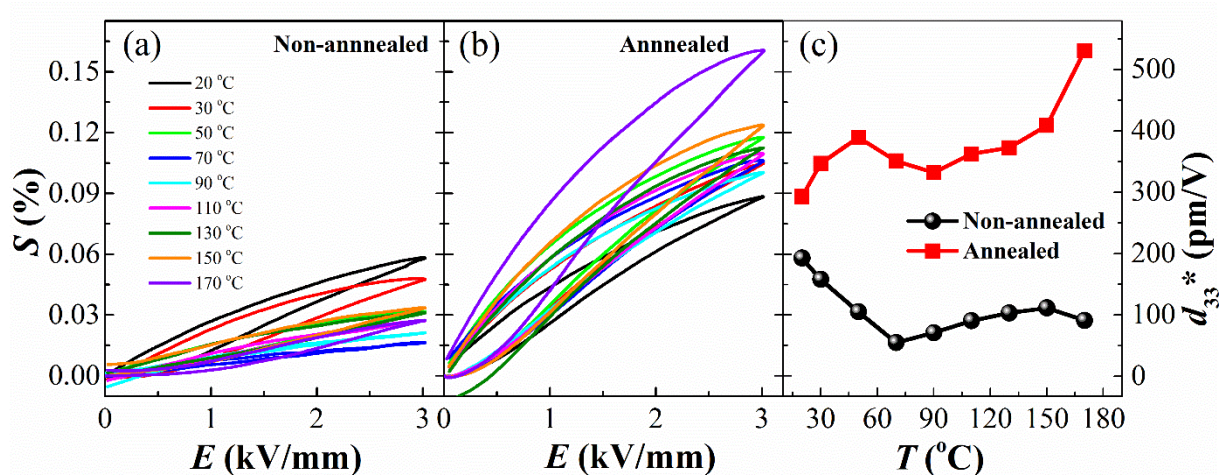


Figure 5.17. Temperature-dependent unipolar strain curves of (a) non-annealed and (b) annealed $[001]_{PC}$ -oriented KNLTNS single crystals. (c) Temperature-dependent maximum unipolar strain and converse piezoelectric coefficient of both $[001]_{PC}$ -oriented samples.

Small-signal Field-dependent Permittivity and Piezoelectric Coefficients at Different Temperatures

Figure 5.18 provides the small-signal field-dependent permittivity $\epsilon_{33}'/\epsilon_0$ and piezoelectric coefficient d_{33}^* of non-annealed and annealed $[001]_{PC}$ -oriented KNLTNS single crystals at various temperatures. The small-signal field dependence of both, permittivity and piezoelectric coefficient curves, is ascribed predominantly to the reversible processes due to the low excitation field amplitude.

The non-annealed sample reveals relatively stable field-dependent permittivity curves from 20 °C to 50 °C (Figure 5.18 (a)-(e)). Afterwards, the permittivity curves start to shift to higher values. Although the values in the orthorhombic phase of the annealed sample are similar to the non-annealed one (at 20 °C and 30 °C), additional local minima are detected at the coercive field, which disappear above 50 °C. Unlike the non-annealed sample, the permittivity curves of the annealed sample shift to lower values at 90 °C and then to higher values at 170 °C. Small-signal field-dependent permittivity is believed to be related to domain wall density and domain wall mobility [229,230]. The stable permittivity of both non-annealed and annealed sample below T_{O-T} indicates the relatively stable domain movement and domain configuration in the orthorhombic phase. The upward shift of the permittivity for the non-annealed sample is ascribed to the increased mobility of domain walls above T_{O-T} at higher temperatures. For the annealed sample, the domain wall density is reduced above T_{O-T} due to the higher amount of macro domains in the pure tetragonal phase, resulting in a lower permittivity. On the other hand, when the

temperature is high enough, the domain wall mobility is largely increased and contributes to the overall permittivity, resulting in a considerable increase of the latter at 170 °C. As compared to the non-annealed crystal, the lower permittivity of the annealed sample above 90 °C is ascribed to the easier poling process and therefore the lower domain wall density after poling.

Temperature dependence of small-signal field-dependent piezoelectric coefficient curves of both samples are presented in Figure 5.18 (f)-(j). At a given temperature, the annealed [001]_{PC}-oriented KNLTNS single crystal reveals much higher piezoelectric coefficients than the non-annealed one. The enhanced piezoelectric coefficients at 170 °C in the annealed sample is related to the easier mobility of domain walls at high temperatures.

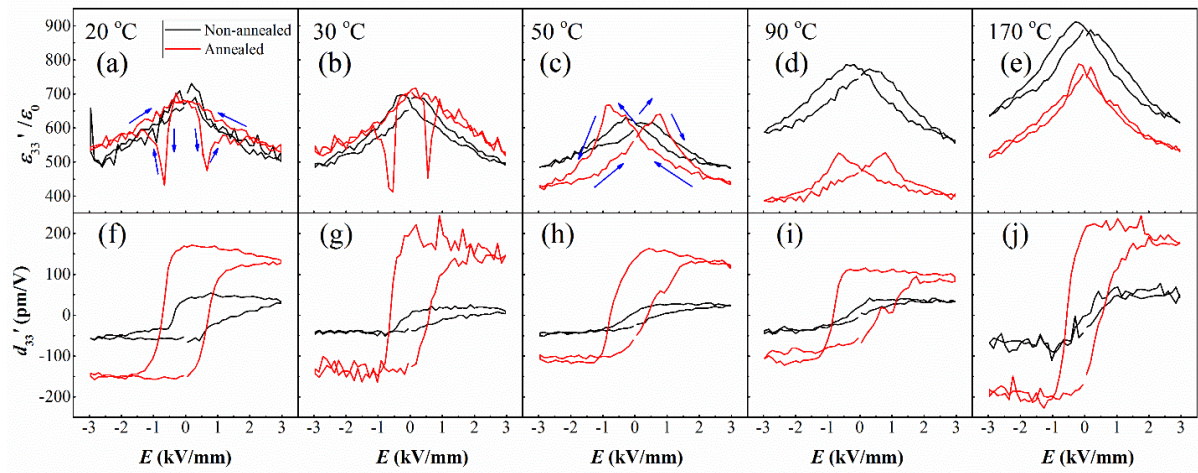


Figure 5.18. Small-signal field-dependent permittivity $\epsilon_{33}'/\epsilon_0$ and piezoelectric coefficients d_{33}' of non-annealed and annealed [001]_{PC}-oriented KNLTNS single crystal states at various temperatures. The arrows in (a) and (c) show the direction of electric field loading processes.

Room Temperature Large-signal Polarization Hysteresis Curves

Figure 5.19 displays large-signal bipolar and unipolar polarization hysteresis P - E and S - E curves of both [001]_{PC}-oriented KNLTNS single crystal states at room temperature. Prior to the measurements, samples were poled at 3 kV/mm and 100 °C for 30 min. The non-annealed [001]_{PC}-oriented sample exhibits a slanted hysteresis loop with remanent polarization P_r of 10 $\mu\text{C}/\text{cm}^2$ and coercive field E_c of 0.6 kV/mm (Figure 5.19 (a)). On the other hand, a rectangular P - E loop with a P_r of 24.5 $\mu\text{C}/\text{cm}^2$ and a coercive field E_c of 0.6 kV/mm is obtained after annealing in O_2 . It should be noted that this P_r is much higher than those previously reported for the [001]_{PC}-oriented single crystals with similar compositions [173,183]. The saturated polarization (P_s) of the annealed [001]_{PC}-oriented sample is estimated to be approximately 26.1 $\mu\text{C}/\text{cm}^2$ (see Figure 5.19 (c)). Room temperature P - E loops after DC poling at 3

kV/mm show that the P_r and P_{max} in the annealed KNLTNS sample are twice as large as in the non-annealed one.

As shown in Figure 5.19 (b), the unipolar P - E loops display a strong hysteresis in the non-annealed sample but almost zero hysteresis in the annealed one during the second electric field loading cycle. This is an evidence for the much higher degree of poling in the annealed sample than in the non-annealed sample.

The bipolar and unipolar S - E curves of both $[001]_{PC}$ -oriented KNLTNS single crystal states are displayed in Figure 5.19 (d) and (e). Both bipolar and unipolar strain curves of the non-annealed $[001]_{PC}$ -oriented sample are nonlinear. However, the annealed sample presents a linear bipolar strain for $E > \pm 1$ kV/mm in Figure 5.19 (d), as well as a linear second cycle unipolar strain curve in Figure 5.19 (e). The maximum bipolar and unipolar strains at 4 kV/mm of the non-annealed $[001]_{PC}$ -oriented sample reach 0.143 % and 0.13 %, respectively. The corresponding values of the $[001]_{PC}$ -oriented annealed sample increase to 0.195 % and 0.2 %, respectively.

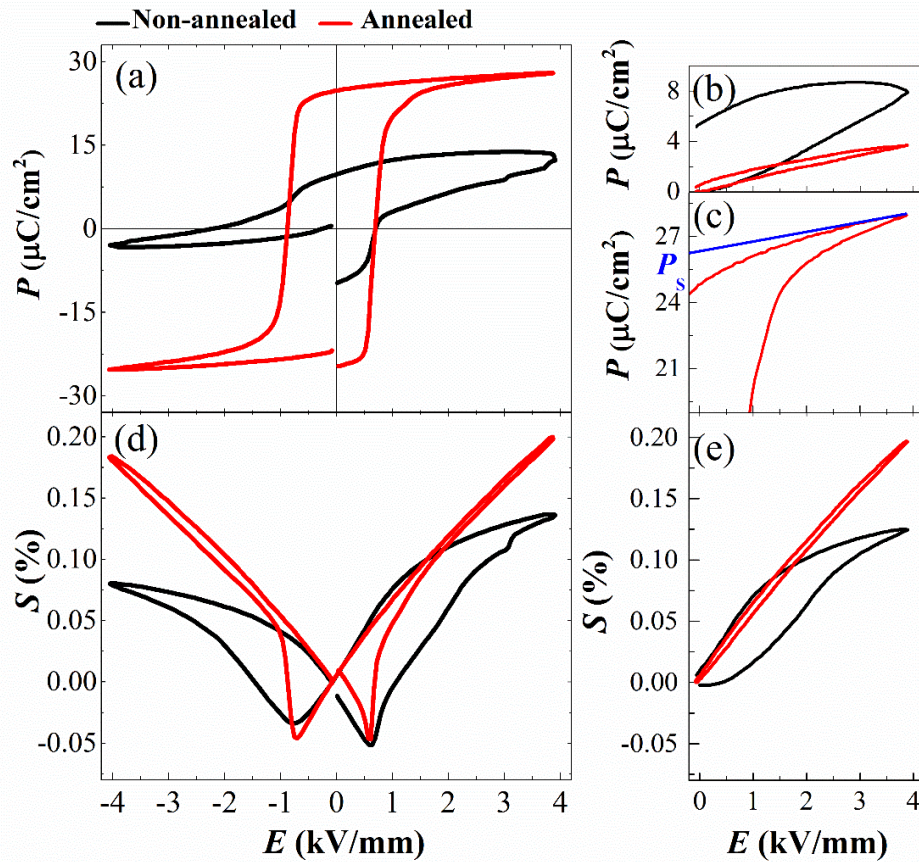


Figure 5.19. (a) Bipolar and (b) unipolar P - E , (c) enlarged bipolar P - E , and (d) bipolar and (e) unipolar S - E curves of both $[001]_{PC}$ -oriented KNLTNS single crystal states at room temperature (2nd electric field loading cycles; measured frequencies: 1 Hz for the bipolar and 2 Hz for the unipolar cycles).

Note that P - E loops of the non-annealed $[001]_{\text{PC}}$ -oriented KNLTNS sample in Figure 5.12 (a) (Page 90) and Figure 5.19 (a) are different from each other, which indicates irreversible processes during electrical measurements. The samples were poled at 3 kV/mm prior to the measurement in Figure 5.19 (Page 97) and subsequently depolarized by other temperature-dependent electrical measurements before performing the measurements shown in Figure 5.12 (Page 90). This phenomenon was observed in several crystals and resembles fatigue processes [231], such as charge accumulation or microcracking, and requires further investigation. Similar phenomenon also happens in the annealed sample.

Room Temperature Piezoelectric Coefficients

The large-signal converse piezoelectric coefficients d_{33}^* along the $[001]_{\text{PC}}$ orientation, calculated as unipolar $S_{\text{max}}/E_{\text{max}}$ (red curve in Figure 5.4 (b) on Page 81 and curves in Figure 5.19 (e)), are 221 pm/V for the non-annealed KNLTN (N8), 320 pm/V for the non-annealed KNLTNS (N11-Sb), and 505 pm/V for the annealed KNLTNS (N11-Sb) single crystal samples.

Their small-signal direct piezoelectric coefficient d_{33} along the $[001]_{\text{PC}}$ orientation, measured by the Berlincourt method after being poled at 3 kV/mm, are 180 pC/N, 284 pC/N, and 450 pC/N, respectively. The samples were poled at 3 kV/mm and 100 °C prior to the measurement.

The 6.7 % Sb substitution increases the large-signal converse piezoelectric coefficient d_{33}^* by approximately 45 % and the small-signal direct piezoelectric coefficient by 58 %, due to a decrease of the $T_{\text{O-T}}$ (close to room temperature). The one-week annealing process increases both the large- and small-signal piezoelectric coefficient by approximately 50 %, resulting from the decrease of conductivity.

Temperature-dependent Small-signal Piezoelectric Coefficients

Figure 5.20 shows temperature-dependent piezoelectric coefficients d_{33} for both non-annealed and annealed $[001]_{\text{PC}}$ -oriented KNLTNS single crystal samples. At room temperature, the piezoelectric coefficients are 381 pC/N and 732 pC/N, respectively. To the author's knowledge, the latter value is the highest room temperature value reported in KNN-based single crystals so far. Note that these values are also higher as compared to the piezoelectric coefficients reported for both samples in the previous section of this chapter. The reason for this are the different poling conditions used in both cases. Both samples presented in this section were first poled at room temperature with 3 kV/mm for 30 min, then kept at 80 °C for 30 min with 3 kV/mm, and subsequently field-cooled. The measurements were performed after 24 h aging. This indicates the importance of the poling conditions [232] of the KNN-based single crystals; however, the study of these was out of the scope of this work.

When the temperature increases to T_{O-T} , the maximum piezoelectric constants of 1431 pm/V and 464 pm/V are achieved for annealed and non-annealed samples. The significant drop above T_{O-T} is ascribed to the depolarization at the orthorhombic-tetragonal phase transition [233].

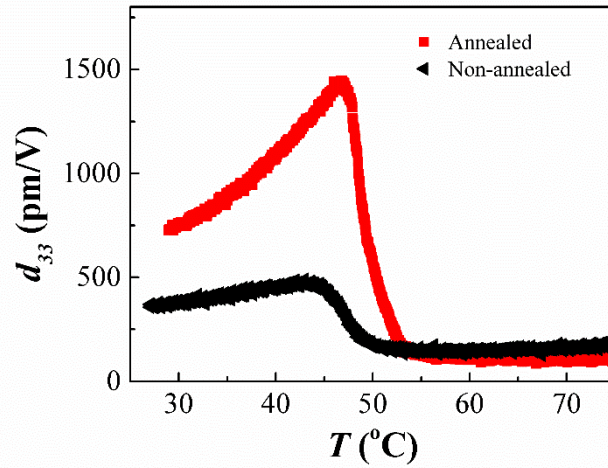


Figure 5.20. Temperature-dependent piezoelectric coefficients d_{33} of non-annealed and annealed $[001]_{pc}$ -oriented poled KNLTNS single crystal samples, measured at 8 V/mm and 1 kHz.

5.2.4 ^{121}Sb Mössbauer Spectra

Figure 5.21 shows ^{121}Sb Mössbauer spectra of both samples of crushed KNLTNS single crystals at -173 °C: (a) non-annealed and (b) annealed. Table 5.3 provides the fitted parameters. Two distinct components exhibit very different values of the isomer shift δ referring to the $\text{Ca}^{121m}\text{SnO}_3$ source. The main peak with δ of about 0.5 mm/s is typical of Sb^{5+} octahedrally coordinated to oxygen, while the other peak with δ of about -15 mm/s corresponds to the presence of Sb^{3+} [234]. The large negative value of Sb^{3+} , which possesses $5s^2$ lone-pair electrons, is ascribed to the negative sign of the change in the nuclear radius between the nuclear excited and ground states, as well as the relatively higher value of the overall electron density, as compared to Sb^{5+} [235]. Moreover, the different shapes of the observed peaks indicate the different strength of the electric quadrupole hyperfine interaction in the Sb^{5+} and Sb^{3+} species. According to the fact that the quadrupole coupling constant $eV_{zz}Q_{5/2}$ of the dominated peak is close to 0, the octahedral sites occupied by Sb^{5+} are inferred as possessing a virtually undistorted local environment. On the contrary, the large positive $eV_{zz}Q_{5/2}$ of the weaker peak implies a stereochemically-active behaviour of the lone-pair electrons on Sb^{3+} . This implies the low coordination number of the sites occupied by Sb^{3+} species. This “discrepancy” is indeed not surprising, taking into account the

expected location of Sb^{3+} at bulk sites in the case of $(\text{K}_{0.287}\text{Na}_{0.691}\text{Li}_{0.022})(\text{Ta}_{0.063}\text{Nb}_{0.870}\text{Sb}_{0.067})\text{O}_3$ single crystal. It is therefore concluded that Sb ions in KNLTNS crystals are located in both, the octahedral B site and similar B-site environments with a lack of oxygen, even after O_2 annealing. It is an indicative of the existence of the dipole association $(\text{Sb}(\text{III})_{\text{B}}^{\prime\prime}-\text{V}_{\text{O}}^{\prime\prime})$.

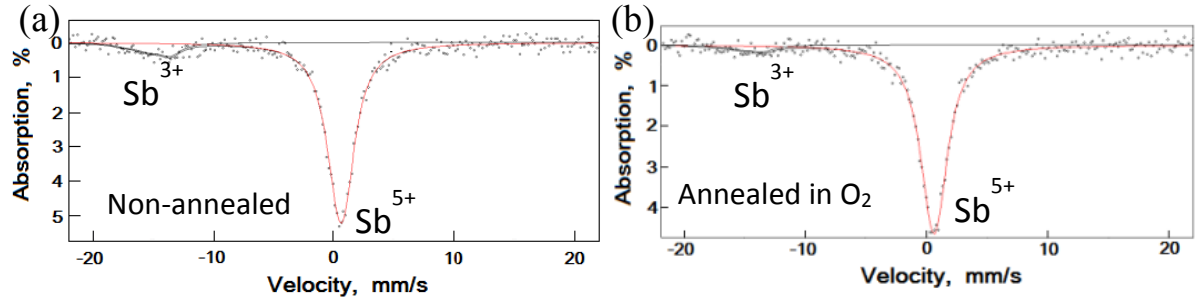


Figure 5.21. ^{121}Sb Mössbauer spectra of powders of the (a) non-annealed and (b) annealed KNLTNS samples, measured at $-173\text{ }^\circ\text{C}$.

Table 5.3. ^{121}Sb Mössbauer parameters for crushed KNLTNS crystals measured at $-173\text{ }^\circ\text{C}$.

Samples	Sb species	Isomer shift δ (mm/s)	Quadrupole coupling constant $eV_{zz}Q_{5/2}$ (mm/s)	Full width at half maximum Γ (mm/s)	Relative area A (%)
Non-annealed KNLTNS	Sb^{5+}	0.51 ± 0.05	3.2 ± 1	2.3 ± 0.2	90 ± 3
	Sb^{3+}	-14.8 ± 0.6	14.1 ± 5	2.2 ± 0.2	10 ± 5
Annealed KNLTNS (in O_2)	Sb^{5+}	0.53 ± 0.05	2.6 ± 1.0	2.5 ± 0.2	95 ± 3
	Sb^{3+}	-14.6 ± 0.9	13 ± 6	2.2 ± 0.1	5 ± 4

Note that the limitation of permittivity measurements (see Figure 5.11, Page 89) prevented the determination of the rhombohedral to orthorhombic phase transition temperature $T_{\text{R-O}}$. Based on the Raman spectroscopy, Trodahl *et al.* [236] reported the rhombohedral phase in $(\text{K}_{0.5}\text{Na}_{0.5})_{0.98}\text{Li}_{0.02}\text{NbO}_3$ polycrystalline ceramics to appear at about $-123\text{ }^\circ\text{C}$. Moreover, the addition of Sb ions rapidly increases the $T_{\text{R-O}}$ [102,237]. It is therefore assumed that the KNLTNS single crystal investigated in this work is in the rhombohedral phase at $-173\text{ }^\circ\text{C}$. Despite the structural change from orthorhombic to rhombohedral phase upon cooling, the chemical states of Sb species are believed to remain the same as at room temperature. Simultaneously, the signals of Sb^{5+} and Sb^{3+} in the ^{121}Sb Mössbauer spectra are more distinguished and visible at a lower temperature.

5.2.5 Mechanism of Enhanced Electrical Properties after Annealing in O₂

The permittivity, ferroelectric, and piezoelectric properties of the KNLTNS single crystal have been improved remarkably after the annealing in O₂. This is an indication for the existence of defects in the as-grown KNLTNS single crystals, which could have 4 possible origins.

The volatilization of the A-site ions (Li, Na, and K ions) during the high temperature process creates A-site vacancies [11,187], as expressed by the following equation with Kröger-Vink notation [27],



In addition, oxygen vacancies are also expected to be present in the KNLTNS single crystal [238,239] during high temperature growth process, following the mechanism,



The third defect type are substituted centers, originating from the multi oxidation states of B-site ions. The oxidation states of Sb ions in KNN-based piezoelectric system were not reported in the literature so far. Note that X-ray photoelectron spectroscopy cannot be used to elucidate Sb oxidation states, due to the overlapping peaks of Sb⁵⁺ and O²⁻ [240]. As an effective method to measure the oxidation state, ¹²¹Sb Mössbauer spectra in Figure 5.21 (a) (Page 100) and Table 5.3 (Page 100) show that the main oxidation state of Sb in the as-grown KNLTNS single crystal is Sb⁵⁺ and 10 % of Sb is present as Sb³⁺. Kizaki *et al.* [187] held the opinion that the Nb⁴⁺ state also appears in as-grown (K,Na)NbO₃ single crystals, however, no direct observation has been reported so far. The two types of substituted centers correspond to the two processes:



The last defect types highlighted here are those defects originating from flux inclusions, dislocations, twinning and cracks in single crystalline form [241,242].

As shown in Equations 5.7, 5.9 and 5.10, the presence of A-site vacancies and B-site substituted centers is accompanied by the formation of holes for charge compensation, which therefore increases the concentration of oxygen vacancies.

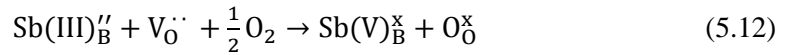
To conclude, there are two origins of oxygen vacancies in the as-grown KNLTNS single crystal: the intrinsic, due to the high temperature growth process, and the extrinsic, induced by the presence of A-

site vacancies and B-site substituted centers to compensate charges. The high concentration of oxygen vacancies is therefore believed to be responsible for high electrical conductivity of as-prepared KNN-based materials [128,170,243,244,245,246].

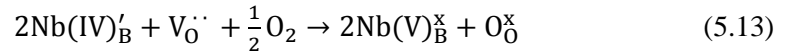
During the annealing process in O₂, the concentration of oxygen vacancies is decreased due to its defect reaction with O₂ and trapped electrons, as described by,



In addition, Mössbauer spectroscopy data in Figure 5.21 (b) and Table 5.3 (Page 100) indicate that the concentration of Sb³⁺ ions decreased by 50 % after the annealing process. This is related to the defect reaction between Sb(III)_B'' center and oxygen vacancy V_O^{··}.



As reported previously [160], the oxidization of Nb⁴⁺ ions may also occur during the annealing process in O₂, as described by Equation (5.13).



The two processes described in Equations (5.12) and (5.13) thus further decrease the concentration of oxygen vacancies in KNLTNS crystals during the annealing process.

The annealed KNLTNS crystal still shows enhanced conductivity at high temperatures, which is evident in Figure 5.11 (b) and (d) (Page 89). This originates from the fact that Sb³⁺ ions were not completely oxidized to Sb⁵⁺ and that A-site vacancies were not removed during annealing in O₂. Previous experimental work of Kizaki *et al.* [187] showed dramatically decreased leakage current densities in pure KNN single crystals after annealing both in air and 35 MPa oxygen pressure. It is believed that the defect concentration in the KNN single crystal relies on both the annealing temperature and oxygen partial pressure. It should be noted that the thermodynamically stable conditions for defects in KNLTNS single crystals (both oxygen vacancy and Sb(III)_B'' center) in the present work are not clear. Further annealing experiments under various oxygen partial pressures and annealing temperatures are therefore necessary to obtain thermodynamically stable defects and validate the proposed mechanisms.

Several mechanisms have been proposed to clarify the influence of defects on the ferroelectric and piezoelectric behaviour. Defects in ferroelectrics are often energetically favourable at or near the domain walls [247,248,249]. After being annealed in O₂, the sample shows decreased concentration of defects, which may reduce the interactions with domain walls and thus increase the contribution of domain walls to the ferroelectric and piezoelectric properties [250]. The defect complex, consisting of at least one

negatively charged defect center and one positively charged center, can reduce the total polarization [251]. The decreased concentration of defect dipoles after annealing in O₂ enhances reversible domain switching and domain growth. Fan *et al.* [252] observed the re-construction of domains in Pb[(Zn_{1/3}Nb_{2/3})_{0.5}(Zr_{0.47}Ti_{0.53})_{0.5}]O₃ ceramics after thermal annealing by TEM. The sample had a needle-like domain structure after being annealed in Ar, but exhibited a lamellar domain structure after annealing in O₂. The needle-like domain structure was related to charged domain walls [253] induced by the high concentration of defects, especially oxygen vacancies. Note that needle-like domain walls are charged, while twin-like domain walls are typically neutral. The charged domain walls in non-annealed sample are believed to additionally decrease the polarization. Further analysis using local techniques, such as piezoresponse force microscopy, is necessary to confirm this hypothesis.

5.2.6 Summary

The room-temperature and temperature-dependent ferroelectric and piezoelectric properties were investigated in the [001]_{PC}-oriented KNLTNS single crystals before and after one-week annealing in O₂. More than a 2 times increase of polarization and piezoelectric properties were achieved in the annealed sample, as compared to the non-annealed one. The room temperature *P-E* loop with a remanent polarization of 24.5 μC/cm² and a spontaneous polarization of 26.1 μC/cm² were obtained in the annealed sample. In addition, a very high room temperature piezoelectric coefficient of 732 pC/N was obtained. The annealed KNLTNS single crystal shows better temperature stability of the remanent polarization and strain (bipolar and unipolar). Maximum polarization, remanent polarization, maximum positive and negative strain, and piezoelectric coefficient reach the maximum value in the vicinity of the orthorhombic-phase transition temperature.

The enhanced electrical properties originate from the decrease of defect concentrations after annealing. The present work reveals the existence of Sb³⁺ in the as-grown KNLTNS single crystal and the decrease of Sb³⁺ after annealing by the Mössbauer spectra. The annealing process decreases the concentration of oxygen vacancies and Sb(III)_B^{''} centers. This improves the domain mobility processes, as evident by the increased field-dependent small-signal piezoelectric coefficients.

5.3 Influence of Mn Doping

Figure 5.22 shows XRD patterns of powders of crushed crystals without Mn (N1 crystal; $(\text{K}_{0.612}\text{Na}_{0.359}\text{Li}_{0.029})(\text{Ta}_{0.024}\text{Nb}_{0.976})\text{O}_3$) and with Mn doping (N2-Mn crystal; $(\text{K}_{0.637}\text{Na}_{0.334}\text{Li}_{0.029})(\text{Ta}_{0.0229}\text{Nb}_{0.9768}\text{Mn}_{0.0003})\text{O}_{2.99955}$). The intensity ratio of two peaks at about $2\theta = 45^\circ$ (I_{022}/I_{200}) is approximately 2, confirming the orthorhombic symmetry in both crystals. No secondary phase is observed. It is found that peak positions move to lower 2θ values after Mn doping, as an evidence of the incorporation of the Mn ions into the perovskite structure and the resulting increase of the unit-cell volume. The ionic radii [101] for all the ions present in both samples are 0.067 nm for Mn^{2+} , 0.064 nm for Mn^{3+} , 0.053 nm for Mn^{4+} , 0.064 nm for Nb^{5+} , 0.064 nm for Ta^{5+} , 0.152 nm for K^+ , 0.118 nm for Na^+ , and 0.092 nm for Li^+ . Therefore, the volume increase suggests the incorporation of the Mn^{2+} into the B-site. Similar results were reported in MnO_2 -doped KNN single crystals [186].

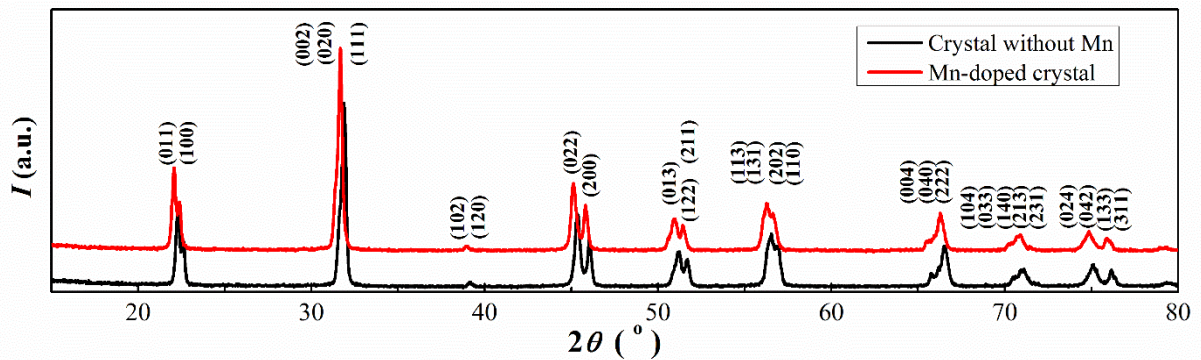


Figure 5.22. XRD patterns of powders of crushed crystals without Mn (N1, $(\text{K}_{0.612}\text{Na}_{0.359}\text{Li}_{0.029})(\text{Ta}_{0.024}\text{Nb}_{0.976})\text{O}_3$) and with Mn doping (N2-Mn, $(\text{K}_{0.637}\text{Na}_{0.334}\text{Li}_{0.029})(\text{Ta}_{0.0229}\text{Nb}_{0.9768}\text{Mn}_{0.0003})\text{O}_{2.99955}$).

Temperature-dependent (a) permittivity and (b) dielectric losses of the $[001]_{\text{PC}}$ -oriented crystals are presented in Figure 5.23. The $T_{\text{O-T}}$ and T_{C} of the N1 and N2-Mn crystals are detected at (119 °C, 123 °C) and (449 °C, 450 °C), respectively. No significant shift of $T_{\text{O-T}}$ and T_{C} is observed after the Mn doping. This is attributed to a relatively low amount of Mn ions (0.03 %), as compared to the work of Lin *et al.* [186], who observed a shift of 15 °C for 0.5 % Mn doping. Frequency-dependent dielectric properties of the $[001]_{\text{PC}}$ -oriented N1 and N2-Mn crystals are shown in Figure A.1 (Page 123) of Appendix and Figure 6.2 (a) and (c) (Page 111), respectively.

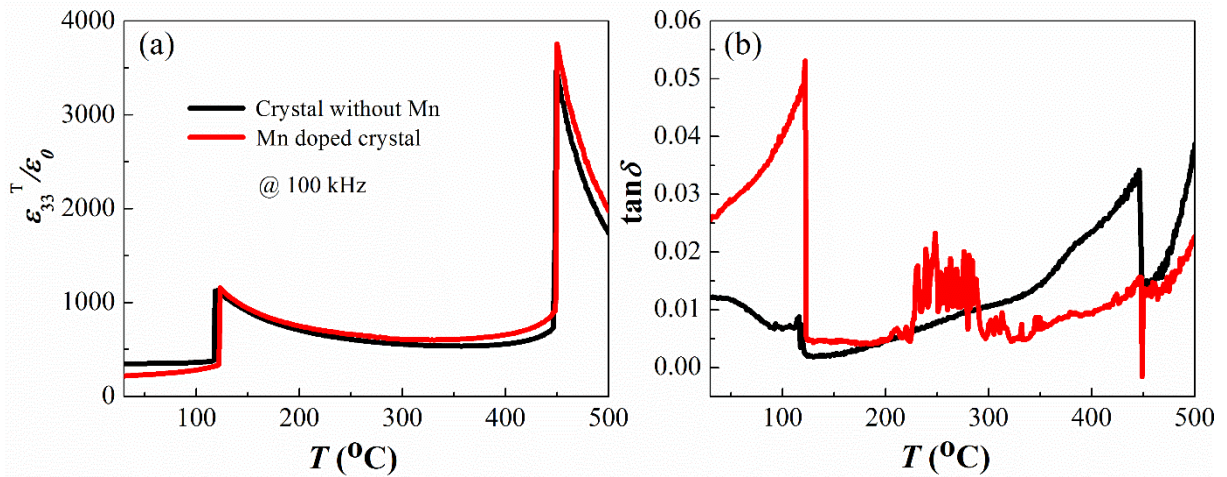


Figure 5.23. Temperature-dependent (a) permittivity and (b) dielectric losses of $[001]_{\text{PC}}$ -oriented crystals without Mn (N1; $(\text{K}_{0.612}\text{Na}_{0.359}\text{Li}_{0.029})(\text{Ta}_{0.024}\text{Nb}_{0.976})\text{O}_3$) and with Mn (N2-Mn; $(\text{K}_{0.637}\text{Na}_{0.334}\text{Li}_{0.029})(\text{Ta}_{0.0229}\text{Nb}_{0.9768}\text{Mn}_{0.0003})\text{O}_{2.99955}$, measured during heating.

Figure 5.24 provides polarization hysteresis P - E , bipolar and unipolar strain curves of the non-annealed N1 crystal, the non-annealed and annealed N2-Mn crystal along the $[001]_{\text{PC}}$ orientation. The annealing was carried out at 900 $^{\circ}\text{C}$ for one week in pure O_2 atmosphere. It is observed that both Mn-doped crystals show much higher maximum polarization P_{max} , remanent polarization P_r , and unipolar maximum strain S_{pos} , as compared to the N1 crystal without Mn doping. Although the bipolar maximum strain for the crystal without Mn is about 70 % of that for the Mn-doped crystal, it exhibits a much more asymmetric shape. After annealing in O_2 , the Mn-doped crystal shows almost no leakage current in P - E loops and a large unipolar strain, approximately twice as large as the one of the non-annealed N2-Mn crystal (Figure 5.24 (a) and (c)). Temperature-dependent P - E and S - E curves of the $[001]_{\text{PC}}$ -oriented N1 and N2-Mn crystals are provided by Figure A.2 in Appendix (Page 123) and Section 6.2 (Page 111).

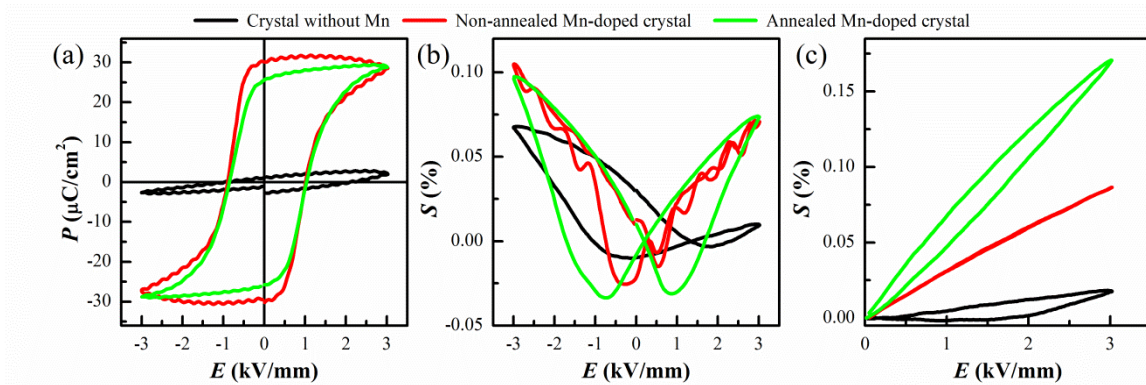


Figure 5.24. (a) P - E , (b) bipolar and (c) unipolar S - E curves of $[001]_{\text{PC}}$ -oriented non-annealed N1 crystal, and non-annealed and annealed N2-Mn crystals at room temperature and a frequency of 1 Hz (bipolar) or 2 Hz (unipolar).

The piezoelectric charge constants d_{33} of all samples were measured with the Berlincourt method. The samples were poled at 3 kV/mm and 100 °C for 30 min prior to the measurement. The d_{33} values for the crystal without Mn, Mn-doped crystal and the annealed Mn-doped crystal are 22 pC/N, 91 pC/N, and 209 pC/N, respectively.

The enhanced ferroelectric and piezoelectric properties of the Mn-doped single crystal are ascribed to the decreased defect concentration after the Mn doping. In general, Mn ions can exist in three oxidation states: Mn^{2+} , Mn^{3+} , and Mn^{4+} , with the $3d^5$ ($S=5/2$), $3d^4$ ($S=2$), and $3d^3$ ($S=3/2$) electronic configurations. Here S is the ground-state electron spin quantum number. The oxidation states and local environments of Mn ions, important to understand the role of Mn in KNN-based materials, are commonly investigated using the electron paramagnetic resonance (EPR) technique. Laguta *et al.* [254] and Eichel *et al.* [255] held the opinion that both Mn^{4+} and Mn^{2+} exist in the perovskite structure. However, Kaftelen *et al.* [256] argued that only Mn^{2+} ions exist in Mn-doped KNN polycrystalline ceramics. Note that the Mn^{3+} cannot be detected with EPR, due to its antiparallel spin. Figure 5.25 (a) shows temperature-dependent X-band EPR spectra of powders of crushed non-annealed N2-Mn crystal in the range from -269 °C to room temperature (RT). As shown in Figure 5.25 (b), the EPR signal at room temperature shows a hyperfine structure with characteristic six-line splitting. The sextets are assigned to the presence of both Mn^{2+} ($3d^5$, $S=5/2$, $I=5/2$) and Mn^{4+} ($3d^3$, $S=3/2$, $I=5/2$) ions on B sites. However, the two sextets cannot be clearly distinguished due to strong overlapping of the peaks. Upon cooling to -173 °C, a new peak starts to appear at about 273 mT and the peak at 315 mT becomes stronger. The stronger peak at 315 mT becomes visible due to the more intense and narrower signal at lower temperatures. Further decreasing the temperature to -213 °C results in detection of 3 peaks in the range of 275 mT to 300 mT. Those three peaks become more visible at lower temperature. Upon further cooling, even though the intensity of the peaks in the range between 304 mT and 362 mT changes, however, no shift of the peak positions was observed. The appearance of the four peaks between 270 mT and 300 mT is still not well understood. Similar phenomenon was detected in Mn-doped $BaTiO_3$ single crystals by Maier *et al.* [257] and it is believed to be related to the rhombohedral-orthorhombic and tetragonal-cubic phase transitions and crystallographic orientation. As mentioned in Section 5.2.4, the rhombohedral to orthorhombic phase transition is expected to be below -123 °C. The observed new peaks below -173 °C may therefore be correlated to the appearance of the rhombohedral phase in the N2-Mn single crystal. Moreover, this response might also result from the hyperfine interaction between Mn nucleus and a nucleus with a high nuclear spin, such as Nb^{4+} ($4d^1$, $S=1/2$, $I=9/2$). Temperature independence of the peak positions of the complex spectra in the range from 304 mT to 362 mT confirms the coexistence of two sextets. It is therefore concluded that both Mn^{2+} and Mn^{4+} exist and are located on the B sites in the N2-Mn single crystal.

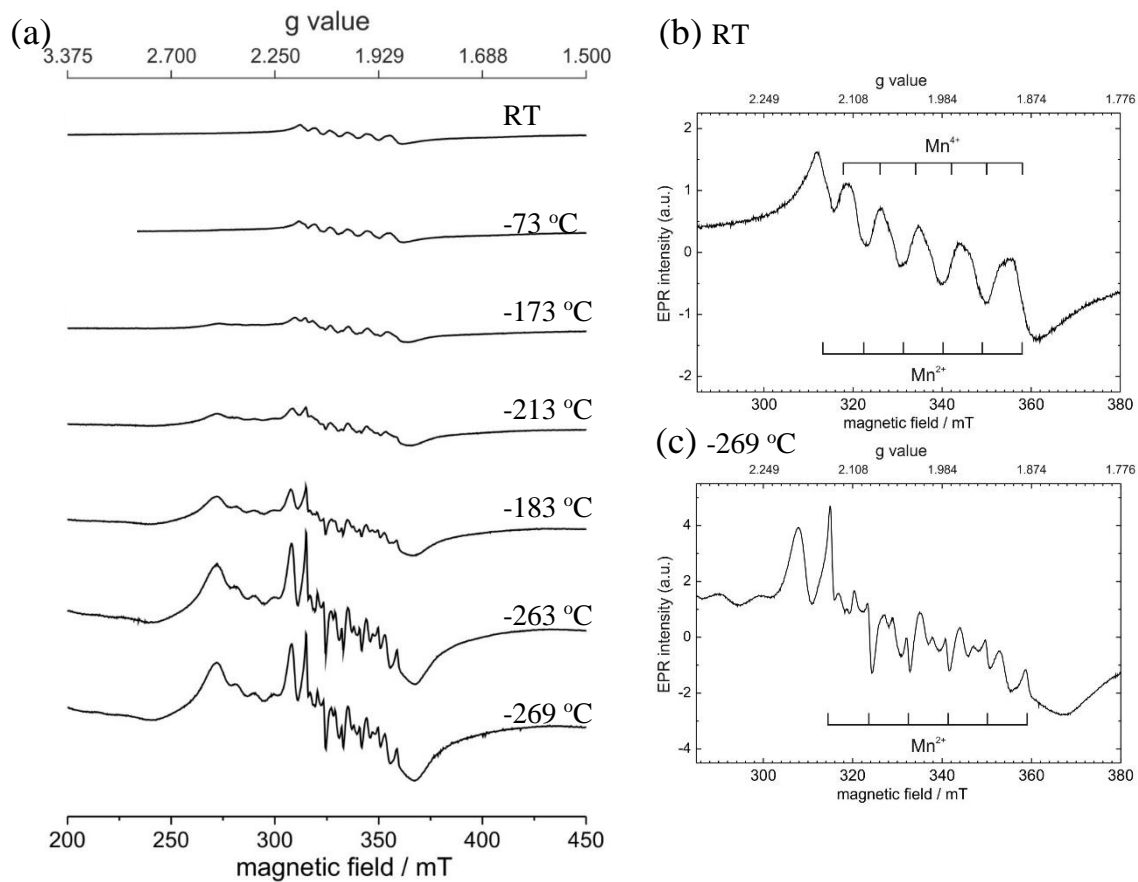


Figure 5.25. (a) EPR spectra of powders of the crushed non-annealed N₂-Mn crystal at various temperatures. Enlarged EPR spectra at (b) RT and (c) -269 °C. The two six-line groups represent the typical hyperfine structure information of Mn²⁺ and Mn⁴⁺.



6 Influence of Crystallographic Orientation

The influence of the Ta, Sb, and Mn substitution on the permittivity, polarization, strain and piezoelectric coefficients of the KNN-based single crystals were discussed in Chapter 5. This chapter will focus on the effect of crystallographic orientations on the electrical properties, which has been investigated in many ferroelectric crystals, such as $\text{Pb}(\text{Mn}_{1/3}\text{Nb}_{2/3})\text{O}_3\text{-PbTiO}_3$ (PMN-PT) [7], $(\text{Na}_{0.5}\text{Bi}_{0.5})\text{TiO}_3$ (NBT) [258], BaTiO_3 [259], $(\text{K},\text{Na})_{0.5}\text{Bi}_{0.5}\text{TiO}_3$ [260], and $(1-x)(\text{Na}_{0.5}\text{Bi}_{0.5})\text{TiO}_3-x\text{BaTiO}_3$ (NBT-BT) [9,10]. The N2-Mn $((\text{K}_{0.637}\text{Na}_{0.334}\text{Li}_{0.029})(\text{Ta}_{0.0229}\text{Nb}_{0.9768}\text{Mn}_{0.0003})\text{O}_{2.99955})$; Mn-KNLTN single crystal is selected for this investigation, considering the relatively low dielectric loss and high ferroelectric response (Section 5.3).

Both $[001]_{\text{PC}}$ and $[110]_{\text{PC}}$ orientations are selected in this work, considering the possible energetically favorable orientations of spontaneous polarizations in tetragonal ($\langle 001 \rangle_{\text{PC}}$) and orthorhombic ($\langle 110 \rangle_{\text{PC}}$) phases. As a consequence, two different cases are investigated: in the first case, the applied electric field is oriented along the spontaneous polarization direction, while in the second case the field direction differs from the spontaneous polarization. Figure 6.1 presents images of Laue back-scattering for the two orientations at room temperature. The important difference is the angle marked in Figure 6.1. The 45° angle corresponds to the angle between $[001]_{\text{PC}}$ and $[110]_{\text{PC}}$, while the 35° is the angle between $[110]_{\text{PC}}$ and $[111]_{\text{PC}}$. The standard stereographic (001) and (110) projection images in the pseudo cubic crystal are provided in Figure A.3 and A.4 of the Appendix (Page 123).

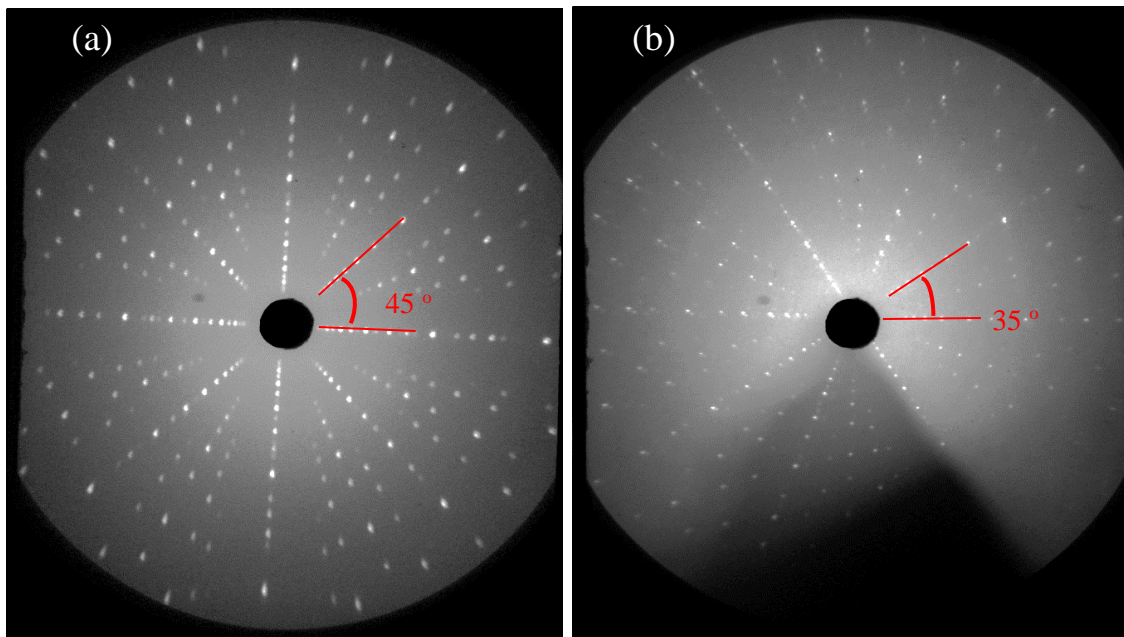


Figure 6.1. Images of Laue back-scattering for the two orientations: (a) $[001]_{\text{PC}}$ and (b) $[110]_{\text{PC}}$.

6.1 Phase and Phase Transitions

The powder XRD pattern of the crushed Mn-KNLTN single crystal at room temperature show a pure orthorhombic perovskite structure without any secondary phase, as shown in Figure 5.22 (Page 104).

The dielectric measurements were performed on unpoled samples at several selected frequencies. Figure 6.2 reveals temperature-dependent dielectric permittivity and losses for the $[001]_{\text{PC}}$ (a, c) and $[110]_{\text{PC}}$ -oriented (b, d) Mn-KNLTN crystals, respectively. Two anomalies were observed: the one at higher temperature was identified as the Curie temperature (T_{C}), corresponding to the tetragonal-cubic phase transition, while the other one at lower temperature denotes the orthorhombic-tetragonal ($T_{\text{O-T}}$) transition [236].

The insets of Figure 6.2 (a1), (a2), (b1), and (b2) display the corresponding enlarged phase-transition regions. Both oriented samples have frequency-independent phase transition temperatures T_{C} and $T_{\text{O-T}}$. The T_{C} and $T_{\text{O-T}}$ of both $[001]_{\text{PC}}$ and $[110]_{\text{PC}}$ orientations during cooling are (442 °C, 102 °C) and (441 °C, 100 °C), respectively. During heating, these values are (450 °C, 123 °C) and (449 °C, 124 °C). The thermal hysteresis indicates that both transitions are first-order [261]. The differences of phase transition temperatures between two orientations are within the measurement error, indicative of the orientation-independent phase transition temperatures.

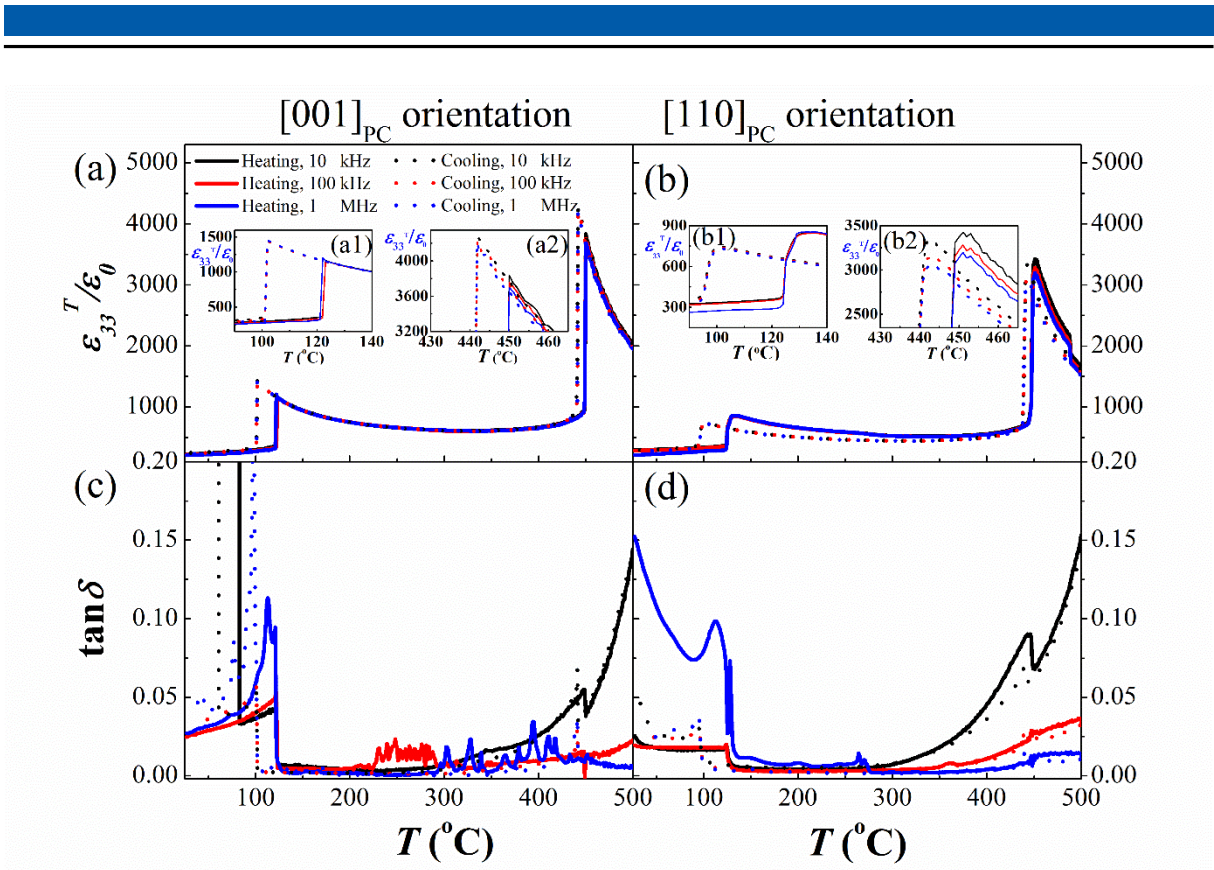


Figure 6.2. Temperature-dependent dielectric permittivity and losses of (a,c) the $[001]_{PC}$ -oriented and (b,d) $[110]_{PC}$ -oriented Mn-KNLTN crystals during heating and cooling with the rate of $1\text{ }^{\circ}\text{C}/\text{min}$.

The temperature-dependent dielectric losses of both orientations, as shown in Figure 6.2 (c) and (d), are very low due to the addition of Mn, even at temperatures above $450\text{ }^{\circ}\text{C}$. A slightly higher loss is detected between room temperature and T_{O-T} , when compared with the temperature range from T_{O-T} to T_C , which was observed in both oriented samples. It is therefore concluded that the orthorhombic phase has comparatively higher losses than the tetragonal phase. At the orthorhombic-tetragonal phase transition, either during the heating or cooling process of both orientations, a higher frequency leads to a higher loss. When the temperature is beyond $450\text{ }^{\circ}\text{C}$, corresponding to T_C , the losses of both $[001]_{PC}$ and $[110]_{PC}$ -oriented samples start increasing with temperature, especially when measured at a lower frequency. This is ascribed to the higher concentration of oxygen vacancies after the addition of Mn ions.

6.2 Electromechanical Properties

Figure 6.3 displays hysteresis P - E loops of $[001]_{PC}$ and $[110]_{PC}$ -oriented Mn-KNLTN single crystals measured at $3\text{ kV}/\text{mm}$ and a frequency of 1 Hz at various temperatures: (a) $20\text{ }^{\circ}\text{C}$, (b) $40\text{ }^{\circ}\text{C}$, (c) $80\text{ }^{\circ}\text{C}$,

(d) 100 °C, (e) 120 °C, and (f) 160 °C. Typical rectangular P - E loops are observed for both orientations below 100 °C. When the temperature is close to 100 °C, P - E loops get distorted and the one measured along the $[110]_{\text{PC}}$ orientation is pinched at lower fields. This pinched P - E loop indicates the high degree of backswitching polarization along the $[110]_{\text{PC}}$ orientation at the $T_{\text{O-T}}$.

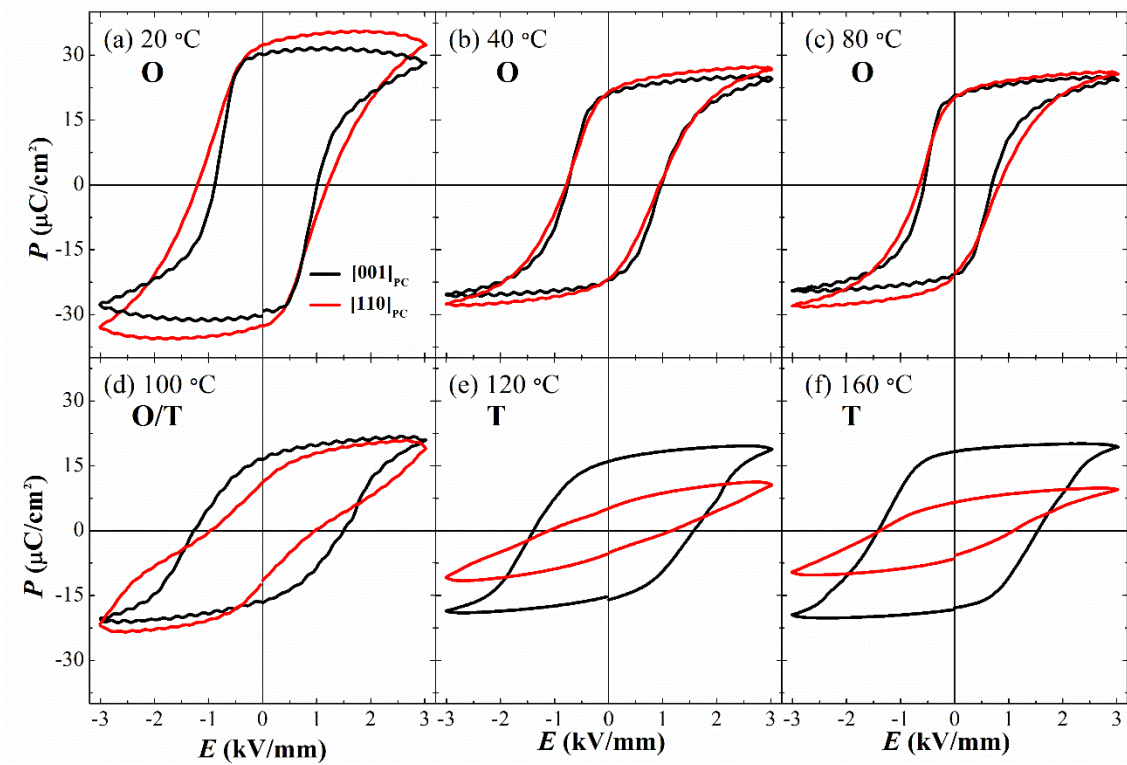


Figure 6.3. Temperature-dependent bipolar ferroelectric hysteresis P - E loops (the second electric field loading cycles; 1Hz) of $[001]_{\text{PC}}$ and $[110]_{\text{PC}}$ -oriented Mn-KNLTN samples.

Figure 6.4 displays temperature-dependent bipolar electric field-induced strain S - E curves for both orientations of the Mn-KNLTN single crystal (second electric cycle). Both orientations show asymmetric S - E curves below 80 °C, as previously observed for the KNLTNS samples. When the temperature reaches 100 °C, significant changes of the bipolar S - E curves of both orientations are observed. A S - E curve with a large negative strain appears in the $[001]_{\text{PC}}$ oriented Mn-KNLTN crystal, whereas a S - E curve with negligible negative strain is obtained along the $[110]_{\text{PC}}$ orientation. Further increasing the temperature above 100 °C, a similar shape is observed in the $[001]_{\text{PC}}$ oriented sample, whereas the $[110]_{\text{PC}}$ oriented crystal shows decreased strain with increasing temperature.

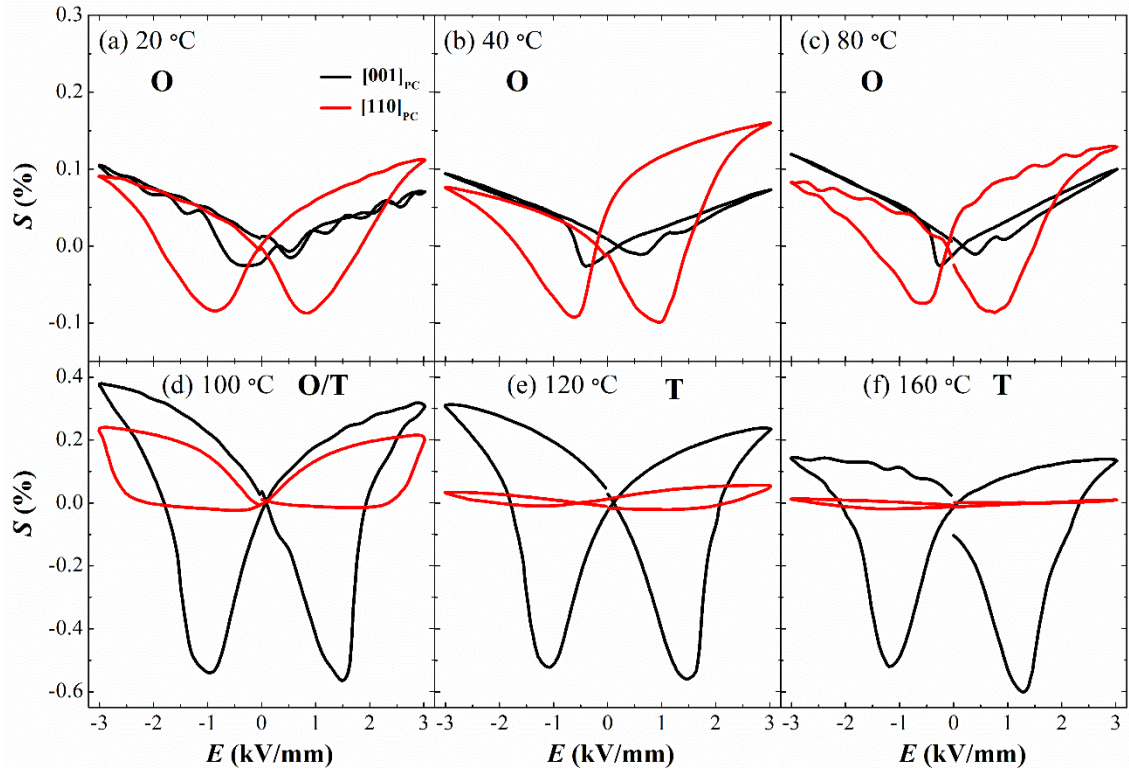


Figure 6.4. Temperature-dependent bipolar electric field-induced strain curves (the second electric field loading cycles; 1Hz) of $[001]_{PC}$ and $[110]_{PC}$ -oriented Mn-KNLTN samples.

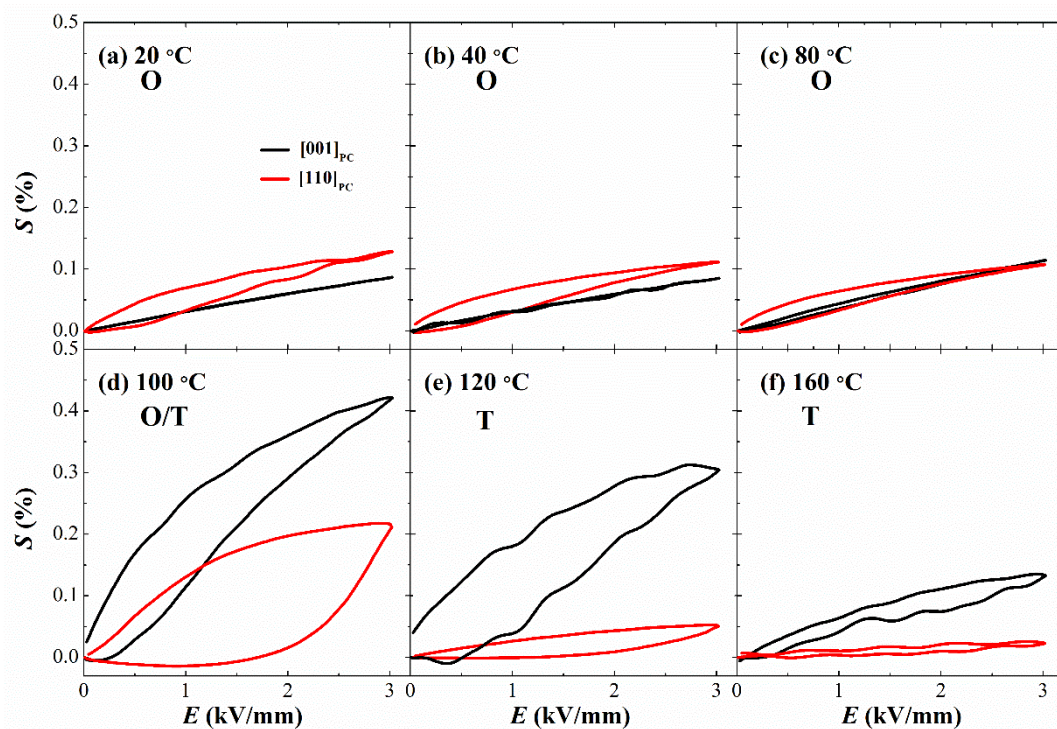


Figure 6.5. Temperature-dependent unipolar electric field-induced strain curves (second electric field loading cycles, 2 Hz) of $[001]_{PC}$ and $[110]_{PC}$ -oriented Mn-KNLTN samples.

Figure 6.5 provides the unipolar S - E curves of both $[001]_{\text{PC}}$ and $[110]_{\text{PC}}$ -oriented single crystals during the second electric cycles at various temperatures. For the both orientations, the maximum positive strain S_{pos} at E_{max} is relatively stable below 80 °C in the orthorhombic phase, increases remarkably at 100 °C ($T_{\text{O-T}}$), and subsequently decreases quickly above 100 °C in the tetragonal phase.

6.3 Influence of Electric Field on Electromechanical Properties

Influence of the Electric Field on Polarization Parameters

Figure 6.6 (a)-(c) summarize the temperature-dependent maximum polarization P_{max} , remanent polarization P_{r} , and coercive field E_{C} for both orientations of the Mn-KNLTN single crystal, extracted from polarization loops. It should be noted that all the parameters listed here are the average of the values at maximum positive and negative fields. For both orientations, P_{max} and P_{r} decrease with increasing temperature and exhibit a sharp drop near 100 °C, while E_{C} first decreases and then increases remarkably when the temperature is close to 100 °C. This temperature corresponds to the orthorhombic-tetragonal phase transition, as seen in Figure 6.2 (b) (Page 111). Above 100 °C, E_{C} of both orientations remains stable. The gradual decrease of P_{max} , P_{r} , and E_{C} with increasing temperature within the single-phase range, either orthorhombic or tetragonal, is related to the increased thermal oscillations and decreased lattice distortions.

In Figure 6.6 (a)-(c), the orthorhombic phase reveals higher P_{max} and P_{r} but lower E_{C} , as compared to the tetragonal phase, which was previously reported in KNLTNS polycrystalline ceramics by Huan *et al.*[262]. This is attributed to the larger number of P_{S} vectors and lower symmetry of the orthorhombic phase [263]. The higher coercive field E_{C} in the tetragonal phase in the vicinity of $T_{\text{O-T}}$ can be explained by the higher lattice distortion of the tetragonal structure, as compared to the orthorhombic one [219]. Furthermore, while the 90 ° domain switching can occur in both phases, the 60 ° domain switching only happens in the orthorhombic phase, which additionally lowers the E_{C} .

Figure 6.6 (a)-(c) also indicates that in the orthorhombic phase the highest values of P_{max} , P_{r} , and E_{C} were obtained for the $[110]_{\text{PC}}$ orientation, while in the tetragonal phase highest values for these parameters were found along the $[001]_{\text{PC}}$ direction. This gives an indication of the relationship between the ferroelectric response and the electric field direction. It is well known that the spontaneous polarizations (P_{S}) of the orthorhombic phase are along $\langle 110 \rangle_{\text{PC}}$ directions (12 equivalent P_{S}), while those of the tetragonal phase are along $\langle 001 \rangle_{\text{PC}}$ directions (6 equivalent P_{S}), as shown in Figure 6.7 (a)-(d). It can thus be concluded that P_{max} , P_{r} , and E_{C} are the largest when electric field is parallel to one of the P_{S} directions (labeled as $E \parallel P_{\text{S}}$). This is due to the higher possibility to achieve a single-domain state

at E_{\max} when $E \parallel P_S$ (see Figure 6.7 (f) and (g)). If the electric field is not parallel to any of the P_S (labeled as $E \nparallel P_S$), dipoles cannot align at E_{\max} , resulting in a multi-domain instead of single-domain state, as provided by Figure 6.7 (h) and (i). After field removal, both $E \parallel P_S$ and $E \nparallel P_S$ cases exhibit a multi-domain state. The higher P_r for $E \parallel P_S$ corresponds to the orientation independence of backswitching in KNN-based single crystals. This can be indicated by Figure 6.6 (a) and (b), which display similar decrease in polarization from P_{\max} to P_r for two orientations in either orthorhombic or tetragonal phase.

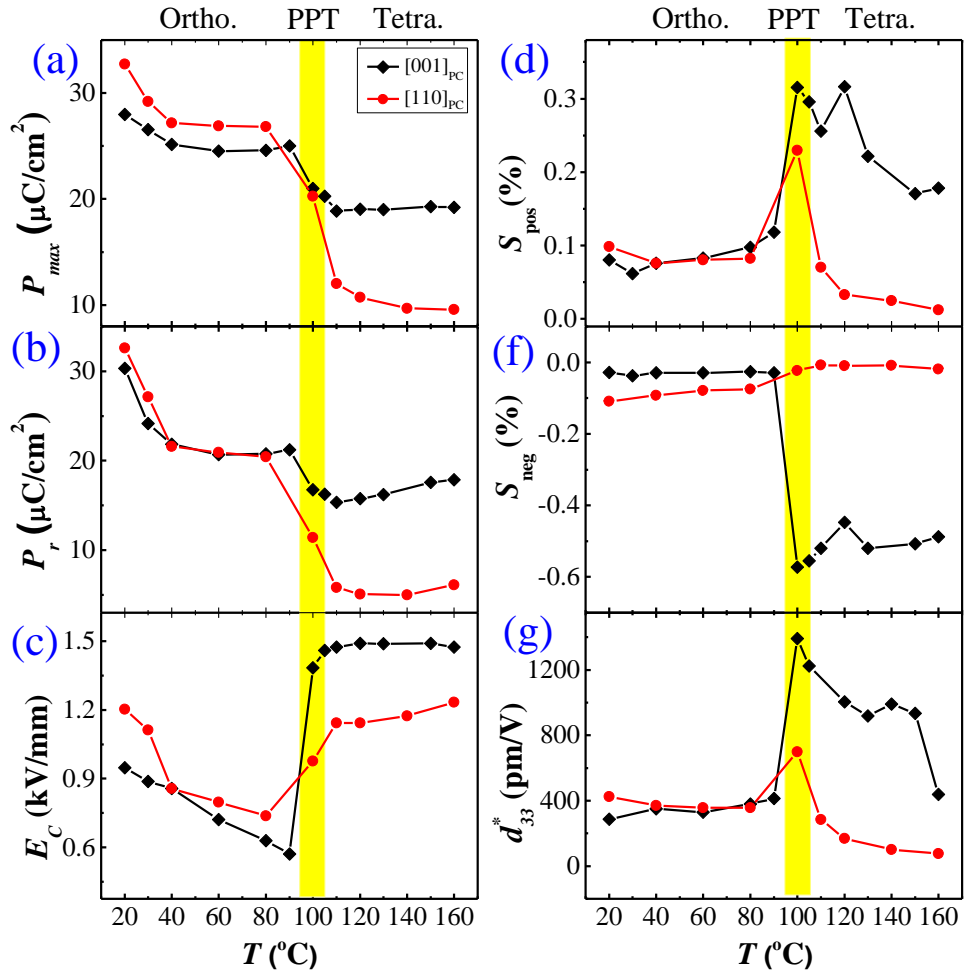


Figure 6.6. Temperature-dependent (a) maximum polarization P_{\max} , (b) remanent polarization P_r , (c) coercive field E_C , (d) bipolar positive strain S_{pos} and (e) negative strain S_{neg} , and (f) large-signal piezoelectric coefficient d_{33}^* values of $[001]_{\text{PC}}$ and $[110]_{\text{PC}}$ -oriented Mn-KNLTN samples.

Influence of the Electric Field on Strain Parameters

The temperature dependences of the maximum bipolar positive strain S_{pos} and negative strain S_{neg} , extracted from the bipolar strain curves, are plotted in Figure 6.6 (d) and (f). In addition, the large-signal piezoelectric constants d_{33}^* , calculated from unipolar measurements as $S_{\text{max}}/E_{\text{max}}$, are presented in Figure 6.6 (g). The highest values for S_{pos} , S_{max} and d_{33}^* are reached at 100 °C: 0.31 %, 0.42 %, 1391 pm/V for $[001]_{\text{PC}}$ and 0.21 %, 0.21 %, 700 pm/V for $[110]_{\text{PC}}$ -oriented samples. Above $T_{\text{O-T}}$, S_{pos} and d_{33}^* become smaller for both orientations with increasing temperature. The absolute value of S_{neg} along the $[001]_{\text{PC}}$ orientation is relatively small at low temperatures, but increases sharply to 0.56 % at $T_{\text{O-T}}$ (Figure 6.6). On the other hand, the absolute value of S_{neg} along the $[110]_{\text{PC}}$ orientation is gradually reduced upon heating and becomes negligible above $T_{\text{O-T}}$. In addition, both S_{pos} and S_{neg} reduce slightly along the $[001]_{\text{PC}}$ direction above $T_{\text{O-T}}$, but the latter is interestingly still higher than the former. The relatively good thermal stability and high values of S_{pos} and S_{neg} indicate the large potential of these crystals for piezoelectric applications if $T_{\text{O-T}}$ is shifted to room temperature. This can be easily achieved by changing the Ta content, as explained in Chapter 5.

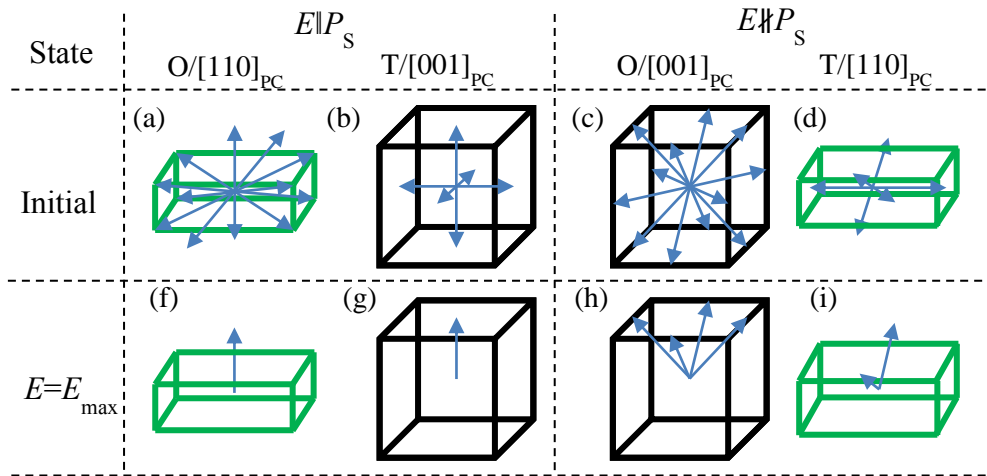


Figure 6.7. Initial polarization distributions for different orientations and polarization distributions at maximum field E_{max} : (a) $[110]_{\text{PC}}$ -oriented orthorhombic, (b) $[001]_{\text{PC}}$ -oriented tetragonal, (c) $[001]_{\text{PC}}$ -oriented orthorhombic, and (d) $[110]_{\text{PC}}$ -oriented tetragonal crystals.

The orientation dependence of E_C and S_{neg} of the Mn-KNLTN crystal in a single-phase region is observed in Figure 6.6 (c) and (f), originating from the different contributions of non-180 ° and 180 ° domain switching events during increasing E from 0 to E_C [264]. For tetragonal phases, the probability of non-

180 ° domain switching is approximately 4/6 if $E \parallel P_S$ ($[001]_{PC}$), but only 2/6 if $E \nparallel P_S$ ($[110]_{PC}$), which can be seen in Figure 6.8 (b)->(g), and (d)->(i). For orthorhombic phases, this probability is about 10/12 when $E \parallel P_S$ ($[110]_{PC}$) and 4/12 when $E \nparallel P_S$ ($[001]_{PC}$), as provided in Figure 6.8 (a)->(c) and (c)->(h). Thus, non-180 ° domain switching events are dominant for the $E \parallel P_S$ case, while the 180 ° events are dominant for $E \nparallel P_S$, when E is increased from 0 to E_C . Since non-180 ° switching creates strain and 180 ° switching does not, higher S_{neg} can be observed when $E \parallel P_S$.

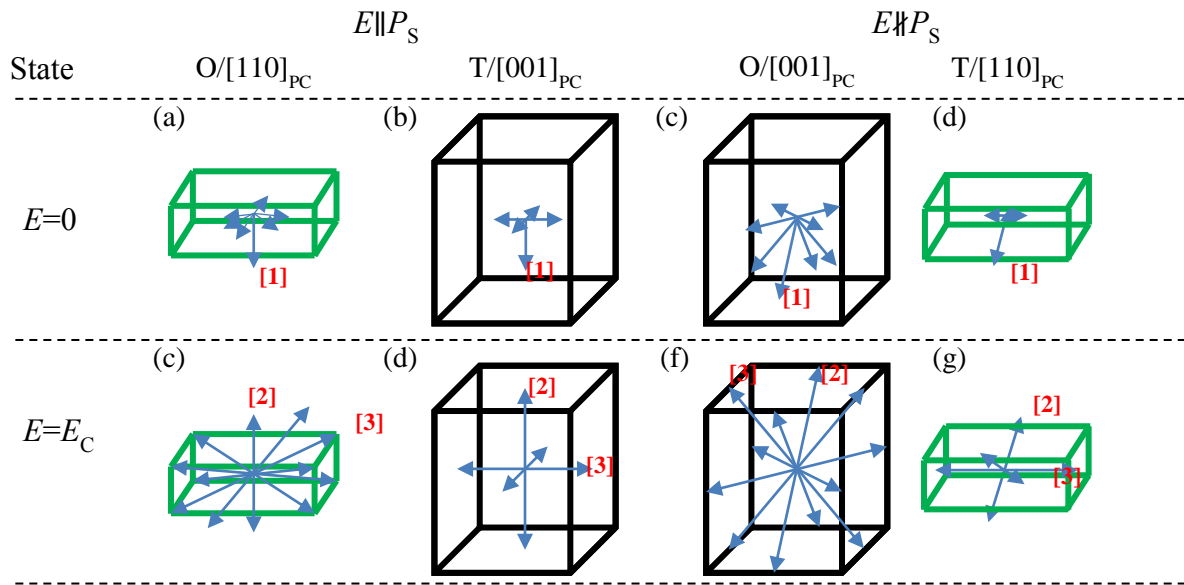


Figure 6.8. Change of the domain structure for different orientations when the field increases from 0 to coercive field E_C : (a) $[110]_{PC}$ -oriented orthorhombic, (b) $[001]_{PC}$ -oriented tetragonal, (c) $[001]_{PC}$ -oriented orthorhombic, and (d) $[110]_{PC}$ -oriented tetragonal crystals.

Trends of Backswitching Polarization and Strain

During the bipolar electric field loading process, backswitching occurs when the field is decreased from the maximum to zero, accompanied by a decrease of polarization and strain. Given the definition of variables in Section 2.1.3 (Page 6) and Figure 6.3 (Page 112), polarization backswitching is defined as $P_{max} - P_r$, while strain backswitching is defined as S_{pos} .

In nonlinear dielectrics, electric field-induced strain is highly dependent on the induced polarization, which can be described by the following fundamental equation,

$$S_{ij} = Q_{ijkl} \cdot P_k \cdot P_l \quad (6.1)$$

where S_{ij} is the strain tensor, Q_{ijkl} is the electrostrictive coefficient tensor, and P_k and P_l are the polarization components. According to the literature reports, Q_{ijkl} is believed to be temperature-independent [1]. The temperature-dependent electric field-induced maximum strain S_{pos} of the [001]_{PC}-oriented sample shows the same trends up to 90 °C as its field-induced polarization change ($P_{\text{max}} - P_r$) (see Figure 6.9 (a)). However, at the phase transition temperature $T_{\text{O-T}}$, the change in ($P_{\text{max}} - P_r$) was negligible, while the electric field-induced strain S_{pos} exhibits a large increase. The observed different behavior suggests a significant increase of the electrostrictive coefficient Q with increasing temperature, which was previously reported in other ferroelectric single crystals [7]. Unfortunately, we cannot calculate the electrostrictive coefficients of our samples due to the relatively low breakdown field of investigated crystals, which prevented full saturation of P - E and S - E curves.

The counterintuitive behavior of the changes in strain and polarization at the phase transition $T_{\text{O-T}}$ is related to the change of the piezoelectric coefficient d_{33} and permittivity ϵ_{33}/ϵ_0 , considering the following equations are valid for the condition of zero stress [265]:

$$D_i = \epsilon_{ij}E_j + \epsilon_{ijk}E_jE_k + \dots \quad (6.2)$$

$$S_{ij} = d_{ijk}E_k + M_{ijkl}E_kE_l + \dots \quad (6.3)$$

where D_i and S_{ij} denote the electric field-induced electric displacement and strain, M_{ijkl} is another electrostrictive coefficient tensor, related to Q_{ijkl} by the permittivity, ϵ_{ij} and ϵ_{ijk} are the permittivity tensors, d_{ijk} is the piezoelectric coefficient tensor, and E_k and E_l are the electric field vectors. Note that in most ferroelectrics $D_i \approx P_i$ due to the large permittivity values, as mentioned in Chapter 2. Figure 6.9 (b) plots the temperature-dependence of the changes in small signal d_{33} and ϵ_{33} of the [001]_{PC}-oriented sample, as compared to the room temperature values. Depolarization above $T_{\text{O-T}}$ yields a significant decrease of d_{33} . Increasing d_{33} and ϵ_{33} were observed from room temperature up to $T_{\text{O-T}}$, which is anticipated for a normal ferroelectric-ferroelectric phase transition. However, when compared with each other, piezoelectric coefficient increases faster than dielectric permittivity. This difference is believed to be the main origin of the larger increase of the electric field-induced strain at $T_{\text{O-T}}$, which depends predominantly on piezoelectric and electrostrictive coefficients (Equation 6.3), while the polarization is related only to the permittivity (Equation 6.2). Note that the small signal d_{33} and ϵ_{33} were used for the comparison here and the temperature dependence of both parameters is expected to display similar trends under large electric fields.

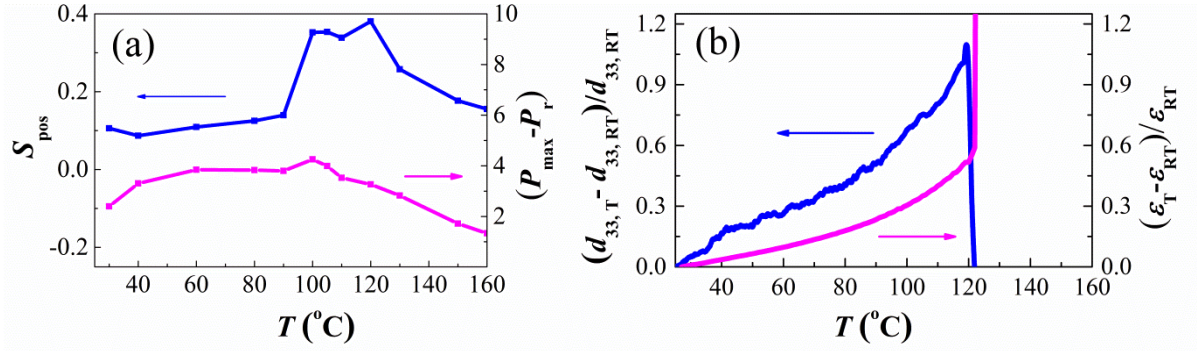


Figure 6.9. Temperature-dependent properties of the [001]_{PC}-oriented Mn-KNLTN sample: (a) large signal S_{pos} and $(P_{\text{max}} - P_r)$, and (b) small signal d_{33} and permittivity, normalized with respect to room temperature value.

Large Strain Response at T_{O-T}

Interestingly, electromechanical strains (bipolar S_{pos} and unipolar S_{max}) in the vicinity of the T_{O-T} along the [001]_{PC} orientation are much larger than those along the [110]_{PC} orientation (yellow regions in Figure 6.6 (d) and (g)). A similar observation was reported for NBT-BT crystals by Ge *et al.* [156] This phenomenon can be described as follows. For the [001]_{PC}-oriented sample, no polarization aligns with electric field below T_{O-T} . When temperature approaches T_{O-T} , the coexisted structure of orthorhombic and tetragonal phases drives polarizations to rotate to the electric field direction. For the [110]_{PC}-oriented sample, some polarizations vectors align with electric field below T_{O-T} . When temperature reaches T_{O-T} , the majority of polarization vectors can be driven to rotate from $\langle 110 \rangle_{\text{PC}}$ to $\langle 001 \rangle_{\text{PC}}$ and some remain aligned with electric field, which reduces the degree of polarization extension under large fields. This hypothesis should be further verified by synchrotron XRD measurements

6.4 Summary

Orientation and temperature dependence of dielectric and electromechanical properties of $(\text{K}_{0.637}\text{Na}_{0.334}\text{Li}_{0.029})(\text{Ta}_{0.0229}\text{Nb}_{0.9768}\text{Mn}_{0.0003})\text{O}_{2.99955}$ single crystals were investigated. Samples exhibited very low dielectric losses, with $\tan\delta$ between 0.03 and 0.05 over a broad temperature range between room temperature and 480 °C. Influences of the crystallographic structure and external electric field on polarization and strain parameters are discussed. The orientation-dependent electrical properties were found to be related to the anisotropic polarization switching and polarization extension in the crystals. Higher maximum polarization, coercive field, and negative strain were achieved when the electric field was oriented along one of the spontaneous polarization directions. The highest maximum unipolar strain of 0.42 % (at 3 kV/mm) and large-signal piezoelectric constant d_{33}^* of 1391 pm/V were obtained in the

[001]_{PC}-oriented sample at 100 °C, which was much higher than the values obtained for the [110]_{PC}-oriented sample. This was ascribed to the vicinity of the structural phase transition and additional contributions from polarization extension. Further insight of the phase transition behavior is given by comparing the temperature-dependence of the small- and large-signal dielectric and piezoelectric properties. The observed changes are rationalized by the different increase rates of the dielectric permittivity and piezoelectric coefficients with temperature.

7 Remarks and Outlook

In this work, eleven $\text{K}_{0.5}\text{Na}_{0.5}\text{NbO}_3$ (KNN)-based crystal growth attempts were carried out using either the submerged-seed solution growth (SSSG) or the top-seeded solution growth (TSSG) technique. The chemical composition, crystallographic structure, and electromechanical properties were analyzed.

In the first part, the segregation coefficients of individual elements during the growth of $(\text{K,Na,Li})(\text{Ta,Nb})\text{O}_3$ (KNLTN) single crystals were investigated and found to be strongly influenced by the initial liquid composition. The Na and Ta ions have segregation coefficients larger than 1 and are preferentially absorbed by the crystal during growth. The K and Nb ions show the opposite behavior with the effective segregation coefficients less than 1. The appearance of the secondary phase with the tetragonal tungsten bronze (TTB) structure was ascribed primarily to the very low segregation coefficient of Li. Two approaches are suggested to solve this issue: growth of KNN-based single crystals under oxygen partial pressure or exploration of novel flux compositions. These two approaches could decrease the defect concentrations in as-grown crystals. An additional drawback of the as-grown crystals in this work is the existence of optically cloudy regions, which were related to the different domain configurations. Further developments of the cooling process (especially across the phase transitions) and control of the thermal gradient of the furnace are required to decrease the area of the cloudy regions.

The influence of the chemical composition on the electrical response were investigated in Chapter 5. Increasing the amount of Ta was found to linearly decrease the T_C and T_{O-T} with a rate of $4.6\text{ }^\circ\text{C/mol\%Ta}$ and $8.6\text{ }^\circ\text{C/mol\%Ta}$, respectively. Different decrease rates were found for Sb substitution, namely $12.2\text{ }^\circ\text{C/mol\%Sb}$ for T_C and $6.6\text{ }^\circ\text{C/mol\%Sb}$ for T_{O-T} , indicating narrowing of the tetragonal temperature range. Moreover, thermal annealing in O_2 was performed to considerably improve the ferroelectric and piezoelectric properties. This is ascribed to the decreased defect concentration, resulting in decreased leakage currents. The defects are suggested to be related to the formation of A-site vacancies, changes of the B-site valence state, and oxygen vacancies. However, further systematic investigations of the electrical behaviour using impedance spectroscopy under different oxygen partial pressures are needed to confirm the proposed mechanisms and fully understand their individual contributions in KNN-based single crystals.

Furthermore, we studied the influence of the addition of a small amount of Mn into the KNLTN single crystals. Large enhancements of the ferroelectric and piezoelectric properties were observed, without apparent changes in the cubic-tetragonal and tetragonal-orthorhombic phase transitions. Electron paramagnetic resonance (EPR) results suggested that both Mn^{2+} and Mn^{4+} ions appear in Mn-doped KNLTN single crystals, and occupy the B sites of the perovskite structure. However, it is still a challenge to control the amount of Mn ions having access to the perovskite structure during the crystal growth. In

our work, the appearance of an impurity phase, which is induced by the addition of Mn ions, was found in as-grown Mn-doped KNLNT crystal boules. This to some extent limits the dimensions of the as-cut crystals.

The very low dielectric losses of the Mn-doped KNLNT crystals enabled a study of the orientation dependent electric field-induced polarization and strain curves over a broad temperature range, which is presented in Chapter 6. Higher maximum polarization, coercive field, and negative strain were observed when the electric field was oriented along one of the spontaneous polarization direction. Large negative strain values along the $[001]_{PC}$ orientation were observed above the T_{O-T} , the possible application of which are still under discussion. Moreover, as compared to annealed KNLNTNS single crystals in Chapter 5, the Mn-doped KNLNTN single crystal exhibits different strain behaviour, which was attributed to the different intrinsic piezoelectric responses of both systems. In order to understand the different intrinsic and extrinsic contributions to the electromechanical strain of Mn-doped KNLNTN and annealed KNLNTNS single crystals further *in-situ* structural investigations are required.

The high piezoelectric properties and reduced leakage currents obtained in some of the investigated samples in our work and other recent literature reports indicate the potential of KNN-based single crystals for applications and will hopefully motivate further studies. The improved understanding of the segregation phenomena can aid the preparation of these crystals with the TSSG method using oriented seeds, which yields larger crystals. These can then be used for a broader analysis of the anisotropy of elastic, dielectric, and piezoelectric coefficients.

Appendix

Appendix I: Electrical Properties of the N1 Single Crystal

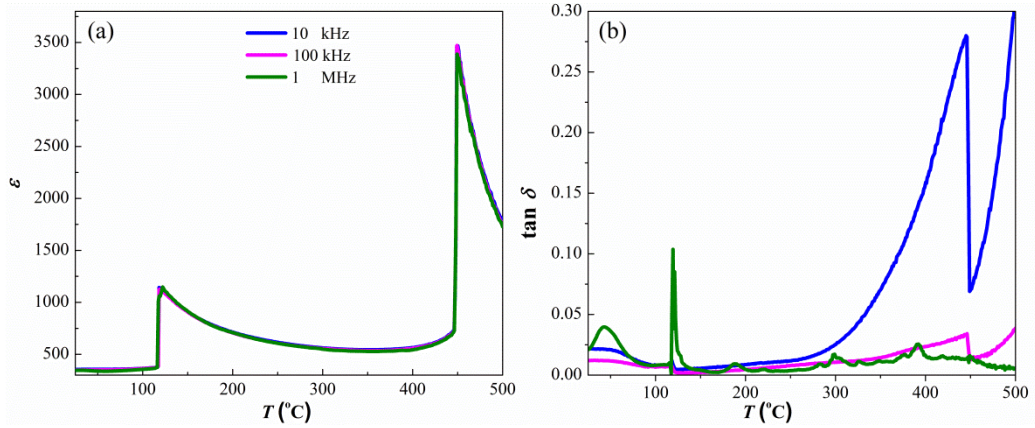


Figure A.1. Temperature-dependent permittivity properties of the [001]_{pc}-oriented N1 single crystal ($\text{K}_{0.612}\text{Na}_{0.359}\text{Li}_{0.029}$)($\text{Ta}_{0.024}\text{Nb}_{0.976}$) O_3).

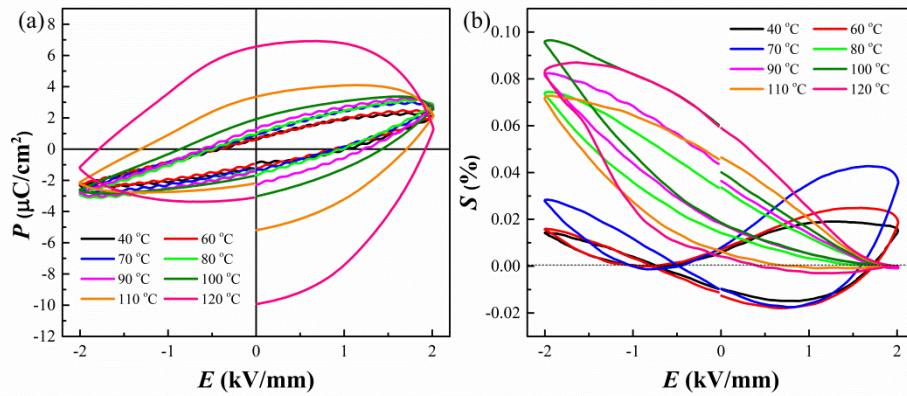


Figure A.2. Ferroelectric hysteresis polarization-electric field (P - E) and electric field-induced strain (S - E) curves of the [001]_{pc}-oriented N1 single crystal ($\text{K}_{0.612}\text{Na}_{0.359}\text{Li}_{0.029}$)($\text{Ta}_{0.024}\text{Nb}_{0.976}$) O_3) at various temperatures from 40 °C to 120 °C.

Appendix II: Stereographic Projection

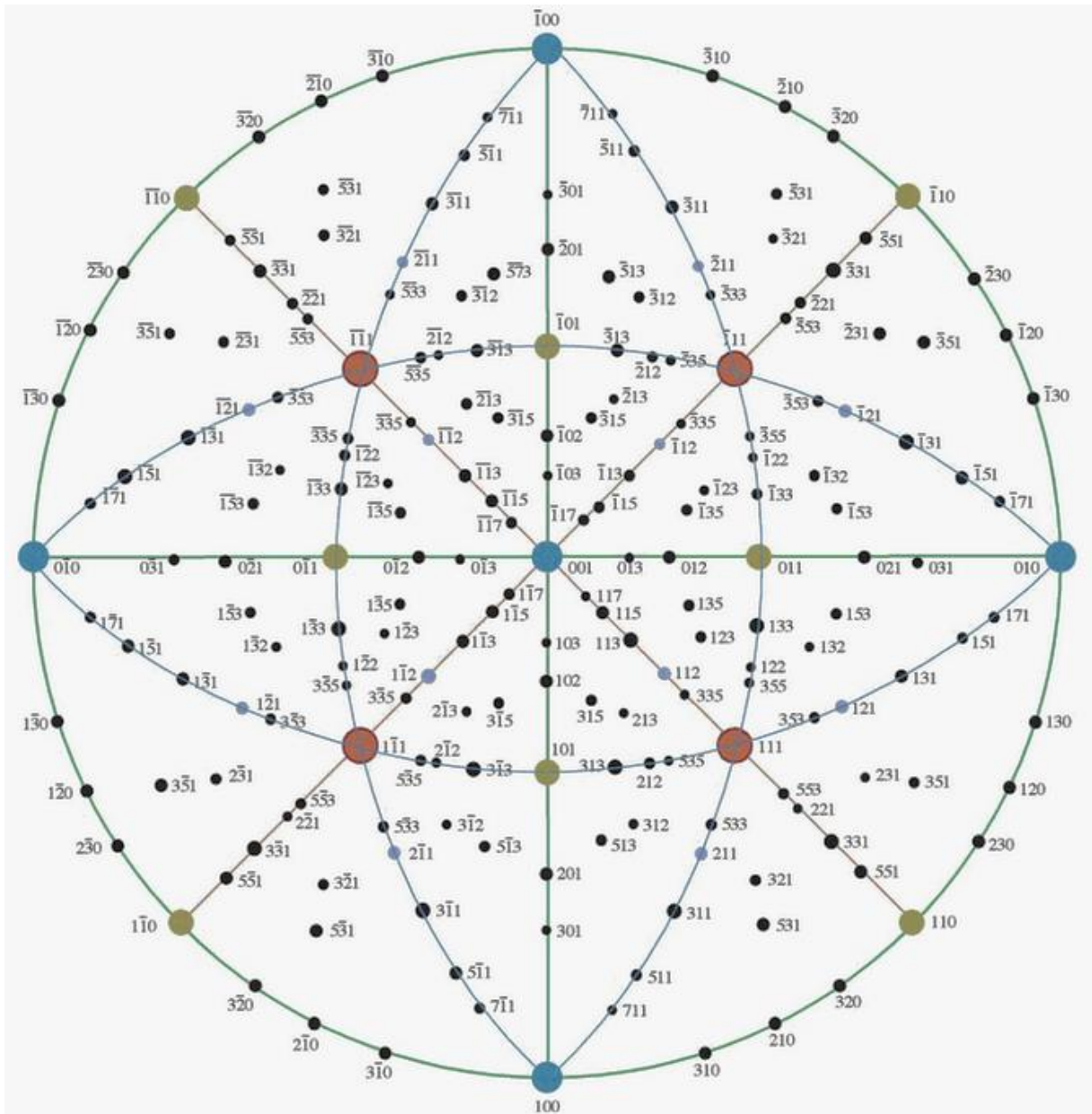


Figure A.3. Stereographic projection for a cubic system along the $[001]$ orientation. Reprinted from Ref. [266], with permission of Springer.

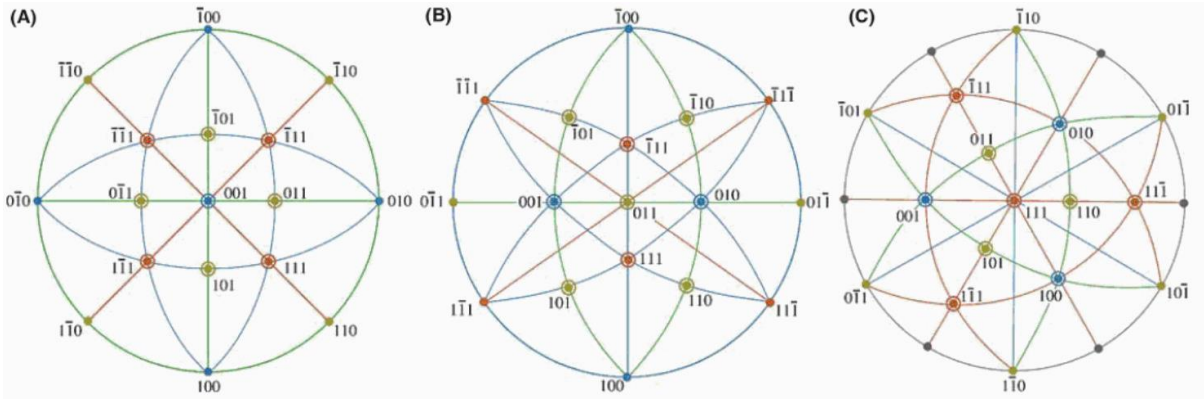


Figure. A.4. Some standard cubic stereographic projections: (A) [001] (B) [110], and (C) [111] orientations. Reprinted from Ref. [266], with permission of Springer.



References

- [1] B. Jaffe, W. R. Cook, and H. Jaffe, *Piezoelectric ceramics*. (Academic press Inc., New York, 1971).
- [2] T. R. Shrout and S. J. Zhang, Lead-free piezoelectric ceramics: Alternatives for PZT?, *Journal of Electroceramics* **19** (1), 113-26 (2007).
- [3] E.-D. 2011/65/EU, Restriction of the use of certain hazardous substances in electrical and electronic equipment, *Official Journal of the European Union L* **174** (88) (2011).
- [4] Y. Saito, H. Takao, T. Tani, T. Nonoyama, K. Takatori, T. Homma, T. Nagaya, and M. Nakamura, Lead-free piezoceramics, *Nature* **432** (7013), 84-87 (2004).
- [5] J. Rödel, K. G. Webber, R. Dittmer, W. Jo, M. Kimura, and D. Damjanovic, Transferring lead-free piezoelectric ceramics into application, *Journal of the European Ceramic Society* **35** (6), 1659-81 (2015).
- [6] B. Mo Park, S. Jin Chung, H. Soon Kim, W. Si, and M. Dudley, Synchrotron white-beam X-ray topography of ferroelectric domains in a BaTiO₃ single crystal, *Philosophical Magazine A* **75** (3), 611-20 (1997).
- [7] X. Liu, D. Wu, B. Fang, J. Ding, X. Li, X. Zhao, H. Luo, J.-H. Ko, and C. W. Ahn, Aging characteristics of 0.7Pb(Mg_{1/3}Nb_{2/3})O₃-0.3PbTiO₃ single crystals with different crystal orientations, *Applied Physics A* **119** (4), 1469-76 (2015).
- [8] S. Wada, S. Suzuki, T. Noma, T. Suzuki, M. Osada, M. Kakihana, S.-E. Park, L. E. Cross, and T. R. Shrout, Enhanced piezoelectric property of barium titanate single crystals with engineered domain configurations, *Japanese Journal of Applied Physics* **38** (9S), 5505 (1999).
- [9] D. Schneider, W. Jo, J. Rödel, D. Rytz, and T. Granzow, Anisotropy of ferroelectric behavior of (1-x)Bi_{1/2}Na_{1/2}TiO₃-xBaTiO₃ single crystals across the morphotropic phase boundary, *Journal of Applied Physics* **116** (4), 044111 (2014).
- [10] D. Schneider, J. Rödel, D. Rytz, and T. Granzow, Orientation-dependence of thermal depolarization and phase development in Bi_{1/2}Na_{1/2}TiO₃-BaTiO₃ single crystals, *Journal of the American Ceramic Society* **98** (12), 3966-74 (2015).
- [11] A. Popovič, L. Bencze, J. Koruza, and B. Malič, Vapour pressure and mixing thermodynamic properties of the KNbO₃-NaNbO₃ system, *RSC Advances* **5** (93), 76249-56 (2015).
- [12] R. Waser, U. Böttger, and S. Tiedke, *Polar oxides: properties, characterization, and imaging*. (John Wiley & Sons, 2006).
- [13] A. K. Tagantsev, L. E. Cross, and J. Fousek, *Domains in ferroic crystals and thin films*. (Springer, 2010).
- [14] W. Heywang, K. Lubitz, and W. Wersing, *Piezoelectricity: Evolution and future of a technology*. (Springer Science & Business Media, 2008).
- [15] D. Damjanovic, Ferroelectric, dielectric and piezoelectric properties of ferroelectric thin films and ceramics, *Reports on Progress in Physics* **61** (9), 1267 (1998).
- [16] D. Damjanovic, Contributions to the piezoelectric effect in ferroelectric single crystals and ceramics, *Journal of the American Ceramic Society* **88** (10), 2663-76 (2005).
- [17] G. H. Haertling, Ferroelectric ceramics: History and technology, *Journal of the American Ceramic Society* **82** (4), 797-818 (1999).

-
- [18] F. Li, L. Jin, Z. Xu, and S. Zhang, Electrostrictive effect in ferroelectrics: An alternative approach to improve piezoelectricity, *Applied Physics Reviews* **1** (1), 011103 (2014).
- [19] T. Sluka, A. K. Tagantsev, D. Damjanovic, M. Gureev, and N. Setter, Enhanced electromechanical response of ferroelectrics due to charged domain walls, *Nature Communications* **3**, 748 (2012).
- [20] E. Eliseev, A. Morozovska, G. Svechnikov, V. Gopalan, and V. Y. Shur, Static conductivity of charged domain walls in uniaxial ferroelectric semiconductors, *Physical Review B* **83** (23), 235313 (2011).
- [21] M. E. Lines and A. M. Glass, *Principles and applications of ferroelectrics and related materials*. (Oxford university press, 1977).
- [22] K. W. Kirby and B. A. Wechsler, Phase relations in the barium titanate-titanium oxide system, *Journal of the American Ceramic Society* **74** (8), 1841-47 (1991).
- [23] E. Wiesendanger, Domain structures in orthorhombic KNbO₃ and characterisation of single domain crystals, *Czechoslovak Journal of Physics B* **23** (1), 91-99 (1973).
- [24] V. M. Goldschmidt, Die gesetze der krystallochemie, *Naturwissenschaften* **14** (21), 477-85 (1926).
- [25] J. Rödel, W. Jo, K. T. Seifert, E. M. Anton, T. Granzow, and D. Damjanovic, Perspective on the development of lead-free piezoceramics, *Journal of the American Ceramic Society* **92** (6), 1153-77 (2009).
- [26] D. M. Smyth, *The defect chemistry of metal oxides*. (Oxford University Press, Oxford, 2000).
- [27] F. Kroger and H. Vink, (Academic Press, NY, 1956).
- [28] R.-A. Eichel, P. Erhart, P. Träskelin, K. Albe, H. Kungl, and M. J. Hoffmann, Defect-dipole formation in copper-doped PbTiO₃ ferroelectrics, *Physical Review Letters* **100** (9), 095504 (2008).
- [29] W. L. Warren, G. E. Pike, K. Vanheusden, D. Dimos, B. A. Tuttle, and J. Robertson, Defect - dipole alignment and tetragonal strain in ferroelectrics, *Journal of Applied Physics* **79** (12), 9250-57 (1996).
- [30] A. V. Kimmel, P. M. Weaver, M. G. Cain, and P. V. Sushko, Defect-mediated lattice relaxation and domain stability in ferroelectric oxides, *Physical Review Letters* **109** (11), 117601 (2012).
- [31] P. V. Lambeck and G. H. Jonker, Ferroelectric domain stabilization in BaTiO₃ by bulk ordering of defects, *Ferroelectrics* **22** (1), 729-31 (1978).
- [32] M. I. Morozov and D. Damjanovic, Charge migration in Pb(Zr,Ti)O₃ ceramics and its relation to ageing, hardening, and softening, *Journal of Applied Physics* **107** (3), 034106 (2010).
- [33] M. A. Larson and J. Palermo, *Crystallization from solutions and melts*. (American Institute of Chemical Engineers, 1969).
- [34] H. Scheel and D. Elwell, *Crystal growth from high-temperature solutions*. (1975).
- [35] G. Dhanaraj, K. Byrappa, V. V. Prasad, and M. Dudley, in *Handbook of crystal growth* (Springer, 2010), pp. 3-16.
- [36] K. A. Jackson, *Kinetic processes: Crystal growth, diffusion, and phase transformations in materials*. (Wiley, New York, 2004).
- [37] A. Benčan, E. Tchernychova, H. Uršič, J. Fisher, and M. Kosec, *Growth and characterization of single crystals of potassium sodium niobate by solid state crystal growth*. (INTECH open access Publisher, 2011).
-

-
- [38] E. Sun and W. Cao, Relaxor-based ferroelectric single crystals: Growth, domain engineering, characterization and applications, *Progress in materials science* **65**, 124-210 (2014).
- [39] S. J. L. Kang, J. H. Park, S. Y. Ko, and H. Y. Lee, Solid - state conversion of single crystals: The principle and the state - of - the - art, *Journal of the American Ceramic Society* **98** (2), 347-60 (2015).
- [40] S. Shimanuki, S. Saito, and Y. Yamashita, Single crystal of the $\text{Pb}(\text{Zn}_{1/3}\text{Nb}_{2/3})\text{O}_3\text{-PbTiO}_3$ system grown by the vertical Bridgeman method and its characterization, *Japanese Journal of Applied Physics* **37** (6R), 3382 (1998).
- [41] K. Harada, S. Shimanuki, T. Kobayashi, S. Saitoh, and Y. Yamashita, Crystal growth and electrical properties of $\text{Pb}((\text{Zn}_{1/3}\text{Nb}_{2/3})_{0.91}\text{Ti}_{0.09})\text{O}_3$ single crystals produced by solution Bridgman method, *Journal of the American Ceramic Society* **81** (11), 2785-88 (1998).
- [42] T. Karaki, M. Adachi, Y. Hosono, and Y. Yamashita, Distribution of piezoelectric properties in $\text{Pb}[(\text{Mg}_{1/3}\text{Nb}_{2/3})_{0.7}\text{Ti}_{0.3}]\text{O}_3$ single crystal, *Japanese Journal of Applied Physics* **41** (4A), L402 (2002).
- [43] R. Bertram, G. Reck, and R. Uecker, Growth and correlation between composition and structure of $(1-x)\text{Pb}(\text{Zn}_{1/3}\text{Nb}_{2/3})\text{O}_3\text{-xPbTiO}_3$ crystals near the morphotropic phase boundary, *Journal of Crystal Growth* **253** (1), 212-20 (2003).
- [44] W. Chen and Z.-G. Ye, Top seeded solution growth and characterization of piezo-/ferroelectric $(1-x)\text{Pb}(\text{Zn}_{1/3}\text{Nb}_{2/3})\text{O}_3\text{-xPbTiO}_3$ single crystals, *Journal of Crystal Growth* **233** (3), 503-11 (2001).
- [45] C. Park, K. Lim, D. Choi, and S. Chung, Crystal growth of $\text{PbMg}_{1/3}\text{Nb}_{2/3}\text{O}_3$ and $\text{PbZn}_{1/3}\text{Nb}_{2/3}\text{O}_3$ and structural studies on the ordering, *Journal of the Korean Physical Society* **32**, S974-S977 (1998).
- [46] M. Prakasam, P. Veber, O. Viraphong, L. Etienne, M. Lahaye, S. Pechev, E. Lebraud, K. Shimamura, and M. Maglione, Growth and characterizations of lead-free ferroelectric KNN-based crystals, *Comptes Rendus Physique* **14** (2), 133-40 (2013).
- [47] M. Garrett and I. Mnushkina, Techniques for top-seeded solution growth of BaTiO_3 , *Journal of Crystal Growth* **166** (1), 550-57 (1996).
- [48] B. M. Park and S. J. Chung, Optical, electron microscopic, and X-ray topographic studies of ferroic domains in barium titanate crystals grown from high-temperature solution, *Journal of the American Ceramic Society* **77** (12), 3193-201 (1994).
- [49] Q. Lu, X. Long, and Y. Hu, Top-seeded solution growth and characterization of PMN-0.31PT piezoelectric single crystals, *CrystEngComm* **12** (12), 4317-20 (2010).
- [50] X. Long and Z.-G. Ye, Top-seeded solution growth and characterization of rhombohedral PMN-30PT piezoelectric single crystals, *Acta Materialia* **55** (19), 6507-12 (2007).
- [51] X. Li, Z. Wang, C. He, X. Long, and Z.-G. Ye, Growth and piezo-/ferroelectric properties of PIN-PMN-PT single crystals, *Journal of Applied Physics* **111** (3), 034105 (2012).
- [52] C. He, X. Li, Z. Wang, X. Long, S. Mao, and Z.-G. Ye, Preparation and characterization of new $\text{Pb}(\text{Yb}_{1/2}\text{Nb}_{1/2})\text{O}_3\text{-Pb}(\text{Mg}_{1/3}\text{Nb}_{2/3})\text{O}_3\text{-PbTiO}_3$ ternary piezo-/ferroelectric crystals, *Chemistry of Materials* **22** (19), 5588-92 (2010).
- [53] W. Ge, H. Liu, X. Zhao, X. Li, X. Pan, D. Lin, H. Xu, X. Jiang, and H. Luo, Orientation dependence of electrical properties of $0.96\text{Na}_{0.5}\text{Bi}_{0.5}\text{TiO}_3\text{-0.04BaTiO}_3$ lead-free piezoelectric single crystal, *Applied Physics A* **95** (3), 761-67 (2009).
- [54] C. Chen, X. Jiang, Y. Li, F. Wang, Q. Zhang, and H. Luo, Growth and electrical properties of $\text{Na}_{1/2}\text{Bi}_{1/2}\text{TiO}_3\text{-BaTiO}_3$ lead-free single crystal with morphotropic phase boundary composition, *Journal of Applied Physics* **108** (12), 124106 (2010).
-

- [55] W. Ge, H. Liu, X. Zhao, B. Fang, X. Li, F. Wang, D. Zhou, P. Yu, X. Pan, and D. Lin, Crystal growth and high piezoelectric performance of $0.95\text{Na}_{0.5}\text{Bi}_{0.5}\text{TiO}_3\text{-}0.05\text{BaTiO}_3$ lead-free ferroelectric materials, *Journal of Physics D: Applied Physics* **41** (11), 115403 (2008).
- [56] Q. Zhang, Y. Zhang, F. Wang, Y. Wang, D. Lin, X. Zhao, H. Luo, W. Ge, and D. Viehland, Enhanced piezoelectric and ferroelectric properties in Mn-doped $\text{Na}_{0.5}\text{Bi}_{0.5}\text{TiO}_3\text{-BaTiO}_3$ single crystals, *Applied Physics Letters* **95** (10), 102904 (2009).
- [57] R. Sun, H. Zhang, J. Wang, F. Wang, B. Fang, X. Zhao, and H. Luo, Growth and electrical properties of $0.88\text{Na}_{0.5}\text{Bi}_{0.5}\text{TiO}_3\text{-}0.12\text{K}_{0.5}\text{Bi}_{0.5}\text{TiO}_3$ lead-free piezoelectric single crystal, *Applied Physics A* **111** (2), 629-32 (2013).
- [58] C. Chen, H. Zhang, X. Zhao, H. Deng, L. Li, B. Ren, D. Lin, X. Li, H. Luo, and Z. Chen, Structure, electrical, and optical properties of $(\text{Na}_{1/2}\text{Bi}_{1/2})\text{TiO}_3 - 1.5 \text{ at.}\% \text{ Bi}(\text{Zn}_{1/2}\text{Ti}_{1/2})\text{O}_3$ lead - free single crystal grown by a TSSG technique, *Journal of the American Ceramic Society* **97** (6), 1861-65 (2014).
- [59] W. Xing, H. Looser, H. Wüest, and H. Arend, Progress in KNbO_3 crystal growth, *Journal of Crystal Growth* **78** (3), 431-37 (1986).
- [60] J. Hulliger, R. Gutmann, and H. Wüest, Growth of large size KNbO_3 crystals and epitaxial layers of $\text{KTa}_{1-x}\text{Nb}_x\text{O}_3$, *Journal of Crystal Growth* **128** (1), 897-902 (1993).
- [61] H. Zeng, T. Chong, L. Lim, H. Kumagai, and M. Hirano, Effects of meniscus on the directional growth of potassium niobate single crystals, *Journal of Crystal Growth* **160** (3), 289-95 (1996).
- [62] H. Tian, C. Hu, X. Meng, P. Tan, Z. Zhou, J. Li, and B. Yang, Top-seeded solution growth and properties of $\text{K}_{1-x}\text{Na}_x\text{NbO}_3$ crystals, *Crystal Growth & Design* **15** (3), 1180-85 (2015).
- [63] J. S. Kim and H.-S. Lee, Growth and properties of ferroelectric potassium lithium niobate (KLN) crystal grown by the Czochralski method, *Journal of Crystal Growth* **223** (3), 376-82 (2001).
- [64] D. Cochet-Muchy, Growth of piezoelectric crystals by Czochralski method, *Le Journal de Physique IV* **4** (C2), C2-33-C2-45 (1994).
- [65] G. Xu, H. Luo, Y. Guo, Y. Gao, H. Xu, Z. Qi, W. Zhong, and Z. Yin, Growth and piezoelectric properties of $\text{Pb}(\text{Mg}_{1/3}\text{Nb}_{2/3})\text{O}_3\text{-PbTiO}_3$ crystals by the modified Bridgman technique, *Solid State Communications* **120** (7), 321-24 (2001).
- [66] Z.-W. Yin, H.-S. Luo, P.-C. Wang, and G.-S. Xu, Growth, characterization and properties of relaxor ferroelectric PMN-PT single crystals, *Ferroelectrics* **229** (1), 207-16 (1999).
- [67] F. Li, S. Zhang, Z. Xu, X. Wei, J. Luo, and T. R. Shrout, Electromechanical properties of tetragonal $\text{Pb}(\text{In}_{1/2}\text{Nb}_{1/2})\text{O}_3\text{-Pb}(\text{Mg}_{1/3}\text{Nb}_{2/3})\text{O}_3\text{-PbTiO}_3$ ferroelectric crystals, *Journal of Applied Physics* **107** (5) (2010).
- [68] J. Chen, X. Li, X. Zhao, H. Zhang, H. Deng, C. Chen, X. a. Wang, B. Ren, W. Di, and H. Luo, Growth and characterization of high-Curie temperature $\text{Pb}(\text{Lu}_{1/2}\text{Nb}_{1/2})\text{O}_3\text{-Pb}(\text{Mg}_{1/3}\text{Nb}_{2/3})\text{O}_3\text{-PbTiO}_3$ ternary single crystal by modified Bridgman technique, *Journal of Crystal Growth* **423**, 50-54 (2015).
- [69] G. Xu, Z. Duan, X. Wang, and D. Yang, Growth and some electrical properties of lead-free piezoelectric crystals $(\text{Na}_{1/2}\text{Bi}_{1/2})\text{TiO}_3$ and $(\text{Na}_{1/2}\text{Bi}_{1/2})\text{TiO}_3\text{-BaTiO}_3$ prepared by a Bridgman method, *Journal of Crystal Growth* **275** (1), 113-19 (2005).
- [70] K. Chen, G. S. Xu, D. F. Yang, X. F. Wang, and J. B. Li, Dielectric and piezoelectric properties of lead-free $0.95(\text{K}_{0.5}\text{Na}_{0.5})\text{NbO}_3\text{-}0.05\text{LiNbO}_3$ crystals grown by the Bridgman method, *Journal of Applied Physics* **101** (4), 044103 (2007).

- [71] K.-W. Benz and W. Neumann, *Introduction to crystal growth and characterization*. (John Wiley & Sons, 2014).
- [72] A. Benayad, G. Sebald, L. Lebrun, B. Guiffard, S. Pruvost, D. Guyomar, and L. Beylat, Segregation study and segregation modeling of Ti in $\text{Pb}[(\text{Mg}_{1/3}\text{Nb}_{2/3})_{0.60}\text{Ti}_{0.40}]\text{O}_3$ single crystal grown by Bridgman method, *Materials Research Bulletin* **41** (6), 1069-76 (2006).
- [73] N. Luo, Y. Li, Z. Xia, and Q. Li, Progress in lead-based ferroelectric and antiferroelectric single crystals: Composition modification, crystal growth and properties, *CrystEngComm* **14** (14), 4547-56 (2012).
- [74] A. Kania, A. Słodczyk, and Z. Ujma, Flux growth and characterization of $(1-x)\text{PbMg}_{1/3}\text{Nb}_{2/3}\text{O}_3-x\text{PbTiO}_3$ single crystals, *Journal of Crystal Growth* **289** (1), 134-39 (2006).
- [75] X. Yi, H. Chen, W. Cao, M. Zhao, D. Yang, G. Ma, C. Yang, and J. Han, Flux growth and characterization of lead-free piezoelectric single crystal $[\text{Bi}_{0.5}(\text{Na}_{1-x}\text{K}_x)_{0.5}]\text{TiO}_3$, *Journal of Crystal Growth* **281** (2), 364-69 (2005).
- [76] R. C. DeVries, Growth of single crystals of BaTiO_3 by exaggerated grain growth, *Journal of the American Ceramic Society* **47** (3), 134-36 (1964).
- [77] T. Yamamoto and T. Sakuma, Fabrication of barium titanate single crystals by solid - state grain growth, *Journal of the American Ceramic Society* **77** (4), 1107-09 (1994).
- [78] P. W. Rehrig, S.-E. Park, S. Trolier-McKinstry, G. L. Messing, B. Jones, and T. R. ShROUT, Piezoelectric properties of zirconium-doped barium titanate single crystals grown by templated grain growth, *Journal of Applied Physics* **86** (3), 1657 (1999).
- [79] A. Khan, F. A. Meschke, T. Li, A. M. Scotch, H. M. Chan, and M. P. Harmer, Growth of $\text{Pb}(\text{Mg}_{1/3}\text{Nb}_{2/3})\text{O}_3$ - 35 mol% PbTiO_3 single crystals from (111) substrates by seeded polycrystal conversion, *Journal of the American Ceramic Society* **82** (11), 2958-62 (1999).
- [80] M. S. Kim, J. G. Fisher, S. J. L. Kang, and H. Y. Lee, Grain growth control and solid - state crystal growth by $\text{Li}_2\text{O}/\text{PbO}$ addition and dislocation introduction in the PMN-35PT system, *Journal of the American Ceramic Society* **89** (4), 1237-43 (2006).
- [81] S. Zhang, S. M. Lee, D. H. Kim, H. Y. Lee, and T. R. ShROUT, Elastic, piezoelectric, and dielectric properties of $0.71\text{Pb}(\text{Mg}_{1/3}\text{Nb}_{2/3})\text{O}_3-0.29\text{PbTiO}_3$ crystals obtained by solid - state crystal growth, *Journal of the American Ceramic Society* **91** (2), 683-86 (2008).
- [82] S. Zhang, S. Lee, D. Kim, H. Lee, and T. R. ShROUT, Characterization of high T_c $\text{Pb}(\text{Mg}_{1/3}\text{Nb}_{2/3})\text{O}_3-\text{PbZrO}_3-\text{PbTiO}_3$ single crystals fabricated by solid state crystal growth, *Applied Physics Letters* **90**, 232911 (2007).
- [83] J. Lim, S. Zhang, H.-Y. Lee, and T. ShROUT, Solid state crystal growth of $\text{BiScO}_3-\text{Pb}(\text{Mg}_{1/3}\text{Nb}_{2/3})\text{O}_3-\text{PbTiO}_3$, *Journal of Electroceramics* **29** (2), 139-43 (2012).
- [84] B. Matthias and J. Remeika, Dielectric properties of sodium and potassium niobates, *Physical Review* **82** (5), 727-29 (1951).
- [85] G. Shirane, H. Danner, A. Pavlovic, and R. Pepinsky, Phase transitions in ferroelectric KNbO_3 , *Physical Review* **93** (4), 672 (1954).
- [86] H. D. Megaw, The seven phases of sodium niobate, *Ferroelectrics* **7** (1), 87-89 (1974).
- [87] S. K. Mishra, N. Choudhury, S. L. Chaplot, P. S. R. Krishna, and R. Mittal, Competing antiferroelectric and ferroelectric interactions in NaNbO_3 : Neutron diffraction and theoretical studies, *Physical Review B* **76** (2), 024110 (2007).

-
- [88] G. Shirane, R. Newnham, and R. Pepinsky, Dielectric properties and phase transitions of NaNbO_3 and $(\text{Na,K})\text{NbO}_3$, *Physical Review* **96** (3), 581 (1954).
- [89] J. F. Li, K. Wang, F. Y. Zhu, L. Q. Cheng, and F. Z. Yao, $(\text{K,Na})\text{NbO}_3$ -based lead-free piezoceramics: Fundamental aspects, processing technologies, and remaining challenges, *Journal of the American Ceramic Society* **96** (12), 3677-96 (2013).
- [90] M. Ahtee and A. Glazer, Lattice parameters and tilted octahedra in sodium–potassium niobate solid solutions, *Acta Crystallographica Section A: Crystal Physics, Diffraction, Theoretical and General Crystallography* **32** (3), 434-46 (1976).
- [91] M. Ahtee and A. Hewat, Structural phase transitions in sodium–potassium niobate solid solutions by neutron powder diffraction, *Acta Crystallographica Section A: Crystal Physics, Diffraction, Theoretical and General Crystallography* **34** (2), 309-17 (1978).
- [92] J. Wu, D. Xiao, and J. Zhu, Potassium–Sodium Niobate Lead-Free Piezoelectric Materials: Past, Present, and Future of Phase Boundaries, *Chemical Reviews* **115** (7), 2559-95 (2015).
- [93] Y. Saito and H. Takao, High performance lead-free piezoelectric ceramics in the $(\text{K,Na})\text{NbO}_3$ - LiTaO_3 solid solution system, *Ferroelectrics* **338** (1), 17-32 (2006).
- [94] Y. Guo, K.-i. Kakimoto, and H. Ohsato, Phase transitional behavior and piezoelectric properties of $(\text{Na}_{0.5}\text{K}_{0.5})\text{NbO}_3$ - LiNbO_3 ceramics, *Applied Physics Letters* **85** (18), 4121-23 (2004).
- [95] H. Du, F. Tang, F. Luo, D. Zhu, S. Qu, Z. Pei, and W. Zhou, Influence of sintering temperature on piezoelectric properties of $(\text{K}_{0.5}\text{Na}_{0.5})\text{NbO}_3$ - LiNbO_3 lead-free piezoelectric ceramics, *Materials Research Bulletin* **42** (9), 1594-601 (2007).
- [96] N. Klein, E. Hollenstein, D. Damjanovic, H. J. Trodahl, N. Setter, and M. Kuball, A study of the phase diagram of $(\text{K,Na,Li})\text{NbO}_3$ determined by dielectric and piezoelectric measurements, and Raman spectroscopy, *Journal of Applied Physics* **102** (1), 014112-12-8 (2007).
- [97] W. Ge, Y. Ren, J. Zhang, C. P. Devreugd, J. Li, and D. Viehland, A monoclinic-tetragonal ferroelectric phase transition in lead-free $(\text{K}_{0.5}\text{Na}_{0.5})\text{NbO}_3$ - $x\%$ LiNbO_3 solid solution, *Journal of Applied Physics* **111** (10), 103503 (2012).
- [98] D. Lin, K. W. Kwok, and H. L. W. Chan, Microstructure, phase transition, and electrical properties of $(\text{K}_{0.5}\text{Na}_{0.5})_{1-x}\text{Li}_x(\text{Nb}_{1-y}\text{Ta}_y)\text{O}_3$ lead-free piezoelectric ceramics, *Journal of Applied Physics* **102** (3), 034102 (2007).
- [99] Z. Feng and S. W. Or, Phase transition-induced high electromechanical activity in $[(\text{K}_{0.5}\text{Na}_{0.5})_{1-x}\text{Li}_x](\text{Nb}_{0.8}\text{Ta}_{0.2})\text{O}_3$ lead-free ceramic system, *Journal of Alloys and Compounds* **480** (2), L5-L8 (2009).
- [100] Y. Chang, Z. Yang, Y. Hou, Z. Liu, and Z. Wang, Effects of Li content on the phase structure and electrical properties of lead-free $(\text{K}_{0.46-x/2}\text{Na}_{0.54-x/2}\text{Li}_x)(\text{Nb}_{0.76}\text{Ta}_{0.20}\text{Sb}_{0.04})\text{O}_3$ ceramics, *Applied Physics Letters* **90** (23), 232905 (2007).
- [101] R. t. Shannon, Revised effective ionic radii and systematic studies of interatomic distances in halides and chalcogenides, *Acta Crystallographica Section A: Crystal Physics, Diffraction, Theoretical and General Crystallography* **32** (5), 751-67 (1976).
- [102] J. Wu, H. Tao, Y. Yuan, X. Lv, X. Wang, and X. Lou, Role of antimony in the phase structure and electrical properties of potassium–sodium niobate lead-free ceramics, *RSC Advances* **5** (19), 14575-83 (2015).
-

-
- [103] X. Pang, J. Qiu, K. Zhu, and Y. Cao, Effects of Sb content on electrical properties of lead-free piezoelectric $(K_{0.4425}Na_{0.52}Li_{0.0375})(Nb_{0.9625-x}Sb_xTa_{0.0375})O_3$ ceramics, *Ceramics International* **38** (2), 1249-54 (2012).
- [104] Y. Chang, Z. Yang, L. Xiong, Z. Liu, and Z. Wang, Phase structure, microstructure, and electrical properties of Sb-modified $(K,Na,Li)(Nb,Ta)O_3$ piezoelectric ceramics, *Journal of the American Ceramic Society* **91** (7), 2211-16 (2008).
- [105] S. Sundar and J. Chakravarty, Antimony toxicity, *International Journal of Environmental Research and Public Health* **7** (12), 4267-77 (2010).
- [106] Y. Sung, J. Lee, S. Kim, T. Lee, J. Kim, J. Cho, T. Song, M. Kim, and T. Park, Enhanced piezoelectric properties of $(Na_{0.53}K_{0.47})(Nb_{1-x}Ta_x)O_3$ ceramics by Ta substitution, *Ceramics International* **38**, S301-S04 (2012).
- [107] J. Schiemer, Y. Liu, M. Carpenter, and R. Withers, The effect of Ta doping on the phase transitions and the piezoelectric and ferroelectric properties of $K_{0.35}Na_{0.65}NbO_3$, *Ferroelectrics* **429** (1), 95-102 (2012).
- [108] Y. Lv, C. Wang, J. Zhang, L. Wu, M. Zhao, and J. Xu, Tantalum influence on physical properties of $(K_{0.5}Na_{0.5})(Nb_{1-x}Ta_x)O_3$ ceramics, *Materials Research Bulletin* **44** (2), 284-87 (2009).
- [109] Y. Chang, Z.-p. Yang, D. Ma, Z. Liu, and Z. Wang, Phase transitional behavior, microstructure, and electrical properties in Ta-modified $[(K_{0.458}Na_{0.542})_{0.96}Li_{0.04}]NbO_3$ lead-free piezoelectric ceramics, *Journal of Applied Physics* **104** (2), 024109 (2008).
- [110] Z. P. Yang, Y. F. Chang, and L. L. Wei, Phase transitional behavior and electrical properties of lead-free $(K_{0.44}Na_{0.52}Li_{0.04})(Nb_{0.96-x}Ta_xSb_{0.04})O_3$ piezoelectric ceramics, *Applied Physics Letters* **90** (4), 042911 (2007).
- [111] Y. Huan, X. Wang, and L. Li, Displacement of Ta-O bonds near polymorphic phase transition in Li-, Ta-, and Sb-modified $(K,Na)NbO_3$ ceramics, *Applied Physics Letters* **104** (24), 242905 (2014).
- [112] Y. S. Sung, S. Baik, J. H. Lee, G. H. Ryu, D. Do, T. K. Song, M. H. Kim, and W. J. Kim, Enhanced piezoelectric properties of $(Na_{0.5+y+z}K_{0.5-y})(Nb_{1-x}Ta_x)O_3$ ceramics, *Applied Physics Letters* **101** (1), 012902 (2012).
- [113] Y. Dai, X. Zhang, and G. Zhou, Phase transitional behavior in $K_{0.5}Na_{0.5}NbO_3$ - $LiTaO_3$ ceramics, *Applied Physics Letters* **90** (26), 262903 (2007).
- [114] E. Hollenstein, M. Davis, D. Damjanovic, and N. Setter, Piezoelectric properties of Li- and Ta-modified $(K_{0.5}Na_{0.5})NbO_3$ ceramics, *Applied Physics Letters* **87** (18), 182905 (2005).
- [115] P. Zhao, B.-P. Zhang, and J.-F. Li, Enhanced dielectric and piezoelectric properties in $LiTaO_3$ -doped lead-free $(K,Na)NbO_3$ ceramics by optimizing sintering temperature, *Scripta Materialia* **58** (6), 429-32 (2008).
- [116] D. Lin, K.-w. Kwok, K.-h. Lam, and H. L. Chan, Structure and electrical properties of $K_{0.5}Na_{0.5}NbO_3$ - $LiSbO_3$ lead-free piezoelectric ceramics, *Journal of Applied Physics* **101** (7), 1-6 (2007).
- [117] G. Z. Zang, J. F. Wang, H. C. Chen, W. B. Su, C. M. Wang, P. Qi, B. Q. Ming, J. Du, L. M. Zheng, and S. J. Zhang, Perovskite $(Na_{0.5}K_{0.5})_{1-x}(LiSb)_xNb_{1-x}O_3$ lead-free piezoceramics, *Applied Physics Letters* **88** (21), 212908 (2006).
- [118] S. Zhang, R. Xia, T. R. Shrout, G. Zang, and J. Wang, Piezoelectric properties in perovskite $0.948(K_{0.5}Na_{0.5})NbO_3$ - $0.052LiSbO_3$ lead-free ceramics, *Journal of Applied Physics* **100** (10), 104108 (2006).
-

- [119] Q. Zheng, D. Lin, X. Wu, C. Xu, C. Yang, and K. Kwok, Structure and piezoelectric properties of new ternary $K_{0.5}Na_{0.5}NbO_3-LiSbO_3-CaTiO_3$ lead-free piezoceramics, *Journal of Materials Science: Materials in Electronics* **21** (6), 625-29 (2010).
- [120] S. J. Zhang, R. Xia, and T. R. Shrout, Modified $(K_{0.5}Na_{0.5})NbO_3$ based lead-free piezoelectrics with broad temperature usage range, *Applied Physics Letters* **91** (13), 132913 (2007).
- [121] J. Wu, D. Xiao, Y. Wang, W. Wu, B. Zhang, and J. Zhu, Improved temperature stability of $CaTiO_3$ -modified $[(K_{0.5}Na_{0.5})_{0.96}Li_{0.04}](Nb_{0.91}Sb_{0.05}Ta_{0.04})O_3$ lead-free piezoelectric ceramics, *Journal of Applied Physics* **104** (2), 4102 (2008).
- [122] K. Yan, K. Matsumoto, T. Karaki, and M. Adachi, Microstructure and piezoelectric properties of $(K_{0.5}Na_{0.5})NbO_3 - BaTiO_3$ lead - free piezoelectric ceramics modified by $B_2O_3 - CuO$, *Journal of the American Ceramic Society* **93** (11), 3823-27 (2010).
- [123] Y. Guo, K.-i. Kakimoto, and H. Ohsato, Structure and electrical properties of lead-free $(Na_{0.5}K_{0.5})NbO_3-BaTiO_3$ ceramics, *Japanese Journal of Applied Physics* **43** (9S), 6662 (2004).
- [124] I.-T. Seo, C.-H. Choi, M.-S. Jang, B.-Y. Kim, G. Han, S. Nahm, K.-H. Cho, and J.-H. Paik, Structural and piezoelectric properties of MnO_2 -added $0.95(Na_{0.5}K_{0.5})NbO_3-0.05SrTiO_3$ ceramics, *Sensors and Actuators A: Physical* **200**, 47-50 (2013).
- [125] F.-Z. Yao, E. A. Patterson, K. Wang, W. Jo, J. Rödel, and J.-F. Li, Enhanced bipolar fatigue resistance in $CaZrO_3$ -modified $(K,Na)NbO_3$ lead-free piezoceramics, *Applied Physics Letters* **104** (24), 242912 (2014).
- [126] F. Chen, Y. H. Li, G. Y. Gao, F. Z. Yao, K. Wang, J. F. Li, X. L. Li, X. Y. Gao, and W. Wu, Intergranular stress induced phase transition in $CaZrO_3$ modified KNN - based lead - free piezoelectrics, *Journal of the American Ceramic Society* **98** (4), 1372-76 (2015).
- [127] F. Rubio-Marcos, P. Marchet, X. Vendrell, J. Romero, F. Rémondière, L. Mestres, and J. Fernández, Effect of MnO doping on the structure, microstructure and electrical properties of the $(K,Na,Li)(Nb,Ta,Sb)O_3$ lead-free piezoceramics, *Journal of Alloys and Compounds* **509** (35), 8804-11 (2011).
- [128] M. A. Rafiq, A. Tkach, M. E. Costa, and P. M. Vilarinho, Defects and charge transport in Mn-doped $K_{0.5}Na_{0.5}NbO_3$ ceramics, *Physical Chemistry Chemical Physics* **17** (37), 24403-11 (2015).
- [129] P. Bomlai, P. Sinsap, S. Muensit, and S. J. Milne, Effect of MnO on the phase development, microstructures, and dielectric properties of $0.95Na_{0.5}K_{0.5}NbO_3-0.05LiTaO_3$ ceramics, *Journal of the American Ceramic Society* **91** (2), 624-27 (2008).
- [130] H. Ogawa, T. Moriyama, A. Kan, and Y. Ueda, Effect of Mn_2O_3 doping on the ferroelectric and piezoelectric properties of $(K_{0.474}Na_{0.474}Li_{0.052})(Nb_{0.948}Sb_{0.052})O_{3-x}$ mol% Mn_2O_3 ceramics derived from Sb_2O_3 and Sb_2O_5 , *Journal of the Ceramic Society of Japan* **121** (1416), 684-89 (2013).
- [131] D. Lin, K. W. Kwok, H. Tian, and H. W. L. w. Chan, Phase transitions and electrical properties of $(Na_{1-x}K_x)(Nb_{1-y}Sb_y)O_3$ lead - free piezoelectric ceramics with a MnO_2 sintering aid, *Journal of the American Ceramic Society* **90** (5), 1458-62 (2007).
- [132] R. Zuo, J. Fu, S. Su, X. Fang, and J.-L. Cao, Electrical properties of manganese modified sodium potassium lithium niobate lead-free piezoelectric ceramics, *Journal of Materials Science: Materials in Electronics* **20** (3), 212-16 (2009).
- [133] H. E. Mgbemere, M. Hinterstein, and G. A. Schneider, Investigation of the structure and electrical properties of $(K_xNa_{0.96-x}Li_{0.04})(Nb_{0.96-y}Ta_ySb_{0.04})O_3$ piezoelectric ceramics modified with manganese, *Journal of the American Ceramic Society* **96** (1), 201-08 (2013).

-
- [134] H. E. Mgbemere, M. Hinterstein, and G. A. Schneider, Structural phase transitions and electrical properties of $(K_xNa_{1-x})NbO_3$ -based ceramics modified with Mn, *Journal of the European Ceramic Society* **32** (16), 4341-52 (2012).
- [135] S. Wongsanmai, K. Kanchiang, S. Chandarak, Y. Laosiritaworn, S. Rujirawat, and R. Yimnirun, Crystal structure and ferroelectric properties of Mn-doped $((K_{0.5}Na_{0.5})_{0.935}Li_{0.065})NbO_3$ lead-free ceramics, *Current Applied Physics* **12** (2), 418-21 (2012).
- [136] M. Park and J. Yoo, Piezoelectric and dielectric properties of nonstoichiometric $(Na_{0.5}K_{0.5})_{0.97}(Nb_{0.90}Ta_{0.1})O_3$ ceramics doped with MnO_2 , *Journal of Electronic Materials* **41** (11), 3095-99 (2012).
- [137] A. Tian and H. Du, Enhanced ferroelectric property of manganese doped lead-free $(K_{0.5}Na_{0.5})NbO_3$ Ceramics, *Ferroelectrics* **463** (1), 72-77 (2014).
- [138] Q. Yin, S. Yuan, Q. Dong, and C. Tian, Effect of CuO and MnO_2 doping on electrical properties of $0.92(K_{0.48}Na_{0.54})NbO_3-0.08LiNbO_3$ under low-temperature sintering, *Journal of Alloys and Compounds* **491** (1), 340-43 (2010).
- [139] D. Lin, K. Kwok, and H. Chan, Piezoelectric and ferroelectric properties of $K_xNa_{1-x}NbO_3$ lead-free ceramics with MnO_2 and CuO doping, *Journal of Alloys and Compounds* **461** (1), 273-78 (2008).
- [140] H. E. Mgbemere, R.-P. Herber, and G. A. Schneider, Effect of MnO_2 on the dielectric and piezoelectric properties of alkaline niobate based lead free piezoelectric ceramics, *Journal of the European Ceramic Society* **29** (9), 1729-33 (2009).
- [141] A. A. Heitmann and G. A. Rossetti, Thermodynamics of ferroelectric solid solutions with morphotropic phase boundaries, *Journal of the American Ceramic Society* **97** (6), 1661-85 (2014).
- [142] E. K. Akdoğan, K. Kerman, M. Abazari, and A. Safari, Origin of high piezoelectric activity in ferroelectric $(K_{0.44}Na_{0.52}Li_{0.04})(Nb_{0.84}Ta_{0.1}Sb_{0.06})O_3$ ceramics, *Applied Physics Letters* **92** (11), 112908 (2008).
- [143] X. Wang, J. Wu, D. Xiao, J. Zhu, X. Cheng, T. Zheng, B. Zhang, X. Lou, and X. Wang, Giant piezoelectricity in potassium–sodium niobate lead-free ceramics, *Journal of the American Chemical Society* **136** (7), 2905-10 (2014).
- [144] X. Cheng, J. Wu, X. Wang, B. Zhang, J. Zhu, D. Xiao, X. Wang, and X. Lou, Giant d_{33} in $(K,Na)(Nb,Sb)O_3-(Bi,Na,K,Li)ZrO_3$ based lead-free piezoelectrics with high T_c , *Applied Physics Letters* **103** (5), 052906 (2013).
- [145] R. Wang, K. Wang, F. Yao, J. F. Li, F. H. Schader, K. G. Webber, W. Jo, and J. Rödel, Temperature stability of lead - free niobate piezoceramics with engineered morphotropic phase boundary, *Journal of the American Ceramic Society* **98** (7), 2177-82 (2015).
- [146] B. Noheda, D. E. Cox, G. Shirane, J. A. Gonzalo, L. E. Cross, and S.-E. Park, A monoclinic ferroelectric phase in the $Pb(Zr_{1-x}Ti_x)O_3$ solid solution, *Applied Physics Letters* **74** (14), 2059-61 (1999).
- [147] H. Fu and R. E. Cohen, Polarization rotation mechanism for ultrahigh electromechanical response in single-crystal piezoelectrics, *Nature* **403**, 281-83 (2000).
- [148] D. Damjanovic, A morphotropic phase boundary system based on polarization rotation and polarization extension, *Applied Physics Letters* **97** (6), 062906 (2010).
- [149] B. Noheda, D. Cox, G. Shirane, S.-E. Park, L. Cross, and Z. Zhong, Polarization rotation via a monoclinic phase in the piezoelectric $92\% PbZn_{1/3}Nb_{2/3}O_3-8\% PbTiO_3$, *Physical Review Letters* **86** (17), 3891 (2001).
-

-
- [150] L. Fan, J. Chen, Y. Ren, Z. Pan, L. Zhang, and X. Xing, Unique piezoelectric properties of the monoclinic phase in $\text{Pb}(\text{Zr,Ti})\text{O}_3$ ceramics: Large lattice strain and negligible domain switching, *Physical Review Letters* **116** (2), 027601 (2016).
- [151] M. Davis, D. Damjanovic, and N. Setter, Temperature dependence of the direct piezoelectric effect in relaxor-ferroelectric single crystals: Intrinsic and extrinsic contributions, *Journal of Applied Physics* **100** (8), 084103 (2006).
- [152] B. Peng, Z. Yue, and L. Li, Evaluation of domain wall motion during polymorphic phase transition in $(\text{K,Na})\text{NbO}_3$ -based piezoelectric ceramics by nonlinear response measurements, *Journal of Applied Physics* **109** (5), 054107 (2011).
- [153] J. Fu, R. Zuo, and Z. Xu, High piezoelectric activity in $(\text{Na,K})\text{NbO}_3$ based lead-free piezoelectric ceramics: Contribution of nanodomains, *Applied Physics Letters* **99** (6), 062901 (2011).
- [154] Y. Huan, X. Wang, Z. Shen, J. Kim, H. Zhou, and L. Li, Nanodomains in KNN - based lead - free piezoelectric ceramics: origin of strong piezoelectric properties, *Journal of the American Ceramic Society* **97** (3), 700-03 (2014).
- [155] S.-E. Park and T. R. Shrout, Ultrahigh strain and piezoelectric behavior in relaxor based ferroelectric single crystals, *Journal of Applied Physics* **82** (4), 1804-11 (1997).
- [156] W. Ge, C. Luo, Q. Zhang, C. P. Devreugd, Y. Ren, J. Li, H. Luo, and D. Viehland, Ultrahigh electromechanical response in $(1-x)(\text{Na}_{0.5}\text{Bi}_{0.5})\text{TiO}_3-x\text{BaTiO}_3$ single-crystals via polarization extension, *Journal of Applied Physics* **111** (9), 093508 (2012).
- [157] W. Ge, J. Li, D. Viehland, Y. Chang, and G. L. Messing, Electric-field-dependent phase volume fractions and enhanced piezoelectricity near the polymorphic phase boundary of $(\text{K}_{0.5}\text{Na}_{0.5})_{1-x}\text{Li}_x\text{NbO}_3$ textured ceramics, *Physical Review B* **83** (22), 224110 (2011).
- [158] W. Feng, H. Du, C. Chen, and Y. Huang, Electric - field-driven phase transition process in $(\text{K,Na,Li})(\text{Nb,Ta,Sb})\text{O}_3$ lead - free piezoceramics, *Journal of the American Ceramic Society* **99** (1), 135-40 (2015).
- [159] T. Iamsasri, G. Tutuncu, C. Uthaisar, S. Wongsanmai, S. Pojprapai, and J. L. Jones, Electric field-induced phase transitions in Li-modified $\text{Na}_{0.5}\text{K}_{0.5}\text{NbO}_3$ at the polymorphic phase boundary, *Journal of Applied Physics* **117** (2), 024101 (2015).
- [160] Y. Kizaki, Y. Noguchi, and M. Miyayama, Defect control for superior properties in $(\text{K}_{0.5}\text{Na}_{0.5})\text{NbO}_3$ single crystals, *Key Engineering Materials* **350**, 85-88 (2007).
- [161] J. G. Fisher, A. Benčan, J. Holc, M. Kosec, S. Vernay, and D. Rytz, Growth of potassium sodium niobate single crystals by solid state crystal growth, *Journal of Crystal Growth* **303** (2), 487-92 (2007).
- [162] J. G. Fisher, A. Benčan, J. Godnjavec, and M. Kosec, Growth behaviour of potassium sodium niobate single crystals grown by solid-state crystal growth using $\text{K}_4\text{CuNb}_8\text{O}_{23}$ as a sintering aid, *Journal of the European Ceramic Society* **28** (8), 1657-63 (2008).
- [163] J. G. Fisher, A. Bencan, M. Kosec, S. Vernay, and D. Rytz, Growth of dense single crystals of potassium sodium niobate by a combination of solid - state crystal growth and hot pressing, *Journal of the American Ceramic Society* **91** (5), 1503-07 (2008).
- [164] J. G. Fisher, A. Benčan, J. Bernard, J. Holc, M. Kosec, S. Vernay, and D. Rytz, Growth of $(\text{Na,K,Li})(\text{Nb,Ta})\text{O}_3$ single crystals by solid state crystal growth, *Journal of the European Ceramic Society* **27** (13), 4103-06 (2007).
-

- [165] M. Jiang, C. A. Randall, H. Guo, G. Rao, R. Tu, Z. Gu, G. Cheng, X. Liu, J. Zhang, and Y. Li, Seed - free solid - state growth of large lead - free piezoelectric single crystals: $(\text{Na}_{1/2}\text{K}_{1/2})\text{NbO}_3$, *Journal of the American Ceramic Society* **98** (10), 2988-96 (2015).
- [166] H. Uršič, A. Benčan, M. Škarabot, M. Godec, and M. Kosec, Dielectric, ferroelectric, piezoelectric, and electrostrictive properties of $\text{K}_{0.5}\text{Na}_{0.5}\text{NbO}_3$ single crystals, *Journal of Applied Physics* **107** (3), 033705 (2010).
- [167] J. Yang, F. Zhang, Q. Yang, Z. Liu, Y. Li, Y. Liu, and Q. Zhang, Large piezoelectric properties in KNN-based lead-free single crystals grown by a seed-free solid-state crystal growth method, *Applied Physics Letters* **108** (18), 182904 (2016).
- [168] Y. Inagaki, K. Kakimoto, and H. Ohsato, Growth condition and ferroelectric property of Mn-doped $\text{Na}_{0.5}\text{K}_{0.5}\text{NbO}_3$ crystal, *Key Engineering Materials* **388**, 213-16 (2009).
- [169] D. Lin, Z. Li, Z. Xu, and X. Yao, Characterization of KNN single crystals by slow-cooling technique, *Ferroelectrics* **381** (1), 1-8 (2009).
- [170] M. A. Rafiq, V. Costa, M. Elisabete, and P. M. Vilarinho, Establishing the domain structure of $(\text{K}_{0.5}\text{Na}_{0.5})\text{NbO}_3$ (KNN) single crystals by piezoforce-response microscopy, *Science of Advanced Materials* **6** (3), 426-33 (2014).
- [171] R. Saravanan, D. Rajesh, S. Rajasekaran, R. Perumal, M. Chitra, and R. Jayavel, Crystal structure, dielectric properties of $(\text{K}_{0.5}\text{Na}_{0.5})\text{NbO}_3$ single crystal grown by flux method using B_2O_3 flux, *Crystal Research and Technology* **48** (1), 22-28 (2013).
- [172] G. Ray, N. Sinha, S. Bhandari, B. Singh, I. Bdikin, and B. Kumar, Flux growth of $0.94[\text{Na}_{0.5}\text{K}_{0.5}\text{NbO}_3]-0.06\text{LiNbO}_3$ piezo-/ferroelectric crystals for long duration and high temperature applications, *CrystEngComm* **16** (30), 7004-12 (2014).
- [173] G. Ray, N. Sinha, B. Singh, I. Bdikin, and B. Kumar, Lead-free relaxor ferroelectric $\text{Na}_{0.47}\text{K}_{0.47}\text{Li}_{0.06}\text{Nb}_{0.94}\text{Sb}_{0.06}\text{O}_3$ crystals for optoelectronic applications, *Crystal Growth & Design* **15** (4), 1852-60 (2015).
- [174] D. Lin, Z. Li, F. Li, C. Cai, W. Liu, and S. Zhang, Tetragonal-to-tetragonal phase transition in lead-free $(\text{K}_x\text{Na}_{1-x})\text{NbO}_3$ ($x = 0.11$ and 0.17) crystals, *Crystals* **4** (2), 113 (2014).
- [175] Y. Liu, G. S. Xu, J. F. Liu, D. F. Yang, and X. X. Chen, Dielectric, piezoelectric properties of MnO_2 -doped $(\text{K}_{0.5}\text{Na}_{0.5})\text{NbO}_3-0.05\text{LiNbO}_3$ crystal grown by flux-Bridgman method, *Journal of Alloys and Compounds* **603**, 95-99 (2014).
- [176] Y. Inagaki, K.-i. Kakimoto, and I. Kagomiya, Crystal growth and ferroelectric property of $\text{Na}_{0.5}\text{K}_{0.5}\text{NbO}_3$ and Mn-doped $\text{Na}_{0.5}\text{K}_{0.5}\text{NbO}_3$ crystals grown by floating zone method, *Journal of the European Ceramic Society* **30** (2), 301-06 (2010).
- [177] M. Bah, F. Giovannelli, R. Retoux, J. Bustillo, E. Le Clezio, and I. Monot-Laffez, Crystal growth and piezoelectric properties of lead-free based $\text{K}_{0.5}\text{Na}_{0.5}\text{NbO}_3$ by floating zone method (FZM), *Crystal Growth & Design* **16** (1), 315-24 (2016).
- [178] H. Tian, Z. Zhou, D. Gong, H. Wang, D. Liu, and Y. Jiang, Growth and optical properties of paraelectric $\text{K}_{1-y}\text{Na}_y\text{Ta}_{1-x}\text{Nb}_x\text{O}_3$ single crystals, *Applied Physics B* **91** (1), 75-78 (2008).
- [179] L. M. Zheng, X. Q. Huo, R. Wang, J. J. Wang, W. H. Jiang, and W. W. Cao, Large size lead-free $(\text{Na,K})(\text{Nb,Ta})\text{O}_3$ piezoelectric single crystal: Growth and full tensor properties, *CrystEngComm* **15** (38), 7718-22 (2013).

-
- [180] H. Deng, X. Y. Zhao, H. W. Zhang, C. Chen, X. B. Li, D. Lin, B. Ren, J. Jiao, and H. S. Luo, Orientation dependence of electrical properties of large-sized sodium potassium niobate lead-free single crystals, *CrystEngComm* **16** (13), 2760-65 (2014).
- [181] P. Bednyakov, D. Rytz, and N. Setter, Dielectric and piezoelectric properties of $\text{K}(\text{Ta}_{0.51}\text{Nb}_{0.49})\text{O}_3$ single crystal, *Ferroelectrics* **447** (1), 108-16 (2013).
- [182] X. Q. Huo, L. M. Zheng, S. J. Zhang, R. Zhang, G. Liu, R. Wang, B. Yang, W. W. Cao, and T. R. ShROUT, Growth and properties of Li, Ta modified (K,Na)NbO₃ lead-free piezoelectric single crystals, *physica status solidi: Rapid Research Letters* **8** (1), 86-90 (2014).
- [183] J. J. Wang, L. M. Zheng, B. Yang, R. Wang, X. Q. Huo, S. J. Sang, J. Wu, Y. F. Chang, H. P. Ning, and T. Q. Lv, Growth and characterization of lead-free ferroelectric (K,Na,Li)(Nb,Ta,Sb)O₃ single crystal, *Journal of Crystal Growth* **409**, 39-43 (2015).
- [184] X. Huo, R. Zhang, L. Zheng, S. Zhang, R. Wang, J. Wang, S. Sang, B. Yang, and W. Cao, (K,Na,Li)(Nb,Ta)O₃:Mn lead-free single crystal with high piezoelectric properties, *Journal of the American Ceramic Society* **98** (6), 1829-35 (2015).
- [185] L. M. Zheng, S. Y. Li, S. J. Sang, J. J. Wang, X. Q. Huo, R. Wang, Z. Y. Yuan, and W. W. Cao, Complete set of material constants of single domain (K,Na)(Nb,Ta)O₃ single crystal and their orientation dependence, *Applied Physics Letters* **105** (21), 212902 (2014).
- [186] D. Lin, Z. Li, S. Zhang, Z. Xu, and X. Yao, Influence of MnO₂ doping on the dielectric and piezoelectric properties and the domain structure in (K_{0.5}Na_{0.5})NbO₃ single crystals, *Journal of the American Ceramic Society* **93** (4), 941-44 (2010).
- [187] Y. Kizaki, Y. Noguchi, and M. Miyayama, Defect control for low leakage current in K_{0.5}Na_{0.5}NbO₃ single crystals, *Applied Physics Letters* **89** (14), 142910 (2006).
- [188] Y. Noguchi and M. Miyayama, Effect of Mn doping on the leakage current and polarization properties in K_{0.14}Na_{0.86}NbO₃ ferroelectric single crystals, *Journal of the Ceramic Society of Japan* **118** (1380), 711-16 (2010).
- [189] L. M. Zheng, J. J. Wang, X. Q. Huo, R. Wang, S. J. Sang, S. Y. Li, P. Zheng, and W. W. Cao, Temperature dependence of dielectric and electromechanical properties of (K,Na)(Nb,Ta)O₃ single crystal and corresponding domain structure evolution, *Journal of Applied Physics* **116** (4), 044105 (2014).
- [190] F. Rubio-Marcos, A. Del Campo, R. López-Juárez, J. J. Romero, and J. F. Fernández, High spatial resolution structure of (K,Na)NbO₃ lead-free ferroelectric domains, *Journal of Materials Chemistry* **22** (19), 9714-20 (2012).
- [191] Y. Inagaki, K. i. Kakimoto, and I. Kagomiya, Ferroelectric domain characterization of orthorhombic sodium–potassium niobate piezoelectric crystals, *Journal of the American Ceramic Society* **93** (12), 4061-65 (2010).
- [192] H. Deng, H. Zhang, X. Zhao, C. Chen, X. a. Wang, X. Li, D. Lin, B. Ren, J. Jiao, and H. Luo, Direct observation of monoclinic ferroelectric phase and domain switching process in (K_{0.25}Na_{0.75})NbO₃ single crystals, *CrystEngComm* **17** (14), 2872-77 (2015).
- [193] A. Reisman and E. Banks, Reactions of the group VB pentoxides. VIII. thermal, density and X-ray studies of the systems KNbO₃-NaNbO₃ and KTaO₃-KNbO₃, *Journal of the American Chemical Society* **80** (8), 1877-82 (1958).
- [194] A. Reisman, S. Triebwasser, and F. Holtzberg, Phase diagram of the system KNbO₃-KTaO₃ by the methods of differential thermal and resistance analysis, *Journal of the American Chemical Society* **77** (16), 4228-30 (1955).
-

-
- [195] P. Veber, F. Benabdallah, H. Liu, G. Buse, M. Josse, and M. Maglione, Growth and characterization of lead-free piezoelectric single crystals, *Materials* **8** (11), 7962-78 (2015).
- [196] R. Guinebretière, *X-ray diffraction by polycrystalline materials*. (John Wiley & Sons, 2013).
- [197] B. Ouladdiaf, J. Archer, G. McIntyre, A. Hewat, D. Brau, and S. York, OrientExpress: A new system for Laue neutron diffraction, *Physica B: Condensed Matter* **385**, 1052-54 (2006).
- [198] T. Schenk, E. Yurchuk, S. Mueller, U. Schroeder, S. Starschich, U. Böttger, and T. Mikolajick, About the deformation of ferroelectric hystereses, *Applied Physics Reviews* **1** (4), 041103 (2014).
- [199] E. Sapper, *Lead-free (1-x)(Bi_{1/2}Na_{1/2})TiO₃-xBaTiO₃: the impact of relaxor characteristics and induced long range order on piezoelectric properties*. (VVB Laufersweiler Verlag, 2014).
- [200] G. Long, J. Stevens, and L. Bowen, 121 Sb Mössbauer spectra of antimony oxides, *Inorganic and Nuclear Chemistry Letters* **5** (10), 799-804 (1969).
- [201] B. Wanklyn and B. Watts, Nucleation sites on platinum surfaces in flux growth, *Materials Research Bulletin* **19** (6), 711-16 (1984).
- [202] A. Magneli, Crystal structure studies on tetragonal sodium tungsten bronze, *Arkiv for Kemi* **1** (3), 269-72 (1949).
- [203] P. Rudolph, in *Springer Handbook of Crystal Growth* (Springer, 2010), pp. 159-201.
- [204] H. J. Scheel and T. Fukuda, *Crystal growth technology*. (Wiley Online Library, 2003).
- [205] E. Scheil, Bemerkungen zur schichtkristall bildung, *Z. Metallk* **34**, 70-83 (1942).
- [206] W. Y. Lee, Y. W. Bae, and D. E. Stinton, Na₂SO₄ - induced corrosion of Si₃N₄ coated with chemically vapor deposited Ta₂O₅, *Journal of the American Ceramic Society* **78** (7), 1927-30 (1995).
- [207] T. Fukuda and H. Hirano, Capillary liquid epitaxial growth of LiNbO₃ and LiTaO₃ single - crystal thin films, *Applied Physics Letters* **28** (10), 575-77 (1976).
- [208] R. Hofmeister, A. Yariv, and A. Agranat, Growth and characterization of the perovskite K_{1-y}Li_yTa_{1-x}Nb_xO₃: Cu, *Journal of Crystal Growth* **131** (3-4), 486-94 (1993).
- [209] A. Sadel, R. Von der Mühl, J. Ravez, J. Chaminade, and P. Hagenmuller, Synthèse et étude des transitions de phases de céramiques et de cristaux de composition Li_{0,02}Na_{0,98}NbO₃, *Solid State Communications* **44** (3), 345-49 (1982).
- [210] J. Ravez and A. Simon, Lead-free relaxor ferroelectrics with 'TTB' structure, *Comptes Rendus Chimie* **5** (3), 143-48 (2002).
- [211] T. Fukuda, Structural and dielectric studies of ferroelectric K₃Li₂(Ta_xNb_{1-x})₅O₁₅, *Japanese Journal of Applied Physics* **9** (6), 599 (1970).
- [212] T. Ikeda and K. Kiyohashi, Study of subsolidus equilibria in K₂O-Li₂O-Nb₂O₅ system, *Japanese Journal of Applied Physics* **9** (12), 1541 (1970).
- [213] M. Cochez, M. Ferriol, L. Pöppel, K. Polgár, and Á. Péter, Ternary system Li₂O-K₂O-Nb₂O₅: Part I: Phase equilibria around the lithium niobate existence field, *Journal of Alloys and Compounds* **386** (1), 238-45 (2005).
- [214] B. Scott, E. Giess, B. Olson, G. Burns, A. Smith, and D. O'kane, The tungsten bronze field in the system K₂O|Li₂O|Nb₂O₅, *Materials Research Bulletin* **5** (1), 47-56 (1970).
-

-
- [215] J. Fu, R. Zuo, X. Fang, and K. Liu, Lead-free ceramics based on alkaline niobate tantalate antimonate with excellent dielectric and piezoelectric properties, *Materials Research Bulletin* **44** (5), 1188-90 (2009).
- [216] K. Nakamura, T. Tokiwa, and Y. Kawamura, Domain structures in KNbO₃ crystals and their piezoelectric properties, *Journal of Applied Physics* **91** (11), 9272-76 (2002).
- [217] S. Lu, Z. Xu, K. Kwok, and H. L. Chan, Hot-stage transmission electron microscopy study of (Na,K)NbO₃ based lead-free piezoceramics, *Applied Physics Letters* **105** (4), 042904 (2014).
- [218] G. E. McGuire, G. K. Schweitzer, and T. A. Carlson, Core electron binding energies in some Group IIIA, VB, and VIB compounds, *Inorganic Chemistry* **12** (10), 2450-53 (1973).
- [219] H. E. Mgbemere, M. Hinterstein, and G. A. Schneider, Electrical and structural characterization of (K_xNa_{1-x})NbO₃ ceramics modified with Li and Ta, *Journal of Applied Crystallography* **44** (5), 1080-89 (2011).
- [220] K. i. Kakimoto, K. Akao, Y. Guo, and H. Ohsato, Raman scattering study of piezoelectric (Na_{0.5}K_{0.5})NbO₃-LiNbO₃ ceramics, *Japanese Journal of Applied Physics* **44** (9S), 7064 (2005).
- [221] S. Sang, Z. Yuan, L. Zheng, E. Sun, R. Zhang, J. Wang, R. Wang, B. Yang, and M. Liu, Optical transmittance and Raman scattering studies of (K,Na)(Nb,Ta)O₃ single crystal, *Optical Materials* **45**, 104-08 (2015).
- [222] Q. Zhang, B. Zhang, H. Li, and P. Shang, Effects of Na/K ratio on the phase structure and electrical properties of Na_xK_{1-x}NbO₃ lead-free piezoelectric ceramics, *Rare Metals* **29** (2), 220-25 (2010).
- [223] W. Jiagang, X. Dingquan, Z. Jianguo, Y. Ping, and W. Yuanyu, Effects of K content on the dielectric, piezoelectric, and ferroelectric properties of 0.95(K_xNa_{1-x})NbO₃-0.05LiSbO₃ lead-free ceramics, *Journal of Applied Physics* **103** (2), 024102 (2008).
- [224] L. Wu, J. L. Zhang, C. L. Wang, and J. C. Li, Influence of compositional ratio K/Na on physical properties in (K_xNa_{1-x})NbO₃ ceramics, *Journal of Applied Physics* **103** (8), 084116 (2008).
- [225] G. Viola, T. Saunders, X. Wei, K. B. Chong, H. Luo, M. J. Reece, and H. Yan, Contribution of piezoelectric effect, electrostriction and ferroelectric/ferroelastic switching to strain-electric field response of dielectrics, *Journal of Advanced Dielectrics* **03** (01), 1350007 (2013).
- [226] A. Achuthan and C. T. Sun, A study of mechanisms of domain switching in a ferroelectric material via loading rate effect, *Acta Materialia* **57** (13), 3868-75 (2009).
- [227] J. Zhang, W. Hao, Y. Gao, Y. Qin, Y. Tan, and C. Wang, Large decrease of characteristic frequency of dielectric relaxation associated with domain-wall motion in Sb⁵⁺-modified (K,Na)NbO₃-based ceramics, *Applied Physics Letters* **101** (25), 252905 (2012).
- [228] B.-Q. Ming, J.-F. Wang, P. Qi, and G.-Z. Zang, Piezoelectric properties of (Li,Sb,Ta) modified (Na,K)NbO₃ lead-free ceramics, *Journal of Applied Physics* **101** (5), 054103 (2007).
- [229] J. Glaum, T. Granzow, and J. Rödel, Evaluation of domain wall motion in bipolar fatigued lead-zirconate-titanate: A study on reversible and irreversible contributions, *Journal of Applied Physics* **107** (10), 104119 (2010).
- [230] S. Schaab and T. Granzow, Temperature dependent switching mechanism of (Pb_{0.92}La_{0.08})(Zr_{0.65}Ti_{0.35})O₃ investigated by small and large signal measurements, *Applied Physics Letters* **97** (13), 132902 (2010).
- [231] Z. Luo, J. Glaum, T. Granzow, W. Jo, R. Dittmer, M. Hoffman, and J. Rödel, Bipolar and unipolar fatigue of ferroelectric BNT - based lead - free piezoceramics, *Journal of the American Ceramic Society* **94** (2), 529-35 (2011).
-

-
- [232] K. Wang and J.-F. Li, Domain engineering of lead-free Li-modified (K,Na)NbO₃ polycrystals with highly enhanced piezoelectricity, *Advanced Functional Materials* **20** (12), 1924-29 (2010).
- [233] F. Rubio-Marcos, J. J. Romero, D. A. Ochoa, J. E. García, R. Perez, and J. F. Fernandez, Effects of Poling Process on KNN-Modified Piezoceramic Properties, *Journal of the American Ceramic Society* **93** (2), 318-21 (2010).
- [234] P. Lippens, Mössbauer isomer shifts of crystalline antimony compounds, *Solid State Communications* **113** (7), 399-403 (2000).
- [235] M. Korolenko, P. Fabrichnyi, M. Afanasov, and C. Labrugère, Manifestation of the photocatalytic activity of anatase powders in Mössbauer spectra of ¹²¹Sb probe nuclei, *Bulletin of the Russian Academy of Sciences: Physics* **79** (8), 1055-57 (2015).
- [236] H. J. Trodahl, N. Klein, D. Damjanovic, N. Setter, B. Ludbrook, D. Rytz, and M. Kuball, Raman spectroscopy of (K,Na)NbO₃ and (K,Na)_{1-x}Li_xNbO₃, *Applied Physics Letters* **93** (26), 262901 (2008).
- [237] R. Zuo, J. Fu, D. Lv, and Y. Liu, Antimony tuned rhombohedral - orthorhombic phase transition and enhanced piezoelectric properties in sodium potassium niobate, *Journal of the American Ceramic Society* **93** (9), 2783-87 (2010).
- [238] M. Maglione, G. Philippot, D. Levasseur, S. Payan, C. Aymonier, and C. Elissalde, Defect chemistry in ferroelectric perovskites: Long standing issues and recent advances, *Dalton Transactions* **44** (30), 13411-18 (2015).
- [239] A. Pramanick, A. D. Prewitt, J. S. Forrester, and J. L. Jones, Domains, domain walls and defects in perovskite ferroelectric oxides: A review of present understanding and recent contributions, *Critical Reviews in Solid State and Materials Sciences* **37** (4), 243-75 (2012).
- [240] V. Atuchin, O. Alekseeva, V. Kesler, L. Pokrovsky, N. Sorokina, and V. Voronkova, Chemical shifts of atomic core levels and structure of K_{1-x}Ti_{1-x}Sb_xOPO₄, x = 0-0.23, solid solutions, *Journal of Solid State Chemistry* **179** (8), 2349-55 (2006).
- [241] S. Zhang, L. Lebrun, S. Rhee, R. E. Eitel, C. A. Randall, and T. R. Shrout, Crystal growth and characterization of new high Curie temperature (1-x)BiScO₃-xPbTiO₃ single crystals, *Journal of Crystal Growth* **236** (1), 210-16 (2002).
- [242] S.-E. E. Park and W. Hackenberger, High performance single crystal piezoelectrics: Applications and issues, *Current Opinion in Solid State and Materials Science* **6** (1), 11-18 (2002).
- [243] M. A. Rafiq, M. E. Costa, A. Tkach, and P. M. Vilarinho, Impedance analysis and conduction mechanisms of lead free potassium sodium niobate (KNN) single crystals and polycrystals: a comparison study, *Crystal Growth & Design* **15** (3), 1289-94 (2015).
- [244] M. Raymond and D. Smyth, Defects and charge transport in perovskite ferroelectrics, *Journal of Physics and Chemistry of Solids* **57** (10), 1507-11 (1996).
- [245] D. Smyth, The role of impurities in insulating transition metal oxides, *Progress in Solid State Chemistry* **15** (3), 145-71 (1984).
- [246] D. Smyth, Comment on electrical properties and defect structure of barium metatitanate within the p-type regime, *Journal of the European Ceramic Society* **9** (6), 463-65 (1992).
- [247] S. Takahashi, Effects of impurity doping in lead zirconate-titanate ceramics, *Ferroelectrics* **41** (1), 143-56 (1982).
- [248] T. Yang, V. Gopalan, P. Swart, and U. Mohideen, Direct observation of pinning and bowing of a single ferroelectric domain wall, *Physical Review Letters* **82** (20), 4106 (1999).
-

-
- [249] J. Scott and M. Dawber, Oxygen-vacancy ordering as a fatigue mechanism in perovskite ferroelectrics, *Applied Physics Letters* **76** (25), 3801-03 (2000).
- [250] T. Rojac, M. Kosec, B. Budic, N. Setter, and D. Damjanovic, Strong ferroelectric domain-wall pinning in BiFeO₃ ceramics, *Journal of Applied Physics* **108** (7), 074107 (2010).
- [251] X. Ren, Large electric-field-induced strain in ferroelectric crystals by point-defect-mediated reversible domain switching, *Nature Materials* **3** (2), 91-94 (2004).
- [252] H. Fan, G.-T. Park, J.-J. Choi, and H.-E. Kim, Effect of annealing atmosphere on domain structures and electromechanical properties of Pb(Zn_{1/3}Nb_{2/3})O₃-based ceramics, *Applied Physics Letters* **79** (11), 1658-60 (2001).
- [253] V. Y. Shur, E. Shishkin, E. Rumyantsev, E. Nikolaeva, A. Shur, R. Batchko, M. Fejer, K. Gallo, S. Kurimura, and K. Terabe, Self-organization in LiNbO₃ and LiTaO₃: Formation of micro-and nano-scale domain patterns, *Ferroelectrics* **304** (1), 111-16 (2004).
- [254] V. Laguta, I. Kondakova, I. Bykov, M. Glinchuk, A. Tkach, P. Vilarinho, and L. Jastrabik, Electron spin resonance investigation of Mn²⁺ ions and their dynamics in Mn-doped SrTiO₃, *Physical Review B* **76** (5), 054104 (2007).
- [255] R.-A. Eichel, Defect structure of oxide ferroelectrics-valence state, site of incorporation, mechanisms of charge compensation and internal bias fields, *Journal of Electroceramics* **19** (1), 11-23 (2007).
- [256] H. Kaftelen, D. E. Kanar, S. Repp, S. Weber, and E. Erdem, Investigation of Mn-doped sodium-potassium niobate (K,Na)NbO₃ ceramics by EPR and impedance spectroscopic methods, *Ferroelectrics* **494** (1), 11-18 (2016).
- [257] R. Maier, T. Pomorski, P. Lenahan, and C. Randall, Acceptor-oxygen vacancy defect dipoles and fully coordinated defect centers in a ferroelectric perovskite lattice: Electron paramagnetic resonance analysis of Mn²⁺ in single crystal BaTiO₃, *Journal of Applied Physics* **118** (16), 164102 (2015).
- [258] M. Suzuki, A. Morishita, Y. Kitanaka, Y. Noguchi, and M. Miyayama, Polarization and piezoelectric properties of high performance bismuth sodium titanate single crystals grown by high-oxygen-pressure flux method, *Japanese Journal of Applied Physics* **49** (9S), 09MD09 (2010).
- [259] Z. Yu, R. Guo, and A. Bhalla, Dielectric behavior of Ba(Ti_{1-x}Zr_x)O₃ single crystals, *Journal of Applied Physics* **88**, 410-15 (2000).
- [260] R. Sun, X. Zhao, Q. Zhang, B. Fang, H. Zhang, X. Li, D. Lin, S. Wang, and H. Luo, Growth and orientation dependence of electrical properties of 0.92Na_{0.5}Bi_{0.5}TiO₃-0.08K_{0.5}Bi_{0.5}TiO₃ lead-free piezoelectric single crystal, *Journal of Applied Physics* **109** (12), 124113 (2011).
- [261] N. Setter and L. E. Cross, The role of B-site cation disorder in diffuse phase transition behavior of perovskite ferroelectrics, *Journal of Applied Physics* **51** (8), 4356-60 (1980).
- [262] Y. Huan, X. Wang, J. Koruza, K. Wang, K. G. Webber, Y. Hao, and L. Li, Inverted electro-mechanical behaviour induced by the irreversible domain configuration transformation in (K,Na)NbO₃-based ceramics, *Scientific reports* **6** (2016).
- [263] D. Wang, M. Cao, and S. Zhang, Piezoelectric ceramics in the PbSnO₃-Pb(Mg_{1/3}Nb_{2/3})O₃-PbTiO₃ ternary system, *Journal of the American Ceramic Society* **94** (11), 3690-93 (2011).
- [264] V. Y. Topolov, Anisotropy of electromechanical properties in KNbO₃ crystals with S-type domain boundaries, *Journal of Physics: Condensed Matter* **7** (37), 7405 (1995).
- [265] R. E. Newnham, *Properties of materials: Anisotropy, symmetry, structure*. (OUP Oxford, 2004).
-



[266] D. B. Williams and C. B. Carter, (Plenum, New York, 1996).



Author Declaration

I hereby declare that this thesis is my own work and effort. This is a true copy of the thesis, including any required final versions, as accepted by my examiners. I understand that my thesis may be made electronically available to the public.

Darmstadt, September 1, 2016

(Hairui Liu)



Curriculum Vitae

Education

- **PhD student:** **October 2013 – Present**

Supported by Erasmus Mundus IDS-FunMat international School and co-supervised by
Department of Material- and Geoscience, *Technische Universität Darmstadt*, Darmstadt, Germany
Institut de Chimie de la Matière Condensée de Bordeaux, *University of Bordeaux*, Bordeaux, France
- **Master of Science:** **September 2010 – July 2013**

Department of Chemistry, *Tsinghua University*, Beijing, China
- **Bachelor of Engineering:** **September 2006 - June 2010**

School of Materials Science and Engineering, *Wuhan University of Technology*, Wuhan, China

Publications

- [Hairui Liu](#), Jurij Koruza, Philippe Veber, Daniel Rytz, Mario Maglione, and Jürgen Rödel, “Orientation dependence of electromechanical properties of Mn-doped (Li,Na,K)(Nb,Ta)O₃ single crystals”, *Applied Physics Letters*, **109** 152902 (2016).
- [Hairui Liu](#), Philippe Veber, Jurij Koruza, Daniel Rytz, Michael Josse, Jürgen Rödel, and Mario Maglione, “Influence of Ta⁵⁺ content on the crystallographic structure and electrical properties of [001]_{PC}-oriented (Li,Na,K)(Nb,Ta)O₃ single crystals”, *CrystEngComm*, **18** 2081-8 (2016).
- [Hairui Liu](#), Matias Acosta, Alexander Zintler, Jurij Koruza, Leopoldo Molina-Luna, Philippe Veber, Eric A Patterson, Mario Maglione, and Jürgen Rödel, “Domain morphology in [111]_{PC} oriented (K,Na,Li)(Nb,Ta)O₃ single crystals”, *Journal of the American Ceramic Society*, **99** back cover (2016). (2015 ACerS Ceramographic Exhibit & Competition Category: Optical Microscopy, 1st Place)
- [Hairui Liu](#), Qiang Li, Yuanyuan Li, Nengneng Luo, Jaeshik Shim, Jinghan Gao, Qingfeng Yan, Yiling Zhang, and Xiangcheng Chu, “Structure evolution and electrical properties of Y³⁺ doped Ba_{1-x}Ca_xZr_{0.07}Ti_{0.93}O₃ ceramics”, *Journal of the American Ceramic Society*, **97** 2076-81 (2014).
- [Hairui Liu](#), Qiang Li, Jun Ma, and Xiangcheng Chu, “Effects of Bi³⁺ content and grain size on electrical properties of SrBi₂Ta₂O₉ ceramic”, *Materials Letters*, **76** 21-4 (2012).
- Yongping Pu, Mouteng Yao, [Hairui Liu](#), and Till Frömling, “Phase transition behavior, dielectric and ferroelectric properties of (1-x)(Bi_{0.5}Na_{0.5})TiO₃-x(Ba_{0.85}Ca_{0.15})(Ti_{0.9}Zr_{0.1})O₃ ceramics”, *Journal of the European Ceramic Society*, **36** 2461-8 (2016).
- Philippe Veber, Feres Benabdallah, [Hairui Liu](#), Gabriel Buse, Michael Josse, and Mario Maglione, “Growth and characterization of lead-free piezoelectric single crystals”, *Materials*, **8** 7962-78 (2015).
- Jinghan Gao, Qiang Li, [Hairui Liu](#), Jaeshik Shim, Qingfeng Yan, Yiling Zhang, and Xiangcheng Chu, “Enhanced temperature stability in Tb-doped (Ba_{0.99}Ca_{0.01})(Ti_{0.98}Zr_{0.02})O₃ lead free ceramics”, *Ceramics International*, **41** 2497-501 (2015).
- Zhao Deng, Ying Dai, [Hairui Liu](#), and Wen Chen, “Large scale synthesis of BaTiO₃ nanorods by a template way”, *Advanced Materials Research*, **79-82** 373-6 (2009).

Conference Contributions

International:

- [Hairui Liu](#), Jurij Koruza, Philippe Veber, Daniel Rytz, and Mario Maglione, “Investigations on Mn-doped (K,Na,Li)(Ta,Nb)O₃ lead-free piezoelectric single crystals”, *2016 Joint IEEE International Symposium on the Applications of Ferroelectrics, European Conference on Applications of Polar Dielectrics & Workshop on Piezoresponse Force Microscopy (ISAF/ECAPD/PFM)*, Darmstadt, Germany, August 2016. (Oral talk)
- [Hairui Liu](#), Philippe Veber, Alexander Zintler, Jurij Koruza, Leopoldo Molina-Luna, Daniel Rytz, Jurgen Rodel, and Mario Maglione, “Growth, characterization and domain configuration of (Li,Na,K)(Ta,Nb)O₃ single crystals”, *18th International Conference on Crystal Growth and Epitaxy*, Nagoya, Japan, August 2016. (Oral talk and poster)
- [Hairui Liu](#), Jurij Koruza, Philippe Veber, Daniel Rytz, Mario Maglione, and Jürgen Rödel, “Influence of Ta⁵⁺ content on structure and electrical properties of [001]_{pc}-oriented (K,Na,Li)(Nb,Ta)O₃ lead-free single crystals”, *European Meeting on Ferroelectricity*, Porto, Portugal, May 2015. (Oral talk)
- [Hairui Liu](#), Philippe Veber, Jurij Koruza, Michaël Josse, Daniel Rytz, Jürgen Rödel, and Mario Maglione, “Characterizations of Li-, Ta-doped KNN piezoelectric single crystals grown by flux method”, *4th Chinese-French Symposium on Advanced Materials*, Beijing, China, October 2014. (Poster)

Local:

- [Hairui Liu](#), Philippe Veber, Jurij Koruza, Michaël Josse, Daniel Rytz, Jürgen Rödel, and Mario Maglione, “Characterizations of Li-, Ta-doped KNN piezoelectric single crystals grown by flux method”, *Cristech 2014*, Autran, France, October 2014. (Poster)

IDS-FunMat Training School and Annual Meeting:

- [Hairui Liu](#), Jurij Koruza, Philippe Veber, Daniel Rytz, Mario Maglione, and Jürgen Rödel, “Orientation-dependent electromechanical properties of Mn-doped (K,Na,Li)(Nb,Ta)O₃ lead-free single crystals”, *IDS-FunMat 6th Training School and Annual Meeting*, Bordeaux, France, March 2016. (Oral talk and poster)
- [Hairui Liu](#), Jurij Koruza, Philippe Veber, Daniel Rytz, Mario Maglione, and Jürgen Rödel, “Influence of Ta⁵⁺ content on structure and electrical properties of [001]_{pc}-oriented (K,Na,Li)(Nb,Ta)O₃ lead-free single crystals”, *IDS-FunMat 5th Training School and Annual Meeting*, Vallendar, Germany, March 2015. (Oral talk and poster)
- [Hairui Liu](#), Mario Maglione, Jürgen Rödel, Philippe Veber, Jurij Koruza, and Daniel Rytz, “Lead-free polycrystals and single crystals for piezoelectric applications”, *IDS-FunMat 4th Training School*, Spa, Belgium, March 2014. (Oral talk)

Seminar

- [Hairui Liu](#), “Growth and characterization of (K,Na)NbO₃-based lead-free piezoelectric single crystals”, Bordeaux, France, March 2016.

Titre: Cristallogenèse et caractérisations de monocristaux piézoélectriques sans plomb à base de KNN

Résumé: Cette thèse vise à trouver des approches possibles pour l'amélioration des propriétés électromécaniques de monocristaux piézoélectriques à base de KNN. La TSSG et la SSSG sont entreprises afin de faire croître des monocristaux. La conclusion de l'aspect de croissance cristalline est: (1) Pour chaque élément pris individuellement, leurs coefficients de ségrégation reposent fortement sur leurs concentrations initiales dans la solution liquide. (2) La compétition entre éléments occupant le même site du réseau est démontrée. (3) Le très faible coefficient de ségrégation de Li dans la matrice KNN est responsable de l'apparition d'une phase secondaire présentant la structure bronze de tungstène quadratique. (4) Les régions optiquement laiteuses observées dans les monocristaux diminuent la réponse électrique et peuvent être réduites par traitement thermique et refroidissement lent. Dans la deuxième partie, nous avons utilisé trois approches pour améliorer le comportement piézo/ferroélectrique des monocristaux à base de KNN. La Ta ou Sb substitution indique qu'une réponse électromécanique améliorée est obtenue lorsque la transition orthorhombique-quadratique est à proximité de la température ambiante. Le traitement thermique sous atmosphère d'O₂ pur a conduit au doublement de la valeur du coefficient piézoélectrique et des paramètres ferroélectriques d'un monocristal de (K,Na,Li)(Ta,Nb,Sb)O₃. Son coefficient piézoélectrique à la température ambiante, qui constitue un record mondial à l'heure actuelle vis-à-vis de ce qui est reporté dans la littérature internationale, vaut 732 pC/N. La troisième approche consiste au dopage des monocristaux de (K,Na,Li)(Ta,Nb)O₃ avec Mn.

Mots clés: Croissance de la solution à haute température, KNN, monocristal, perovskite, ferroélectrique, piézoélectrique

Title: Growth and Characterization of Lead-free (K,Na)NbO₃-based Piezoelectric Single Crystals

Abstract: The thesis aims to find possible approaches for improved electromechanical properties in KNN-based piezoelectric single crystals. Both submerged-seed and top-seeded solution growth techniques were employed to produce single crystals. Conclusions from the crystal growth aspect are: (i) For individual elements, segregation coefficients highly rely on the initial concentration in the liquid solution. (ii) A competition between elements occupied on the same lattice site was found. (iii) The very low Li segregation coefficient in the KNN matrix is responsible for the occurrence of a secondary phase with the tetragonal tungsten bronze structure. (iv) Observed optically-cloudy regions in as-grown crystals decrease the electrical response and can be reduced by thermal treatment with slow cooling. In the second part, we used three approaches to enhance the piezoelectric and ferroelectric behavior of KNN-based single crystals. Ta or Sb substitutions indicates that enhanced electromechanical response is achieved when the orthorhombic-tetragonal phase transition is near room temperature. Thermal treatment in pure O₂ atmosphere resulted in a twofold increase of the piezoelectric coefficient and ferroelectric parameters of a (K,Na,Li)(Ta,Nb,Sb)O₃ single crystal. The highest room-temperature piezoelectric coefficient in annealed KNN-based single crystals of 732 pC/N was obtained. The third approach, doping with Mn ions in (K,Na,Li)(Ta,Nb)O₃ single crystals, is also presented.

Keywords: High temperature solution growth, KNN, single crystal, perovskite, ferroelectric, piezoelectric

Unité de recherche

ICMCB, UPR 9048, 87 av. Du Dr. Schweitzer, 33608 PESSAC CEDEX